

NOTE TO USERS

This reproduction is the best copy available.

UMI[®]

THE HEAT TRANSFER AND THE SOOT DEPOSITION CHARACTERISTICS
IN DIESEL ENGINE EXHAUST GAS RECIRCULATION SYSTEM
COOLING DEVICES

By

BASEL ISMAIL A. ISMAIL, B.Sc., M.Sc.

A Thesis

Submitted to the School of Graduate Studies

in Partial Fulfillment of the Requirements

for the Degree

Doctor of Philosophy

McMaster University

© Copyright by Basel Ismail A. Ismail, September 2004

THE HEAT TRANSFER & SOOT DEPOSITION
IN EGR COOLING DEVICES

DOCTOR OF PHILOSOPHY (2004)
(Mechanical Engineering)

MCMASTER UNIVERSITY
Hamilton, Ontario

TITLE: The Heat Transfer and the Soot Deposition Characteristics in
 Diesel Engine Exhaust Gas Recirculation System Cooling
 Devices

AUTHOR: Basel Ismail A. Ismail, B.Sc., M.Sc.
 (King Fahd University of Petroleum & Minerals)

SUPERVISORS: Dr. Daniel Ewing, Dr. Jen-Shih Chang

NUMBER OF PAGES: xxv, 240

Abstract

Exhaust gas recirculation (EGR) cooling devices are used in EGR systems to significantly reduce NO_x emissions from diesel engines. However, the thermal and hydraulic performances of these devices change over time during operation due to the deposition of soot from the diesel exhaust gas in these devices. The objective of this work was to investigate in detail the heat transfer and the soot deposition characteristics in diesel engine EGR cooling devices.

Controlled soot deposition tests were performed on a series of generic single-tube and three-tube EGR cooling devices that were exposed to exhaust gas for different periods of times in the diesel exhaust test facility to investigate the time-dependent heat transfer and pressure drop characteristics of these devices. A non-destructive technique was developed to characterize the three-dimensional soot layers that occurred in the EGR cooling devices using the neutron radiography test facility of the McMaster Nuclear Reactor.

The results showed that the deposited soot layer in the single-tube devices was much larger for the higher flow rate which corresponded to turbulent flow, particularly in the entrance region. The thickness of the deposited soot in the entrance region of the tube was much larger than the remainder of the tube, and appeared to restrict the flow area by up to 75% over a length of 4 tube diameters. The variation in the deposited soot thickness throughout the rest of the tube is similar in magnitude to the layer itself indicating that the soot layer in the tube was three-dimensional. The results also showed that the profiles of the

deposited soot had a wave-like structure in all cases. The thermal effectiveness of the devices decreased from approximately 82% to 71% over 5 hours for the laminar flow test case, and from 70% to 35% for the turbulent flow test. The pressure drop across these devices increased by up to 320% during the 5 hours of testing.

Measurements were also performed using three-tube EGR cooling devices with 45° and 60° expansion angle inlet headers exposed to diesel exhaust for 3 hours. The soot deposition was more evenly distributed in the tube bundle with the 60° expansion angle inlet header suggesting that the flow may be more evenly distributed in this device. There was more soot deposited in the center tube than outer tubes in the three-tube bundle with the 45° expansion angle inlet header suggesting that the flow was not evenly distributed. The thermal effectiveness in both cooling devices decreased during the 3 hours of testing, but the change in the effectiveness was larger for the device with the 45° expansion angle inlet header. The pressure change in the exhaust gas across the cooling devices increased more rapidly for the device with the 45° expansion inlet header, reaching a nearly constant value of nearly 5 times the initial value after 3 hours.

Acknowledgements

As this work is coming to a completion, I would like to acknowledge a number of groups of people for their contributions and support throughout my doctoral project. I would like to sincerely thank my thesis co-supervisors Dr. Daniel Ewing and Dr. Jen-Shih Chang for their research guidance and supervision during this endeavor, and for motivating my research intellectuality through interaction and discussion. I would also like to thank the members of my Ph.D. supervisory committee, Dr. Ross L. Judd and Chan Y. Ching for their valuable input and supervision.

This project was partly supported by the Center for Research in Earth and Space Technologies (CRESTech), CFI, and Dana-Long Manufacturing Ltd. of Canada, whose financial support is appreciated. I acknowledge the technical assistance and facilities related to this investigation, provided by the staff of the Department of Mechanical Engineering including the workshop, and the staff of the McMaster Nuclear Research Building.

I would like to thank my colleagues and friends from various research laboratory groups at McMaster University for their active discussions and friendship, including the Pollution Control Research Laboratory (PCRL), the Thermal-Hydraulics and Electro-Hydrodynamics Laboratory (THL-EHL), and the Thermal Management Research Laboratory (TMRL). My former colleagues, friends, and professors at KFUPM are also acknowledged for their

encouragement and friendship, and I regret not being able to acknowledge everyone by name in this limited space.

Most important, I'm deeply grateful to my family, including my wonderful parents, my dear wife Rania, and my lovely children Fares, Haneen, and Kareem for their love, patience, and support. I wish also to thank the rest of my family, my dear sisters Dina and Enas, and my great brothers Hazim, Mazen, and Hatim for their continued love and support. This dissertation is dedicated to my beloved father and mother, my prime motivators.

Table of Contents

List of Figures	x
List of Tables	xxi
Nomenclature	xxiii
1. Introduction	1
2. Literature Review	12
2.1 EGR systems and EGR Cooling Devices	12
2.2 Heat Transfer Characteristics in EGR Cooling Devices	18
2.3 Soot Deposition Characteristics in EGR Cooling Devices	21
2.3.1 Properties of the Diesel Soot Particles	23
2.4 Particulate Deposition Characteristics in Tubes of Heat Exchangers	25
2.5 Flow and Heat Transfer Characteristics for Two-Phase Gas-Particle Flow.....	30
2.6 Deposition Models for the Gas-Particle Flow	34
2.7 Non-Destructive Measurement Techniques for the Deposited Soot Layer Thickness	44
3. Model for the Soot Deposition Layer and its Effect on the Performance of EGR Cooling Devices	47
3.1 The Conservation Equations	47
3.2 The Conservation Equations in Dimensionless Forms	51
3.3 The Fully-Dispersed-Dilute Flow Model	52

3.4	One-Dimensional Heat Transfer and Soot Deposition Model	55
3.4.1	Modeling of the Thermophysical Properties of the Gas and Coolant Mixture	59
3.4.2	Numerical Scheme.....	60
3.5	Calculations of the Deposited Soot Layer and its Effect on the Performance of the EGR Cooling Device.....	64
4.	Experimental Facilities and Methodology	68
4.1	The Generic EGR Cooling Devices	68
4.2	The Diesel Engine Exhaust Gas Test Facility	73
4.3	Characterizing the Soot Particle Size and Number Density in Diesel Exhaust	93
4.4	The Neutron Radiography Non-Destructive Test Facility.....	99
5.	The Soot Deposition Characteristics in the EGR Cooling Devices .	111
5.1	Calibration and Validation of the Neutron Radiography Technique	111
5.2	Characterization of the Soot Thickness Profiles in the EGR Cooling Devices Using Neutron Radiography	126
6.	The Heat Transfer and Pressure Drop Characteristics of the EGR Cooling Devices	149
6.1	The Single-Tube EGR Cooling Devices	149
6.2	The Three-Tube EGR Cooling Devices	162
6.3	Thermal Characteristics of the Secondary Side Coolant Flow	171

7. Conclusion	174
8. Recommendations for Future Work	178
References	181
Appendix A: Predictions Results	195
Appendix B: Additional Experimental Work	197
Appendix C: Calibration of the IR Thermal Camera System	199
Appendix D: The Two-Phase Flow Conservation Equations and Constitutive Relations.....	200
Appendix E: The Equations and Correlations Used for the 1-D Heat Transfer Model.....	204
Appendix F: The Numerical Scheme Used in this Investigation.....	221
Appendix G: Uncertainty Analysis.....	226
Appendix H: Image Processing Procedure.....	228
Appendix I: Additional Results of the Thermal Characteristics of the Secondary Coolant Flow across the Three-Tube Cooling Device.....	229
Appendix J: Author’s Publications.....	237
Appendix K: Copyright Exceptions	240

List of Figures

<u>No.</u>	<u>Title</u>	<u>Page</u>
1.1	The relative contribution of major sources of NO _x emissions in North America for the base year 1995. (AQA,2000; US EPA, 1998; Taylor, 2003.)	2
1.2	Relative contribution of various sources of NO _x emissions in Ontario province for the years 1992-2000. (MOE 2000.)	2
1.3	Proposed NO _x emissions limit values for diesel cars in the major industrialized countries. (Walsh, 2001.)	5
1.4	Emissions standards of automotive vehicles for Europe. (Valaszikai and Jouannet, 2000.)	5
1.5	Schematic of a typical exhaust gas recirculation (EGR) system.	9
2.1	The change in NO _x emissions generated from DI diesel engine for different loads, defined in Table 2.2, with EGR rate. (Lapuerta et al., 1995.)	14
2.2	Typical flow regimes of gas-solid particle mixture in horizontal tube. (Rudinger,1980.)	31
3.1	The mono-sized fully-dispersed gas-particle flow system used in the present model.	48
3.2	The two-phase momentum interaction parameter as a function of particle number density for the fully dispersed gas-particle flow system for various particle average diameters for $Re_{g,i} = 1500$.	53
3.3	The two-phase thermal interaction parameter as a function of particle number density for the fully dispersed gas-particle flow system for various particle average diameters for $Re_{g,i} = 1500$.	53
3.4	The thermophoresis parameter as a function of temperature difference between the gas inlet temperature and tube wall temperature ($\Delta T = T_{g,i} - T_w$) of the EGR cooling device for various soot particle diameters.	56

- 3.5 Schematic showing control volume in a nominal cooling tube, including the thermal circuit and soot deposited layer concept used in the model. 58
- 3.6 Schematic of the one-dimensional dilute flow and deposition model used in this investigation. 58
- 3.7 Predictions of the change in soot deposited layer thickness along the EGR cooling device for different inlet gas temperatures. ($L=20$ cm, $d_t=4.5$ mm, $\dot{m}_g=2$ kg/hr per tube, $T_{c,i}=30^\circ\text{C}$, $C_s=50$ mg/m³, $N_p=10^{10}$ #pt./m³.) 65
- 3.8 Predictions of the change in the exit gas temperature from the EGR cooling device for different gas mass flow rates. ($L=20$ cm, $d_t=4.5$ mm, $T_{g,i}=250^\circ\text{C}$, $T_{c,i}=30^\circ\text{C}$, $C_s=50$ mg/m³, $N_p=10^{10}$ #pt./m³.) 65
- 3.9 Predictions of the change in the thermal effectiveness of the EGR cooling device for different gas mass flow rates. ($L=20$ cm, $d_t=4.5$ mm, $T_{g,i}=250^\circ\text{C}$, $T_{c,i}=30^\circ\text{C}$, $C_s=50$ mg/m³, $N_p=10^{10}$ #pt./m³.) 67
- 3.10 Predictions of the change in the pressure drop across the EGR cooling device for different gas mass flow rates. ($L=20$ cm, $d_t=4.5$ mm, $T_{g,i}=250^\circ\text{C}$, $T_{c,i}=30^\circ\text{C}$, $C_s=50$ mg/m³, $N_p=10^{10}$ #pt./m³.) 67
- 4.1 Schematic of the single-tube EGR cooling device used in this investigation. (Material: Aluminum. All dimensions in cm.) 70
- 4.2 Schematic of the three-tube EGR cooling device used in this investigation. (Material: Aluminum. All dimensions in cm.) 71
- 4.3 The generic EGR cooling devices used in this investigation; (a) single-tube device and (b) three-tube device. 72
- 4.4 The diesel engine exhaust gas test facility used for the controlled soot deposition tests. 74
- 4.5 Photograph of the diesel engine exhaust gas test facility used in this investigation. 75

4.6	Schematic and photograph of the coolant/water transport loop.	78
4.7	Variation in the gas mass flow rate with time for the single-tube EGR cooling devices tested for 1, 2, and 5 hours.	81
4.8	Schematic of the mini-dilution tunnel used in the present study for the measurements of the soot mass concentration during EGR soot deposition tests. T/C: T-type thermocouple; [NO]: concentration of Nitric oxide.	81
4.9	Variation in the NO concentration measured in ◦ the undiluted exhaust loop, and ◻ the diluted flow, for the single-tube EGR cooling device tested for an exhaust mass flow rate of 0.8 kg/hr.	83
4.10	Variation in the NO concentration measured in ◦ the undiluted exhaust loop, and ◻ the diluted flow, for the single-tube EGR cooling device tested for an exhaust mass flow rate of 2.8 kg/hr.	83
4.11	Change in the dilution ratio determined from NO measurement for the single-tube EGR cooling devices for gas mass flow rates Δ 0.8 kg/hr, and ◻ 2.8 kg/hr.	84
4.12	Change in the soot mass concentration in the gas flow ◦ measured after diluting the flow, and ◻ calculated for the exhaust flow, for the single-tube EGR cooling device with an exhaust gas mass flow rate of 0.8 kg/hr.	84
4.13	Change in the soot mass concentration in the gas flow ◦ measured after diluting the flow, and ◻ calculated for the exhaust flow, for the single-tube EGR cooling device with an exhaust mass flow rate of 2.8 kg/hr.	86
4.14	Change in the inlet gas and inlet coolant temperatures during the single-tube EGR cooling device tests for the average exhaust mass flow rate of 0.8 kg/hr and soot mass concentration of 45 mg/m ³ .	86
4.15	Change in the inlet gas and inlet coolant temperatures during the single-tube EGR cooling device tests with the average gas mass flow rate of 2.8 kg/hr and soot mass concentration of 46 mg/m ³ .	87
4.16	Change in the gas mass flow rate for the three-tube EGR cooling devices with the 45° expansion angle inlet header and the 60°	87

- expansion angle inlet header tested for 3 hours.
- 4.17 Variation in the NO concentration in ◦ the undiluted exhaust flow, 89
and ◻ the diluted gas, for the three-tube EGR cooling device with
the 45° expansion angle inlet header tested for 3 hours with a gas
mass flow rate of 6.0 kg/hr.
- 4.18 Variation in the NO concentration in ◦ the undiluted exhaust flow, 89
and ◻ the diluted gas, for the three-tube EGR cooling device with
the 60° expansion angle inlet header tested for 3 hours with a gas
mass flow rate of 6.0 kg/hr.
- 4.19 Comparison of the change in the calculated dilution ratio for the 90
three-tube EGR cooling device tests with 45° and 60° expansion
angle inlet headers for the gas flow rate of 6 kg/hr.
- 4.20 Comparison of the soot mass concentration in the exhaust flow 90
for the three-tube EGR cooling device tests with 45° and 60°
expansion angle inlet headers for the gas flow rate of 6 kg/hr.
- 4.21 Change in the inlet gas and inlet coolant temperatures for the 91
three-tube EGR cooling device test with the 45° expansion angle
inlet header during 3 hours for gas mass flow rate of 6.0 kg/hr,
and average soot concentration of 47 mg/m³.
- 4.22 Change in the inlet gas and inlet coolant temperatures for the 91
three-tube EGR cooling device test with the 60° expansion angle
inlet header during 3 hours for gas mass flow rate 6.0 kg/hr, and
average soot concentration 46 mg/m³.
- 4.23 Schematic of the sampling system used in this investigation to 94
characterize the soot particle size distribution and number density
in diesel exhaust sampled from the EGR section.
- 4.24 SEM measurements of the soot particles size distribution in diesel 95
exhaust sampled upstream of the EGR cooling device.
- 4.25 SEM measurements of the soot particles size distribution in diesel 96
exhaust sampled downstream of the EGR cooling device.
- 4.26 In-flight measurements of the soot particle size and number 98
density of diesel exhaust in EGR loop using CNPC system.

4.27	Change in the soot mass concentration measured upstream and downstream of the cooling device.	98
4.28	Schematic of the top view of the neutron radiography non-destructive test (NR-NDT) facility in beam port 2 of the McMaster Nuclear Reactor.	100
4.29	Schematic of the movable wax shielding system for beam port 2 of the McMaster Nuclear reactor.	102
4.30	Photographs of the computer controlled revolving table system used in the present work.	103
4.31	The digital neutron imaging system (DNIS).	104
4.32	Schematic showing the concept of the neutron attenuation through a soot deposited pipe.	108
4.33	Schematic of the aluminum tube partially filled with diesel soot used to determine the attenuation coefficient and the build-up factor for the diesel soot.	108
5.1	(a) Neutron image of the soot filled tube, and (b) measurements of the intensity across different locations along the tube used to determine the attenuation coefficient and build-up factor for the diesel soot.	113
5.2	Schematic showing the change in the length of the neutron path across the tube containing the soot at different lateral positions.	115
5.3	Change in the attenuation of the neutron flux with path length used to determine the attenuation coefficient, μ_s , and build-up factor, $B\mu_s$, for diesel soot.	115
5.4	(a) Schematic of the soot deposited pipe on the rotating table, and (b) the processed neutron image of the soot deposited pipe viewed from a typical angle of $\theta = 300^\circ$.	117
5.5(a)	Profiles of the neutron intensity across the fouled pipe at positions along the pipe separated by 20.4 mm as shown in Figure 5.4. Image plane angle $\theta = 0^\circ$.	119

5.5(b)	Profiles of the neutron intensity across the soot deposited pipe for H1 to H8 positions along the pipe. Image plane angle $\theta = 60^\circ$.	119
5.5(c)	Profiles of the neutron intensity across the fouled pipe for H1 to H8 positions along the pipe. Image plane angle $\theta = 120^\circ$.	120
5.5(d)	Profiles of the neutron intensity across the soot deposited pipe for H1 to H8 positions along the pipe. Image plane angle $\theta = 180^\circ$.	120
5.5(e)	Profiles of the neutron intensity across the soot deposited pipe for H1 to H8 positions along the pipe. Image plane angle $\theta = 240^\circ$.	121
5.5(f)	Profiles of the neutron intensity across the soot deposited pipe for H1 to H8 positions along the pipe. Image plane angle $\theta = 300^\circ$.	121
5.6	Change in the soot thickness profile along the pipe at different azimuthal positions measured using the digital neutron radiography technique.	122
5.7	Photographs of the sectioned pieces of the soot deposited pipe from H1 to H7 at different azimuthal positions, θ , taken through an optical microscope.	124
5.8	Change in the soot thickness profile along the pipe at different azimuthal positions measured from the sectioned pieces using the optical microscope.	125
5.9	Comparison of the soot thickness profile with the azimuthal angle at two different locations along the pipe measured \square from the sectioned pieces using the optical microscope and \blacksquare using the digital neutron radiography technique.	125
5.10	Comparison in the circumferential average soot thickness along the pipe measured \square from the sectioned pieces using the optical microscope, and \blacksquare using the neutron radiography technique.	127
5.11	Typical neutron images for the single-tube devices tested with a mass flow rate of 0.8 kg/hr ($Re_{initial}=2000$) and average soot concentration of $C_s=45 \text{ mg/m}^3$. Images at view plane angle $\theta=300^\circ$.	129

5.12	Typical neutron images for the single-tube test with a mass flow rate of 2.8 kg/hr ($Re_{initial}=7000$) and average soot concentration of $C_s=46 \text{ mg/m}^3$. Images at view angle $\theta=300^\circ$.	129
5.13	Measurement of the intensity along the centerline of the single-tube devices for the 5 hour test. Image plane angle $\theta = 300^\circ$.	130
5.14	Profiles of local soot thickness along the tube at different angular position θ for the 5 hour single-tube test with a mass flow rate of 0.8 kg/hr and $C_s= 45 \text{ mg/m}^3$.	132
5.15	Profiles of local soot thickness along the tube at different angular position θ for the 5 hour single-tube test with a mass flow rate of 2.8 kg/hr and $C_s= 46 \text{ mg/m}^3$.	132
5.16	Variation in the circumferentially averaged soot thickness with time for the single-tube test with a mass flow rate of 0.8 kg/hr and $C_s= 45 \text{ mg/m}^3$.	133
5.17	Variation in the circumferentially averaged soot thickness with time for the single-tube test with a mass flow rate of 2.8 kg/hr and $C_s= 46 \text{ mg/m}^3$.	133
5.18	Photographs of the inlet header for the single-tube test with a mass flow rate of 2.8 kg/hr after 5 hours.	136
5.19	Typical neutron images for the three-tube test with a mass flow rate of 6.0 kg/hr ($Re_{initial}=8000$), and soot mass concentration of $C_s = 46\text{-}47 \text{ mg/m}^3$.	138
5.20	The change in the soot thickness profiles along the three-tube device with 60° inlet header. Total gas mass flow rate = 6 kg/hr, $C_s = 47\text{mg/m}^3$, and 3 hours soot deposition.	138
5.21	The change in the soot thickness profiles along the three-tube device with 45° inlet header. Total gas mass flow rate = 6 kg/hr, $C_s = 46\text{mg/m}^3$, and 3 hours soot deposition.	139
5.22	Schematic of the three-tube EGR cooling device; (a) top view, and (b) side view, and the selected sections across the cooling device used to determine the temperature distribution from the thermal images.	141

- 5.23 Change in the coolant shell temperature profile at different cross sections along the three-tube cooling device determined from the thermal images of the (a) top view, and (b) side view during 3 hours test for the coolant flow rate of 2.5 l/min. 143
- 5.24 Schematic diagram showing a section of a soot-deposited layer inside a three-tube inlet header. 145
- 5.25 The change in the local averaged soot deposition inside the 60° expansion angle inlet header. Image view angles: \diamond 0° \square 60° \triangle 120° \times 180° $+$ 240° \circ 300°. 146
- 5.26 The change in the local averaged soot deposition inside the 45° expansion angle inlet header. Image view angles: \diamond 0° \square 60° \triangle 120° \times 180° $+$ 240° \circ 300°. 146
- 5.27 Photographs of the soot deposited three-tube cooling devices with their inlet headers. 147
- 5.28 Comparison of the averaged soot thickness profiles along the single-tube EGR cooling device measurement using the neutron radiography technique and predicted using the present model. (Gas flow rate= 0.8 kg/hr; 5 hours soot deposition.) 147
- 6.1 Change in the gas temperature drop with time across the single-tube EGR cooling device during 1, 2, and 5 hours tests for the gas mass flow rate of 0.8 kg/hr and soot mass concentration of 45 mg/m³. 150
- 6.2 Change in the coolant temperature rise with time across the single-tube EGR cooling device during 1, 2, and 5 hours tests for the gas mass flow rate of 0.8 kg/hr and soot mass concentration of 45 mg/m³. 150
- 6.3 Change in the gas heat transfer rate with time for the single-tube EGR cooling device during 1, 2, and 5 hours tests for the gas flow rate of 0.8 kg/hr and soot mass concentration of 45 mg/m³. 152
- 6.4 Change in the coolant heat transfer rate with time for the single-tube EGR cooling device during 1, 2, and 5 hours tests for the gas mass flow rate of 0.8 kg/hr and soot mass concentration of 45 mg/m³. 152

6.5	Variation in the thermal effectiveness with time for the single-tube EGR cooling device during 1, 2, and 5 hours tests for the gas flow rate of 0.8 kg/hr and soot mass concentration of 45 mg/m ³ .	154
6.6	Change in the total thermal resistance (R_t), and soot deposition thermal resistance (R_s), for the single-tube EGR cooling device during 1, 2, and 5 hours tests for the gas flow rate of 0.8 kg/hr and soot mass concentration of 45 mg/m ³ .	154
6.7	Variation in the gas pressure drop with time across the single-tube EGR cooling device during 1, 2, and 5 hours tests for the gas mass flow rate of 0.8 kg/hr and soot mass concentration of 45 mg/m ³ .	156
6.8	Change in the gas temperature drop across the single-tube EGR cooling device during 1, 2, and 5 hours tests for the gas flow rate of 2.8 kg/hr and soot mass concentration of 46 mg/m ³ .	156
6.9	Change in the coolant temperature rise with time across the single-tube EGR cooling device during 1, 2, and 5 hours tests for the gas mass flow rate of 2.8 kg/hr and soot mass concentration of 46 mg/m ³ .	158
6.10	Change in the gas heat transfer rate with time for the single-tube EGR cooling device during 1, 2, and 5 hours tests for the gas flow rate of 2.8 kg/hr and soot mass concentration of 46 mg/m ³ .	158
6.11	Change in the coolant heat transfer rate with time for the single-tube EGR cooling device during 1, 2, and 5 hours tests for the gas flow rate of 2.8 kg/hr and soot mass concentration of 46 mg/m ³ .	159
6.12	Variation in the thermal effectiveness with time for the single-tube EGR cooling device during 1, 2, and 5 hours tests for the gas flow rate of 2.8 kg/hr and soot mass concentration of 46 mg/m ³ .	159
6.13	Change in the total thermal resistance (R_t), and soot deposition thermal resistance (R_s), for the single-tube EGR cooling device during 1, 2, and 5 hours tests for the gas mass flow rate of 2.8 kg/hr and soot mass concentration of 46 mg/m ³ .	160
6.14	Variation in the gas pressure drop with time across the single-tube EGR cooling device during 1, 2, and 5 hours tests for the gas	160

- flow rate of 2.8 kg/hr and soot mass concentration of 46 mg/m³.
- 6.15 Comparison of the change in the thermal effectiveness for the single-tube cooling device tested with gas flow rate of 0.8 kg/hr for 5 hours and from predictions using the present model. 163
- 6.16 Comparison of the change in the pressure drop across the single-tube cooling device tested with gas flow rate of 0.8 kg/hr for 5 hours and from predictions using the present model. 163
- 6.17 Comparison of the variation in the gas temperature drop across the three-tube EGR cooling devices with the 45° and 60° expansion inlet headers during 3 hours tests for the gas flow rate of 6.0 kg/hr and soot mass concentrations of 47 and 46 mg/m³. 164
- 6.18 Comparison of the variation in the coolant temperature rise across the three-tube EGR cooling devices with the 45° and 60° expansion inlet headers during 3 hours tests for the gas flow rate of 6.0 kg/hr and soot mass concentrations of 47 and 46 mg/m³. 164
- 6.19 Comparison between the change in the gas heat transfer rate in the three-tube EGR cooling devices with the 45° and 60° expansion inlet headers during 3 hour tests for the gas flow rate of 6.0 kg/hr and average soot mass concentrations of 47 and 46 mg/m³. 166
- 6.20 Comparison of the change in the coolant heat transfer rate in the three-tube EGR cooling devices with the 45° and 60° expansion inlet headers during 3 hour tests for the flow rate of 6.0 kg/hr and soot mass concentrations of 47 and 46 mg/m³. 166
- 6.21 Change in the thermal effectiveness in the three-tube EGR cooling devices with the 45° and 60° expansion inlet headers during 3 hours tests for the gas flow rate of 6.0 kg/hr and average soot mass concentrations of 47 and 46 mg/m³. 168
- 6.22 Change in the total thermal resistance (R_t), and soot deposition thermal resistance (R_s), in the three-tube EGR cooling devices with the 45° and 60° expansion inlet headers during 3 hour tests for the gas flow rate of 6.0 kg/hr and average soot mass concentrations of 47 and 46 mg/m³. 168

- 6.23 Comparison of the variation in the gas pressure drop across the three-tube EGR cooling devices with the 45° and 60° expansion inlet headers during 3 hour tests for the gas mass flow rate of 6.0 kg/hr and average soot mass concentrations of 47 and 46 mg/m³. 170
- 6.24 Transient average surface coolant temperature determined from top and side views at (a) gas-side entrance of cooling device (z=0), (b) z=L/2, and (c) z=L for coolant flow rates tests of 2.5 and 6 l/min. 173

List of Tables

<u>No.</u>	<u>Title</u>	<u>Page</u>
1.1	Typical composition of diesel exhaust gas. (Lloyd and Cackette, 2001.)	4
1.2	Typical emission levels contained in the diesel exhaust.	4
1.3	Typical strategies used to reduce NO _x emissions from vehicles.	7
2.1	Summary of studies on the effect of EGR on NO _x & PM emissions.	13
2.2	Reference diesel engine tests used in the study of the effect of EGR rate on NO _x emissions. (Lapuerta et al., 1995.)	14
2.3	Studies on the effects of cooling the recirculated exhaust gas on NO _x emissions.	16
2.4	Typical operating conditions for EGR cooling devices. (Stolz et al., 2001.)	16
2.5	Schematic of typical commercial shell-and-tube EGR cooling devices.	17
2.6	Summary of particle transport and deposition mechanisms.	36
3.1	Summary of the one-dimensional heat transfer model used in this study.	56
3.2	Summary of the models used to predict the thermophysical properties of exhaust gas mixture. (n : number of pure gases in the mixture; x_i : mole or weight fraction of the i^{th} gas in the mixture; R : universal gas constant.)	61
3.3	Summary of the correlations used to estimate the thermophysical properties of the ethylene glycol-water mixture. (Bohne et al., 1984.)	62
3.4a	The coefficients A_{ij} for the correlation of dynamic viscosity for the ethylene glycol-water mixture. (Bohne et al., 1984.)	63

3.4b	The coefficients B_{ij} for the correlation of density for the ethylene glycol-water mixture. (Bohne et al., 1984.)	63
3.4c	The coefficients C_{ij} for the correlation of Prandtl number for the ethylene glycol-water mixture. (Bohne et al., 1984.)	63
4.1	Typical characteristics of the diesel engine used in this investigation.	75
4.2	Summary of the characteristics of the instruments used in the diesel exhaust and coolant transport test facility.	79
4.3	The test conditions during sampling the soot particles for size distribution using SEM.	94
4.4	Characteristics of the stepper motor driven revolving-table system.	103

Nomenclature

Bu_s	Build-up factor of the diesel soot layer
$C_{p,p}$	Specific heat for the particle phase, (kJ/kg.K)
$C_{p,g}$	Specific heat for the gas phase, (kJ/kg.K)
$C_{p,p}$	Specific heat for the particle phase, (kJ/kg.K)
d_i	Tube inner diameter, (m)
d_p	Particle diameter, (m)
D_p	Diffusion coefficient, (m)
h_g	Convective heat transfer coefficient, (W/m ² .K)
k_g	Thermal conductivity for the gas phase, (W/m.K)
Kn	Knudsen number, $\left(\frac{2\lambda_g}{d_p}\right)$
K_{th}	Thermophoretic coefficient
m^*	Mass (dust)-loading ratio, $\frac{\dot{m}_s}{\dot{m}_g}$
\dot{m}_g	Mass flow rate of gas, (kg/s)
\dot{m}_s	Mass flow rate of solid, (kg/s)
N_p	Particle number density (concentration), (#pt/m ³)
$N_{p,i}$	Particle number density at tube entrance, (#pt/m ³)
\tilde{N}_p	Dimensionless particle number density, $\left(\frac{N_p}{N_{p,i}}\right)$
p_g	Pressure of the gas phase, (Pa)
\tilde{p}_g	Dimensionless pressure for the gas phase, $\left(\frac{p_g}{\rho_g u_{g,i}^2}\right)$
p_p	Pressure of the particle phase, (Pa)
\tilde{p}_p	Dimensionless pressure for the particle phase, $\left(\frac{p_p}{\rho_p u_{g,i}^2}\right)$
R	Tube radius, (m)

Re_g	Reynolds number for the gas, $\left(\frac{2u_g R}{\nu_g}\right)$
Sc_p	Schmidt number for the aerosol particle, $\left(\frac{\nu_g}{D_p}\right)$
Sh	Sherwood number, $\left(\frac{2u_d R}{D_p}\right)$
t	Time, (s)
T_g	Gas temperature, ($^{\circ}\text{C}$)
T_p	Particle temperature, ($^{\circ}\text{C}$)
T_w	Tube wall temperature, ($^{\circ}\text{C}$)
ΔT	Temperature difference, $(T_g - T_w)$
u_g	Gas velocity, (m/s)
$u_{g,i}$	Gas velocity at the inlet, (m/s)
u_p	Particle velocity, (m/s)
u_d	Deposition velocity, (m/s)
\bar{U}_g	Dimensionless velocity for the gas phase, $\left(\frac{u_g}{u_{g,i}}\right)$
\bar{U}_p	Dimensionless velocity for the particle phase, $\left(\frac{u_p}{u_{g,i}}\right)$
z	Axial distance, (m)

Greek:

δ_s	Local soot layer thickness, (mm)
η_{TP}	Thermophoretic deposition efficiency
η_{diff}	Diffusion deposition efficiency
μ_g	Gas dynamic viscosity, (Pa.s)
μ_s	Thermal neutron attenuation coefficient for the diesel soot, (mm^{-1})
$\tilde{\nabla}$	Dimensionless Nabla operator, $(d_i \nabla)$

ν_g	Gas kinematic viscosity, (m ² /s)
ρ_g	Gas (material) density, (kg/m ³)
$\tilde{\rho}_g$	Dimensionless density for the gas phase, $\left(\frac{\rho_g}{\rho_{g,i}}\right)$
ρ_p	Particle (material) density, (kg/m ³)
θ_g	Dimensionless temperature for the gas phase, $\left(\frac{T_g}{T_{g,i} - T_w}\right)$
θ_p	Dimensionless temperature for the particle, $\left(\frac{T_p}{T_{g,i} - T_w}\right)$
τ	Dimensionless time, $\left(\frac{t u_{g,i}}{d_i}\right)$

CHAPTER 1: Introduction

The objective of this investigation was to study the heat transfer and the soot deposition characteristics in exhaust gas recirculation (EGR) system cooling devices used for nitrogen oxides (NO_x) emissions control in diesel engines. The emissions of NO_x generated by fuel combustion processes, such as by diesel engines, are one of the main causes of air pollution. The NO_x emissions are toxic, causing respiratory problems and chronic lung diseases, and contribute to acid rain, smog formation, and destruction of the ozone layer (Cohen and Higgins, 1995; Lloyd and Cackette, 2001). On-road vehicles are one of the significant sources of NO_x emissions in most industrialized countries. For example, on-road vehicles accounted for 36% of NO_x emissions in Canada, and 32% of emissions in the United States in 1995 (AQA, 2000; US EPA, 1998; Taylor, 2003), as shown in Figure 1.1. This is also true for the province of Ontario where automotive vehicles were the highest contributor of NO_x emissions for the years 1992-2000, as shown in Figure 1.2. There is currently an increased interest in replacing gasoline engines with more efficient and higher fuel economy diesel engines in order to reduce the greenhouse gas emissions to meet the requirements of the Kyoto protocol (UNFCCC, 2003). Diesel engines have higher emissions of NO_x and soot (Lloyd and Cackette, 2001), so the emissions from

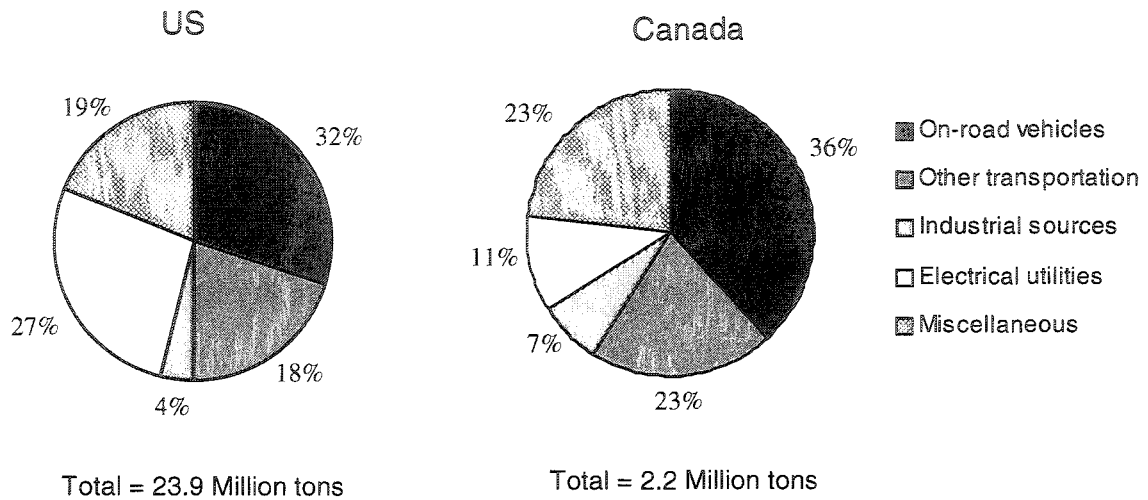


Figure 1.1. The relative contribution of major sources of NOx emissions in North America for the base year 1995. (AQA, 2000; US EPA, 1998; Taylor, 2003.)

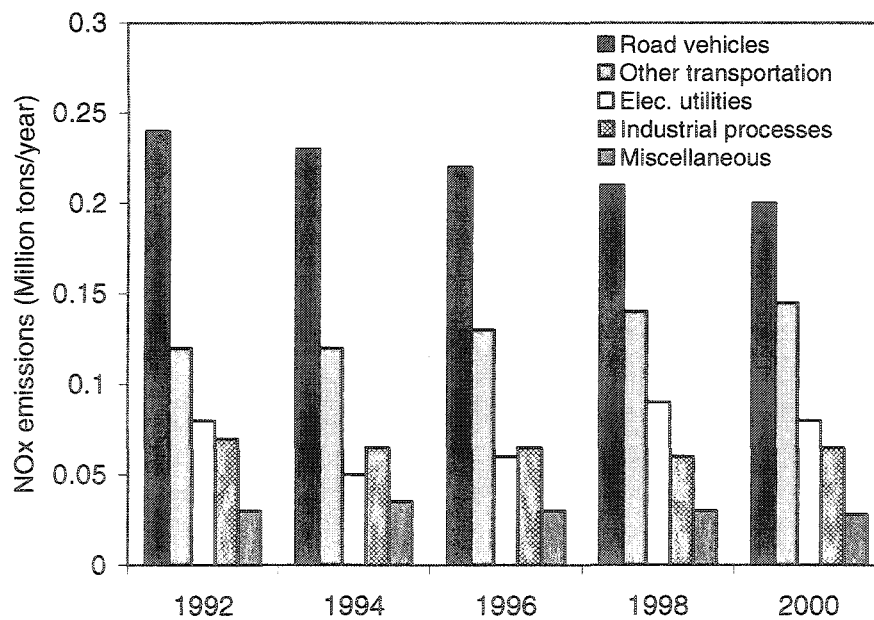


Figure 1.2. Relative contribution of various sources of NOx emissions in Ontario province for the years 1992-2000. (MOE 2000.)

these engines must be reduced to be a viable replacement for gasoline engines, when these emissions standards are implemented. The typical composition of diesel exhaust gas and emission levels of main pollutants from automotive diesel engines are shown in Tables 1.1 and 1.2, respectively.

There is also increasingly stringent government regulations imposed on the automotive sector by industrialized countries to limit the emissions of NO_x, and the other combustion-based air pollutants, such as carbon monoxide (CO), unburned hydrocarbons (HC), and particulate matter or soot (PM). For example, the NO_x emissions standards for diesel cars in Europe, Japan, and USA are shown in Figure 1.3, while the emissions standards for automotive vehicles in Europe are shown in Figure 1.4. Thus, there must be a significant reduction in NO_x emissions from vehicles by the year 2008; approximately 93% reduction of the emissions of year 2000 in USA, and 63% and 50 % reductions in Japan and Europe. Diesel engines only make up a small segment of the North American market but they are the dominant engines in Europe and Japan where fuel prices are relatively high.

NO_x is composed of nitric oxide (NO), constituting the major portion of NO_x, and nitrogen dioxide (NO₂) that is formed when nitrogen and oxygen react at high temperatures in the engine cylinder. There are two primary mechanisms of NO_x formation during a combustion process, fuel or chemical NO_x and thermal NO_x (Glassman, 1987). Fuel NO_x is formed from the nitrogen chemically bonded

Table 1.1: Typical composition of diesel exhaust gas. (Lloyd and Cackette, 2001.)

Constituent	Composition by mole (%)
O ₂	14.6-15.2
N ₂	72.2-73.5
CO ₂	4.9-5.3
CO	1.5-1.8
H ₂ O	4.4-5.1
NO ₂	0.4-0.5
SO ₂	0.05-0.07
NO	1.4-1.6
HC and ash	0.05-0.1

Table 1.2: Typical emission levels of pollutants contained in the diesel exhaust.

Pollutant	Concentration ranges
NO _x	50-2500 ppm
PM	0.1-0.25 g/m ³
CO	5-1500 ppm
HC	20-400 ppm

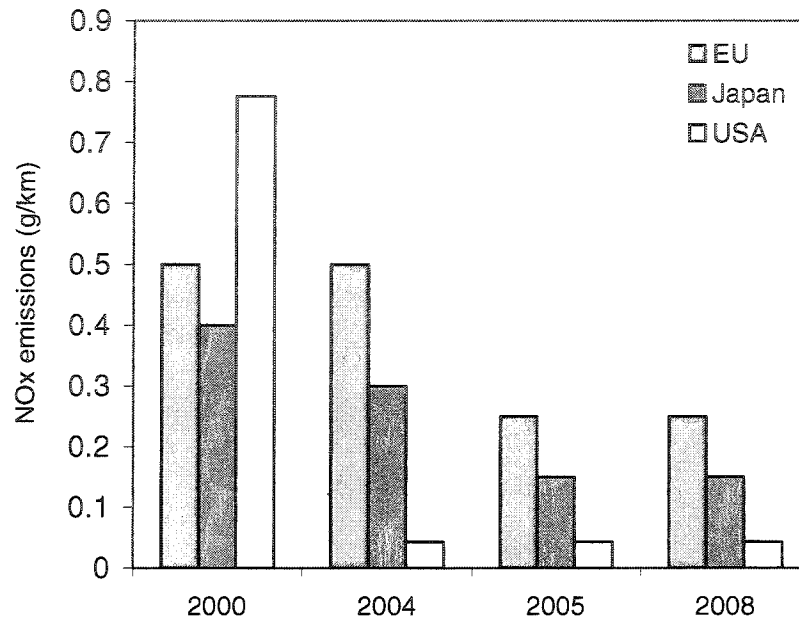


Figure 1.3. Proposed NOx emissions standards for diesel cars in EU, Japan, and USA. (Walsh, 2001.)

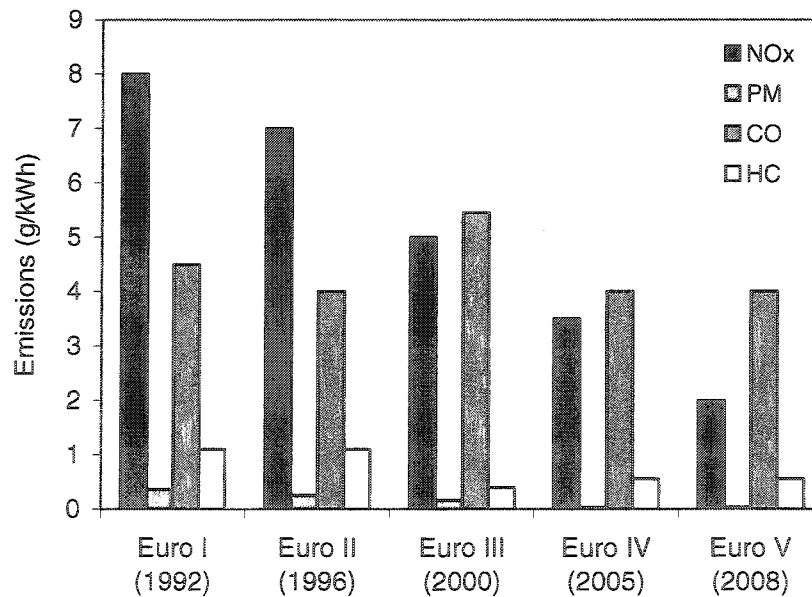


Figure 1.4. Emissions standards of automotive vehicles for Europe. (Valaszka and Jouannet, 2000.)

in the fuel that depends on the nitrogen content of the fuel compounds, and thermal NO_x, the larger source formed when nitrogen in the intake air is oxidized at high temperature in the combustion chamber.

The thermal NO_x emissions from automotive diesel engines can be reduced using a number of approaches. The thermal NO_x can be reduced by controlling the combustion process peak flame temperature using methods such as exhaust gas recirculation (EGR), retardation of fuel injection timing, and water-fuel injection. The NO_x can also be reduced by trapping and converting it into nitrogen and oxygen in post-combustion or aftertreatment systems, such as NO_x catalytic or non-catalytic converters (adsorbers), and non-thermal plasma assisted catalysis methods. A summary of the typical effectiveness of these techniques is summarized in Table 1.3, where there NO_x reduction is defined as

$$(\text{NO}_x) \text{ reduction} \equiv \frac{(\text{NO}_x)_{\text{w/o}} - \text{NO}_x}{(\text{NO}_x)_{\text{w/o}}} \quad (1.1)$$

Here, $(\text{NO}_x)_{\text{w/o}}$ is the amount of NO_x produced by the diesel engine without the pollution control system, and NO_x is the amount that would have been produced from the same engine with the pollution control system.

Table 1.3 shows that exhaust gas recirculation (EGR) with cooling is one of the most effective techniques of reducing the thermal NO_x emissions from diesel engines, achieving NO_x reductions up to approximately 70% (Ladommatos et al., 1998; Lapuerta et al., 2000; Zehenka and Reczek, 1998). A schematic

Table 1.3: Typical strategies used to reduce NO_x emissions from vehicles.

NO _x Reduction Approach	Associated technique	Principle of operation & Specifications	Attainable NO _x reduction (%)
I) In-Cylinder Combustion Methods	Exhaust Gas Recirculation (EGR) w/cooling	<ul style="list-style-type: none"> ▪ Recirculating a portion of the exhaust gas back into the intake of the engine ▪ Applies for most types of vehicles ▪ Increase of PM emissions ▪ Increase fuel consumption (1-3%) 	40 ~ 70 % (Ladommatos et al., 1998; Lapuerta et al., 2000; Zehenka and Reczek, 1998; Abd-Alla, 2002)
	Retardation of Fuel Injection Timing	<ul style="list-style-type: none"> ▪ Delaying fuel injection that retards combustion process ▪ Increases fuel consumption (5-10%) and smoke 	30 – 40 % (Dickey et al., 1998; Suzuki, 2000)
	Water-Fuel Injection	<ul style="list-style-type: none"> ▪ Injecting water with fuel, or by emulsifying the fuel as water-fuel blend ▪ Applies for DI and HD diesel engines ▪ Corrosion to injection system, engine wear, and noise ▪ Increases fuel consumption (7-15%) 	30 – 40 % (Bedford et al., 2000; Abd-Alla, 2002)
II) Post-Combustion (After-treatments) Methods	NO _x catalytic or non-catalytic converters (NO _x adsorbers)	<ul style="list-style-type: none"> ▪ Chemically converting NO_x into N₂ and water using ammonia or nitrogen-based compounds (e.g. Urea) with the presence of a catalyst (SCR), or without catalyst (SNCR) ▪ Applies for HD diesel trucks ▪ Complex and costly ▪ Safety concerns 	70 – 90 % (Dickey et al., 1998; Agrawal and Wood, 2001; Tennison et al., 2004)
	Non-Thermal Plasma – assisted catalysis	<ul style="list-style-type: none"> ▪ Creating plasma that converts NO into NO₂ for catalytic conversion to N₂, O₂, or H₂O ▪ Dry NO_x removal process ▪ Still at the proto-type test stage 	40 – 60 % (Hammer and Boroer, 1999; Hoard and Lou Balmer, 1998; Urashima et al., 1999)

diagram of a typical EGR system is shown in Figure 1.5. In this technique, the EGR system recirculates a portion of the cooled exhaust gases into the intake of the engine. This reduces or dilutes the oxygen concentration level in the incoming stream that acts to reduce both the peak combustion temperature and the surplus oxygen level available during combustion process in the engine cylinder. Thus, the rate of NO_x production can be reduced using this approach. In these systems, the EGR rate is commonly defined as (Lapuerta et al., 1995; Mattarelli et al., 2000)

$$\text{EGR Rate} = \frac{\dot{m}_{EGR}}{\dot{m}_{Intake}} = \frac{\dot{m}_{EGR}}{\dot{m}_{EGR} + \dot{m}_{Air}}, \quad (1.2)$$

where \dot{m}_{EGR} is the mass rate of recirculated exhaust gas, and \dot{m}_{Air} is the mass rate of air being mixed with recirculated exhaust in the intake. The recirculated exhaust gas is cooled using an EGR cooling device before being mixed with the air intake that reduces the peak combustion temperature beyond the non-cooled EGR system, thus further reducing the NO_x emissions from the engine. Cooling the recirculated exhaust gas tends also to reduce the power penalty, or improves the fuel economy, by increasing the intake mass charge in the engine. Akihama et al. (2001) observed that the specific fuel consumption penalty for diesel engines with EGR systems can be reduced from approximately 3 to 1% by cooling a large amount (~55%) of recirculated exhaust gas flow rates.

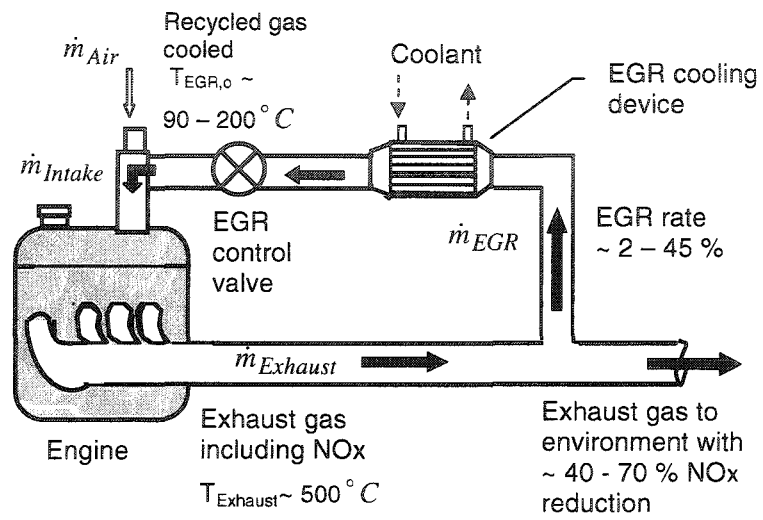


Figure 1.5. Schematic of a typical exhaust gas recirculation (EGR) system.

It has been observed that the heat transfer performance of EGR cooling devices in diesel engines changes over time because of the typically high concentration of soot in diesel exhaust. The soot particles can influence the heat transfer mechanisms in these devices by interacting with the gas flow passing through the tubes of the cooling device, and more importantly by depositing on the walls of the EGR cooling devices. This impacts the short- and long-term performances of these devices, thus reducing the decrease in NO_x emissions that can be achieved using the EGR systems with the cooling devices.

There have been a number of investigations that characterized the performance of EGR systems, but there have been few investigations characterizing the performance of the cooling device. The soot deposition characteristics in the cooling devices have not been studied in detail previously and are not well understood. The objective of this research was to investigate the heat transfer, pressure drop, and soot deposition characteristics in diesel exhaust gas recirculation system cooling devices.

An experimental technique was developed to non-destructively measure the three-dimensional soot deposition thickness profiles in diesel exhaust EGR cooling devices using a digital neutron imaging technique. Measurements were performed to characterize the time-dependent soot deposition profiles in single-tube cooling devices. The effect of the gas mass flow rate on the soot deposition characteristics were also investigated using the single-tube cooling devices.

Measurements were also performed using three-tube cooling devices to characterize the effects that the design of the inlet header of the cooling device had on the soot deposition characteristics in the devices. The change in the heat transfer and flow performance of the EGR cooling devices was also characterized during these tests. The results were compared to predictions from models for the soot deposition and the effect of the soot deposited layer on the heat transfer and pressure drop performances.

The presentation in this investigation was divided into eight chapters including chapter 1, the introductory chapter. The literature on EGR cooling devices, the heat transfer and the soot deposition characteristics in these devices, and techniques to measure the soot deposition thickness are reviewed in chapter 2. The model for the soot deposition and the effect of the soot deposition layer on the heat transfer and pressure drop performances of the cooling devices are presented in chapter 3. The experimental facilities and techniques used in this investigation are discussed in chapter 4. The experimental investigations to characterize the heat transfer, pressure drop, and soot deposition in diesel engine EGR cooling devices are presented in chapters 5 and 6. The conclusion of the present work and recommendations for future work are presented in chapters 7 and 8, respectively. This work has been presented in a number of journal and conference papers summarized in Appendix J.

CHAPTER 2: Literature Review

This chapter reviews the existing literature relating to the scope of this investigation, including EGR cooling devices, heat transfer and soot deposition characteristics in EGR cooling devices, heat transfer characteristics and deposition models for two-phase gas-particle tube flow, and non-destructive techniques that can be used to measure the deposition layer thickness.

2.1 EGR Systems and EGR Cooling Devices

There are numerous investigations that studied the effect of EGR systems on NO_x and particulate matter or soot (PM) emissions from automotive diesel engines. A summary of the most relevant investigations is presented in Table 2.1. Lapuerta et al. (1995) observed that the NO_x emissions decreased significantly as the EGR rate increased at all loads, as shown in Figure 2.1. Recirculating the exhaust gas in the system increases the intake air temperature causing reduction in the charge density, thus decreasing the power output of the engine, and in some cases, increases the soot produced by the diesel engine (Ladommatos et al., 1998; Lundqvist et al., 2000). For instance, Dickey et al. (1998) observed the PM emissions increased significantly, by approximately 10 fold, from 0.06 to 0.6 g/hp-hr at EGR rate of 20%.

Table 2.1: Summary of studies on the effect of EGR on NO_x & PM emissions. HD DI: heavy-duty direct-injection; IDI indirect-injection.

Investigators & type of Investigation	Engine type & operating conditions	EGR Rate	NO _x Reduction	Effect on PM/Black smoke
Dickey et al. (1998)- Experimental	HD DI Diesel at rated load	0-20%	30-80%	PM increased 0~1000%
Lapuerta et al. (2000)- Experimental	Various DI and IDI automotive diesel engines (from Nissan) for different operating modes tested at transient cycles	0-30%	20-67%	Not reported
Mattarelli, et al. (2000)- Experimental & modeling	Various new automotive DI diesel engines tested at different driving cycles	0-35%	44-68%	Black smoke increased ~ 100%
Ladommatos, et al. (1998)- Experimental	DI 4-cylinder diesel engine Tested at partial loads	0-40%	~ 50%	PM increased ~ 50%
Lapuerta et al. (1995)- Experimental & modeling	Single cylinder supercharged DI Diesel engine at different loads	0-41%	50-68%	Black smoke increased ~ 150%
Satoh, et al. (1997)- Experimental	Single-cylinder DI diesel engine tested at various loads	0-48%	~33-91%	Black smoke increased ~ 500%

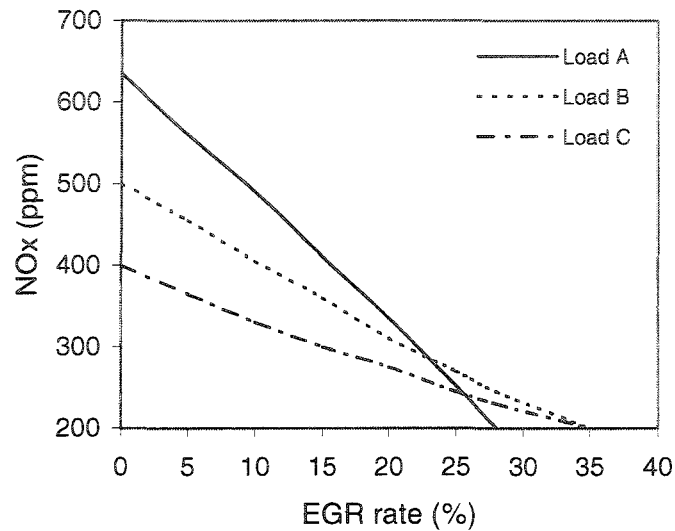


Figure 2.1. The change in NOx emissions generated from DI diesel engine for different loads, defined in Table 2.2, with EGR rate. (Lapuerta et al., 1995.)

Table 2.2: Reference diesel engine tests used in the study of the effect of EGR rate on NOx emissions. (Lapuerta et al., 1995.)

Engine Load	A	B	C
Engine speed (RPM)	2500	2500	2500
Intake pressure (Bar)	1.783	1.513	1.317
Injection timing (deg BTDC)	6.0	5.5	6.5
Exhaust pressure (Bar)	1.936	1.664	1.466
Intake temperature (K)	333	333	333
Exhaust temperature (K)	770	660	568

The NO_x produced by the diesel engine can be further reduced by cooling the recirculated exhaust gas (Zehenka and Reczek, 1998; Mattarelli et al., 2000) using an EGR cooling device. Several investigations were performed to study the effect of cooling EGR on NO_x emissions from diesel engines. A summary of studies on the effects of cooling EGR on NO_x emissions is shown in Table 2.3. Satoh et al. (1997) and Mattarelli et al. (2000) observed that cooling the recirculated exhaust gas using cooling devices reduced NO_x emissions from diesel engines by additional 15-34 %. The typical operating conditions for EGR cooling devices for different applications are summarized in Table 2.4.

The exhaust gas recirculation (EGR) cooling devices, such as those shown in Table 2.5, are normally small scale shell-and-tube heat exchangers, with the exhaust gas passing through the tubes, and ethylene glycol-water mixture from the engine coolant system passing over the tubes through the shell. The shells in these EGR cooling devices are normally plain or non-baffled. The diameter and length of the tubes vary for different designs, and the number of tubes in an EGR cooling device varies according to gas mass flow rate and exit gas temperature expected in the application. The tubes and shell in most designs are circular, but some square tube designs exist as shown in Table 2.5. The EGR cooling devices are typically short ranging from approximately 10 to 70 cm, and the diameter of the tubes are small ranging from approximately 4 to 7 mm. The length-to-diameter ratio for most designs ranges from 44 to 60. The EGR cooling

Table 2.3: Studies on the effects of cooling the exhaust gas recirculation on NOx emissions.

Investigators & type of Investigation	Type of engine (EGR rate used)	Method of controlling charge inlet temperature	Effects of cooling on NOx emissions
Ladommatos, et al. (1998)- Experimental	DI 4-cylinder diesel engine (40%)	Electric heater (40-120 °C)	NOx reduced by ~65%
Akihama et al. (2001)- Experimental & modeling	DI 4-cylinder diesel engine (20-60%)	EGR cooling device (100 & 150 °C)	NOx reduced by ~50%
Mattarelli, et al. (2000)- Experimental & modeling	Various automotive DI diesel engines tested at different driving cycles (35%)	EGR cooling device	NOx reduction: 25% (without cooling) 40 % (with cooling)
Sato, et al. (1997)- Experimental	DI diesel engine (12%)	EGR cooling device	NOx reduction: 33% (without cooling) 67% (with cooling)

Table 2.4: Typical operating conditions for EGR cooling devices. (Stolz et al., 2001.)

	Passenger car application	Heavy-duty truck application
Gas mass flow rate, \dot{m}_g (kg/hr)	20 - 80	100 - 480
Inlet gas temperature, $T_{g,i}$ (°C)	250 - 450	300 - 700
Outlet gas temperature, $T_{g,o}$ (°C)	160 - 200	95 - 250
Heat transfer rate, \dot{Q} (kW)	1 - 5	10 - 35
Gas pressure drop (kPa)	1 - 3	2 - 10

Table 2.5: Schematic of typical commercial shell-and-tube EGR cooling devices.

Configuration		Dimensions (cm)		
A		L_1	10 - 60	
		L_2	8 - 56	
		ϕ_1	3 - 4	
		ϕ_2	5 - 6	
		ϕ_3	0.4 - 0.7	
		ϕ_4	1 - 3	
		S_T	0.2 - 0.3	
		Number of tubes ($N_T = 19, 21, 27, 31, 33, 37, 41$)		
	 A1-Circular arrangement	 A2-Triangular arrangement		
B		$L_1 \sim 28$	$L_2 \sim 25$	
		$\phi_1 \sim 3$	$\phi_2 \sim 6$	
		$\phi_3 \sim 0.6$	$\phi_4 \sim 1.6$	
		$S_T \sim 0.2$	$N_T = 37$	
C		$L_1 \sim 32$	$L_2 \sim 28$	
		$\phi_1 = \phi_2 \sim 5.5$		
		$\phi_3 \sim 0.6$	$\phi_4 \sim 1.5$	
		$S_T \sim 0.2$	$N_T = 41$	
D		$L_1 \sim 12, 23$		
		$L_2 \sim 10, 16$		
		$L_3 \sim 5$	$L_4 \sim 3.0$	
		$\phi_1 \sim 3$		
		$\phi_4 \sim 1.6, 2$		
		$a \sim 0.5$	$b \sim 1.3$	
		$S_T \sim 0.3$	$N_T = 12$	

devices are commonly made of materials that are durable, heat- and corrosion-resistant, such as high quality stainless steel and in some cases aluminum (Stolz et al., 2001; Honma et al., 2004).

2.2 Heat Transfer Characteristics in EGR Cooling Devices

There is a typically large temperature gradient between the high temperature gas-flow in tubes of EGR cooling devices and the coolant temperature across the tube walls that cause a large change in the gas temperature across the tube walls that cause a large change in the gas temperature ($\sim 200 - 300^{\circ}\text{C}$) across the heat exchanger that tend to cause a large change in the flow properties. There have been a number of investigations characterizing shell-and-tube heat exchangers with large gas temperature drops used in large scale applications, such as, oil industry, power plants, and gas-cooled reactors (Taborek, 1983). For example, Groehn (1991) performed a study on the performance of large scale straight tube banks and helical-type heat exchangers using tube banks at different inclination angles in the transitional flow regime for a high-temperature nuclear process heat application. He observed that there were thermal-hydraulic advantages when having the tube banks inclined at certain angles. However, few investigations exist on high gas temperature gradient in small scale shell (liquid)-and-tube (gas) heat exchangers similar to those used in EGR systems. Stolz et al. (2001) developed two EGR cooling devices for truck and passenger car application and performed CFD

simulations to characterize their performances and observed that both heat transfer rate and pressure drop monotonically increased with increasing gas mass flow rate, and the highest thermal load occurred at the inlet region of the EGR cooling device.

Ismail et al. (2002) developed a one-dimensional model to characterize the heat transfer and flow performance of EGR cooling devices. The results predicted from the model agreed with measurements using a small-scale six-tube EGR cooling device ($L/d_i = 44$) tested on a high-temperature air-water heat exchanger facility for gas inlet temperatures from 300 to 400°C. The results showed that the exit gas temperature from the cooling device increased with increasing the gas mass flow rate at fixed gas inlet temperature and coolant flow rate. It was also found that the thermal effectiveness of the cooling device decreased from approximately 80% to 60% with increasing the gas mass flow rate from 4 to 18 kg/hr, but depended slightly on the inlet gas temperature. The gas pressure drop increased monotonically from approximately 0.1 to 1.6 kPa and was not a strong function of the gas inlet temperature. Ismail et al. (2002) also performed a parametric characterization using the one-dimensional model to identify performance parameters that could potentially be used to control the performance of the EGR cooling device. The results showed that the exit gas temperature from the cooling device was essentially independent of the coolant flow rate for the typical operating range, but did depend on the coolant inlet

temperature and heat exchanger length. The results also showed that the gas pressure drop across the cooling device was mainly due to conventional frictional losses with an average of approximately 44% of the total pressure drop. The contributions to the pressure drop due to entrance and exit effects for the developing flow, and the deceleration effects due to the cooling process were found to be also important with averages of 32 and 23%, respectively, for the conditions considered in the simulations.

Zhang (2003) and Zhang et al. (2004) performed measurements to characterize the heat transfer and flow performance of the six-tube EGR cooling device tested in the high-temperature air-water heat exchanger facility used by Ismail et al. (2002). The measurements were performed for gas mass flow rates ranging from 2 to 18 kg/hr and gas inlet temperature ranging from 250 to 400 °C. Zhang et al. (2004) observed that the thermal effectiveness and Nusselt number for the clean device were approximately independent of the gas inlet temperature for temperatures between 250 °C and 400 °C, when the flow through the tubes was turbulent, whereas the thermal characteristics did vary when the flow was laminar. The thermal performance of the clean device was not significantly influenced by the presence of a corner upstream of the cooling device, but the pressure drop across the device did depend on the flow conditions.

Melgar et al. (2004) characterized the heat transfer performance of a thirteen-tube EGR cooling device ($L/d_i = 20$) using experimental measurements

and CFD simulations. They observed that the exit air temperature from the cooling device increased from approximately 205°C to 240°C when the total gas mass flow rate increased from 30 to 60 kg/hr. The air temperature at the inlet of the cooling device was maintained at 450°C . They also observed that the gas pressure drop across the cooling device increased from approximately 0.7 to 3.5 kPa for the same range of gas mass flow rate.

2.3 Soot Deposition Characteristics in EGR Cooling Devices

There were a few investigations that studied the soot deposition characteristics in small scale shell-and-tube heat exchangers such as those used as EGR cooling devices. Ismail et al. (2002) performed a series of simulations using a one-dimensional model to examine the magnitude of the effect that a soot deposited layer would have on the thermal and hydraulic characteristics in the EGR cooling device for different soot deposited thickness layers in a six-tube EGR cooling device ($L/d_i = 44$). The results showed that the exit temperature from the sooted device was higher than from the clean device for most of the flow rates considered. For the case in which the device had a larger deposited soot layer thickness (i.e., 20% case), the exit gas temperature was much higher than the other cases especially at higher gas flow rates. The results also showed that the soot deposited layers increased the pressure drop particularly when there was a large scale soot deposited layer, as expected, since the layer on the tube

wall decreased the effective hydraulic diameter of the tubes. Therefore, the velocity increased in order to achieve the same mass flow rate. Ismail et al. (2002) also characterized the effect that the thermal conductivity of the deposited soot layer had on the heat transfer characteristics of EGR cooling devices using the one-dimensional model. Three thermal conductivities, 0.1, 0.5, and 1.0 W/m.K, were considered in the simulations typical of those corresponding to diesel soot. The results showed that the thermal conductivity of the soot layer had a profound effect on the exit gas temperature from the EGR cooling device, which for the lowest conductivity case, was the limiting factor on the heat transfer rate.

Zhang (2003) examined the performance of a small-scale six-tube EGR cooling device ($L/d_i = 44$) when it was used to cool diesel exhaust gas. He found that the diameter at the entrance was reduced by at least 33% after 12 hours of operation. The pressure drop and thermal resistance of the device increased by 150% or more. Zhang (2003) did not examine the soot deposition at the entrance at intermediate times so that it was not possible to determine how rapidly the soot deposition at the entrance formed in these experiments.

Usui et al. (2004) characterized the deposition of soot from diesel exhaust, generated from a 4-cylinder diesel engine, onto the surface of three cooling plate specimens located inside a test chamber at inlet, middle, and outlet. The study focused on the effects of engine operation duration, and cooling plate

temperature on the weight of deposited soot onto the specimens of the cooling chamber. The results showed that the weight of deposited soot increased linearly with increasing engine operating time, and the measured deposition rate was 6.56 mg/hr, highest on the inlet plate. The deposition rate was 5.33 and 4.30 mg/hr for the middle and outlet plates, respectively, for a fixed cooling plate temperature $T_{plate} = 80^{\circ}C$ and inlet gas temperature $T_{g,i} = 236^{\circ}C$. Usui et al. (2004) also observed that the weight of deposited soot increased with decreasing plate specimen temperature for fixed inlet gas temperature and concluded that the thermophoresis effect was the dominating deposition mechanism. The weight of the deposited soot was highest for the inlet specimen and lightest for the outlet specimen, and the cooling plate temperature varied from approximately 50 to $175^{\circ}C$.

2.3.1 Properties of the Diesel Soot Particles

There have been a number of investigations to characterize the soot particles in diesel exhaust. Harris and Maricq (2001) conducted soot particle size distribution measurements for the diesel exhaust produced from a large number of vehicles and test engines using a variety of diesel fuels. They observed that the soot particle distributions had lognormal characteristics for typical diesel engines of the form given by

$$f(d_p) = \frac{N_o}{\sqrt{2\pi \ln \sigma_g}} \exp \left[-0.5 \left(\frac{\ln(d_p / \bar{d}_p)}{\ln \sigma_g} \right)^2 \right], \quad (2.1)$$

even for different EGR rates. Here, N_o is the total particle number density or concentration, d_p and \bar{d}_p are the particle diameter and the mean particle diameter, and σ_g is the geometric standard deviation for the diesel soot particles that varies between 1.68 and 1.86. The mean diameters for the soot particles ranged from 0.06 to 0.12 μm . The total particle number density in the diesel exhaust typically varies from 10^{11} to 10^{13} #pt./m³ depending on engine type and operating conditions (Ishiguro et al., 1997; Harris and Maricq, 2001; Ning et al., 2004). Bartscher et al. (1998) and Ishiguro et al. (1997) characterized the soot particles in combustion diesel engine exhaust and observed that the primary soot particles were nearly spherical in shape and consisted mainly of core or “elemental” carbon surrounded by a shell-like structure consisting of organic species of volatile hydrocarbons and sulfate compounds that increase the adhesive nature of the soot particles. Bartscher et al. (1998) observed that the number density of emitted particles changes due to the formation of agglomerates, but the chemical composition did not change with engine load.

Ning et al. (2004) observed that the mass concentration of the diesel soot increased up to 20% when the exhaust gas temperature was cooled from approximately 200 to 50°C. The peak diameter of the soot number distribution

shifted slightly from approximately 0.09 to $0.08 \mu\text{m}$, and the total particle number density decreased by factor of 2 when the exhaust gas temperature was decreased from 200 to 50°C . They concluded that main mechanisms leading to these changes were nucleation and condensation of volatile materials, and coagulation or agglomeration of soot.

The conductivity of the soot is difficult to predict because it depends on both the composition and the porosity of the deposited soot layer. The thermophysical properties of the soot are often characterized using the properties of carbon blacks generated from combustion processes, such as candles and furnaces. Maquin et al. (1999) observed that carbon blacks with spherical particles of size $0.2 \mu\text{m}$ and porosity 0.54 have apparent thermal conductivity of approximately 0.1 W/m.K at atmospheric pressure.

2.4 Particulate Deposition Characteristics in Tubes of Heat Exchangers

The deposition or fouling process in heat exchangers is caused by the deposition or accumulation of solid materials suspended or generated in a fluid onto the heat transfer surfaces of the heat exchangers. This deposition of solids on the tube walls of a heat exchanger changes the thermal and hydraulic performances of the exchanger, by initially increasing the surface roughness of the tube surface which increases the hydraulic resistance of the tube flow depending on the flow regime. In small diameter tubes, the soot deposition can

reduce the flow area, thus increasing the hydraulic resistance. The deposited layer also increases the thermal resistance of the tube wall which reduces the heat transfer rate across the tube walls, causing reduction in the thermal effectiveness of the exchanger, although the surface roughness of the deposited layer could initially offset this for turbulent flow.

Epstein (1999) categorized fouling in heat exchangers into crystallization fouling, chemical reaction fouling, particulate fouling, and corrosion fouling. The effect of fouling in heat exchangers has been fairly extensively investigated. For example, there have been many investigations that studied chemical, particulate, corrosion, and crystallization fouling in liquid-flow heat exchangers (Kern and Seaton, 1959; Bott et al., 1999; Fryer et al., 1985; Knudsen, 1999; Knudsen et al., 1999; Blochl and Muller-Steinhagen, 1990). There have been fewer studies of the effect of particulate deposition in tubes of heat exchangers that involved gas flow such as those used as EGR cooling devices.

One of the simplest models of particulate deposition in heat exchangers was developed by Kern and Seaton (1959) who reviewed many experimental particulate fouling data from recovery liquid flow heat exchangers. They modeled the growth of a deposited layer on the heat transfer surface as the difference between rates of deposition and removal fluxes, i. e.,

$$\frac{dm_f}{dt} = \dot{m}_d - \dot{m}_r, \quad (2.2)$$

and

$$\frac{dm_f}{dt} = k_d \rho_d \frac{dR_f}{dt}, \quad (2.3)$$

where m_f is the mass of the deposited layer per surface area, \dot{m}_d and \dot{m}_r are the rate of deposition and removal fluxes of the deposited layer, k_d and ρ_d are the thermal conductivity and density of the deposited material, and R_f is the deposition or fouling resistance. Kern and Seaton (1959) obtained the general time-dependent fouling resistance curve by integrating Eq. (2.3) assuming that the rates of transport and deposition are constant with time, and the rate of removal flux was $\dot{m}_r = c_r m_f$, where c_r is the removal coefficient. The asymptotic deposition or fouling resistance trend is then given by (Kern and Seaton, 1959)

$$R_f(t) = R_f^* (1 - e^{-t/t_c}), \quad (2.4)$$

where R_f^* is the asymptotic deposition or fouling resistance and t_c is the characteristic time scale of the problem.

The deposition and adhesion of particles on tube walls and the subsequent re-entrainment is a complex process. The adhesion of particles to solid surfaces depends on a number of factors, including the physical and chemical properties of the particles (e.g. shape, size, and surface texture) and the surface of the heat exchanger. Particles deposited on the surface can be

detached and re-suspended into the flow if the force from the flow applied to the deposited particles exceeds the adhesion force (Davies, 1966). Cleaver and Yates (1973) studied the detachment of colloidal particles from a flat surface in a turbulent flow. They reported that particle re-entrainment from the surface was due to the lifting force which was created by turbulent eddies hitting the wall. The pressure at the stagnation point at the wall was greater than the pressure in the high velocity region on top of the particle, resulting in a force directly opposed to the net adhesive force. Abu-Qudais and Kittelson (1997) performed an experimental and theoretical study of soot re-entrainment from the combustion chamber walls of a diesel engine. They observed that a high concentration of diesel soot particles emitted during the combustion process are adhesive, and deposited on the walls of a combustion chamber due to a thermophoresis mechanism. They also observed that the deposited particles were subsequently re-entrained during the blowdown process of the exhaust stroke due to unsteady turbulent eddies that disrupted the sublayer.

There have been a number of investigations since Kern and Seaton (1959) that have characterized the deposition or fouling caused by particulates from gases. For example, Bott and Bemrose (1983) performed measurements to study particulate fouling, using dust particles, on the gas side of a finned tube bundle heat exchanger for Reynolds number ranging from 1350 to 3800. They observed that the friction factor of the flow increased to an asymptotic level

between 1.4 and 2.5 times the initial value. Muller-Steinhagen et al. (1988) performed experiments to study the effect of flow velocity and particle size on the deposition of alumina particles with diameters of 0.45 and $2\ \mu\text{m}$ suspended in heptane onto heat transfer surfaces. They observed that the asymptotic fouling resistance was inversely proportional to the flow velocity and particle diameter. Blochl and Muller-Steinhagen (1990) performed experimental investigations on the influence of particle size and particle/fluid combination on particulate deposition rates in liquid flows in heat exchangers. They performed experiments using aluminum oxide particles with nominal diameters ranging from 0.06 to $15\ \mu\text{m}$ suspended in organic liquids for a wide range of concentrations. They observed that with increasing particle size, the asymptotic thermal resistance caused by the particulate deposition decreases continuously and that the deposition of the relatively smaller particles on the tube walls increased mainly due to increase in their particle diffusivity or mass transfer coefficient. They also observed that the asymptotic resistance caused by the particulate deposition for the smaller particles occurred over approximately 6 hours.

The particles in diesel exhaust are relatively small ($< 20\ \text{nm}$) and agglomerated with nominal particle diameters near $0.1\ \mu\text{m}$ (Burtscher, 1998), so the deposition of the soot particles due to diffusion may be important for these relatively smaller particle diameters (Davies, 1966). For the larger agglomerated soot particles that can typically be larger than approximately $0.2\ \mu\text{m}$, the

asymptotic resistance caused by the soot deposition might depend on the flow and particle characteristics.

2.5 Flow and Heat Transfer Characteristics for Two-Phase Gas-Particle Flow

The recirculated exhaust gas that passes through tubes of an EGR cooling device is a two-phase flow of gas and diesel soot particles. Thus, the two-phase flow that would occur through the EGR cooling devices would depend on flow characteristics, such as the soot concentration and cooling device orientation. EGR cooling devices are often positioned horizontally aligned with the engine. A number of flow regimes have been observed for horizontal gas-particle two-phase flow systems. For example, Rudinger (1980) categorized these regimes as dispersed, stratified, annular, and slug flow shown in Figure 2.2. The slug regime is characterized by intermittent and unstable nature, unlike the dispersed flow regime, or the stratified flow regime that occurs for particles with relatively large particles ($d_p \geq 10\mu m$). Yan and Byrne (1997) observed that an annular flow regime is possible for low concentrations of particles having low densities for high flow velocities.

There have also been a number of investigations of the heat transfer characteristics for gas-particle flow mixture. Vyskubenko et al. (1979) performed an experimental study to characterize the heat transfer and deposition in the

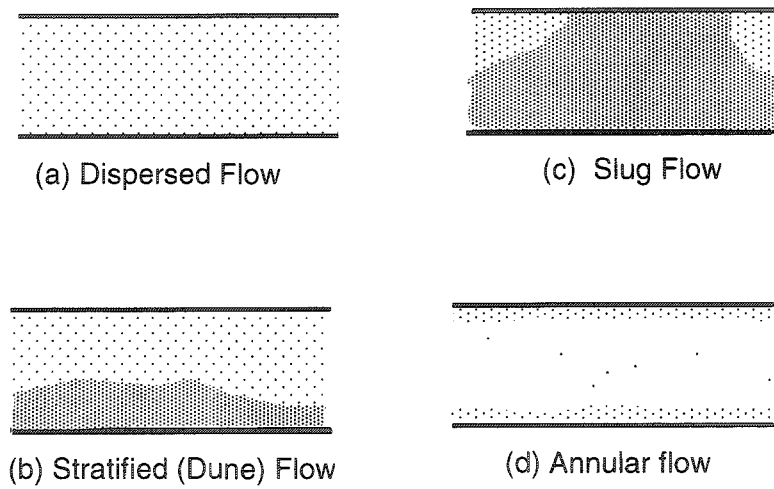


Figure 2.2. Typical flow regimes of gas-solid particle mixture in horizontal tube. (Rudinger,1980.)

initial section of a pipe during cooling of a flow of dispersed gas with submicron particles. They observed that there was an inhomogeneity of the intensity of heat transfer along the pipe that was larger than for the case of homogeneous flow due to the formation of a non-uniform layer of deposits along the pipe caused by the thermophoretic effect. They also observed that the heat transfer was reduced by a ratio of approximately two as opposed to that for pure gas flow, and the thermal resistance of the deposited layer was the main component of the total resistance between the wall and the flow of dispersed gas.

There have been a number of investigations of large diameter particles in the range 15-200 μm , but these are different than the diesel exhaust flow with submicron soot particles. For example, Boothroyd (1970) performed an experimental investigation of heat transfer in the entrance region of a heated duct conveying spherical zinc particles with an average diameter of 15 microns suspended in the air for a wide range of flow conditions. Boothroyd (1970) observed that the particles increased the thermal capacity of the fluid delaying development of the thermal boundary layer and increasing the entrance length. This effect was found to be more significant for larger particles, such as agglomerated particles. Wahi (1977) measured the local Nusselt number for a turbulent air flow with suspended spherical glass particles of diameters 30, 62, and 200 μm , for different solid loading ratios. The Nusselt number was increased up to 50% in the thermal-entry region, with higher values for the higher mass-

loading ratio. The Nusselt number in the fully developed region for the horizontal flow was higher for the larger particles than for the smaller particles at mass loading ratios below 2.0. At higher mass loading ratios the Nusselt number for the smaller particles was higher. Wilkinson et al. (1967) performed an experimental study to characterize the heat transfer for a flow of air with suspended glass and graphite particles of diameters from 40 to 120 μm , in a vertical heated tube for turbulent flow with loading ratios of solids up to 45. The results showed that the suspension of particles improved the heat transfer coefficients up to 500% compared to that for pure air, and that the improvement was greater with high concentrations, with the relatively smaller particles, and with graphite.

Radiative heat transfer can be important for high temperature two-phase flow. Kakac et al. (1987) showed that the radiative heat transfer between phases could be neglected for temperatures below approximately 1000 K, such as in EGR cooling devices applications, and that conduction heat transfer could also be neglected in most cases except in stagnant packed bed heat exchangers.

The hydraulic characteristics for two-phase flow are different from the single-phase flow. For example, Boothroyd (1966) observed that the frictional pressure drop in the tube flow containing suspensions of fine particles were higher than the pure gas flow depending on particle size and loading conditions. Smaller particles at higher loadings tended to increase the frictional pressure

drop. Hetsroni (1982) observed that friction factors for the flow of gas-solid mixtures in pipes are normally greater than that for pure gas, so that an additional pressure drop term has to be accounted for due to the presence of solid particles in the two-phase flow mixture.

Modeling of two-phase flows was considered in depth since the 1970s. For example, several authors, including Ishii (1975), Delhaye et al. (1981), Drew and Lahey (1977), and Ishii and Mishima (1984) developed a general Eulerian approach to predict the flow in two-phase flow systems that was subsequently called the two-fluid model. In this approach, the two phases are considered as interacting continua described by averaged conservation equations governing the balance of mass, momentum, and energy for each phase. The two phases are coupled by interaction terms in the transport equations for mass, momentum, and energy that describe the microscopic phenomena in the equations. These equations are summarized in Appendix D and discussed in the next chapter.

2.6 Deposition Models for the Gas-Particle Flow

The transport and deposition of the particles from a gas-particle flow onto the tube walls are often influenced by a number of mechanisms (Chang et al., 1995), including (1) convection by the gas velocity, (2) diffusion of the particles due to concentration gradient, (3) thermophoresis due to temperature gradient in the flow that causes the particles to migrate in the direction of decreasing

temperature, (4) sedimentation due to gravity for relatively large particles ($d_p > 10\mu m$) that tend to deposit by gravitational settling, (5) drift motion of charged particles under the influence of an electric field, (6) agglomeration of particles and dissociation of particle chains, and (7) re-entrainment or re-suspension of particles from tube surface. The relative influences of these mechanisms vary depending on flow conditions, particle size, duct geometry, and duct orientation (Davies, 1966). A number of analytical solutions and correlations exist for deposition of particles on tube surfaces due to individual mechanisms and in some cases combined effects are included as shown in Table 2.6.

The deposition of charged submicron particles in channel flow could be modeled by solving the continuity equation given by (Beuthe and Chang, 1995)

$$\nabla \cdot \bar{J}_i = -\frac{d[N_i]}{dt} + \text{source} - \text{sink} \quad (2.5)$$

in conjunction with a transport equation for the particles given by

$$\bar{J}_i = N_i \bar{u}_g \pm \mu_i N_i \bar{E} - D_i \nabla N_i - G_i N_i \nabla T_g, \quad (2.6)$$

where \bar{J} is the particle flux density, N is the particle density ($N_p = \alpha_p \rho_p$), \bar{E} is the electric field, D is the diffusion coefficient for the particle, and T is the temperature. The subscripts i and g refer to ions (particles), and gas respectively, and $[]$ denotes the concentration of species in cm^{-3} . In Eq. (2.6), $N_i \bar{u}_g$ represents the particle flux due to charged particles transported by the

Table 2.6: Summary of particle transport and deposition mechanisms.

Particle transport system	Deposition Mechanisms Included
Aerosol in laminar flow in cylindrical channels (Tan and Hsu, 1971)	Convection-Diffusion
Aerosol in a stream flowing through cylindrical channels (Ingham, 1975)	Convection-Diffusion
Particles deposition in a heated boundary layer (Talbot et al., 1980)	Thermophoresis
Aerosol in laminar flow in horizontal channels (Pich, 1972)	Sedimentation
Aerosol in Poiseuille laminar flow in cylindrical channels (Davies, 1973)	Convection-diffusion and sedimentation
Aerosol in laminar flow in horizontal channels (Taulbee and Yu, 1977)	Convection-diffusion and sedimentation
Aerosol in Poiseuille laminar flow in channels (Chen et al., 1983)	Convection-diffusion and sedimentation
Aerosol flows in rectangular channels (Taulbee and Yu, 1975)	Convection-diffusion and sedimentation
Aerosol flows in rectangular channels (Ingham, 1976)	Convection-diffusion and sedimentation
Charged particles in aerosol flow in an unbounded region (Chang, 1991)	Electrostatic, thermophoresis and diffusion

convection of the gas, $\mu_i N_i \bar{E}$ represents the flux due to the drift motion of charged particles under the influence of an electric field, $D_i \nabla N_i$ represents the flux caused by diffusion, and $G_i N_i \nabla T_g$ represents the thermophoresis flux caused by the spatial temperature gradient. Taking the divergence of each side of Eq. (2.6) and substituting in Eq. (2.5) yields the continuity or mass conservation equation for the charged particle given by (Beuthe and Chang, 1995)

$$\frac{\partial N_i}{\partial t} = -\nabla \cdot (N_i \bar{u}_g) \pm \mu_i \nabla \cdot (N_i \bar{E}) + D_i \nabla^2 N_i + G_i \nabla \cdot (N_i \nabla T_g) + (\text{sink} - \text{source}). \quad (2.7)$$

The gas-particle flow in EGR cooling devices normally operates in the absence of an electric field. The residence time of the particles in the typically short tubes of EGR cooling devices are normally small, on the order of milliseconds, relative to the time scale of gas/particle conversion (> 100 ms) such as homogeneous nucleation and condensation (Davies, 1966), so the growth or loss of the particles from the gas phase can be ignored. Thus, the steady-state transport equation for the submicron soot particles can be written as

$$\nabla \cdot (N_p \bar{u}_g) = D_p \nabla^2 N_p + G_p \nabla \cdot (N_p \nabla T_g). \quad (2.8)$$

There are a number of studies that characterized the deposition of aerosol particles in cooled tube flow due to combined convection, diffusion, and thermophoresis. For example, Berger et al. (1995) compiled a model using models for diffusive and thermophoretic deposition available in the literature to

predict the deposition rate of diesel soot particles through pipes. Their numerical results were tested by experimental measurements and showed reasonable agreement under the considered test conditions and assuming that the surface roughness of the pipe was between $40 - 60 \mu m$ and the density of the soot was 1000 kg/m^3 . They concluded that the inaccuracy of their model was due the difficulties with the computations of the temperature profiles necessary to determine the thermophoretic deposition due to temperature loss through the pipe walls.

A number of investigations that studied the transport and deposition of particles due to convection-diffusion mechanism exist in the literature. Tan and Hsu (1971), and Ingham (1975) solved the steady-state convection-diffusion equation given by

$$\nabla \cdot (N_p \bar{u}_g) = D_p \nabla^2 N_p \quad (2.9)$$

to determine the particle concentration profile in laminar cylindrical tube flow. The closed form solution in terms of the diffusion deposition efficiency are given by

$$\eta_{diff} = 1 - \frac{N_{p,z}}{N_{p,i}} = 1 - \sum_{n=1}^{\infty} \left(\frac{4}{\alpha_n^2} \right) \exp(-\alpha_n^2 \xi) \quad (2.10)$$

assuming uniform (slug) flow, and

$$\eta_{diff} = 1 - 0.819 \exp(-3.66\xi) + 0.0976 \exp(-22.31\xi) + 0.0325 \exp(-57.0\xi) + 0.0509 \exp(-49.96\xi^{2/3}), \quad (2.11)$$

assuming parabolic (Poiseuille) flow. Here, α_n are the roots of the Bessel's function of degree zero, and ξ is the dimensionless diffusion parameter defined as

$$\xi = \frac{D_p z}{u_g R^2}, \quad (2.12)$$

where D_p is the diffusion coefficient for the particle and R is the tube radius. The diffusion coefficient, D_p , can be determined using Stokes-Einstein equation given by (Hinds, 1982)

$$D_p = \frac{\kappa T_g}{3\pi\mu_g d_p} C_c, \quad (2.13)$$

where κ is the Boltzmann constant, μ_g is the gas viscosity, d_p is the particle nominal diameter, and C_c is the Cunningham correction factor expressed as (Davies, 1966)

$$C_c = 1 + Kn[1.257 + 0.4 \exp(-1.10 / Kn)]. \quad (2.14)$$

Here, Kn is Knudsen number given by $2\lambda_g / d_p$, where λ_g is the gas mean free path.

Malet et al. (2000) performed analytical and experimental investigations to characterize the deposition of particles in cylindrical tubes for laminar and turbulent flow conditions. They correlated their data for the diffusion efficiency for turbulent tube flow using

$$\eta_{diff} = 1 - \exp\left(-\frac{2u_d z}{u_g R}\right), \quad (2.15)$$

where u_d is the deposition velocity due to diffusion that was correlated by

$$\text{Sh} = 0.0118 \text{Re}_g^{7/8} \text{Sc}_p^{1/3}, \quad (2.16)$$

where Sh is the Sherwood number given by

$$\text{Sh} = \frac{2u_d R}{D_p}, \quad (2.17)$$

Re_g is the Reynolds number for the gas given by

$$\text{Re}_g = \frac{2u_g R}{\nu_g}, \quad (2.18)$$

and Sc_p is the Schmidt number for the aerosol particles given by

$$\text{Sc}_p = \frac{\nu_g}{D_p}. \quad (2.19)$$

There have also been a number of expressions developed in the literature that predict the deposition of particles due to thermophoresis in tube flow. For example, Nishio et al. (1974) performed modeling and experimental investigations to characterize thermophoretic deposition of aerosol particles in the range of $0.3-1.3\mu\text{m}$ in a counter-current heat-exchanger tube for laminar and turbulent flow regimes assuming uniform gas velocity at the tube inlet (i.e., slug flow). Nishio et al. (1974) ignored the effect of deposition thickness on the

convective heat transfer coefficient and other parameters in their model, and the thermophoretic efficiency was obtained as

$$\eta_{TP} = 1 - \frac{\text{Particle number concentration at } z}{\text{Particle number concentration at tube inlet}} = 1 - \frac{N_{p,z}}{N_{p,i}}, \quad (2.20)$$

$$= 1 - \exp \left\{ - \frac{\rho_g c_{p,g}}{k_g} \frac{K_{th} \nu_g (T_{g,i} - T_w)}{T_g} \left[1 - \exp \left(\frac{-4h_g z}{u_g \rho_g c_{p,g} d_i} \right) \right] \right\}, \quad (2.21)$$

where ν_g , ρ_g , k_g , and $c_{p,g}$ are the kinematic viscosity, density, thermal conductivity, and specific heat for the gas. T_w and $T_{g,i}$ are the wall temperature and gas inlet temperature; u_g and T_g are the temperature and velocity for the gas; z is the axial length along the pipe; d_i is the pipe inner diameter; and h_g is the convective heat transfer coefficient for the gas. K_{th} the thermophoretic coefficient in Eq.(2.21) is given by (Talbot et al., 1980)

$$K_{th} = 2C_s \frac{(k_g / k_p + C_t Kn)[1 + Kn(1.2 + 0.41 e^{-0.88Kn})]}{(1 + 3C_m Kn)(1 + 2k_g / k_p + 2C_t Kn)}, \quad (2.22)$$

for the full range of Knudsen number. Here, C_s is the thermal creep coefficient=1.147, C_t is the temperature jump coefficient=2.20, C_m is the velocity jump coefficient=1.146. Nishio et al. (1974) found that the experimental results were in reasonable agreement with the predictions.

The thermophoresis parameter G_p is related to the thermophoresis coefficient by

$$G_p = \frac{-v_g K_{th}}{\bar{T}_g}, \quad (2.23)$$

where \bar{T}_g is the absolute temperature of the gas in the vicinity of the particle near the tube wall. The thermophoretic particle motion is usually described by the thermophoretic velocity, u_{th} , given by (Talbot et al., 1980)

$$\bar{u}_{th} = -K_{th} \frac{v_g}{\bar{T}_g} \nabla T_g, \quad (2.24)$$

Byers and Calvert (1969) studied the particle deposition from turbulent streams in a circular tube by means of a thermophoretic force. They showed that the thermophoretic deposition efficiency for a slug flow can be calculated using

$$\eta_{TP} = 1 - \exp\left\{-\frac{\rho_g c_{p,g} f \text{Re}_g K_{th} v_g (T_{g,i} - T_w)}{4d_i h_g \bar{T}_g} \left[1 - \exp\left(\frac{-4h_g z}{u_g \rho_g c_{p,g} d_i}\right)\right]\right\}, \quad (2.25)$$

where f is the friction factor for the flow.

Romay et al. (1998) studied the thermophoretic deposition of aerosol particles, in the range $0.1-0.7 \mu m$ for pipe flow at Reynolds number between 4000 and 10000. They also derived the thermophoretic deposition efficiency for a slug flow based on a one-dimensional analysis, given as

$$\eta_{TP} = 1 - \left[\frac{T_w + (T_{g,i} - T_w) \exp\left(-\pi d_i h_g z / \rho_g \dot{V}_g c_{p,g}\right)}{\bar{T}_{g,i}} \right]^{\text{Pr} K_{th}}, \quad (2.26)$$

where \dot{V}_g is the gas volumetric flow rate, and Pr is the Prandtl number for the gas. They observed that this expression had reasonable agreement with their measurements for smaller particle size ($\approx 0.1\mu m$) and lower Reynolds number ($Re \approx 5000$). As the particle size and Reynolds number increased, the measured deposition rate was up to 2.0 times greater than that predicted using Eq. (2.26). A similar trend was observed when they compared the results to the experimental measurements of Byers and Calvert (1969) and Nishio et al. (1974), where the experimental thermophoretic deposition efficiency was up to 3.5 times larger. Romay et al. (1998) concluded that this tendency for the theoretical models to underpredict the experimental results in the turbulent flows were caused by either turbulent transport and impaction, or non-uniform particle concentration gradients at the entrance to the pipe cooling section, that were not included in the theoretical derivation.

Messerer et al. (2003) recently performed an experimental study to characterize the thermophoretic deposition of diesel soot particles in a plate-to-plate thermal precipitation system under flow and temperature conditions relevant for modern heavy-duty diesel engine exhaust gas systems. They observed that the thermophoretic deposition efficiency for the precipitation system was independent of particle size and Knudsen number, throughout the investigated particle size range of $0.034 - 0.3\mu m$. The experimental results of Messerer et al. (2003) were in good agreement with the theoretical calculations if

it were assumed $K_{th} \approx 0.55$ that is used for the free molecular regime ($Kn \gg 1$). Their results also demonstrate that $K_{th} \approx 0.55$ was applicable for agglomerate soot particles in the transition regime ($Kn \approx 1$).

2.7 Non-Destructive Measurement Techniques for the Deposited Soot Layer Thickness

The measurements of film thickness of powder layers in pipes, such as those involved in powder conveying systems in gas-solid flow, could be performed using a range of non-destructive electrical impedance and optical transmission techniques (Harvel and Chang, 1995). For example, Irons and Chang (1983a) tested strip- or ring-type capacitance transducers that could be used in non-electrically conductive pipes to non-destructively detect powder flow or measure powder thickness using the dielectric constant difference of the gas and powder. Non-destructive optical methods could be used in transparent pipes to measure film thickness of powder that has a fairly high coefficient of reflectivity, such as a detergent powder. Optical techniques are generally unreliable in situations where the optical surfaces can become dirty (Beck and Wainwright, 1969). Davazoglou (1997) performed measurements for the thickness of semiconducting layers deposited on fully or partly transparent substrates of finite thickness, such as Si layers deposited on silica substrates, using optical transmission technique. Root and Kaufman (1992) developed a

non-contacting and non-destructive technique to measure film thickness of solids, such as coatings, using a microstrip resonance or microwave test system that used differences in relative permittivities of the media. Powder layer thickness on smooth contacting surfaces, or smooth two-phase interfacial areas could also be measured using a non-destructive pulse-echo ultrasound technique (Chang and Morala, 1990). The soot powder layer experienced in diesel applications is, however, a porous (void fraction $\approx 40\%$) non-smooth contacting substance, so the ultrasound technique would not be effective in measuring the thin (1 mm order) soot thickness profile in these systems due to signal attenuation and multiple scattering problems.

Neutron radiography has been used extensively to examine the distribution of light hydrogenous compounds in metal objects because the neutron flux is significantly attenuated when it passes through the light hydrogenous compound, but not significantly attenuated as it passes through the metal. For example, Tyufyakov (1983) used this technique to visualize the aluminum hydroxide corrosion layer formed on aircraft structures by the interaction of the aluminum and hydrogen in the surrounding. Real-time neutron radiography (RTNR) has also been used in a number of investigations to non-destructively visualize and measure light hydrogen compounds such as oil, water, or refrigerants, in metal pipes and containers, or to visualize and measure the void fraction in two-phase flow of these fluids. For example, Takenaka et al.

(1998) and Harvel et al. (2000) used real-time neutron radiography to measure the void fraction distributions of two-phase flow in the rod bundles of water-cooled nuclear reactors, while Glickstein et al. (1995) and Harvel et al. (1995) used this technique to measure the void fraction distributions in bubbly two-phase flow. Asano et al. (1999) extended the application to the two-phase refrigerant flow in a refrigerator. The technique can also be used to visualize solids. For example, Umekawa et al. (1999) used thermal neutron radiography and B_4C tracers to visualize the flow of sand, coated with $CdSO_4$, in a fluidized bed heat exchanger.

The soot in diesel exhaust primarily consists of a solid core of black “elemental” carbon particles surrounded by a shell-like structure consisting of hydrocarbons and sulphate compounds as mentioned earlier. Therefore, a non-destructive neutron radiography technique could be used to measure the deposited diesel soot profiles in tubes of EGR cooling devices. The determination of the soot thickness using neutron radiography requires knowledge of the value of the thermal neutron attenuation coefficient for diesel soot material that does not exist in the literature, so it must be determined by calibration.

CHAPTER 3: Model for the Soot Deposition Layer and its Effect on the Performance of EGR Cooling Devices

The objective of this chapter is to develop a simplified model to be used to characterize the heat transfer, pressure drop, and soot deposition in diesel engine EGR cooling devices. The model was derived from two-phase gas-particle conservation equations with appropriate constitutive relations. The non-dimensional conservation equations were used to evaluate the coupling between the gas and particle phases for thermal and momentum conservation equations. Predictions were performed to investigate the effects of the soot deposited layer on the heat transfer characteristics in EGR cooling devices.

3.1 The Conservation Equations

The flow of soot particles and exhaust gas in the tubes of an EGR cooling device was considered as a mono-sized fully-dispersed gas-particle flow as shown in Figure 3.1 with $\alpha_g \geq 0.95$ (Irons and Chang, 1983b). The exhaust gas was the “carrier” phase and the suspension of soot particles in the flow was the “fully dispersed” phase. The two phases were thermally and dynamically coupled depending on the concentration of the soot particles in the flow or “dust loading”.

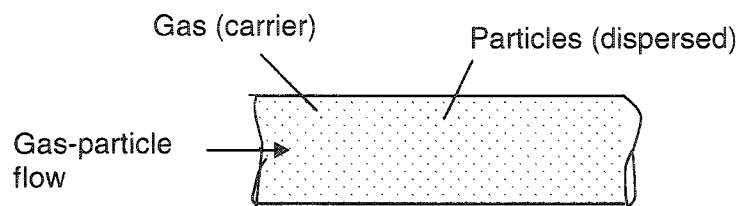


Figure 3.1 The mono-sized fully-dispersed gas-particle flow system used in the present model.

Using the two-phase flow conservation equations (Appendix D), the unsteady continuity equations for the gas ($k = g$) and particle ($k = p$) phases can be written as

$$\frac{\partial \rho_g}{\partial t} + \nabla \cdot (\rho_g \bar{u}_g) = 0, \quad (3.1)$$

and

$$\frac{\partial \alpha_p}{\partial t} + \nabla \cdot (\alpha_p \bar{u}_p) = 0. \quad (3.2)$$

Here, the two-phase interfacial mass transfer terms due to homogeneous nucleation or condensation were assumed negligible since the residence time of the particles in the tubes are normally small, on the order of milliseconds, relative to the time scale of gas/particle conversion (> 100 ms) (Davies, 1966), for short tubes typically used in EGR cooling devices. Thus, phase change, such as the effect of condensation of hydrocarbon in the tubes of EGR cooling devices can be ignored.

The interfacial momentum and heat transfer between the two phases were assumed to be due to drag force and forced convective heat transfer. The inter-particle collisions were neglected since the flow was assumed fully dispersed (Fan and Zhu, 1998), so the motion of an isolated particle is not influenced by the wake of the others. Thus, the interfacial heat transfer and drag force between the gas and particle phases were given by Eqs. (D.7) and (D.10), i.e.,

$$q_{g-p} = N_p h_{g-p} A_p (T_g - T_p), \quad (3.3)$$

and

$$\bar{F}_{g-p} = N_p K_p (\bar{u}_g - \bar{u}_p), \quad (3.4)$$

where $K_p = 3\pi\mu_g d_p$ is the Stokes interfacial drag coefficient (Soo, 1967).

Assuming negligible gravitational forces on the particles and considering a horizontal flow, the unsteady momentum equations for the gas and inelastic particle phases are given by

$$\rho_g \left(\frac{\partial \bar{u}_g}{\partial t} + \bar{u}_g \cdot \nabla \bar{u}_g \right) = -\nabla p_g + \nabla \cdot (\mu_g \nabla \bar{u}_g) + N_p K_p (\bar{u}_p - \bar{u}_g), \quad (3.5)$$

and

$$\alpha_p \frac{\partial \bar{u}_p}{\partial t} + \alpha_p \bar{u}_p \cdot \nabla \bar{u}_p = -\frac{\alpha_p}{\rho_p} \nabla p_p - \frac{N_p K_p}{\rho_p} (\bar{u}_p - \bar{u}_g). \quad (3.6)$$

The unsteady energy conservation equations for the gas and particle phases are given by

$$\rho_g \left[\frac{\partial (C_{p,g} T_g)}{\partial t} + \bar{u}_g \cdot \nabla (C_{p,g} T_g) \right] = \nabla \cdot (k_g \nabla T_g) + N_p h_{g-p} A_p (T_p - T_g), \quad (3.7)$$

and

$$\alpha_p \frac{\partial T_p}{\partial t} + \alpha_p \nabla \cdot (\bar{u}_p T_p) = -\frac{N_p h_{g-p} A_p}{\rho_p C_{p,p}} (T_p - T_g), \quad (3.8)$$

where the viscous dissipation and pressure energy conditions were assumed negligible.

3.2 The Conservation Equations in Dimensionless Forms

Using the dimensionless parameters $\tilde{\rho}_g, \tilde{k}_g, \tilde{C}_{p,g}, \tau, \tilde{\nabla}, \tilde{N}_p, \bar{U}_p, \bar{U}_g, \tilde{p}_g, \tilde{p}_p, \theta_g,$ and θ_p (defined in the list of nomenclature), the non-dimensional gas and particle continuity equations become

$$\frac{\partial \tilde{\rho}_g}{\partial \tau} + \tilde{\nabla} \cdot (\tilde{\rho}_g \bar{U}_g) = 0, \quad (3.9)$$

and

$$\frac{\partial \alpha_p}{\partial \tau} + \tilde{\nabla} \cdot (\alpha_p \bar{U}_p) = 0. \quad (3.10)$$

The dimensionless momentum conservation equations for the gas and particle phases are given by

$$\tilde{\rho}_g \left(\frac{\partial \bar{U}_g}{\partial \tau} + \bar{U}_g \cdot \tilde{\nabla} \bar{U}_g \right) = -\tilde{\nabla} \tilde{p}_g + \frac{1}{\text{Re}_{g,i}} \tilde{\nabla} \cdot (\tilde{\mu}_g \tilde{\nabla} \bar{U}_g) + \tilde{N}_p \Sigma_{2\phi} (\bar{U}_p - \bar{U}_g), \quad (3.11)$$

and

$$\alpha_p \frac{\partial \bar{U}_p}{\partial \tau} + \alpha_p \bar{U}_p \cdot \tilde{\nabla} \bar{U}_p = -\alpha_p \tilde{\nabla} \tilde{p}_p - \frac{\rho_{g,i}}{\rho_p} \tilde{N}_p \Sigma_{2\phi} (\bar{U}_p - \bar{U}_g). \quad (3.12)$$

The dimensionless energy conservation equations for the gas and particle phases are given by

$$\tilde{\rho}_g \left[\frac{\partial (\tilde{C}_{p,g} \theta_g)}{\partial \tau} + \bar{U}_g \cdot \tilde{\nabla} (\tilde{C}_{p,g} \theta_g) \right] = \frac{1}{\text{Re}_{g,i} \text{Pr}_{g,i}} \tilde{\nabla} \cdot (\tilde{k}_g \tilde{\nabla} \theta_g) + \tilde{N}_p \Sigma_{\text{TH}} (\theta_p - \theta_g), \quad (3.13)$$

and

$$\alpha_p \frac{\partial \theta_p}{\partial \tau} + \alpha_p \nabla \cdot (\bar{U}_p \theta_p) = - \left(\frac{C_{p,g,i}}{C_{p,p}} \right) \left(\frac{\rho_{g,i}}{\rho_p} \right) \left(\frac{d_p}{d_t} \right) \tilde{N}_p \Sigma_{TH} (\theta_p - \theta_g), \quad (3.14)$$

where $Pr_{g,i}$ and $Re_{g,i}$ are the Prandtl number and Reynolds number for the gas phase evaluated using cross-sectionally averaged gas properties at tube inlet. The relative importance of the interfacial terms for the mono-sized fully-dispersed gas-particle flow were evaluated using the dimensionless momentum and heat two-phase flow parameters $\Sigma_{2\phi}$ and Σ_{TH} given by

$$\Sigma_{2\phi} = \frac{K_p N_{p,i} d_t}{\rho_{g,i} u_{g,i}}, \quad (3.15)$$

and

$$\Sigma_{TH} = \frac{h_{g-p} A_p N_{p,i} d_t}{\rho_{g,i} u_{g,i} C_{p,g,i}}. \quad (3.16)$$

3.3 The Fully-Dispersed-Dilute Flow Model

The values of $\Sigma_{2\phi}$ and Σ_{TH} for typical diesel exhaust flow were evaluated and are shown in Figures 3.2 and 3.3, for different soot particle number densities. These results indicate that the interaction parameters were negligible for soot particle number density N_p less than approximately 10^{11} #pt./m³. In these cases, the soot particle momentum and energy do not tend to have a significant influence on the velocity and temperature fields for the conveying gas phase.

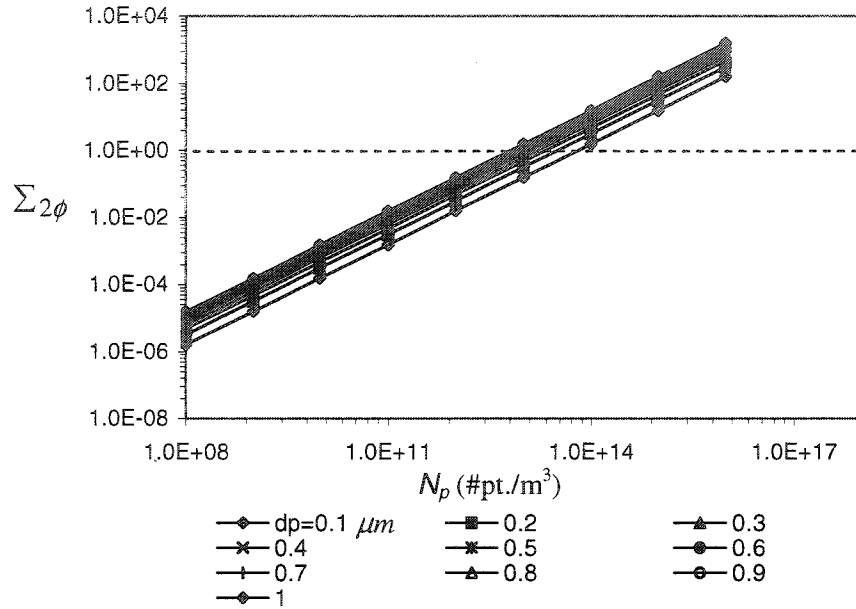


Figure 3.2. The two-phase momentum interaction parameter as a function of particle number density for a typical diesel exhaust gas flow for various soot particle diameters for $Re_{g,i} = 1500$.

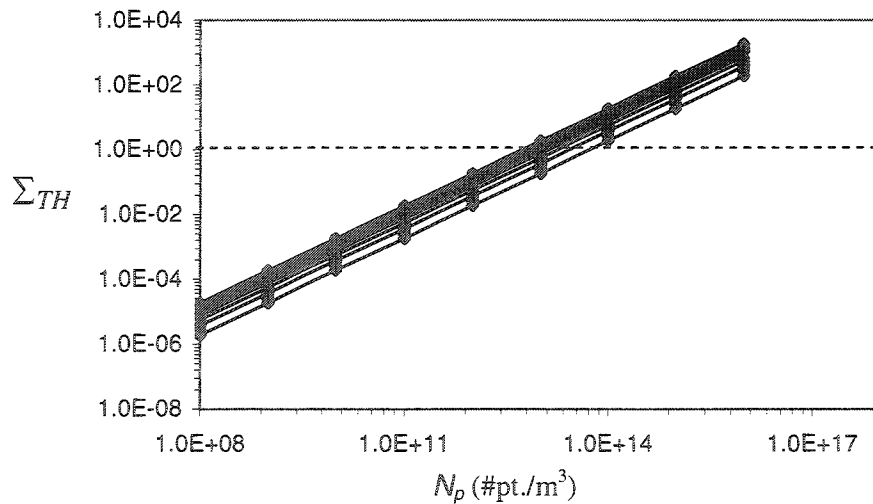


Figure 3.3. The two-phase heat interaction parameter as a function of particle number density for a typical diesel exhaust gas flow for various soot particle diameters for $Re_{g,i} = 1500$.

Thus, these cases can be modeled by the fully-dispersed-dilute flow. The steady-state velocity and temperature fields of the gas-particle flow system can be determined using only the gas-phase conservation equations only given by

$$\tilde{\nabla} \cdot (\tilde{\rho}_g \bar{U}_g) = 0 \quad (3.17)$$

$$\tilde{\rho}_g \bar{U}_g \cdot \tilde{\nabla} \bar{U}_g = -\tilde{\nabla} \tilde{p}_g + \frac{1}{\text{Re}_{g,i}} \tilde{\nabla} \cdot (\tilde{\mu}_g \tilde{\nabla} \bar{U}_g) \quad (3.18)$$

$$\tilde{\rho}_g \bar{U}_g \cdot \tilde{\nabla} (\tilde{C}_{p,g} \theta_g) = \frac{1}{\text{Re}_{g,i} \text{Pr}_{g,i}} \tilde{\nabla} \cdot (\tilde{k}_g \tilde{\nabla} \theta_g). \quad (3.19)$$

The transport and deposition of the soot particles onto the tube surfaces for the dilute flow were modeled here using the particle transport equation in the tubes assuming that the transport and deposition process were determined by the individual (or combined) mechanisms of convection, diffusion and/or thermophoresis, depending on the relevant magnitudes of these competing mechanisms. The steady-state particle transport equation in non-dimensional form is given by

$$(Sc_p \text{Re}_{g,i}) \tilde{\nabla} \cdot (\bar{U}_g \tilde{N}_p) - \tilde{\nabla}^2 \tilde{N}_p - \sigma_p \tilde{\nabla} \cdot (\tilde{N}_p \tilde{\nabla} \theta_g) = 0, \quad (3.20)$$

where $\Delta T = T_{g,i} - T_w$, and σ_p is the dimensionless thermophoresis parameter for the particle given by (Chang, 1991)

$$\sigma_p = \frac{G_p}{D_p} \Delta T. \quad (3.21)$$

The dimensional thermophoresis parameter, G_p (valid for $0 < Kn < \infty$) is given by (Talbot et al., 1980)

$$G_p = -2C_s \frac{(k_g/k_p + C_t Kn)[1 + Kn(1.2 + 0.41e^{-0.88Kn})] v_{g,i}}{(1 + 3C_m Kn)(1 + 2k_g/k_p + 2C_t Kn) \bar{T}_g}. \quad (3.22)$$

This is related to the thermophoretic coefficient K_{th} used in previous models by

$$G_p = \frac{-v_g K_{th}}{\bar{T}_g}. \quad (3.23)$$

Equation (3.20) provides basis for assessing the relative significance of the competing deposition effects caused by thermophoresis and diffusion for the transported soot particles in the system. Thus, the deposition of soot particles due to thermophoretic effect can be neglected for $|\sigma_p| \ll 1$, while it tends to be important for $|\sigma_p| \geq 1$. The value of σ_p was evaluated as a function of temperature difference ΔT and is shown in Figure 3.4. The significance of the thermophoretic effect relative to the diffusion effect increases with increasing ΔT and particle diameter as shown in Figure 3.4.

3.4 One-Dimensional Heat Transfer and Soot Deposition Model

The fully-dispersed-dilute flow model was considered here and the governing equations were integrated across the tube cross-section to yield one dimensional equations with bulk-stream flow characteristics given in Table 3.1.

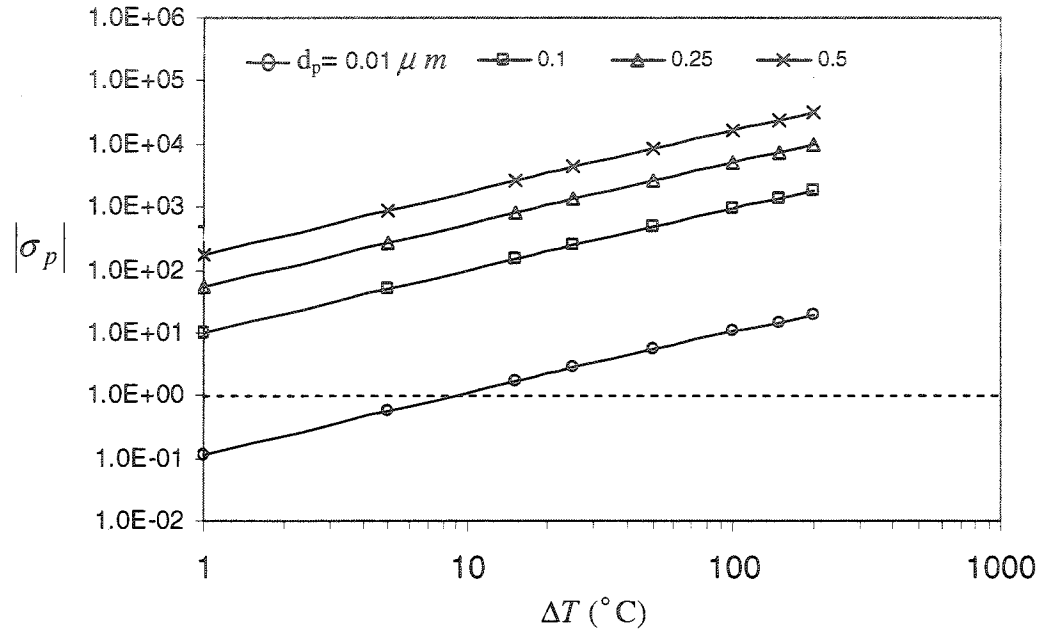


Figure 3.4. The thermophoresis parameter as a function of temperature difference between the gas inlet temperature and tube wall temperature ($\Delta T = T_{g,i} - T_w$) of the EGR cooling device for various soot particle diameters.

Table 3.1: Summary of the one-dimensional heat transfer model used in this study.

Conservation equation	
Mass	$\frac{d(\rho_g u_g A_t)}{dz} = \frac{d\dot{m}_g}{dz} = 0$, $\dot{m}_g = \text{constant}$
Momentum	$-\frac{dp_g}{dz} = \frac{1}{A_t} \frac{d\dot{M}_{a,g}}{dz} + \frac{1}{A_t} \frac{d}{dz} (\dot{m}_g u_g) + \frac{2f_z}{d_t} \rho_g u_g^2$
Energy	$-d\dot{Q} = [\dot{m} d(c_p T)]_{gas} = -[\dot{m} d(c_p T)]_{coolant}$
Constitutive relation	$d\dot{Q} = U_z dA_s [T_g(z) - T_c(z)]$

More details of the heat transfer model are given in Appendix E. The control volume considered in a nominal cooling tube, including thermal circuit and deposited soot layer concept used in the model are shown in Figure 3.5. A schematic of the dilute flow soot deposition model used in this investigation is shown in Figure 3.6. The deposition of the soot particles caused by combined diffusion and thermophoresis effects could be approximately determined using (Chen and Yu, 1993)

$$(\eta_{dep})_{comb} \approx \eta_{diff} + \eta_{TP} - f_{1,2}, \quad (3.24)$$

where $f_{1,2}$ is a function of the two deposition efficiencies. This function was assumed here to be zero as a first approximation. The deposition of the soot particles onto the circular tube walls caused by the diffusion mechanism under laminar flow, assuming uniform inlet gas velocity, was determined using (Ingham, 1975)

$$(\eta_{diff})_{Lam} = 1 - \frac{N_{p,z}}{N_{p,i}} = 1 - \sum_{n=1}^{\infty} \left(\frac{4}{\alpha_n^2} \right) \exp(-\alpha_n^2 \xi), \quad (3.25)$$

where α_n are the roots of the Bessel's function of degree zero, and ξ is the dimensionless diffusion parameter given by

$$\xi = \frac{D_p z}{4u_g R^2}. \quad (3.26)$$

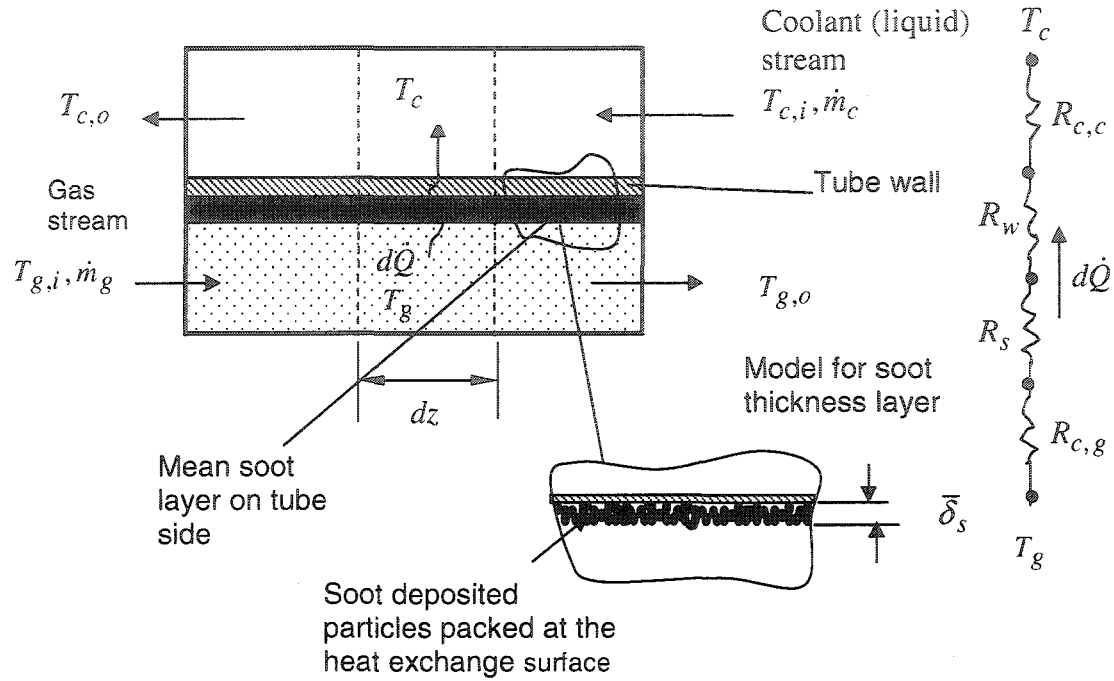


Figure 3.5. Schematic showing control volume in a nominal cooling tube, including thermal circuit and soot deposited layer concept used in this model.

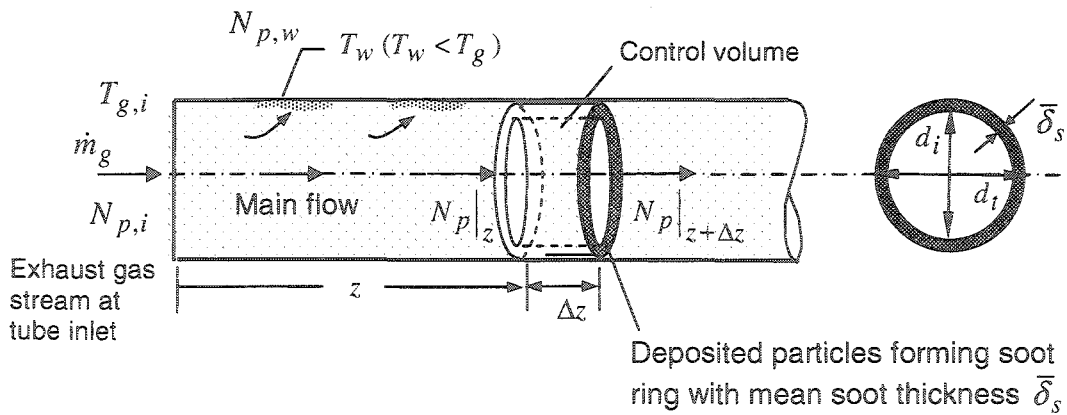


Figure 3.6. Schematic of the one-dimensional dilute flow and deposition model used in this investigation.

Here, again, D_p is the diffusion coefficient for the particle and R is the tube radius. The deposition of the soot particles caused by diffusion mechanism under turbulent flow was modeled by (Malet et al., 2000)

$$(\eta_{diff})_{Tur} = 1 - \exp\left(-\frac{2u_d z}{u_g R}\right), \quad (3.27)$$

where u_d is the deposition velocity due to diffusion given by Eqs. (2.16) to (2.18).

The deposition of the soot particles caused by the thermophoresis effect was determined here using (Nishio et al., 1974)

$$\eta_{TP} = 1 - \exp\left\{-\frac{\rho_g c_{p,g}}{k_g} \frac{K_{th} v_g (T_{g,i} - T_w)}{T_g} \left[1 - \exp\left(\frac{-4h_g z}{u_g \rho_g c_{p,g} d_i}\right)\right]\right\}. \quad (3.28)$$

Thus, the soot particles deposited on the tube walls for a certain tube length z , due to diffusion or thermophoresis effects were determined using

$$N_{p,w}|_z = \eta_{dep} N_{p,i}, \quad (3.29)$$

where η_{dep} is the deposition efficiency given by Eqs. (3.25), (3.27), or (3.28).

3.4.1 Modeling of the Thermophysical Properties of the Gas and Coolant Mixtures

The exhaust gas passing through the tubes of the EGR cooling device constitutes a gaseous mixture typically consisting of N_2 , O_2 , CO_2 , NO , NO_2 , CO , SO_2 , and H_2O , with different volumetric or weight proportions in the mixture. The

accurate prediction of the heat transfer characteristics of the flow in the EGR cooling device requires accurate estimation of the temperature-dependent thermophysical properties of the exhaust gas mixture flowing in tubes, and the coolant mixture flowing in shell. A summary of the gas mixture models used in this investigation is given in Table 3.2.

The coolant passing through the shell side is also a mixture that typically contains approximately 50% ethylene-glycol 50% water mixture from the engine coolant system. The correlations used in this investigation to predict the thermophysical properties of the coolant mixture are shown in Tables 3.3 and 3.4. Bohne et al. (1984) found that these correlations were accurate within $\pm 5\%$.

3.4.2 Numerical Scheme

The model calculations were performed for a nominal tube of an EGR cooling device. The flow field was discretized in the stream-wise direction and tests were performed to ensure the results were independent of the computational cell size. An iterative numerical scheme was used to compute the performance of the EGR cooling device operating in a counter-current mode. A quasi steady state model was used as an approximation to predict the short-term heat transfer and pressure drop performance of EGR cooling devices. This was done by computing the incremental local soot deposited layer thickness δ_s in time Δt and summing it over a total period of time t , taking into consideration the

Table 3.2: Summary of the models used to predict the thermophysical properties of exhaust gas mixture. (n : number of pure gases in the mixture; x_i : mole or weight fraction of the i^{th} gas in the mixture; R : universal gas constant.)

Thermo-physical property of gas mixture	Model
(i) Dynamic viscosity $\mu_{g,mix}$ (kg / m.sec)	<p>Wilke model (Bird et al., 1960):</p> $\mu_{g,mix} = \frac{\sum_{i=1}^n x_i \mu_{g,i}}{\sum_{j=1}^n x_j \Phi_{ij}}$ <p>Chapman-Enskog model (Chapman and Cowling, 1960):</p> $\mu_{g,i} = 2.6693 \times 10^{-6} \frac{\sqrt{M_i T_g}}{\sigma^2 \Omega_{\mu}}$ $\Phi_{ij} = \frac{1}{\sqrt{8}} \left(1 + \frac{M_i}{M_j} \right)^{-1/2} \left[1 + \left(\frac{\mu_{g,i}}{\mu_{g,j}} \right)^{1/2} \left(\frac{M_i}{M_j} \right)^{1/4} \right]^2$
(ii) Specific heat at constant pressure $c_{p,g,mix}$ (J / kg.K)	<p>Planck-type model (Bird et al., 1960):</p> $c_{p,g,mix} = \frac{1}{M_{mix}} \sum_i^n (x_i M_i c_{p,g,i})$ $M_{mix} = \sum_i^n x_i M_i$
(iii) Thermal conductivity $k_{g,mix}$ (W / m.K)	<p>Euken model (Bird et al. 1960):</p> $k_{g,mix} = \left[c_{p,mix} + \frac{5}{4} \left(\frac{1000R}{M_{mix}} \right) \right] \mu_{g,mix}$
(iv) Density $\rho_{g,mix}$ (kg / m ³)	<p>Planck-type model (Bird et al., 1960):</p> $\rho_{g,mix} = \frac{1}{M_{mix}} \sum_i^n x_i M_i \rho_{g,i}$ <p>Ideal-gas model:</p> $\rho_{g,i} = \frac{P_g}{RT_g}$

Table 3.3: Summary of the correlations used to estimate the thermophysical properties of the ethylene glycol-water mixture. (Bohne et al., 1984.)

Thermo-physical property	Correlation
$\mu_{c,mix}$ (Pa.sec)	$\mu_{c,mix} = \frac{1}{1000} \text{Exp} \left\{ \sum_{i=1}^3 \sum_{j=1}^3 A_{ij} \cdot x^{(j-1)} \cdot T_c^{(i-1)} + \left(\sum_{j=1}^3 A_{3,j} \cdot x^{(i-1)} \right)^{1/4} \cdot T_c^2 \right\}$ <p>A_{ij} - Table 3.4a. x : mass fraction of ethylene glycol in the mixture T_c : coolant mixture temperature ($^{\circ}\text{C}$) (Applicable range: -10 to 100°C)</p>
$k_{c,mix}$ (W / m.K)	$k_{c,mix} = (1-x) \cdot k_w + x \cdot k_{eg} - F \cdot (k_w - k_{eg}) \cdot (1-x) \cdot x$ $k_w = 0.56276 + 1.874 \cdot 10^{-3} \cdot T_c - 6.8 \cdot 10^{-6} \cdot T_c^2$ $k_{eg} = 0.24511 + 1.755 \cdot 10^{-4} \cdot T_c - 8.52 \cdot 10^{-7} \cdot T_c^2$ $F = 0.6635 - 0.3698 \cdot x - 8.85 \cdot 10^{-4} \cdot T_c \quad (\text{Filippov, 1970})$ <p>Applicable range: -20 to 180°C</p>
$\rho_{c,mix}$ (g / cm ³)	$\rho_{c,mix} = \sum_{i=1}^3 \sum_{j=1}^3 B_{ij} \cdot x^{(j-1)} \cdot T_c^{(i-1)}$ <p>B_{ij} - Table 3.4b. Applicable range: -10 to 150°C</p>
$\text{Pr}_{c,mix}$	$\text{Pr}_{c,mix} = \text{Exp} \left\{ \sum_{i=1}^3 \sum_{j=1}^3 C_{ij} \cdot x^{(j-1)} \cdot T_c^{(i-1)} + \left(\sum_{j=1}^3 C_{3,j} \cdot x^{(i-1)} \right)^{1/4} \cdot T_c^2 \right\}$ <p>C_{ij} - Table 3.4c. Applicable range: -10 to 110°C.</p>
$C_{p,c,mix}$ (kJ/kg. $^{\circ}\text{C}$)	$C_{p,c,mix} = \frac{\text{Pr}_{c,mix} \cdot k_{c,mix}}{\mu_{c,mix}}$

Table 3.4a: The coefficients A_{ij} for the correlation of dynamic viscosity for the ethylene glycol-water mixture. (Bohne et al., 1984.)

	$j = 1$	$j = 2$	$j = 3$
$i = 1$	$5.5164 \cdot 10^{-1}$	2.6492	$8.2935 \cdot 10^{-1}$
$i = 2$	$-2.7633 \cdot 10^{-2}$	$-3.1496 \cdot 10^{-2}$	$4.8136 \cdot 10^{-3}$
$i = 3$	$6.0629 \cdot 10^{-17}$	$2.2389 \cdot 10^{-15}$	$5.8790 \cdot 10^{-16}$

Table 3.4b: The coefficients B_{ij} for the correlation of density for the ethylene glycol-water mixture. (Bohne et al., 1984.)

	$j = 1$	$j = 2$	$j = 3$
$i = 1$	1.0004	$1.7659 \cdot 10^{-1}$	$-4.9214 \cdot 10^{-2}$
$i = 2$	$-1.2379 \cdot 10^{-4}$	$-9.9189 \cdot 10^{-4}$	$4.1024 \cdot 10^{-4}$
$i = 3$	$-2.9837 \cdot 10^{-6}$	$2.4614 \cdot 10^{-6}$	$-9.5278 \cdot 10^{-8}$

Table 3.4c: The coefficients C_{ij} for the correlation of Prandtl number for the ethylene glycol-water mixture. (Bohne et al., 1984.)

	$j = 1$	$j = 2$	$j = 3$
$i = 1$	2.5735	3.0411	$6.0237 \cdot 10^{-1}$
$i = 2$	$-3.1169 \cdot 10^{-2}$	$-2.5424 \cdot 10^{-2}$	$3.7454 \cdot 10^{-3}$
$i = 3$	$1.1605 \cdot 10^{-16}$	$2.5283 \cdot 10^{-15}$	$2.3777 \cdot 10^{-16}$

local changes of the flow properties and tube diameter along the cooling device over the specified time interval. A schematic showing the numerical scheme used in this model and a summary of the computational equations used in this model are given in Appendix F.

3.5 Calculations of the Deposited Soot Layer and its Effect on the Performance of EGR Cooling Devices

A series of simulations were performed to calculate the diesel soot deposition layer using the dilute flow model and how the deposited soot layer would affect the performance of EGR cooling devices. The predicted change in the deposited soot layer thickness along the EGR cooling device ($L/d_i=44$) for 5 hours of deposition is shown in Figure 3.7. The simulations were performed for different gas inlet temperatures typically used in EGR applications. The results indicate that the deposited soot layer decreases nonlinearly along the cooling device for all cases, and increased with increasing the gas inlet temperature. This was not surprising since the deposition caused by the thermophoretic effect was a maximum at the entrance of the cooling device where the driving temperature difference is largest. This effect increases with increasing the gas inlet temperature, so it should be noted that the change in the soot layer thickness that occurred at a location approximately 0.2 L from the entrance of the cooling device was due to the fact that the thermophoretic effect became less

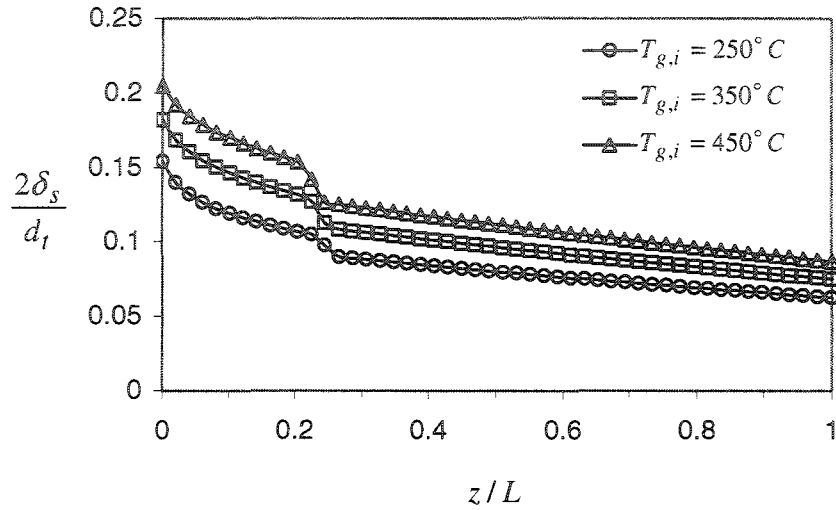


Figure 3.7. Predictions of the change in deposited soot layer thickness along the EGR cooling device for different inlet gas temperatures. ($L=20$ cm, $d_t=4.5$ mm, $\dot{m}_g=2$ kg/hr per tube, $T_{c,i}=30^\circ\text{C}$, $C_s=50$ mg/m³, $N_p=10^{10}$ #pt./m³.)

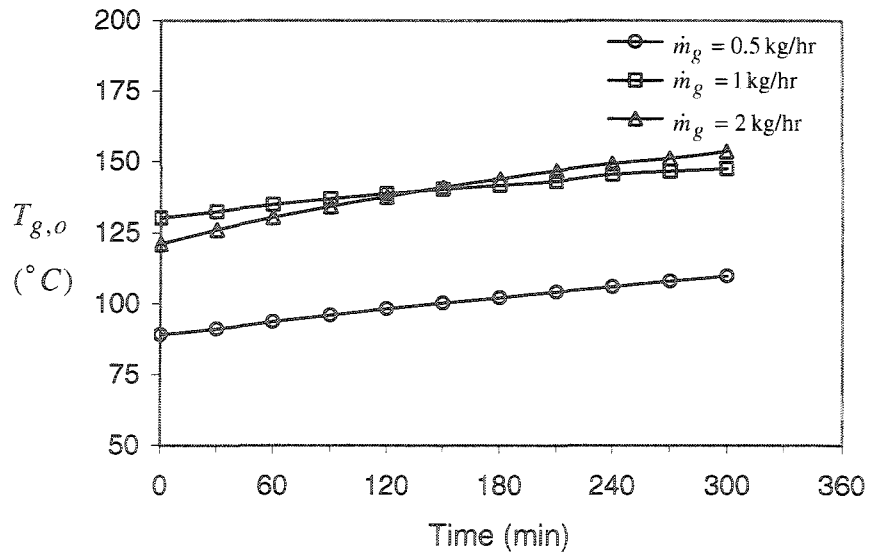


Figure 3.8. Predictions of the change in the exit gas temperature from the EGR cooling device for different gas mass flow rates. ($L=20$ cm, $d_t=4.5$ mm, $T_{g,i}=250^\circ\text{C}$, $T_{c,i}=30^\circ\text{C}$, $C_s=50$ mg/m³, $N_p=10^{10}$ #pt./m³.)

significant at this location as the gas temperature cooled approached the tube wall temperature. The predictions in the change of the thermal performance of the EGR cooling device for different gas mass flow rate, using the present model are shown in Figures 3.8 and 3.9. The results show that as the deposited soot layer builds up the exit gas temperature from the cooling device increases, and therefore the thermal effectiveness of the tube decreases with time. The change in the pressure drop for the gas across the cooling device predicted from the model for different gas mass flow rates is shown in Figure 3.10. The predictions indicate that the pressure drop increases as the deposited soot layer grows especially for the case of the higher gas mass flow rate where the pressure drop increased by approximately 85%.

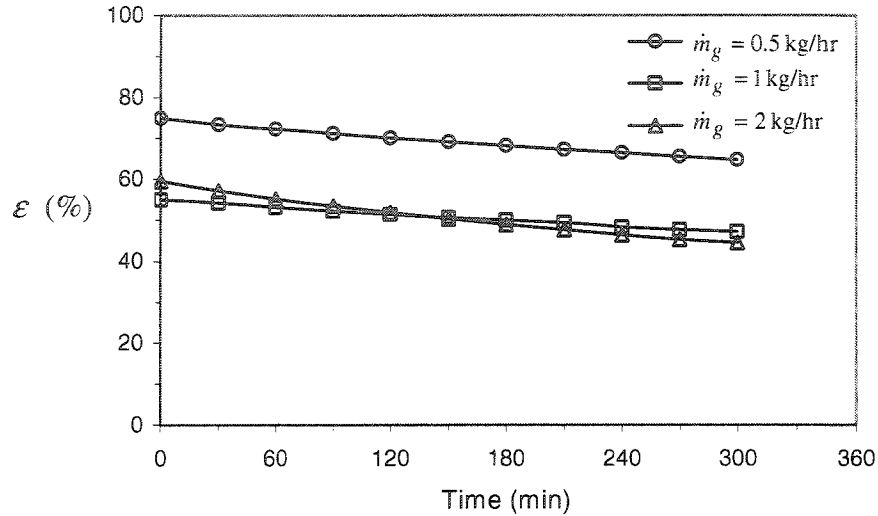


Figure 3.9. Predictions of the change in the thermal effectiveness of the EGR cooling device for different gas mass flow rates. ($L=20\text{cm}$, $d_t=4.5\text{ mm}$, $T_{g,i}=250^\circ\text{C}$, $T_{c,i}=30^\circ\text{C}$, $C_s=50\text{ mg/m}^3$, $N_p=10^{10}\text{ \#pt./m}^3$.)

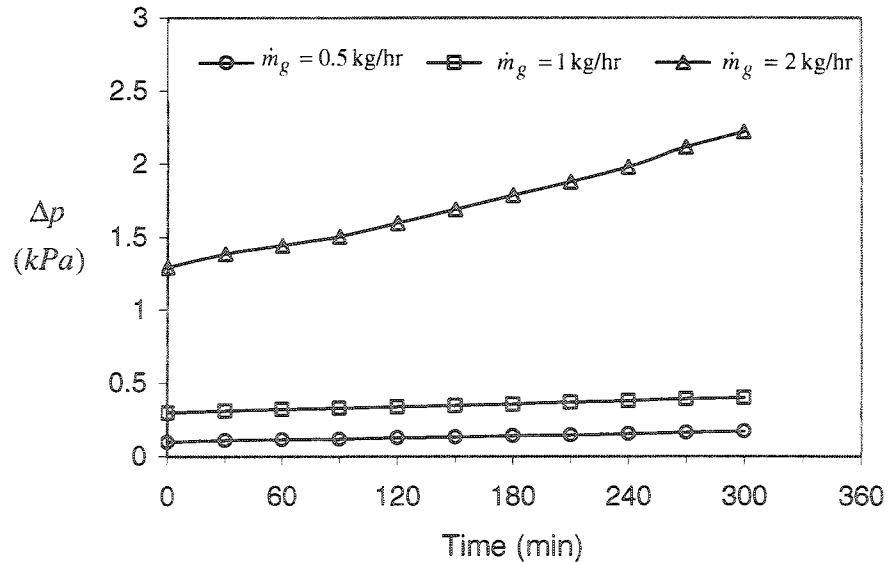


Figure 3.10. Predictions of the change in the pressure drop across the EGR cooling device for different gas mass flow rates. ($L=20\text{cm}$, $d_t=4.5\text{ mm}$, $T_{g,i}=250^\circ\text{C}$, $T_{c,i}=30^\circ\text{C}$, $C_s=50\text{ mg/m}^3$, $N_p=10^{10}\text{ \#pt./m}^3$.)

CHAPTER 4: Experimental Facilities and Methodology

This chapter outlines the experimental facilities and procedures used in this study to investigate the heat transfer and the soot deposition characteristics in EGR cooling devices used in automotive diesel engines applications. Tests were performed for single-tube and three-tube heat exchangers, designed to model the typical EGR cooling devices currently used in commercial applications, and the six-tube EGR cooling device used by Ismail et al. (2002) and Zhang (2003). The time-dependent effects of the diesel soot deposition on the heat transfer and pressure drop performance of the cooling devices were characterized using the diesel engine exhaust gas test facility. The soot deposition that occurred in the tested EGR cooling devices was investigated in the neutron radiography non-destructive test (NR-NDT) facility developed in the McMaster Nuclear Reactor. The design of the EGR cooling devices is discussed first, and the experimental facilities are then presented and discussed.

4.1 The Generic EGR Cooling Devices

The experimental investigation presented here was performed using generic single-tube and three-tube EGR cooling devices that are small-scale

shell-and-tube heat exchangers designed to model those used in commercial applications.

The single-tube EGR cooling devices were made from an aluminum tube with inner diameter of 6.2 mm and length of 205 mm that fits into a 41.9 mm diameter shell as shown in Figure 4.1. A series of seven identical inner sections were manufactured and six of these devices were used for the soot deposition tests in the diesel exhaust test facility. The last device was kept clean and used as a reference device for the measurement of the deposited soot layer profiles in the neutron radiography non-destructive test (NR-NDT) facility.

Tests were also performed for three-tube bundles made using tubes with inner diameters of 4.1 mm and lengths of 205 mm that fit into 41.9 mm diameter shells as shown in Figure 4.2. Three devices were manufactured, one with inlet and outlet headers with expansion and contraction angles of 60° , one with headers with angles of 45° , and a third device was left clean as a reference in the neutron radiography tests. The angles in the inlet and exit headers of the device were consistently kept the same, so that any effect on the flow in the tube bundle might be caused from different contraction angle at the exit was eliminated. Photographs of the single-tube and three-tube EGR cooling devices used in this investigation are shown in Figure 4.3.

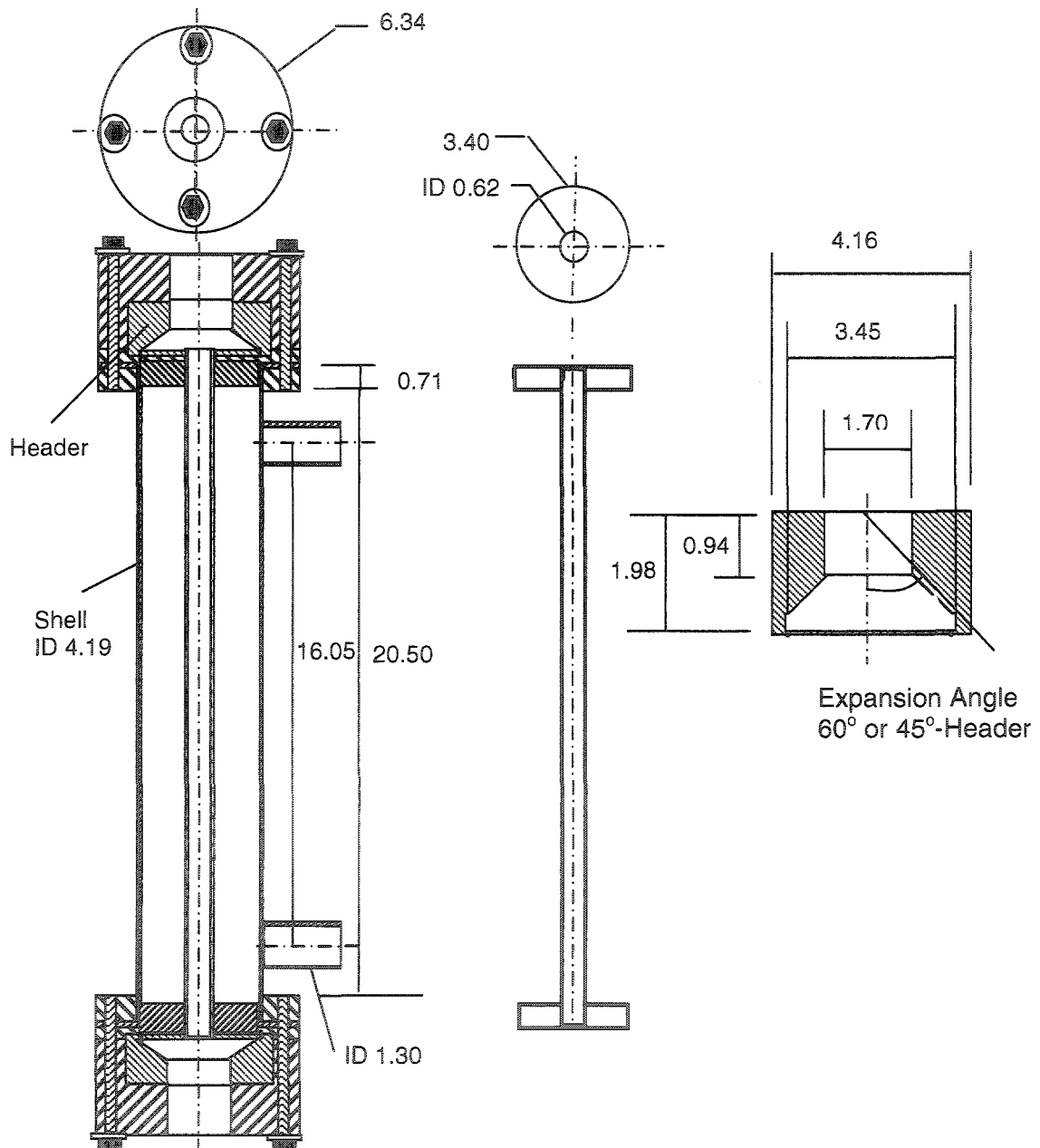


Figure. 4.1. Schematic of the single-tube EGR cooling device used in this investigation.
(Material: Aluminum. All dimensions in cm.)

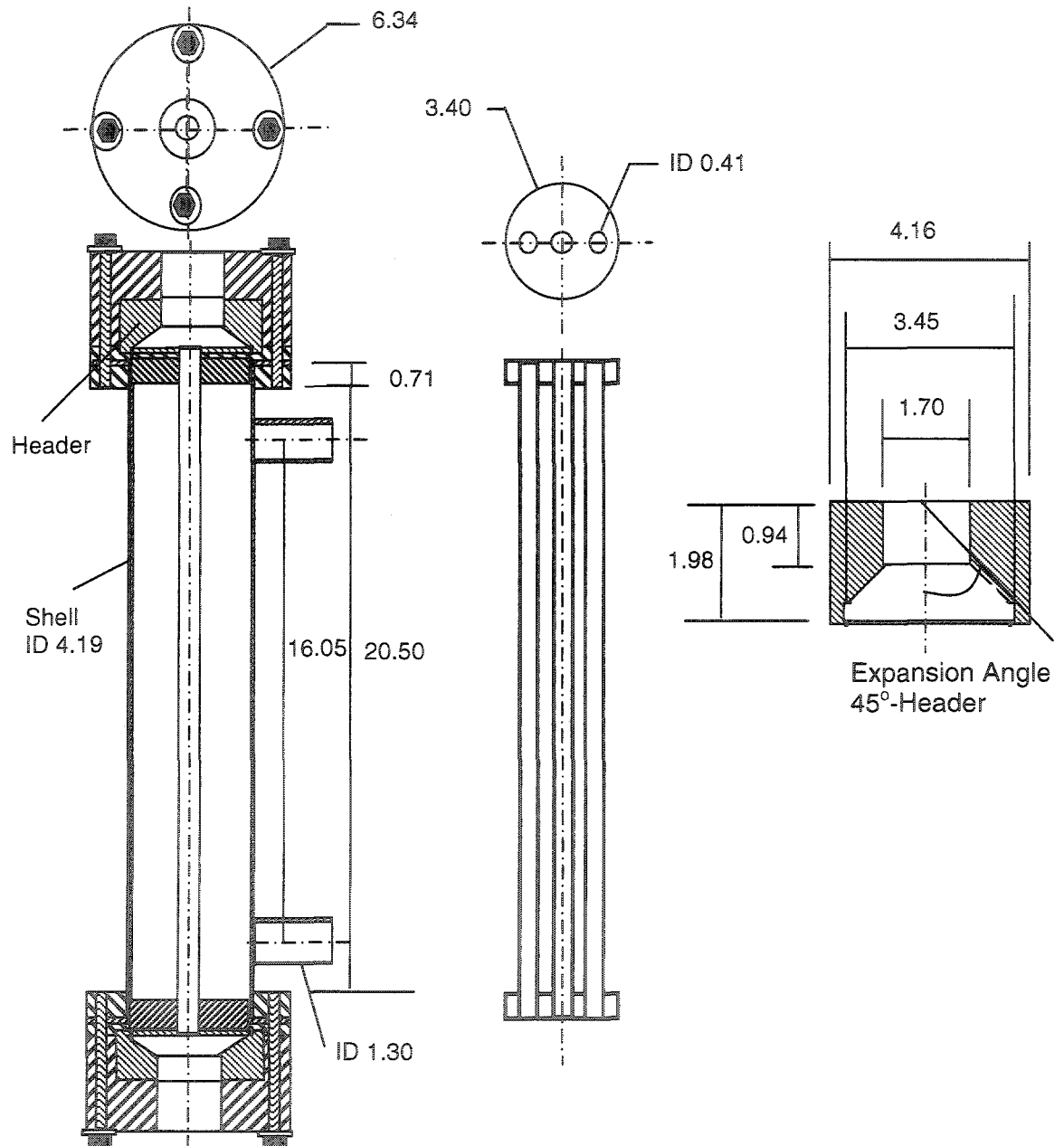
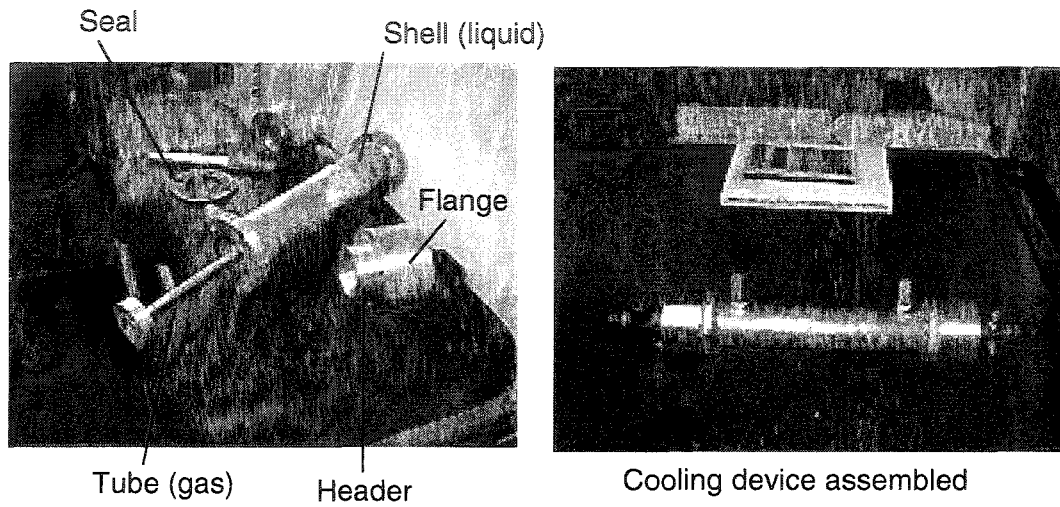
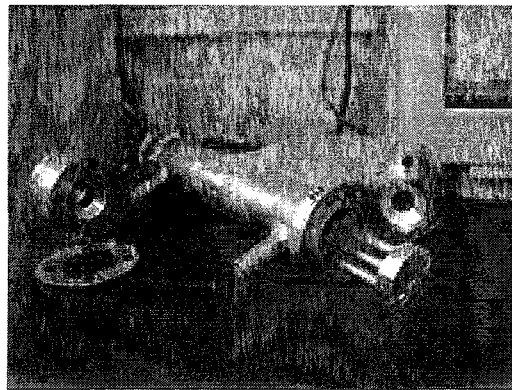


Figure. 4.2. Schematic of the three-tube EGR cooling device used in this investigation. (Material: Aluminum. All dimensions in cm.)



(a)



(b)

Figure 4.3. The generic EGR cooling devices used in this investigation; (a) single-tube device and (b) three-tube device.

4.2 The Diesel Engine Exhaust Gas Test Facility

The controlled tests to deposit soot in the generic EGR cooling devices were performed using the diesel engine exhaust gas test facility shown in Figure 4.4. A photograph of the facility is shown in Figure 4.5. The diesel exhaust gas in this facility was produced by a 5 kW single-cylinder diesel engine with a variable-load generator (Lombardini AK50-CSA). The characteristics of the diesel engine are summarized in Table 4.1. The air in this facility was drawn to the engine intake through an intake filter that was connected to the engine by a 3.17 cm inner diameter stainless steel pipe with length of 36 cm. The exhaust manifold from this engine was connected to an insulated 60 cm long vertical tube with an inner diameter of 3.17 cm that carried the exhaust flow to the insulated test section. A 45 L accumulator tank was connected in parallel with this pipe through a regulating valve to reduce the unsteady fluctuations generated by the single-cylinder engine. At the top of the vertical pipe, the diesel exhaust flow was split into two branches. Most of the exhaust flow was directed through a 3.17 cm diameter high-flow rate leg that included a venturi meter to measure the flow rate through this leg. This leg also included an additional 45 L accumulator tank to further damp out the pulsations from the engine. A smaller portion of the exhaust flow passed through the 15 mm diameter low-flow rate leg that was used to test the EGR cooling devices. The EGR cooling devices were positioned approximately 64 cm or 43 diameters downstream from the start of the 15 mm

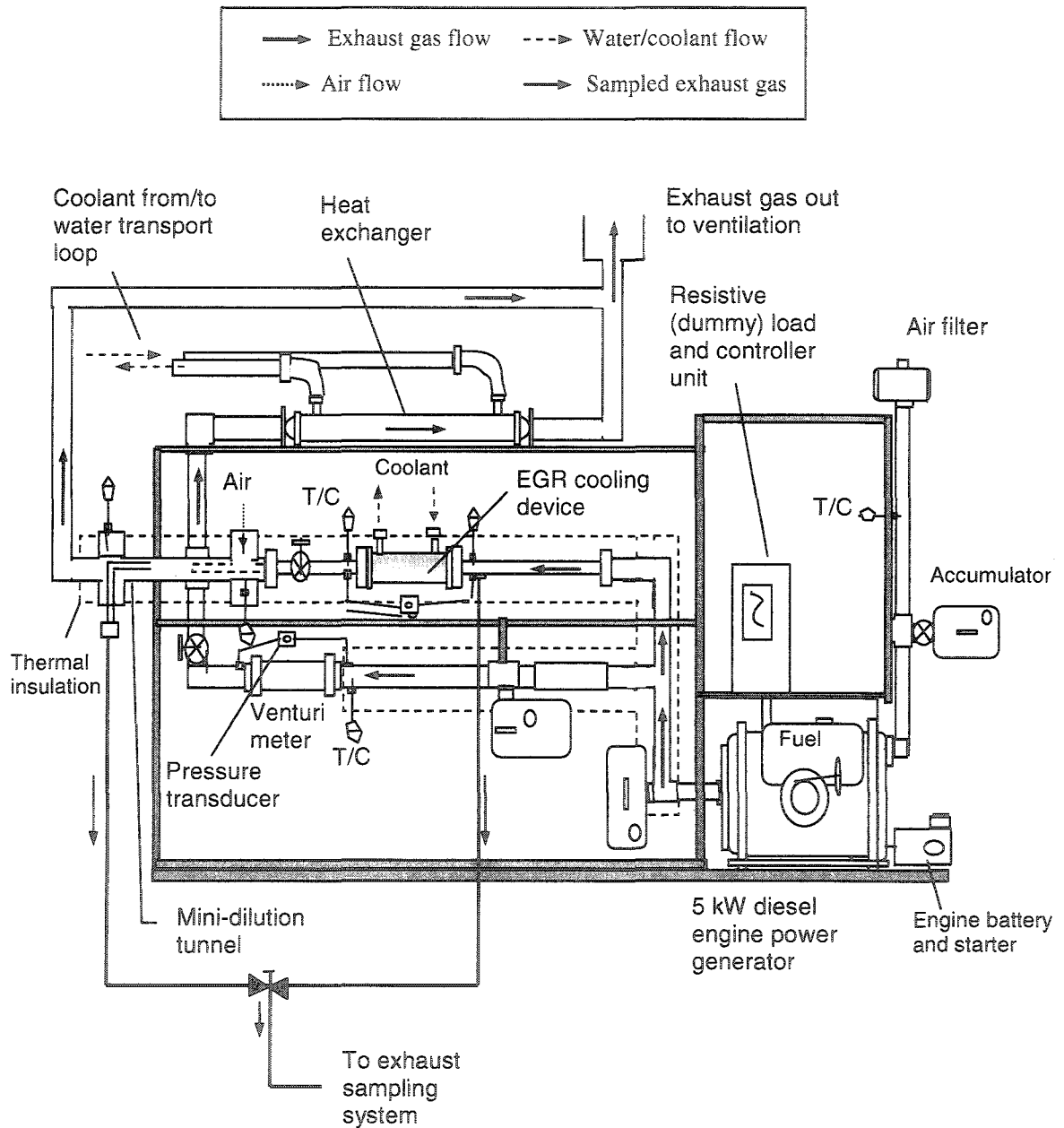


Figure 4.4. The diesel engine exhaust gas test facility used for the controlled soot deposition tests.

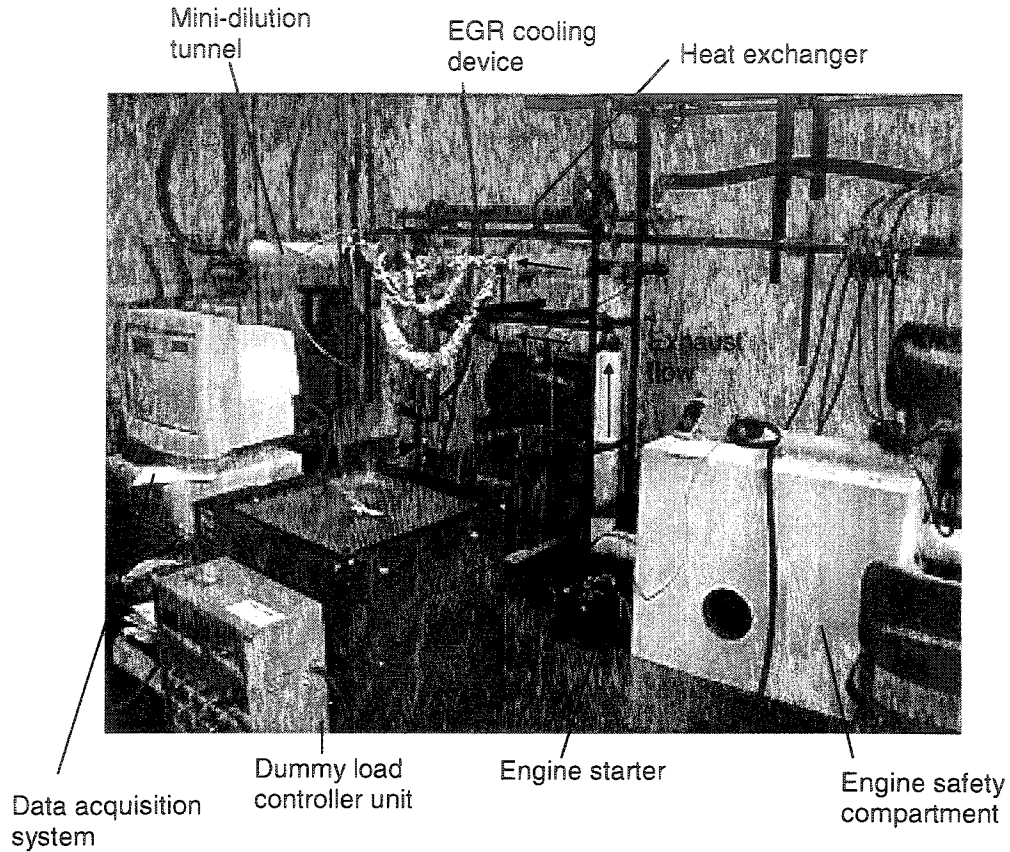


Figure 4.5. Photograph of the diesel engine exhaust gas test facility used in this investigation.

Table 4.1: Typical characteristics of the diesel engine used in this study.

Model	Lombardini AK50-CSA
# Cylinders	1
Dimensions (L x W x H)	30cm x 37cm x 45cm
Displacement	315 cm ³
Bore & Stroke	78cm x 66cm
Rated speed	3600 RPM
Max. Torque	15.0 N.m at 2000 RPM
Max. Power	5.0 kW

diameter low-flow rate leg.

The flow rate through the low-flow rate leg, used to test the EGR cooling device, was determined indirectly. The gas mass flow rate through the high-flow rate leg was measured throughout the experiment. The mass flow rate through the small leg was then determined by subtracting the measurement from the high-flow rate leg from the total exhaust mass flow rate measured after the engine was at steady state. The fraction of the exhaust gas traveling down each of the legs was varied using gate valves on each of the legs. The exhaust gas exiting the two legs was cooled by a shell-and-tube heat exchanger before being discharged to the fume hood.

The temperature of the exhaust gas before and after the EGR cooling device mounted on the low-flow rate leg were measured using K-type thermocouples positioned approximately 6.4 cm upstream and downstream of the EGR cooling device. There were pressure taps at the same locations and the pressure drop across the EGR cooling device was measured using a Validyne DP15TL differential diaphragm type pressure transducer. The temperature measurements of the exhaust gas were acquired using a PCI-DAS-TC thermocouple data acquisition board, while the output of the pressure transducers was acquired using a Microstar IDC -1816 board using a LabView data based acquisition program. The temperature and pressure measurements data were sampled at a rate 1 Hz over the test.

On the other side, a closed-loop coolant transport system shown in Figure 4.6 was used to provide cooling water by means of a pump to cool the hot exhaust gas passing through the EGR cooling device on the diesel test facility. The coolant loop included a 30 cm x 70 cm plate type heat exchanger to cool the returned fluid from the EGR cooling device. The coolant loop also included a 50 L water reservoir to reduce the rate of change of temperature in the system so that thermal equilibrium could be maintained. A globe valve was used to regulate the water flow and a rotameter (Brooks 10-1307) was used to measure the flow rate that could measure up to 24 l/min to within $\pm 3\%$ of full scale. The temperature of the coolant at inlet and exit ports of the EGR cooling device were measured using T-type thermocouples positioned upstream and downstream of the cooling device. A summary of the instruments used for the thermal and hydraulic performance measurements of the EGR cooling device is given in Table 4.2. The temperature measurements were again acquired using the PCI-DAS-TC thermocouple data acquisition board.

The heat transfer rates between the hot gas and cold liquid streams of the EGR cooling device were computed by applying an energy balance over the cooling device. The heat transfer rate from the gas was determined using

$$\dot{Q}_g \approx \dot{m}_g \bar{c}_{p,g} [T_{g,i} - T_{g,o}] = (\rho \dot{V} \bar{c}_p)_g \Delta T_g, \quad (4.1)$$

where $\bar{c}_{p,g}$ is the specific heat for the gas estimated at the average gas temperature between inlet and exit of the cooling device. Similarly, the heat

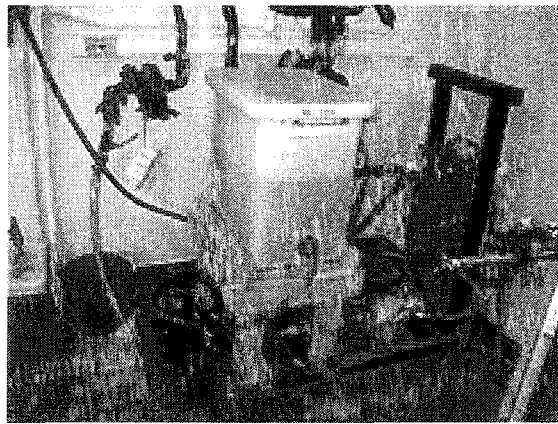
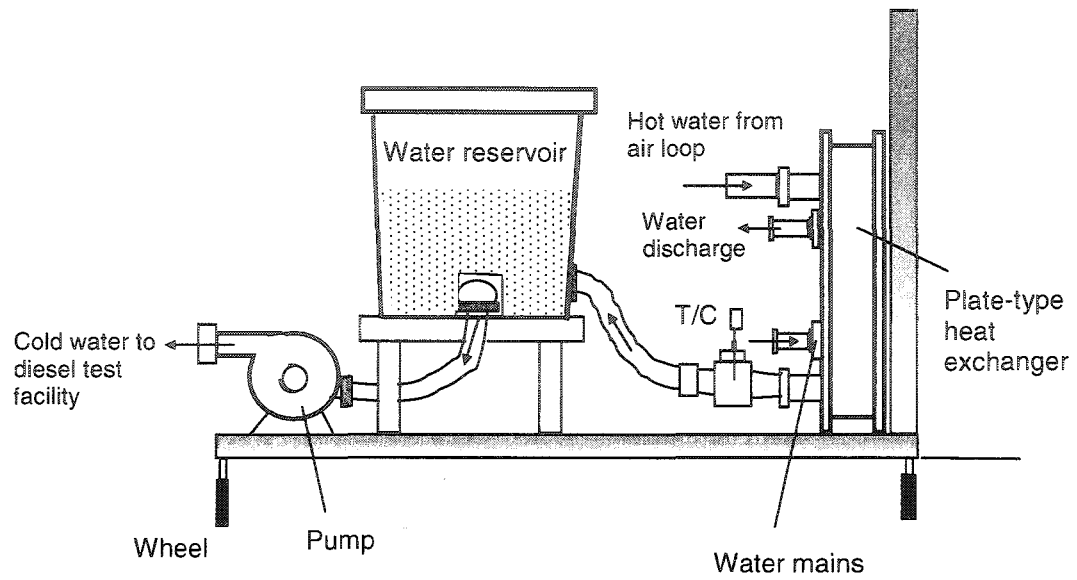


Figure. 4.6. Schematic and photograph of the coolant/water transport loop.

Table 4.2: Summary of the characteristics of the instruments used in the diesel exhaust and coolant transport test facility.

Type of Measurement	Type of measuring device	Applicable measurement range	Range used in test	Uncertainty
Inlet and outlet gas temperatures of EGR cooling device ($T_{g,in}, T_{g,out}$)	Thermocouple type K (Shielded)	-200 – 1250 °C	250 – 400 °C	± 1.4 °C
Inlet and outlet coolant/water temperatures of EGR cooling device ($T_{c,in}, T_{c,out}$)	Thermocouple type T (Shielded)	-270 – 350 °C	12 – 35 °C	± 0.9 °C
Gas-side pressure difference between inlet & exit of EGR cooling device $\Delta P_{EGR}, g$	Diaphragm-type Pressure transducer (Validyne DP15TL)	Depending on Diaphragm	25 ~ 7000 Pa	~ ±1% of the reading
Gas volumetric flow rate \dot{V}_g	Rotameter (King 7520)	1.32x10 ⁻³ – 4.43x10 ⁻³ m ³ /s	1.32x10 ⁻³ – 4.43x10 ⁻³ m ³ /s	~ ±3%
	Rotameter (Dwyer Instrument Inc. RMC-103-SSV)	4.72x10 ⁻⁴ – 1.57x10 ⁻³ m ³ /s	4.72x10 ⁻⁴ – 1.57x10 ⁻³ m ³ /s	~ ±3%
Coolant volumetric flow rate \dot{V}_c	Rotameter (Brooks 10-1307)	1 – 24 l/min	4.0 l/min	~ ±3%

transfer on the coolant or water side was determined using

$$\dot{Q}_c \approx \dot{m}_c \bar{c}_p [T_{c,o} - T_{c,i}] = (\rho \dot{V} \bar{c}_p)_c \Delta T_c. \quad (4.2)$$

The controlled soot deposition measurements were performed for the series of the single-tube and three-tube EGR cooling devices. The measurements were all performed when an electrical load of approximately 2.9 kW was applied to the diesel generator. The tests for the single-tube EGR cooling devices were performed for two gas mass flow rates, 0.8 kg/hr and 2.8 kg/hr. The nominal Reynolds number in the tube for the first test was approximately 2000, so that the flow should be initially laminar. The nominal Reynolds number is given by

$$\text{Re} = \frac{4\dot{m}_g}{\pi \mu_g d_i}. \quad (4.3)$$

The gas viscosity μ_g here was evaluated using the initial gas inlet temperature of the test. The nominal Reynolds number in the tube for the second test was at the higher Reynolds number, approximately 7000, so that the flow was turbulent. In these tests, three different single-tube EGR cooling devices were exposed to the diesel exhaust flow for 1, 2, and 5 hours, at each gas flow rate. The variation of the gas mass flow rate during the 1, 2, and 5 hours of the low and high flow rate tests are shown in Figure 4.7. It is clear that the gas mass flow rate passing through the cooling device was approximately 0.8 ± 0.1 kg/hr during the low-flow rate tests, and 2.8 ± 0.2 kg/hr during the high-flow rate tests. The exhaust gas

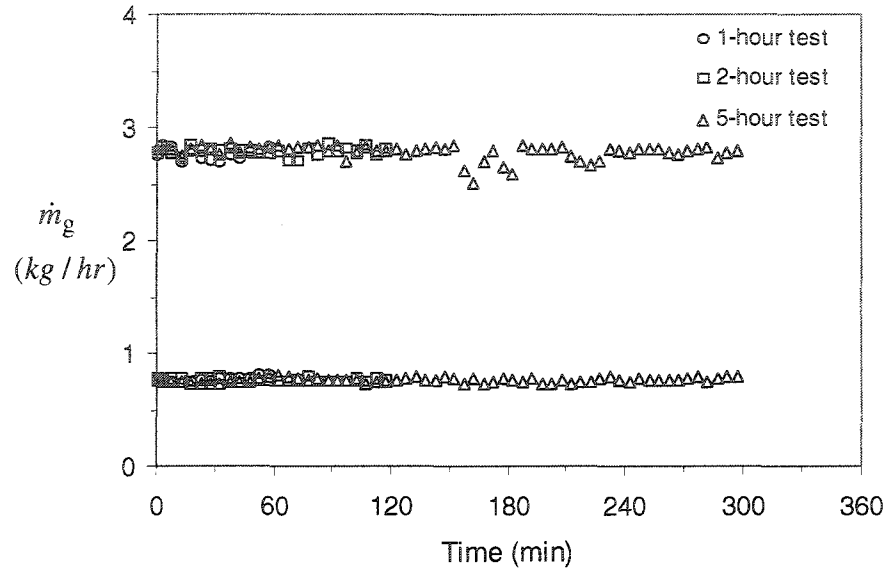


Figure 4.7. Variation in the gas mass flow rate with time for the single-tube EGR cooling devices tested for 1, 2, and 5 hours.

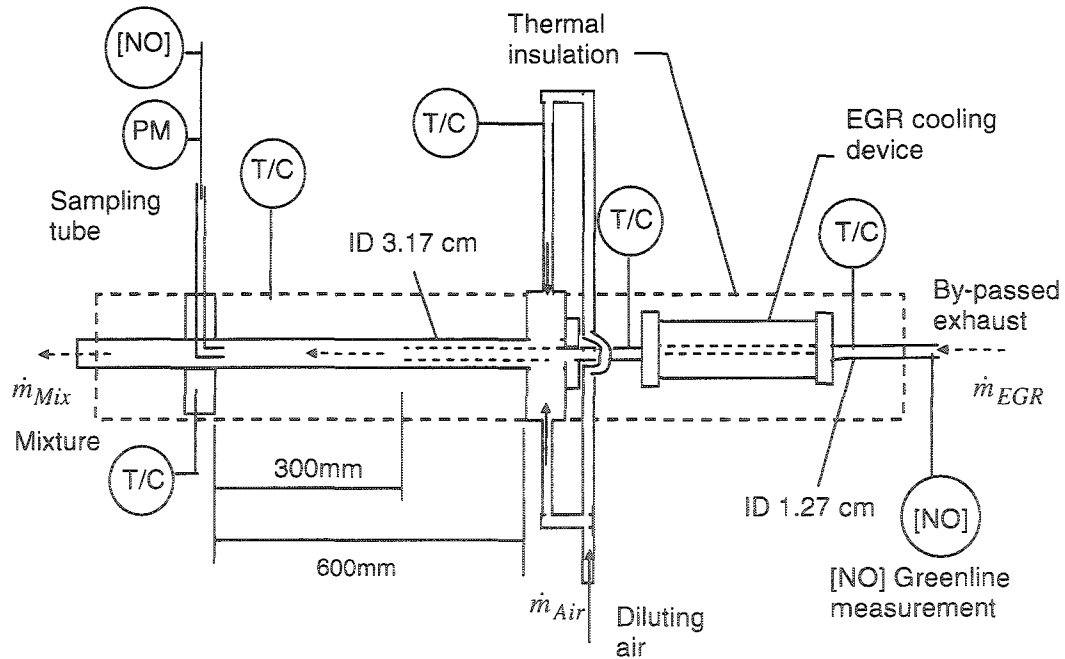


Figure 4.8. Schematic of the mini-dilution tunnel used in this investigation for the measurements of the soot mass concentration during EGR soot deposition tests. T/C: T-type thermocouple; [NO]: concentration of Nitric oxide.

generated by the diesel engine was changing slightly during the tests, so periodical adjustments were made to the valve in the main leg of the test loop to maintain the flow through the EGR cooling devices at 0.8 and 2.8 kg/hr. The total exhaust gas flow rate during the 1, 2, and 5 hours tests was approximately 32 kg/hr, when the engine was operating at steady state. For the low and high flow rates tests, the coolant volumetric flow rate was maintained at 1 l/min that was measured with a Brooks 10-1307 rotameter.

The concentration of the soot, C_s , in the exhaust gas flow through the EGR loop was determined using the measurement of the soot concentration from the Haz-dust III (model HD-1003) optical particle counter connected to the 35 mm diameter mini-dilution tunnel (Kittelson et al., 2000) located downstream of the cooling device as shown in Figures 4.4 and 4.8. The optical counter could measure the soot concentration to within $\pm 1\%$ of the reading. The dilution ratio of the exhaust and diluting air mixture was determined from the nitric oxide, NO, concentration of the mixture in the mini-dilution tunnel and the NO concentration of the undiluted exhaust, shown in Figures 4.9 and 4.10, using a Eurotron Greenline II combustion gas analyzer that could measure the concentration to within $\pm 4\%$ of the reading. This dilution ratio varied slightly over the tests, 3.7 ± 0.3 for the low gas flow rate, and 3.5 ± 0.2 for the high flow rate as shown in Figure 4.11. The transient soot mass concentration measured in the mini-dilution tunnel, and the soot mass concentration computed for the diesel exhaust gas for

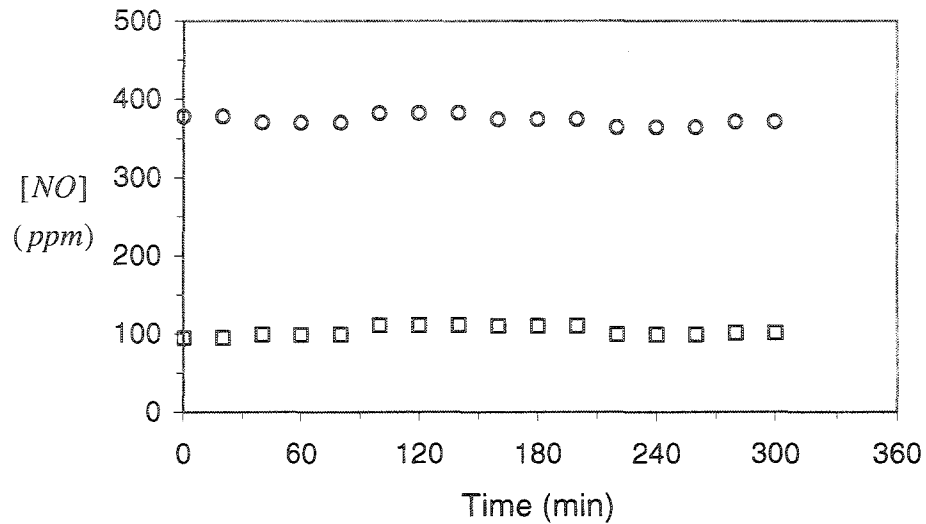


Figure 4.9. Variation in the NO concentration measured in \circ the undiluted exhaust loop, and \square the diluted flow, for the single-tube EGR cooling device tested for an exhaust mass flow rate of 0.8 kg/hr.

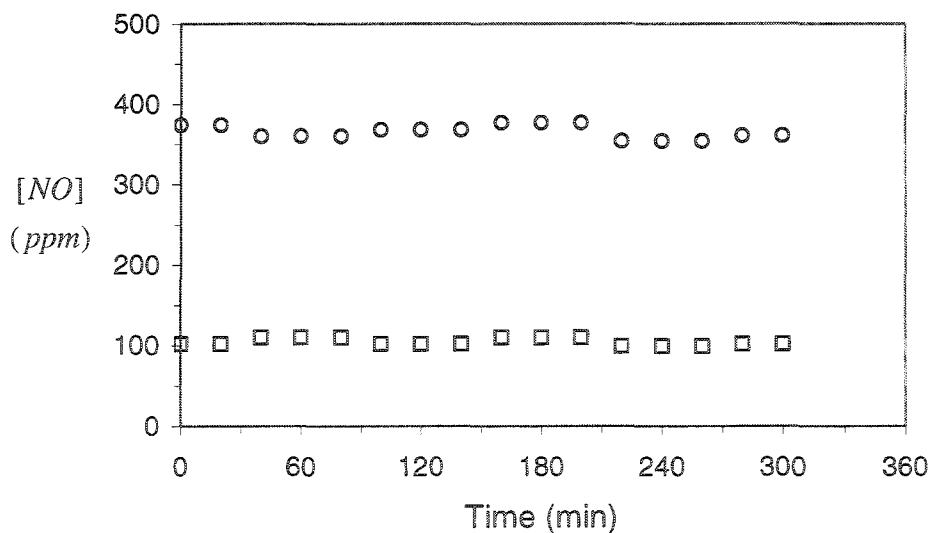


Figure 4.10. Variation in the NO concentration measured in \circ the undiluted exhaust loop, and \square the diluted flow, for the single-tube EGR cooling device tested for an exhaust mass flow rate of 2.8 kg/hr.

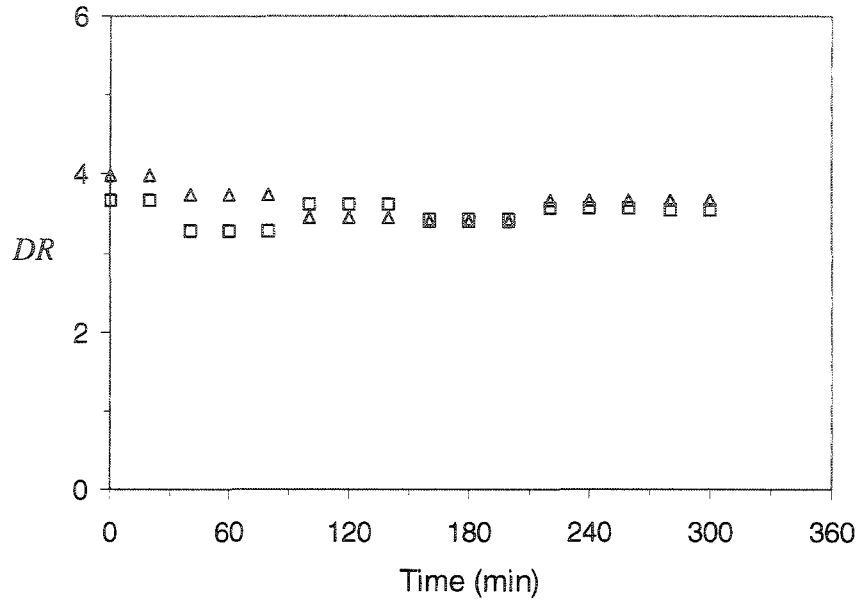


Figure 4.11. Change in the dilution ratio determined from NO measurement for the single-tube EGR cooling devices for gas mass flow rates Δ 0.8 kg/hr, and \square 2.8 kg/hr.

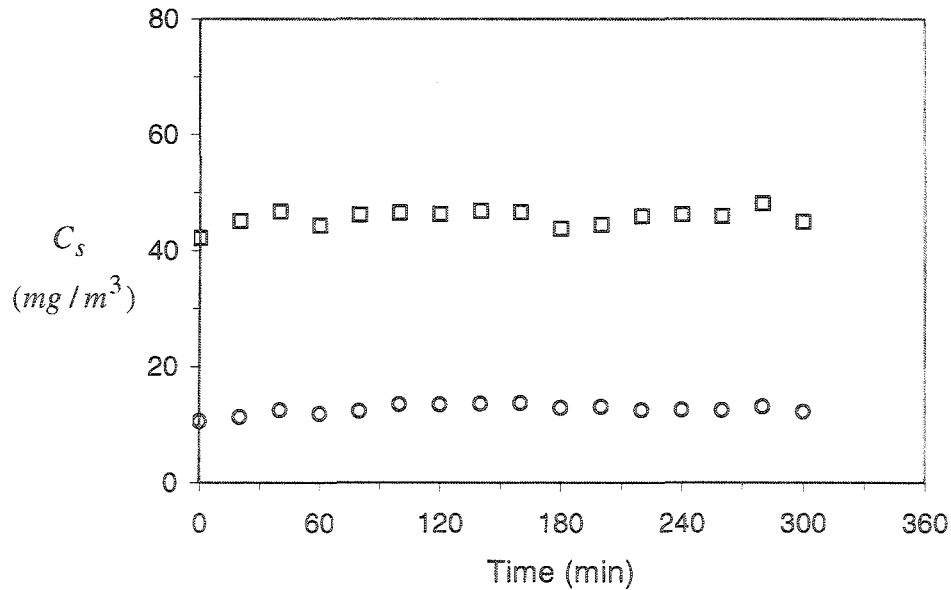


Figure 4.12. Change in the soot mass concentration in the gas flow \circ measured after diluting the flow, and \square calculated for the exhaust flow, for the single-tube EGR cooling device with an exhaust gas mass flow rate of 0.8 kg/hr.

the low and high flow rate tests are shown in Figures 4.12 and 4.13, respectively. The soot mass concentration in the diesel exhaust exiting the tested single-tube EGR cooling devices was observed to be $45 \pm 3 \text{ mg/m}^3$ for the low gas flow rate tests, and $46 \pm 2 \text{ mg/m}^3$ for the high gas flow rate tests. The total uncertainty in the soot mass concentration measurement was found to be approximately $\pm 2.1\%$.

The transient inlet gas temperature and inlet water temperature for the single-tube EGR cooling devices for the 0.8 kg/hr and 2.8 kg/hr tests are shown in Figures 4.14 and 4.15, respectively. The inlet gas temperature was $120 \pm 3 \text{ }^\circ\text{C}$ for the low gas flow rate tests, and $194 \pm 6 \text{ }^\circ\text{C}$ for the high flow rate tests. These fluctuations were due in part to the fluctuations in the gas mass flow rate, the largest at 1 hour in the 5-hour test for 0.8 kg/hr, and 2 hours in the 5-hour test for 2.8 kg/hr. The inlet coolant temperature was maintained between $25 \pm 2 \text{ }^\circ\text{C}$ for the low gas flow rate tests, and $26 \pm 3 \text{ }^\circ\text{C}$ for the high flow rate tests. The periodic fluctuations in the coolant inlet temperatures were due to the periodic fluctuations of the water temperature caused by replacing a portion of the cooling water in the water tank in the closed coolant loop with cold water.

The tests for the three-tube EGR cooling devices were also performed for a total flow rate of 6.0 kg/hr that corresponded to a nominal Reynolds number of 8000. The three-tube cooling devices were exposed to the exhaust gas for 3 hours to characterize the effect that the expansion angle in the inlet header had

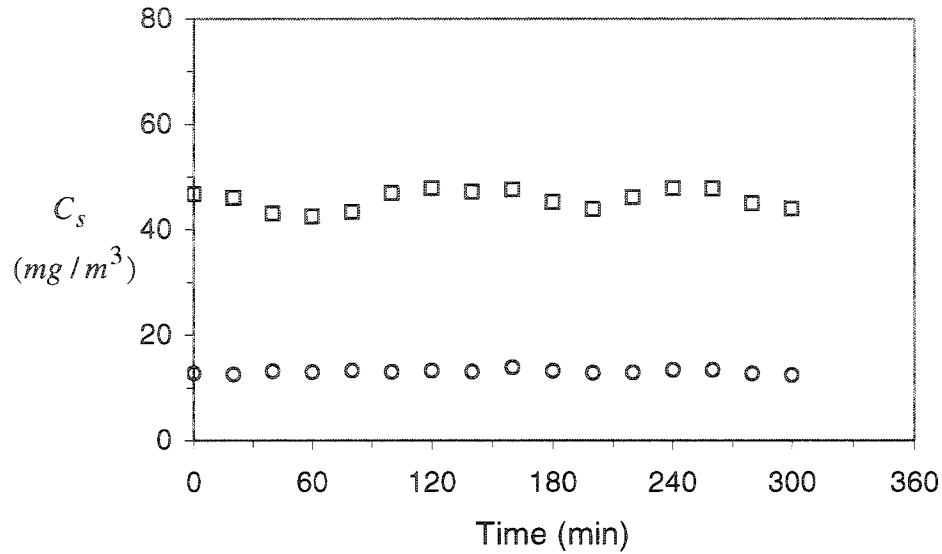


Figure 4.13. Change in the soot mass concentration in the gas flow \circ measured after diluting the flow, and \square calculated for the exhaust flow, for the single-tube EGR cooling device with an exhaust mass flow rate of 2.8 kg/hr.

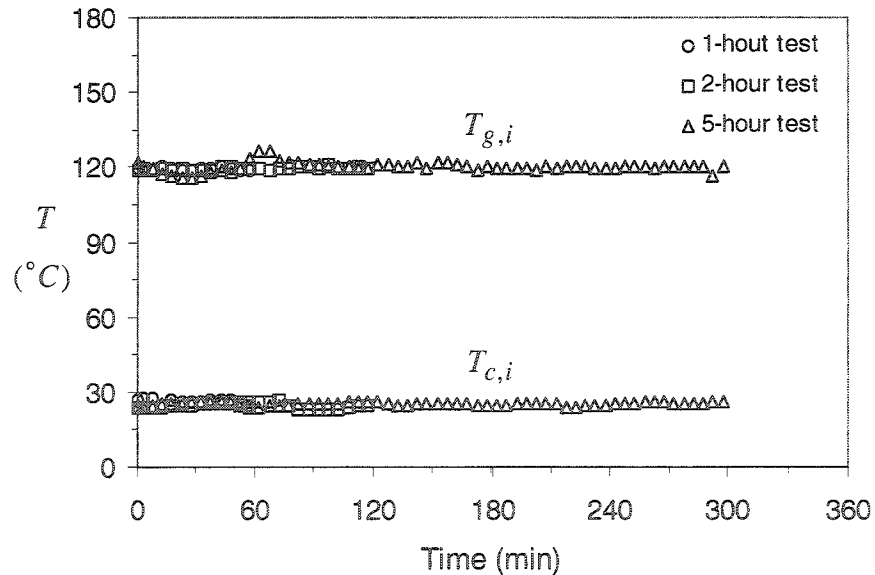


Figure 4.14. Change in the inlet gas and inlet coolant temperatures during the single-tube EGR cooling device tests for the average exhaust mass flow rate of 0.8 kg/hr and soot mass concentration of $45 \text{ mg}/\text{m}^3$.

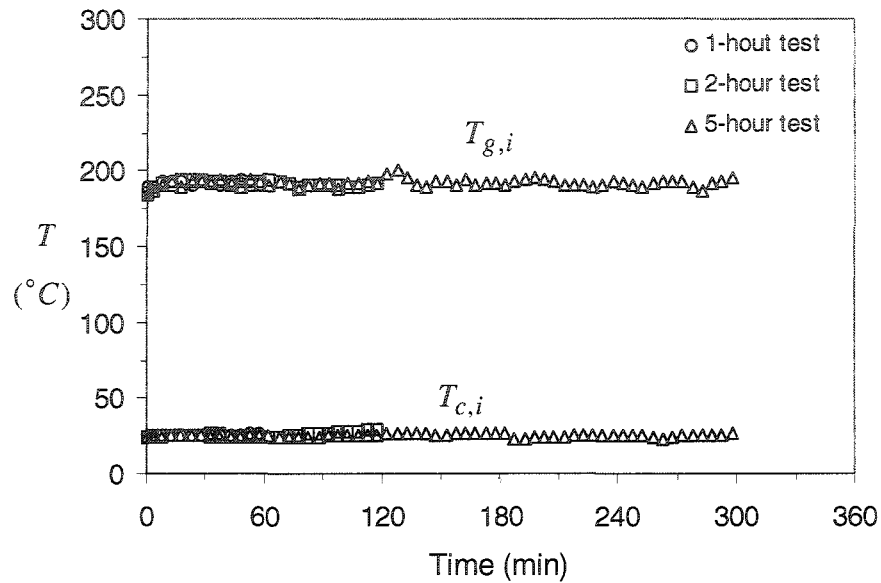


Figure 4.15. Change in the inlet gas and inlet coolant temperatures during the single-tube EGR cooling device tests with the average gas mass flow rate of 2.8 kg/hr and soot mass concentration of 46 mg/m³.

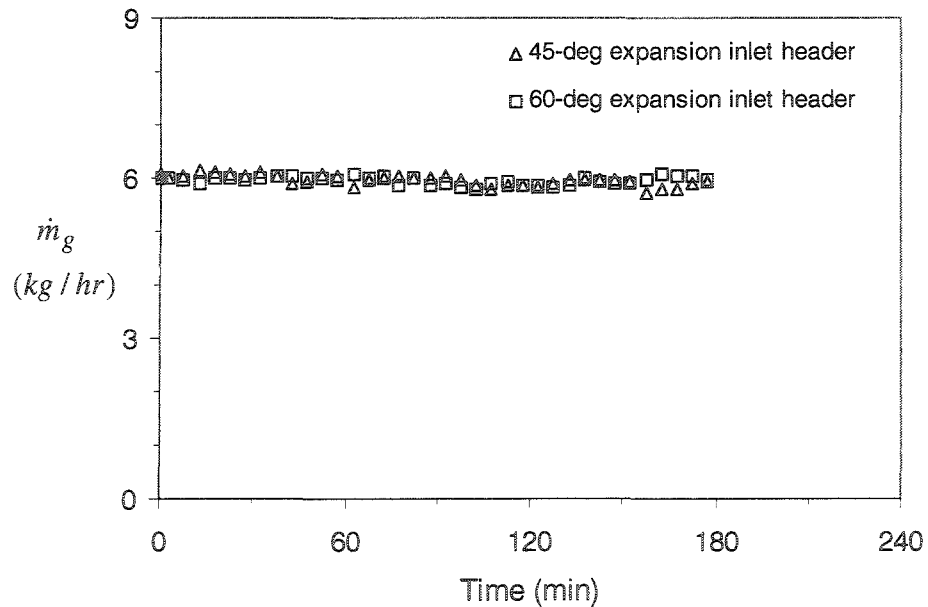


Figure 4.16. Change in the gas mass flow rate for the three-tube EGR cooling devices with the 45° expansion angle inlet header and the 60° expansion angle inlet header tested for 3 hours.

on the soot deposition profiles in these devices. The variation in the gas mass flow rate over the 3-hour tests for the three-tube cooling devices is shown in Figure 4.16. For these tests, the gas mass flow rate passing through the cooling device was approximately 6.0 ± 0.1 kg/hr for the three-tube EGR cooling device with the 45° expansion angle inlet header, and 6.0 ± 0.2 kg/hr for the three-tube EGR cooling device with the 60° expansion angle inlet header. In both tests, the coolant volumetric flow rate was maintained at approximately 2.5 l/min. The variation in NO concentration used to compute the dilution ratio for the three-tube cooling devices tests is shown in Figures 4.17 and 4.18. The change in the dilution ratio computed for the three-tube cooling devices tests is shown in Figure 4.19. The dilution ratio for the three-tube cooling device with the 45° expansion angle inlet header was 8.9 ± 1.5 , while it was 9.6 ± 0.4 for the device with the 60° expansion angle inlet header. A comparison of the change in the soot mass concentration in the exhaust gas for the three-tube EGR cooling device tests with the 45° and 60° expansion angle inlet headers is shown in Figure 4.20. The results show that the soot mass concentration was 47 ± 3 mg/m³ for the test with the 45° expansion angle inlet header, while it was 46 ± 3 mg/m³ for the test with the 60° expansion angle inlet header.

The change in the inlet gas temperature and inlet coolant temperature for the three-tube EGR cooling devices tests with the 45° and 60° expansion angle inlet headers is shown in Figures 4.21 and 4.22. The inlet gas temperature in

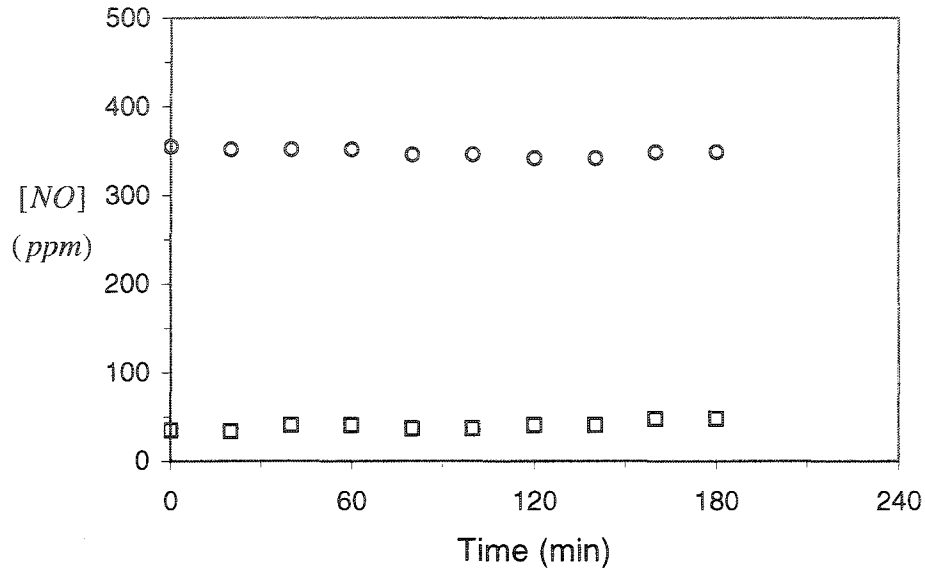


Figure 4.17. Variation in the NO concentration in \circ the undiluted exhaust flow, and \square the diluted gas, for the three-tube EGR cooling device with the 45° expansion angle inlet header tested for 3 hours with a gas mass flow rate of 6.0 kg/hr.

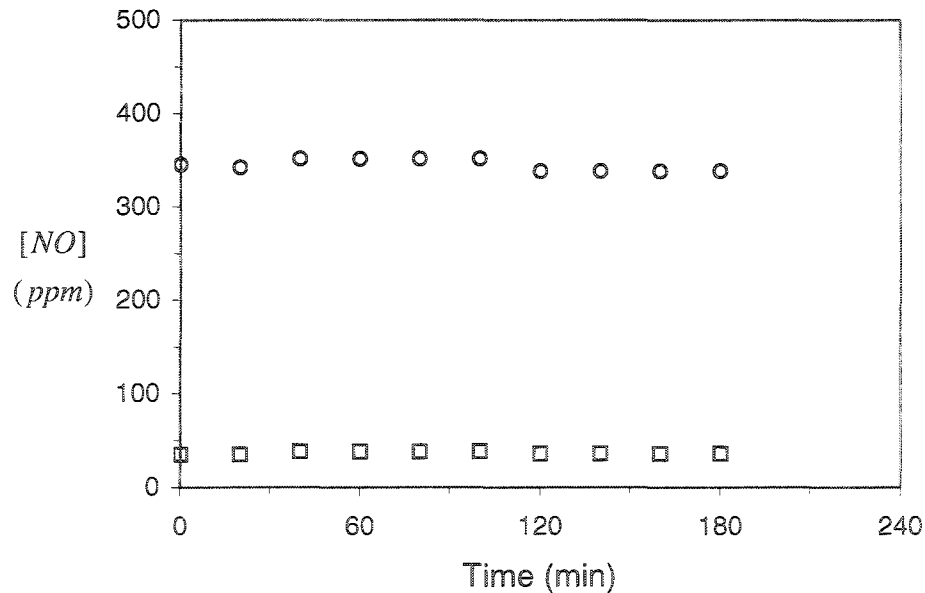


Figure 4.18. Variation in the NO concentration in \circ the undiluted exhaust flow, and \square the diluted gas, for the three-tube EGR cooling device with the 60° expansion angle inlet header tested for 3 hours with a gas mass flow rate of 6.0 kg/hr.

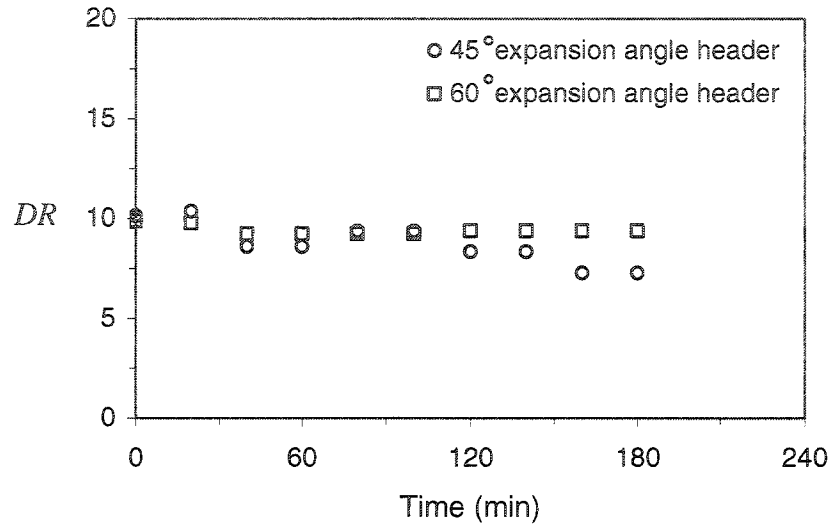


Figure 4.19. Comparison of the change in the calculated dilution ratio for the three-tube EGR cooling device tests with 45° and 60° expansion angle inlet headers for the gas flow rate of 6 kg/hr.

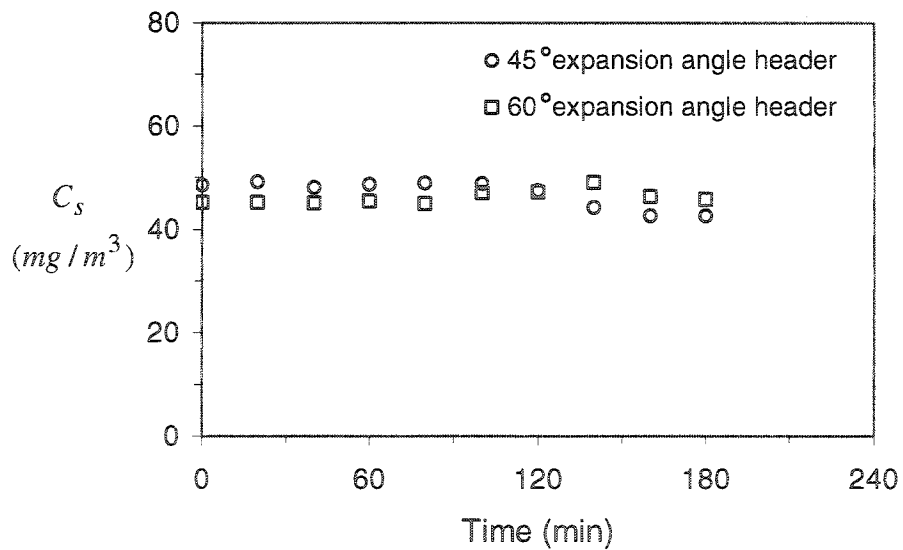


Figure 4.20. Comparison of the soot mass concentration in the exhaust flow for the three-tube EGR cooling device tests with 45° and 60° expansion angle inlet headers for the gas flow rate of 6 kg/hr.

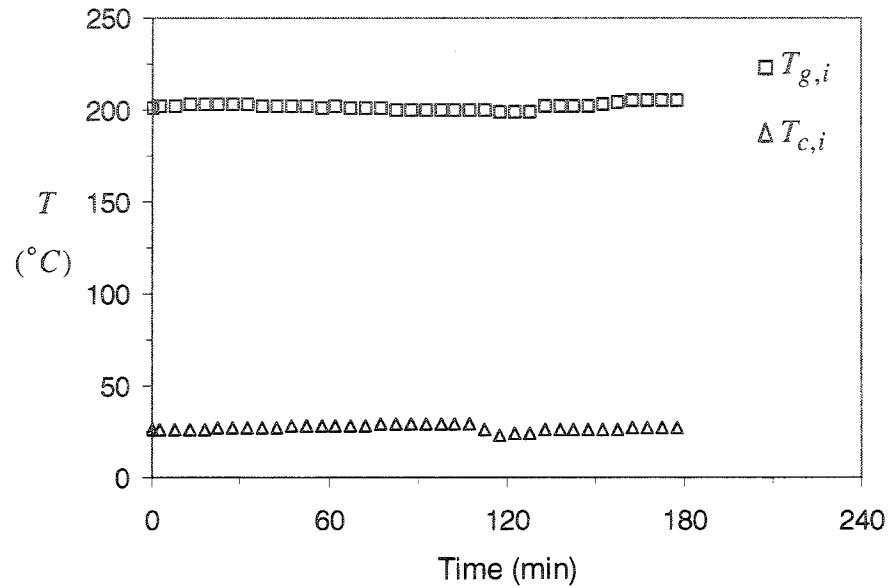


Figure 4.21. Change in the inlet gas and inlet coolant temperatures for the three-tube EGR cooling device test with the 45° expansion angle inlet header during 3 hours for gas mass flow rate of 6.0 kg/hr, and average soot concentration of 47 mg/m³.

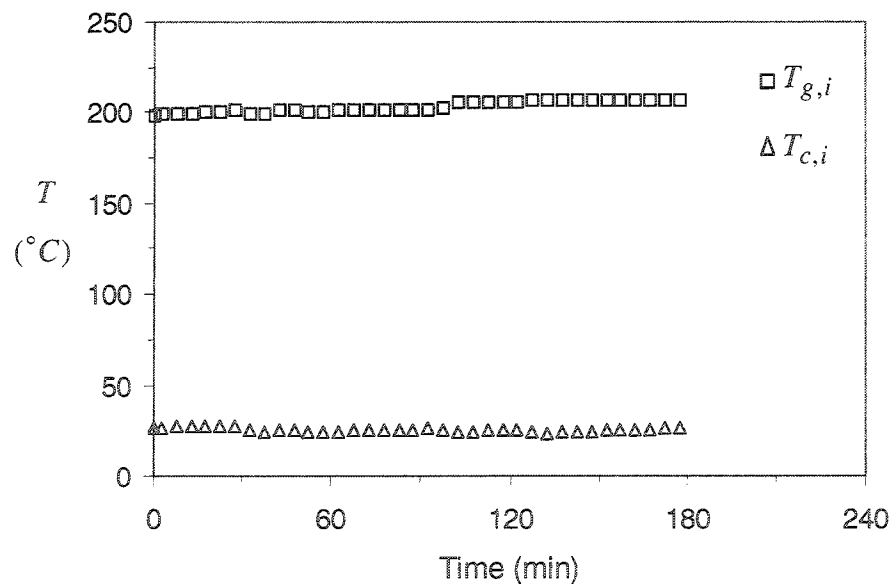


Figure 4.22. Change in the inlet gas and inlet coolant temperatures for the three-tube EGR cooling device test with the 60° expansion angle inlet header during 3 hours for gas mass flow rate 6.0 kg/hr, and average soot concentration 46 mg/m³.

both tests were 202 ± 3 °C and 203 ± 4 °C, respectively, while the inlet coolant temperature varied between 26 ± 3 °C for the first test, and between 25 ± 2 °C for the second test.

The thermal characteristics of the secondary side coolant flow across the three-tube cooling device were investigated for two coolant flow rates, 2.5 and 6 l/min, using a Flir SC3000 infrared (IR) thermography camera system. The outer surface of the EGR cooling device was coated with black paint that has an emissivity value of approximately 0.98. The IR camera was calibrated using a reference T-type thermocouple that was placed on the shell of the EGR cooling device. The calibration information is provided in Figure C.1 in Appendix C. Adhesive and thermally conductive paste was applied at the contact point between the tip of the reference thermocouple and the shell surface.

For these tests, the gas mass flow rate was maintained at 6 kg/hr. The inlet coolant temperature was kept at 26 ± 1 °C, while the inlet exhaust temperature was maintained at 180 ± 2 °C. The objective was to study the temperature distributions for the coolant flowing over the three-tube bundle in the EGR cooling device. Thermal images were acquired of the top and side views of the cooling device during 0, 1, 2, and 3 hours. The images were then analyzed to determine the time-dependent temperature distributions for these tests.

4.3 Characterizing the Soot Particle Size and Number Density in Diesel Exhaust

Measurements were performed to characterize the soot particle size distribution in the diesel exhaust by sampling the exhaust from the EGR loop on the diesel test facility and collecting the soot particles from the exhaust on a carbon tape that was placed in a sealed chamber in the sampling system shown in Figure 4.23. The test conditions used while sampling the soot particles are summarized in Table 4.3. Two samples were obtained, upstream and downstream of the three-tube EGR cooling device. The objective was to characterize the soot particles size distribution in the EGR loop. Images were obtained for the sampled soot particles on the carbon tape using scanning electron microscopy (SEM), and the images were then analyzed to determine the soot particle size distribution using Western Vision HLImage++ image analysis software. The majority of the diesel soot particles were in the particle diameter range $0.05 - 0.1 \mu\text{m}$ as shown in Figures 4.24 and 4.25.

In-flight measurements were also performed to directly characterize the soot particle size and number density distribution in the diesel exhaust using a TSI3010 condensation-nucleation particle counter (CNPC) sampling system. Measurements were conducted when the engine reached steady state with a load of approximately 2.4 kW applied to the generator, and the exhaust was sampled iso-kinetically downstream of the EGR cooling device using a 3.3 mm

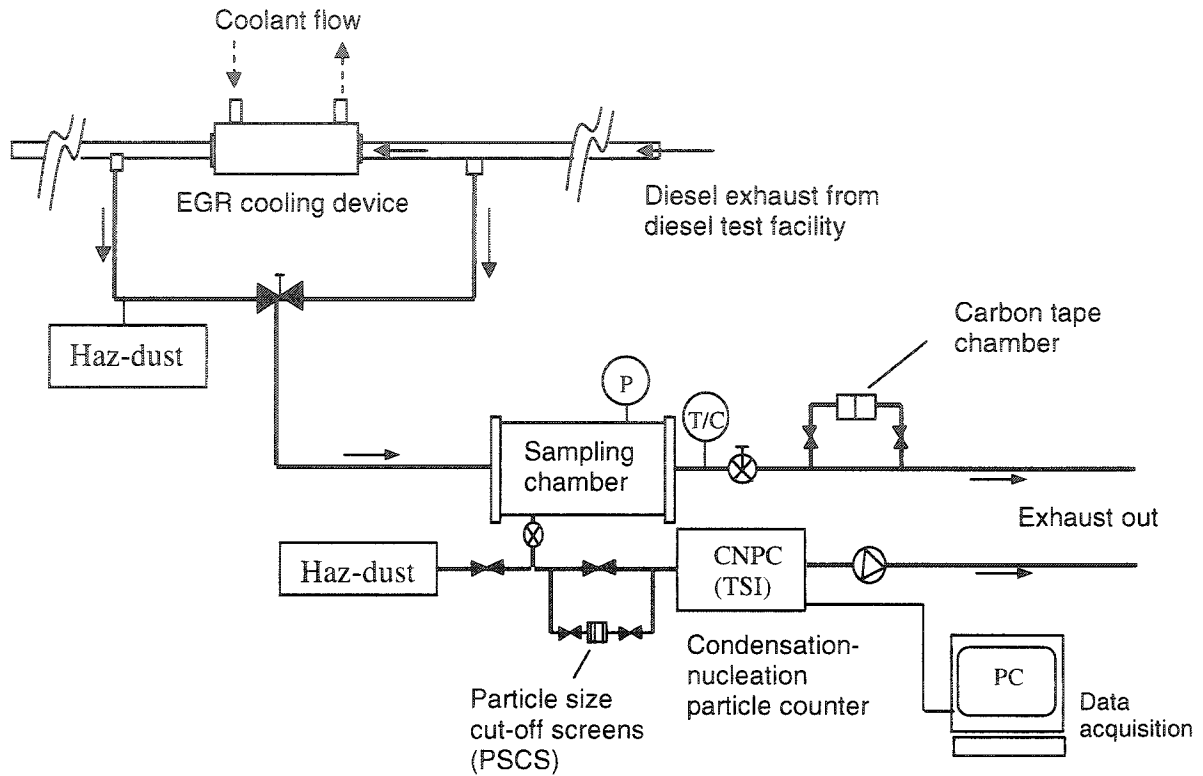


Figure 4.23. Schematic of the sampling system used in this investigation to characterize the soot particle size distribution and number density in diesel exhaust sampled from the EGR section.

Table 4.3: The test conditions during sampling the soot particles for size distribution using SEM.

Operated engine load (kW)	2.4
EGR cooling device type	Three-tube
Gas mass flow rate (kg/hr)	6
Coolant flow rate (l/min)	2.5
Inlet gas temperature to EGR cooling device ($^{\circ}\text{C}$)	180 ± 2
Exit gas temperature from cooling device ($^{\circ}\text{C}$)	54 ± 2
Inlet coolant temperature to cooling device ($^{\circ}\text{C}$)	27 ± 1
Soot mass concentration (mg/m^3)	48 ± 2
Sampling time (sec) - upstream EGR cooling device	120
Sampling time (sec) - downstream EGR cooling device	60

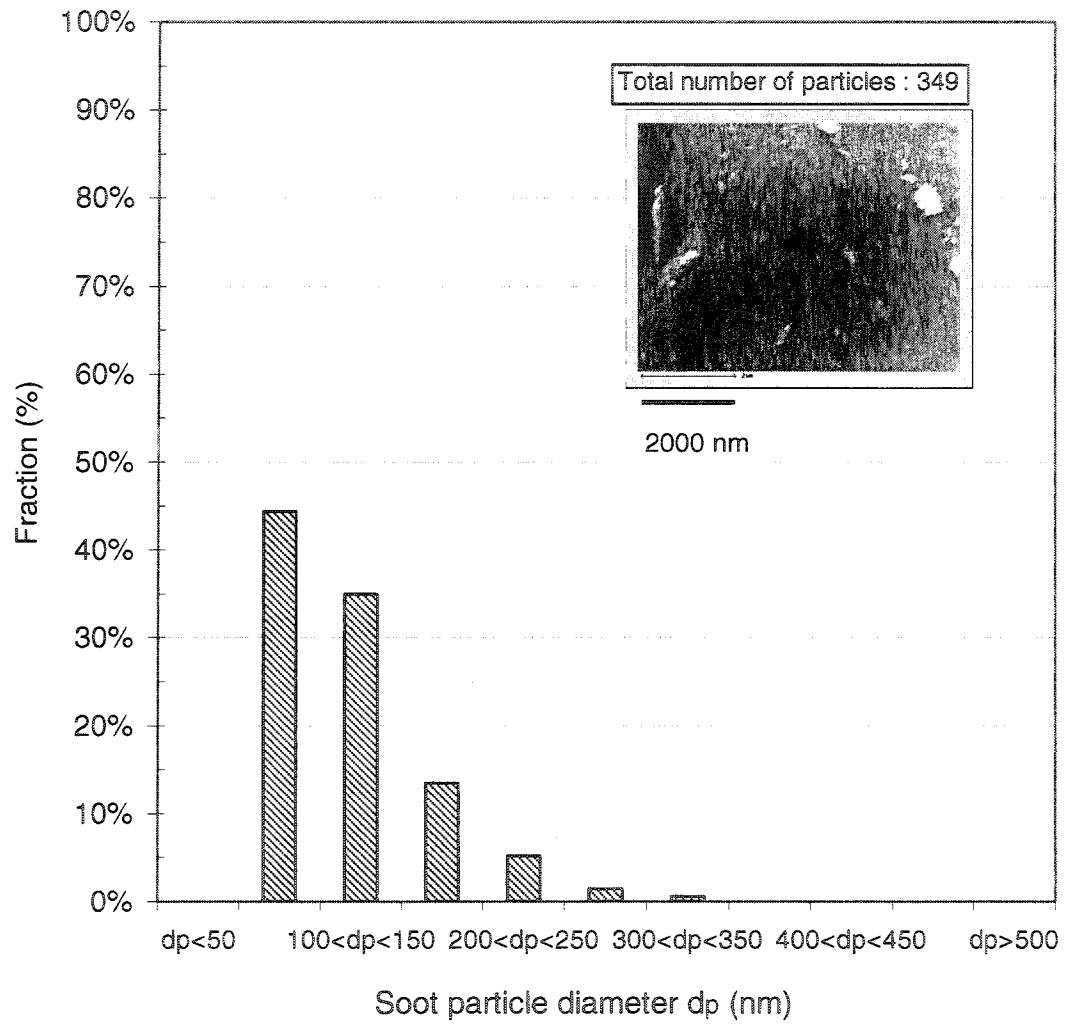


Figure 4.24. SEM measurements of the soot particles size distribution in diesel exhaust sampled upstream of the EGR cooling device.

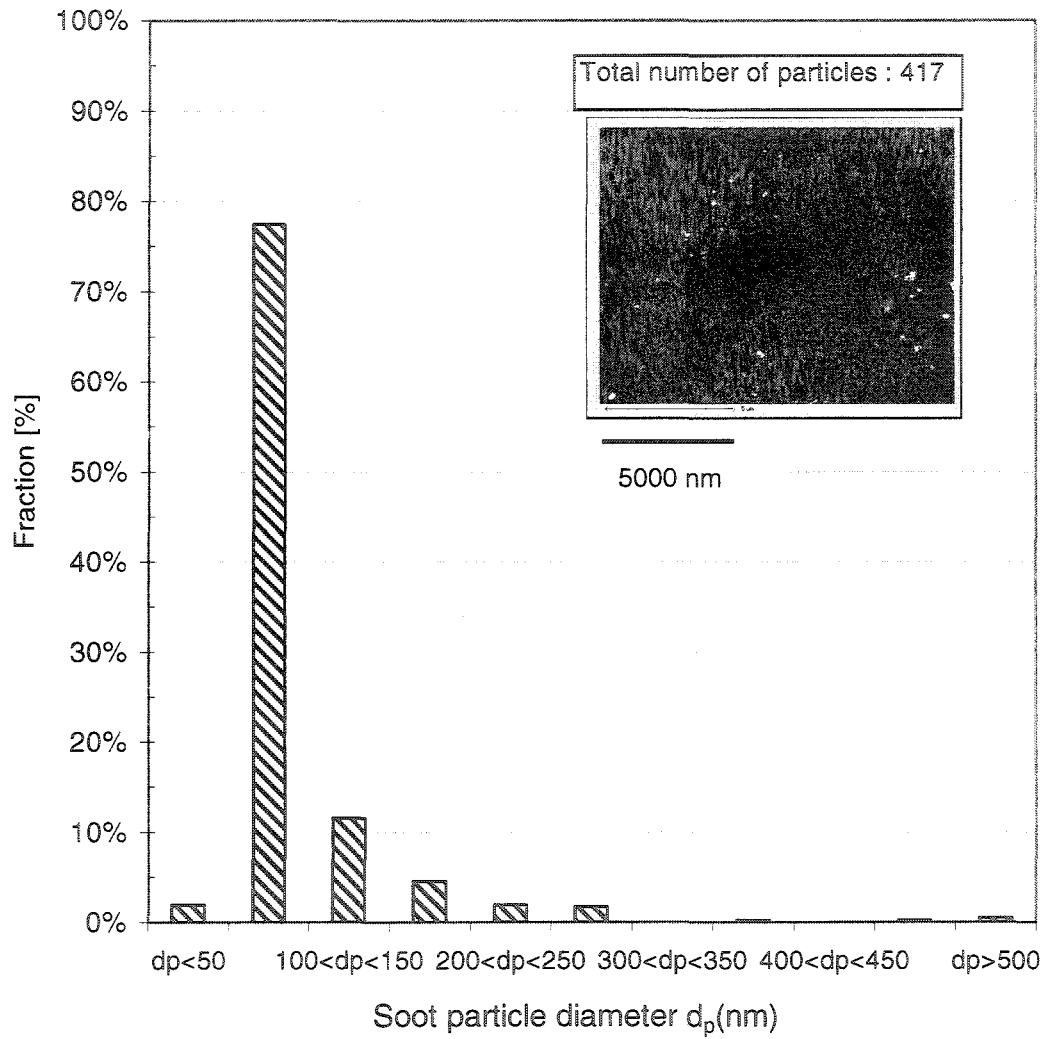


Figure 4.25. SEM measurements of the soot particles size distribution in diesel exhaust sampled downstream of the EGR cooling device.

inside diameter sampling tube. An 8L sampling chamber was used in the sampling system, so that the operating temperature and pressure of the sampled exhaust gas for the CNPC were maintained within the acceptable limits. Here, the operating conditions were monitored during a sampling time of approximately 4.5 minutes, using a pressure gage and a T-type thermocouple incorporated in the sampling chamber. Particle size cut-off screens (PSCS) or diffusion screens were used with the CNPC sampling system to determine the particle concentration or number density and the particle size distribution. The total soot particle number density for the diesel exhaust gas was found to be on the order of 10^{10} #pt./m³ with the bimodal distribution peak particle diameter around $0.01 \mu\text{m}$ and larger than $0.16 \mu\text{m}$, as shown in Figure 4.26. It should be noted that the CNPC could not discriminate particle sizes for particle diameters in the range $0.162\text{-}20 \mu\text{m}$ due to its limitations. However, SEM results indicated there was not a significant number of particles with sizes greater than approximately $0.5 \mu\text{m}$, so that the particle number density in this range from the CNPC was attributed to the agglomerated particles.

The change in the soot mass concentration in the exhaust gas upstream and downstream of the cooling device was characterized as shown in Figure 4.27. Measurements of the soot mass concentration were performed at the sampling chamber, shown in Figure 4.23, using Haz-dust-III for approximately 1 hour. The gas flow rate 6 kg/hr entered the three-tube EGR cooling device at

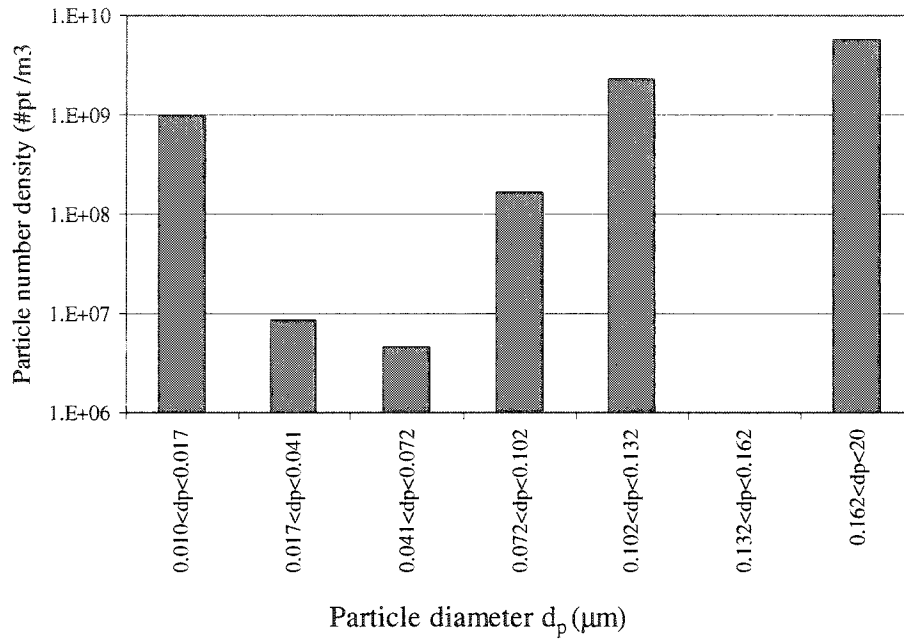


Figure 4.26. In-flight measurements of the soot particle size and number density of diesel exhaust in EGR loop using CNPC system.

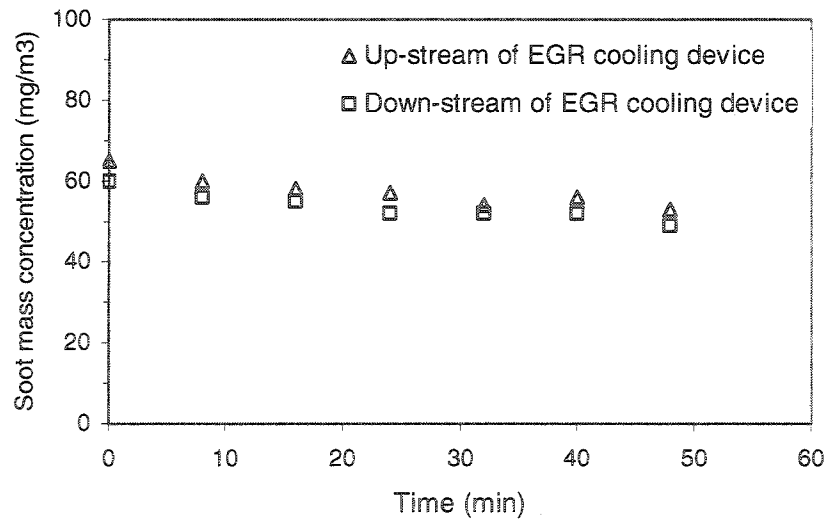


Figure 4.27. Change in the soot mass concentration measured upstream and downstream of the cooling device.

temperature 182 ± 3 °C and the coolant inlet temperature and flow rate were approximately 26 ± 2 °C and 2.5 l/min. The results indicate that the soot mass concentration was 58 ± 7 mg/m³, and the soot mass concentration measured upstream of the cooling device was 4-9% higher than that measured downstream as shown in Figure 4.27. This may be due to the soot deposition that occurred in the cooling device that caused a decrease in the soot mass concentration after exiting the cooling device.

4.4 The Neutron Radiography Non-Destructive Test Facility

A measurement technique was developed to non-destructively characterize the deposited diesel soot profiles in exhaust system components, such as the EGR cooling devices using the digital neutron radiography imaging technique. The measurements were performed using the neutron radiography non-destructive test (NR-NDT) facility (Harvel et al., 1995) at the McMaster Nuclear Reactor (MNR) shown in Figure 4.28. The MNR is a designated 5 MW pool type research reactor located at McMaster University that has a total of 7 beam ports or tubes that can be used to extract pure neutron beams from the reactor core to the site of particular tests, and uses light water as a moderator. The neutron radiography facility used in this investigation is located in Beam Port #2. The Beam Port #2 has a concrete shielded cave-like room where the test objects or the EGR cooling devices were placed during experiments. The access

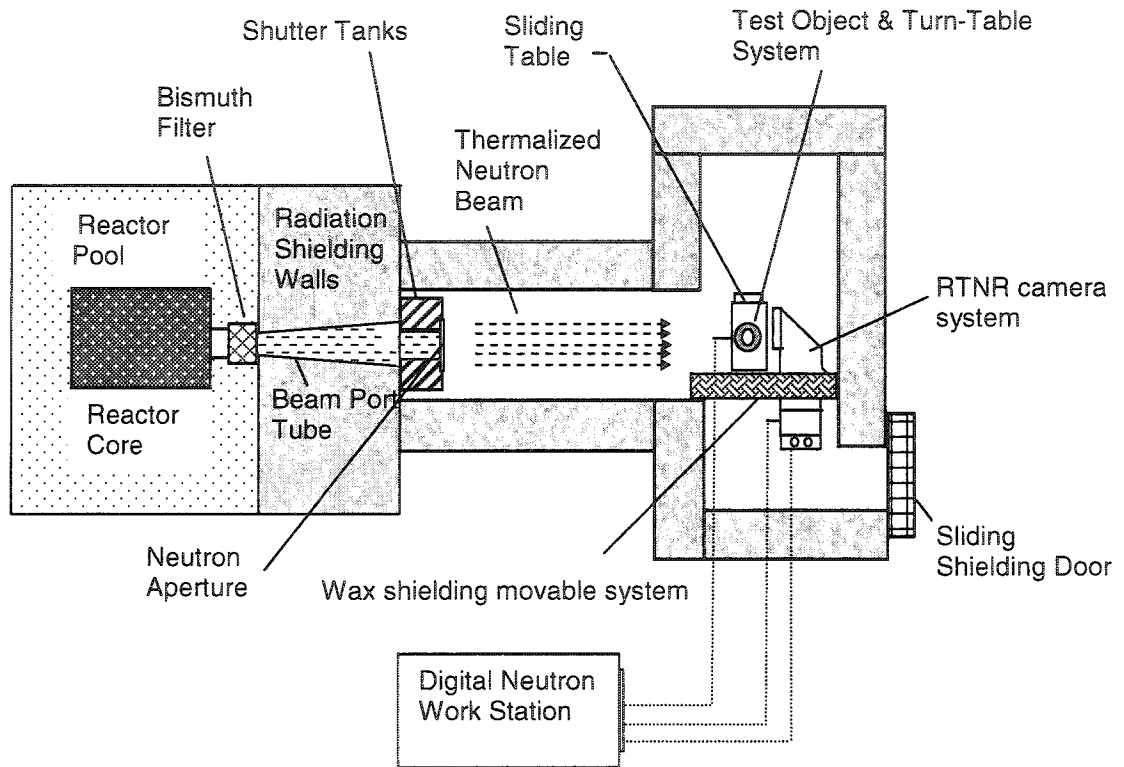


Figure 4.28. Schematic of the top view of the neutron radiography non-destructive test (NR-NDT) facility in beam port 2 of the McMaster Nuclear Reactor.

to the beam port is provided by a 0.7 m x 2.0 m shielding sliding door located away from the beam center to minimize radiation leakage. The facility provides steady and well thermalized pure neutron beam with a flux on the order of 10^6 n/cm².s when the reactor is operating at 2 MW of thermal power. The thermal neutron beam is collimated using a Cadmium collimator with a ratio of collimator length to aperture diameter of 70. The operation of the beam port is activated by raising a shutter of water-filled tanks using a manual crank-and-pulley system. A wax shielding sliding door system was designed and added to the facility as shown in Figure 4.29. The specimen-replacement window on this door facilitated replacing of test specimens while minimizing the exposure to residuals of radiation that were present even after the shutter was closed.

The test objects containing the diesel soot were placed on a computer controlled turn table that was added to the facility. The turn table, positioned in the path of the thermal neutron beam, was used to incrementally rotate the specimen through 360° using a NF90-1 Velmex stepper motor that was controlled using a programmable controller. A photograph of the computer controlled revolving table system is shown in Figure 4.30, and the characteristics of the step motor used in the revolving-table system are summarized in Table 4.4.

The intensity of the neutron beam transmitted through the test specimen at each angle of interest was measured using the digital neutron imaging system (DNIS) shown in Figure 4.31. This included a NRTV-2 real-time neutron

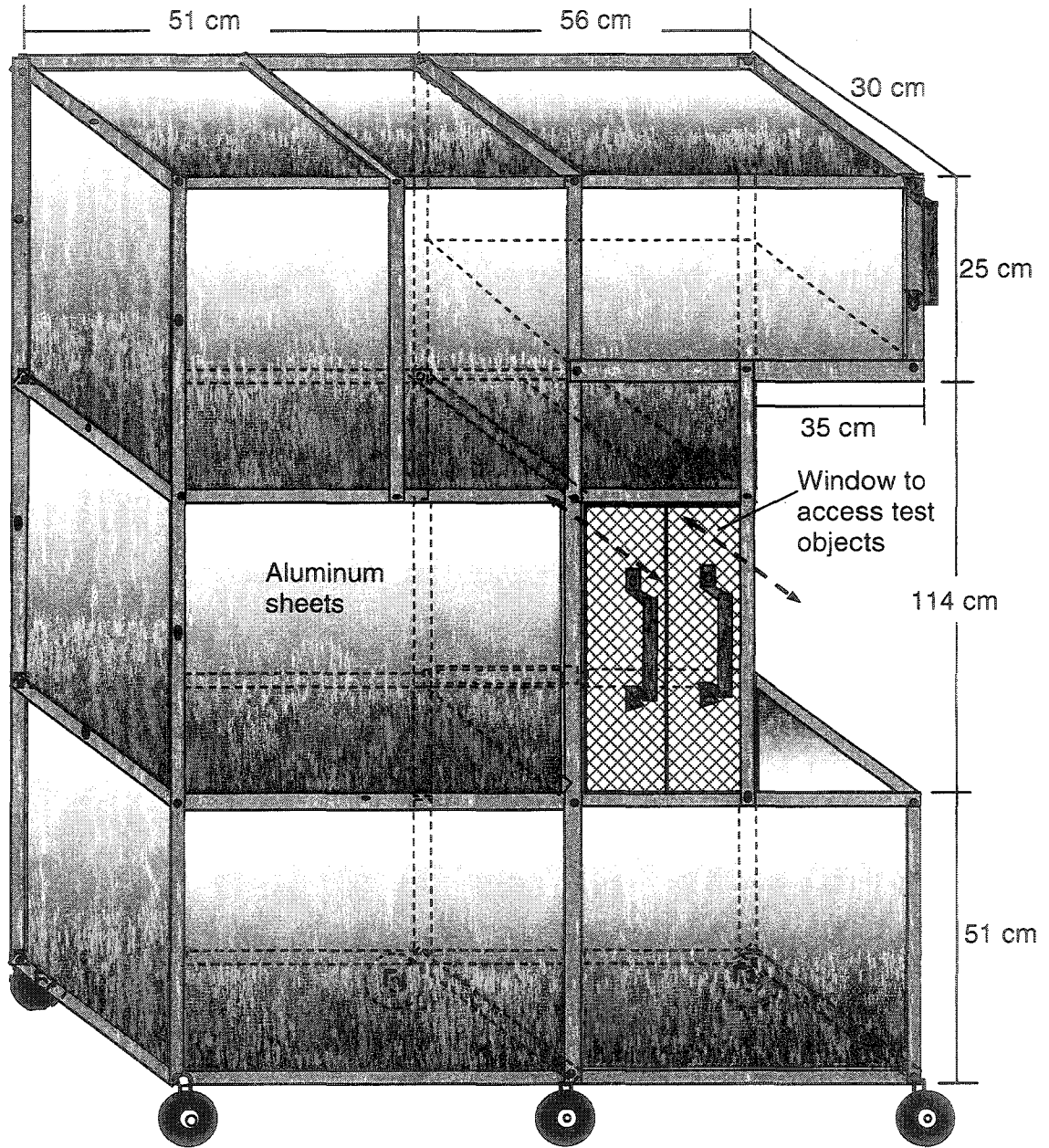


Figure 4.29. Schematic of the movable wax shielding system of the beam port 2 of the McMaster Nuclear reactor.

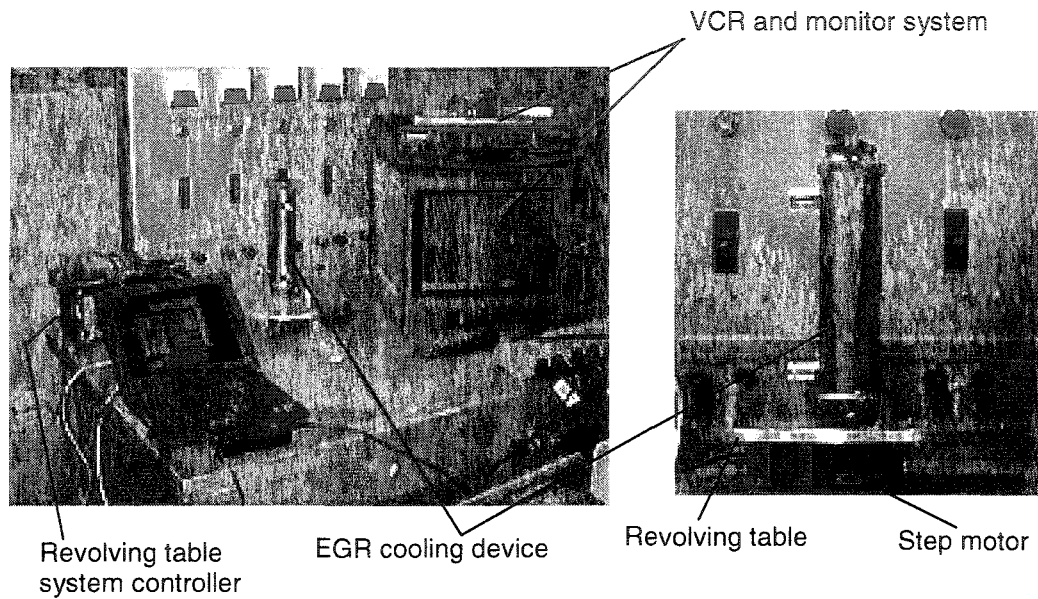


Figure 4.30. Photographs of the computer controlled revolving table system used in the present work.

Table 4.4: Characteristics of the stepper motor driven revolving-table system.

Model #	B5990TS (Velmex Inc.)
Gear ratio	90:1
RPM	1.66
Time per revolution	36 sec.
Speed	10°/sec
Degrees per step	0.010
Accuracy	±0.0278°

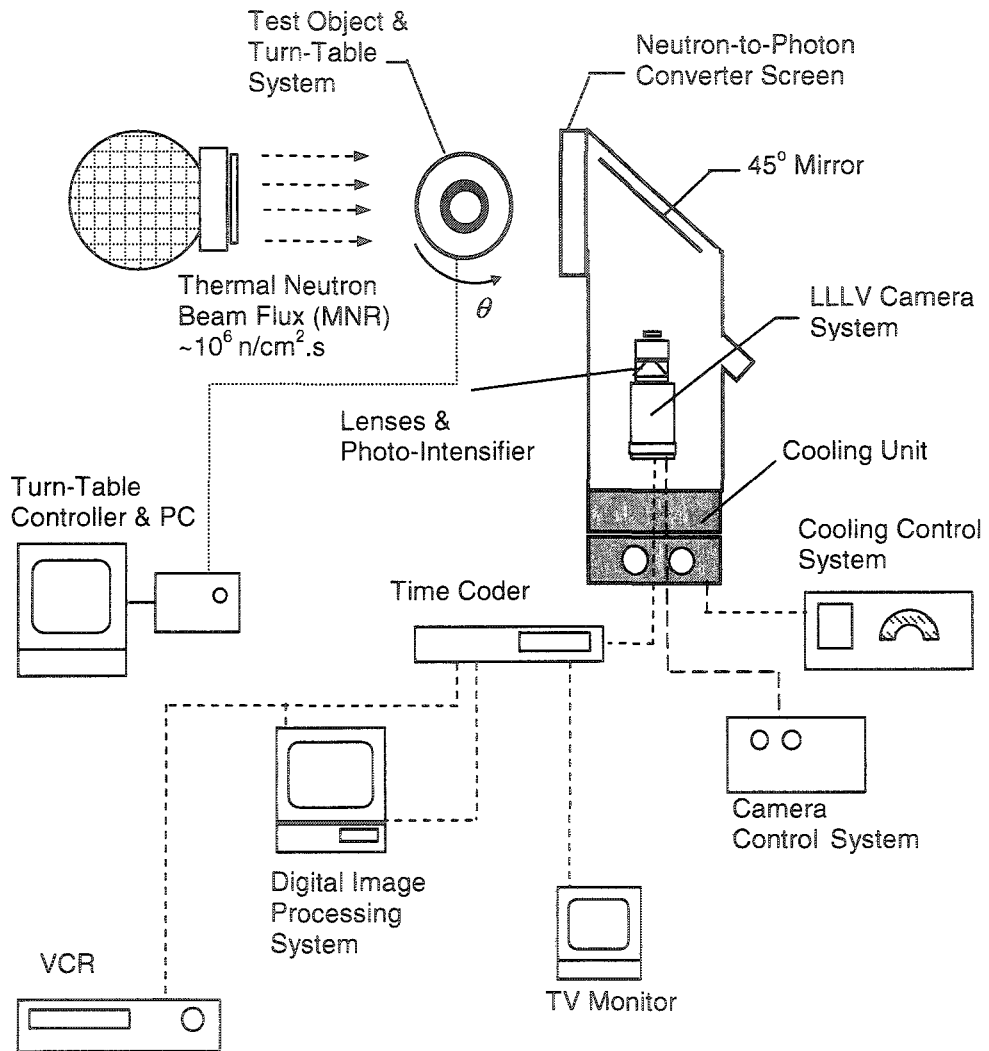


Figure 4.31. The digital neutron imaging system (DNIS).

radiography (RTNR) camera system that used a 28 cm x 28 cm Lithium doped Ag activated ZnS screen to convert the neutrons to light photons and a silicon intensifier target (SIT) tube to intensify the image before it was recorded by a low-light camera. The sensitive electronics of the camera system were protected from the directed neutron beam using a 45° mirror that was used to deflect the photons produced in the converter screen into the SIT tube. In each test, the camera system was pressurized to 9 PSIG with dry nitrogen to provide electrical and thermal insulation for the target and to reduce noise. The RTNR system was then allowed to thermalize for approximately 3 hours. The image associated noise was also minimized by locating the cooling system and the focusing controllers for the camera system outside the beam room. These were connected to the camera system using electrically shielded cables. The camera system outputs a standard RS-330 video signal at 30 frames/s that could be recorded on standard cassette tapes using a S-VHS video cassette recording VCR (Panasonic model) system.

The individual images were later captured with a Data Translator (DT3152) image grabber system for analysis. The images from each set of measurements were averaged using the Western Vision HLImage++ software to reduce the random noise associated with the system and enhance the quality of the image. The averaged image was then converted to an 8-bit grayscale using Adobe Photoshop software. A gain was also applied to the image to enhance the contrast in the image. The process was applied consistently to all the images so

that it would not affect the final results. The same procedure was applied to the background image without the test object and the image was then subtracted from the image of the test object using HImage++ to eliminate the camera target effects that caused some non-uniformity of the intensity profile in the images. Line profiles of the image intensity in the region of interest were then extracted using HImage++. The extracted data were then exported to MS Excel for later analysis. A flow chart of the image processing procedure used here is given in Appendix H.

The thickness of the soot in the different images was determined by analyzing the attenuation of the incident neutron beam as it passes through the test object. The intensity of the attenuated neutron beam transmitted through an object consisting of different layers can be approximated by (Duderstadt and Hamilton, 1996)

$$\frac{I}{I_0} = \prod_{i=1}^n Bu_i(\mu_i \delta_i) e^{-\mu_i \delta_i}, \quad (4.4)$$

where I_0 is the incident intensity of the neutron beam, I is the intensity of the neutron beam transmitted through the test object. Here, $Bu_i(\mu_i \delta_i)$ is the build-up factor for i^{th} layer to account for secondary neutron scatterings back into the beam pathway, μ_i is the thermal attenuation coefficient for the i^{th} layer, δ_i is the length of neutron path through this i^{th} layer, and n is the number of layers. Thus,

the model equation for the attenuation of the neutron flux as the beam passes through a metal component containing diesel soot, such as the pipe shown in Figure 4.32, is given by

$$\frac{I_s(x, z, \theta)}{I_o} = Bu_m Bu_s e^{[-2\mu_s \delta_s(x, z, \theta) - 2\mu_m \delta_m(x)]}, \quad (4.5)$$

where I_s is the intensity of the neutron beam transmitted through the soot deposited device, μ_s is the average attenuation coefficient for the soot, δ_s is the local thickness of the soot, μ_m is the attenuation coefficient for the metal, and δ_m is the thickness of the metal container. It should be noted that there is a factor 2 in front of δ_s (and δ_m) in Eq. (4.5), because there is a soot layer on the front and back of the object in Figure 4.32. Thus, δ_s is the average thickness on the front and back, and $2\delta_s$ is the local total thickness on both. The attenuation caused by the metal container was determined by measuring the attenuation of the neutron beam passing through the clean container, I_m , that can be approximated by

$$\frac{I_m(x)}{I_o} = Bu_m e^{-2\mu_m \delta_m(x)}, \quad (4.6)$$

Aluminum pipes were used for the tests here because they have a low thermal neutron attenuation coefficient, in order to minimize the effect of the pipe on the image. Since the attenuation coefficient is small, it can also be assumed the

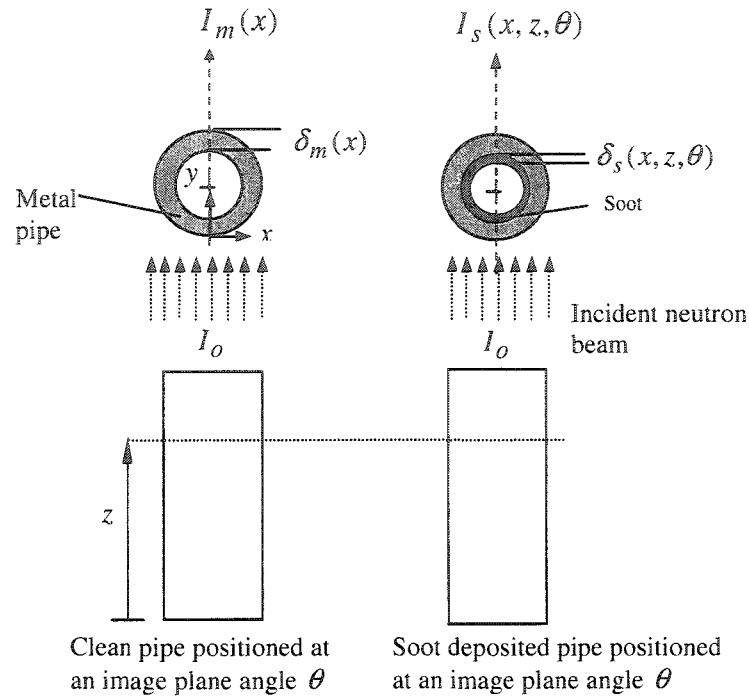


Figure 4.32. Schematic showing the concept of the neutron attenuation through a soot deposited pipe.

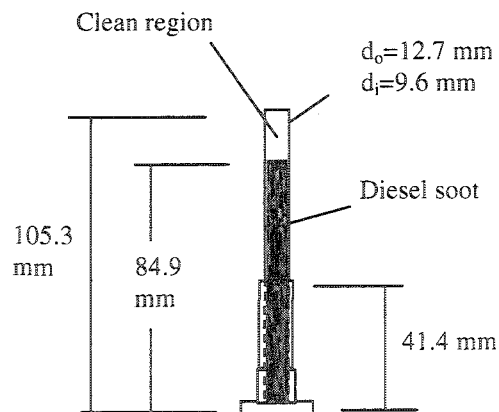


Figure 4.33. Schematic of the aluminum tube partially filled with diesel soot used to determine the attenuation coefficient and the build-up factor for the diesel soot.

build-up factor of the aluminum was 1. The attenuation of the beam caused by the soot was then determined by taking the ratio of the intensity of the images for the soot deposited component and the clean component, i.e.,

$$\frac{I_s(x, z, \theta)}{I_m(x)} = Bu_s e^{-2\mu_s \delta_s(x, z, \theta)}. \quad (4.7)$$

The thickness of the soot δ_s was then determined by inverting Eq. (4.7) once the attenuation coefficient, μ_s , and the build-up factor, Bu_s , for the diesel soot were known.

A calibration experiment was performed to determine the average thermal neutron attenuation coefficient and build-up factor for the diesel soot. The calibration experiment was done by freely pouring diesel soot powder produced from the diesel exhaust test facility into an aluminum tube with a length 105.3 mm and inner diameter 9.6 mm as shown in Figure 4.33. The tube was then gently tapped so that the powder was evenly distributed in the tube. The tube was then imaged using the digital neutron imaging system. The profiles for different positions across the tube were then averaged to determine the average attenuation coefficient and buildup factor for the diesel soot produced by the diesel engine test facility. The density for the porous soot was not determined. Instead, it was implicitly included in the neutron attenuation coefficient, where the neutron attenuation coefficient is equal to the mass attenuation coefficient times the density of the soot (Duderstadt and Hamilton, 1996).

The accuracy of the neutron radiography technique was then examined by measuring the soot layer thickness deposited in a 20.4 cm long and 3.58 cm diameter pipe using the neutron radiography technique. The pipe had been exposed to diesel exhaust in the high flow rate leg of diesel exhaust test facility, shown in Figure 4.4, for approximately 12 hours with exhaust gas temperature of 250 ± 5 °C and gas mass flow rate of 34 ± 2 kg/hr, produced when the load on the generator was approximately 3 kW. The pipe was then sectioned into eight pieces or rings, and the thickness of the soot in these rings was measured using an optical microscope system that has an accuracy of approximately $\pm 3\%$. The measurements of the soot thickness from these destructive tests were then compared with the measurements using the neutron radiography technique. The results are presented in chapter 5.

CHAPTER 5: The Soot Deposition Characteristics in the EGR Cooling Devices

This chapter presents and discusses the experimental results for the diesel soot deposition characteristics in the tubes of the EGR cooling devices measured using the non-destructive neutron radiography technique. The technique was first calibrated by performing controlled experiments to determine the neutron attenuation coefficient and build-up factor for the diesel soot. The accuracy of the neutron radiography technique was then examined by comparing the thickness of the deposited soot layers in an aluminum pipe measured using the neutron radiography technique with direct measurements of the soot thickness after the pipe was sectioned. Measurements were then performed to characterize the soot deposited profiles in single-tube EGR cooling devices for two different gas flow rates, and the three-tube cooling devices with 45° and 60° expansion angle inlet headers. The results for each of these experiments are discussed in turn.

5.1 Calibration and Validation of the Neutron Radiography Technique

The neutron attenuation coefficient and build-up factor for the diesel soot were first determined by imaging a 9.6 mm diameter aluminum tube (shown in

Figure 4.33) partially filled with diesel soot produced by the diesel engine. A typical processed image of neutron intensity transmitted through the tube is shown in Figure 5.1(a). There is a clear difference between the neutron intensity in the lower portion of the tube that contained the soot, and the upper empty portion of the tube. The line profiles of the relative intensity across the tube at one height in the upper region without the soot, and at three heights in the lower portion with the soot are shown in Figure 5.1(b). The first profile is typical of the intensity of the neutron flux transmitted through the thinner section of the aluminum tube, while the other three profiles are representative of the neutron flux transmitted through the aluminum tube and the diesel soot. The attenuation of the beam for the clean tube is approximately uniform across the central portion because the length of the neutron path through the tube walls does not vary significantly over much of the tube. The attenuation of the neutron flux measured in the region with the soot does vary across the tube because the length of the neutron path through the soot differs at different lateral positions, being longest near the center of the tube. The length of the path that the neutron beam travels through the soot is not simply the distance across the cylinder because the packed soot is porous. The porosity of the packed soot could vary with height. The profiles from the three heights are in reasonable agreement indicating that the porosity is reasonably uniform along the tube. The profiles were averaged, though, to reduce the error associated with the non-uniformity of the soot

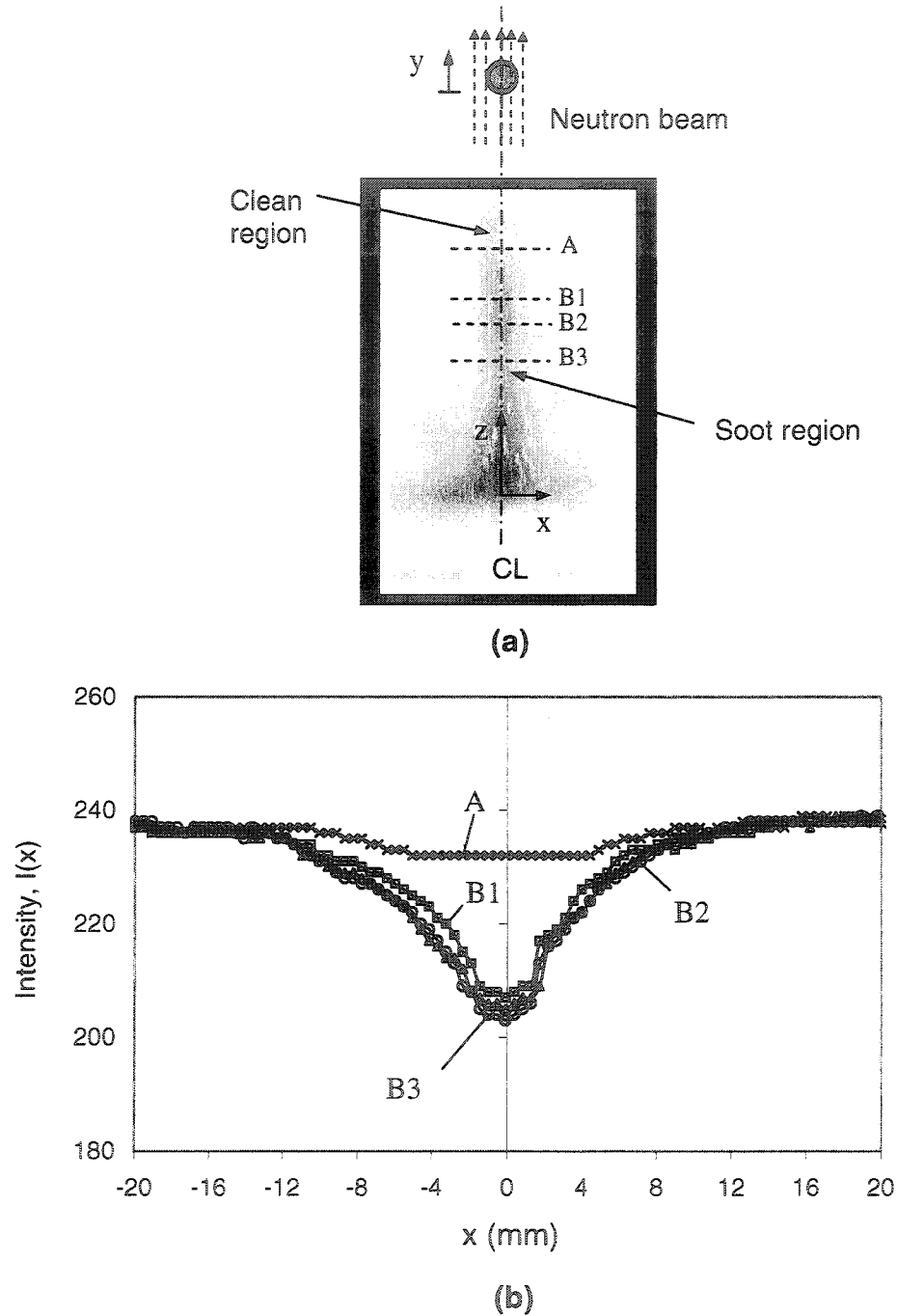


Figure 5.1. (a) Neutron image of the soot filled tube and (b) measurements of the intensity across different locations along the tube used to determine the attenuation coefficient and build-up factor for the diesel soot.

packing and the averaged profile was used to determine the attenuation coefficient of the soot.

The attenuation coefficient and build-up factor were determined using the attenuation of the beam at different lateral positions, as shown in Figure 5.2. In particular, taking the logarithm of Eq. (4.16) yields

$$-\ln\left(\frac{I_s}{I_m}\right) = 2\mu_s\delta_s - \ln Bu_s, \quad (5.1)$$

assuming that the attenuation coefficient of the soot is a constant. The path length of the neutron beam through the soot was estimated by assuming the porosity was similar to closely packed mono-sized spherical particles that have an average line packing fraction, PF, of approximately 0.6 (Cumberland and Crawford, 1987), so that the local path length through the soot can be approximated by $\delta_s = PF\delta(x)$ as shown in Figure 5.2. This assumption should not cause an error in later measurements, as long as packing factor of the soot deposited in the test is similar to that in the packed tube. The change in the logarithm of the ratio of the intensities, for the different neutron paths at different lateral positions across the tube is shown in Figure 5.3. The attenuation coefficient determined from a best linear fit of the data was $\mu_s \cong 0.023 \text{ mm}^{-1}$. The build-up factor determined from the y intercept of this best fit was $Bu_s \cong 1$. The error associated with determining the attenuation coefficient was less than approximately 4%. The main source of this error was the uncertainty in locating

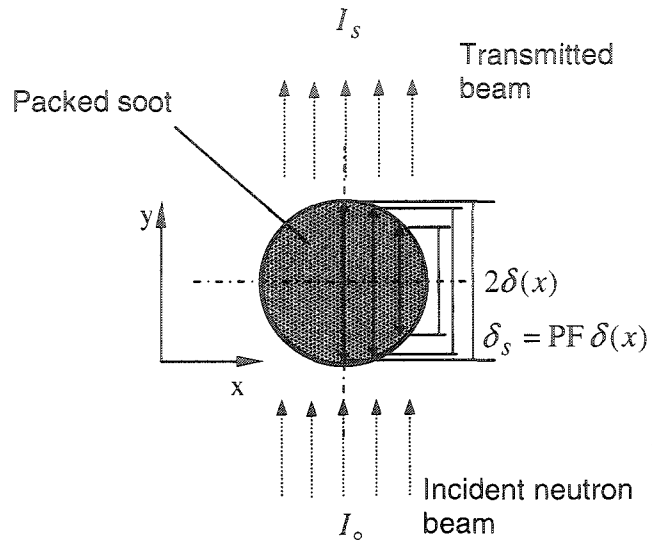


Figure 5.2. Schematic showing the change in the length of the neutron path across the tube containing the soot at different lateral positions.

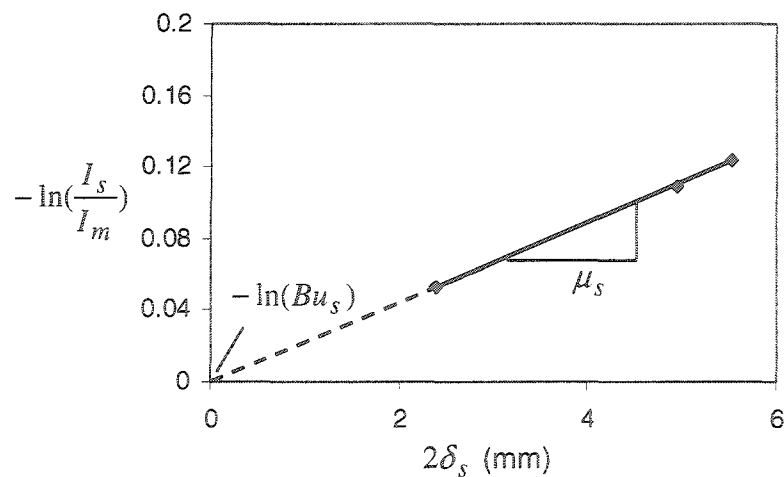


Figure 5.3. Change in the attenuation of the neutron flux with path length used to determine the attenuation coefficient, μ_s , and build-up factor, Bu_s , for diesel soot.

the edges of the tube due to the blurriness of the image near the edges. This caused an uncertainty in locating the pixel intensity along the centerline of the tube.

The accuracy of using the neutron radiography technique to measure the soot thickness profiles was assessed by measuring the soot profiles in a 20.4 cm long and 3.58 cm diameter pipe that was exposed to soot deposition in the diesel test facility. The thickness of the soot was initially measured using the neutron radiography technique. Before these tests were performed, the soot layer was removed from approximately 41.0 mm at the exit end, so the attenuation of the neutron beam caused by the clean pipe could be determined. The pipe was then imaged using the neutron radiography technique at every 60° from 0 to 300°. A schematic of the soot deposited pipe and a typical processed image of the neutron flux from an angle of 300° are shown in Figure 5.4. The clean section in the pipe is at the top of the image in these figures. It is clear that there is a difference between the attenuation of the neutron flux caused by the metal pipe at the top of the image, and the soot deposited pipe. The attenuation of the neutron flux increases along the pipe and becomes a maximum at the bottom where the diesel exhaust gas entered the pipe in the soot deposition experiment indicating that the thickness of the soot deposited layer was larger at the upstream end of the pipe. It should be noted that the darkest regions at the bottom end of the pipe image were caused by the attenuation of the incident

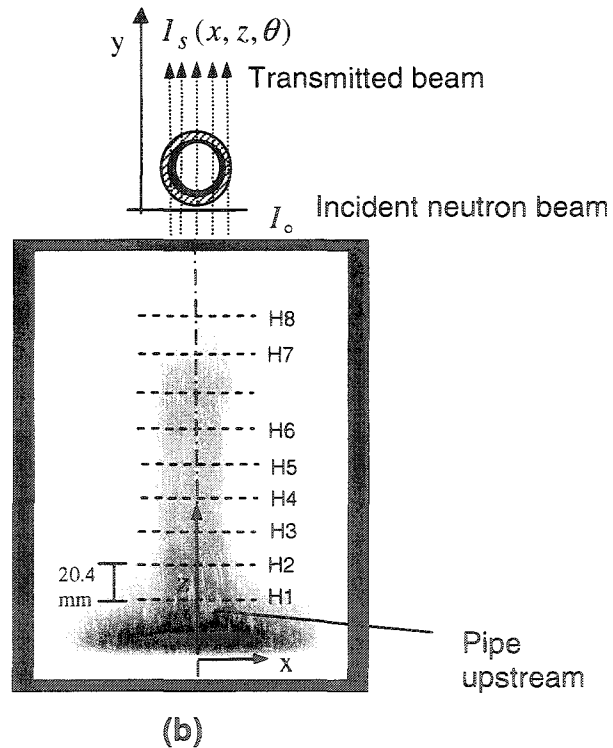
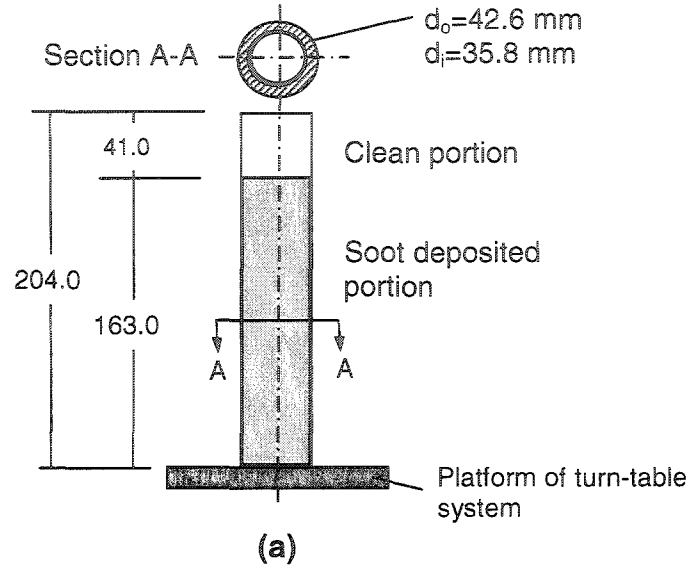


Figure 5.4. (a) Schematic of the soot deposited pipe on the rotating table, and (b) the processed neutron image of the soot deposited pipe viewed from a typical angle of $\theta = 300^\circ$.

beam due to neutrons scattering from the thick aluminum rotating plate and the steel motor.

The profiles of the measured intensity across the pipe at locations spaced 20.4 mm apart, where the pipe was later sectioned, are shown in Figure 5.5. It is clear that the intensity of the neutron flux transmitted through the pipe increases along the pipe from the entrance region of the pipe (H1) to the exit of the pipe (H7) in the test. The intensity also varies laterally across the pipe as the length of the neutron path through the metal and soot changes. It should be noted that the change in the intensity was not sharp near the edges of the pipe due to neutron scattering caused by the tube wall that produced a slightly blurred image, thus limiting the resolution near the tube edges. The ratio of the intensity at the centerline position of each profile to the intensity at the centerline position from the profile in the clean region was then used to compute the soot thickness at this angle. This process was repeated for all the angles where the measurements were taken.

The change in the local soot thickness along the pipe at typical circumferential locations determined using the digital neutron radiography technique is shown in Figure 5.6. It is clear that the thickness of the soot decreases nonlinearly from approximately 2.0 mm at the entrance of the pipe to 0.3 mm near the exit of the pipe. There is also a significant variation of the soot profile around the pipe. In particular, the local thickness varies by approximately

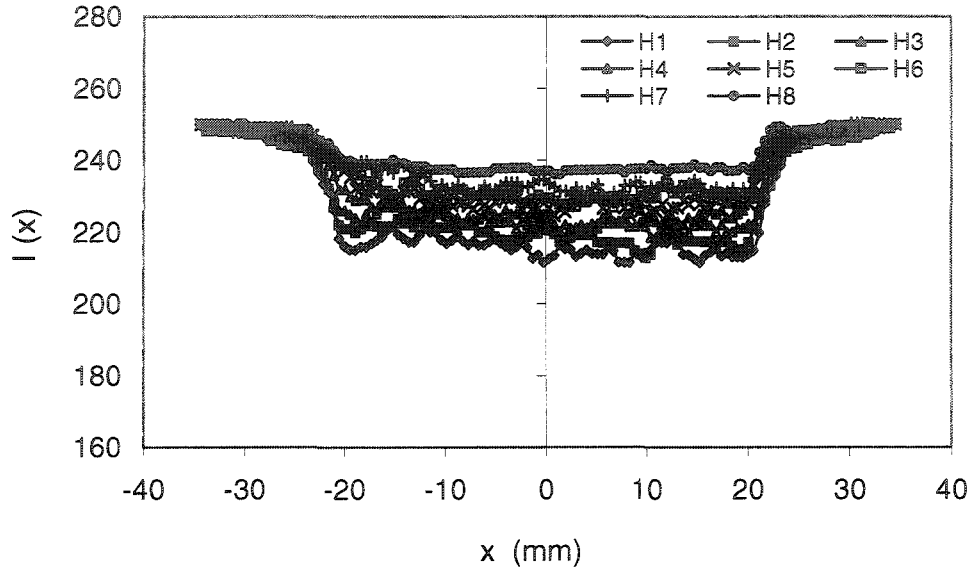


Figure 5.5(a). Profiles of the neutron intensity across the fouled pipe at positions along the pipe separated by 20.4 mm as shown in Figure 5.4. Image plane angle $\theta = 0^\circ$.

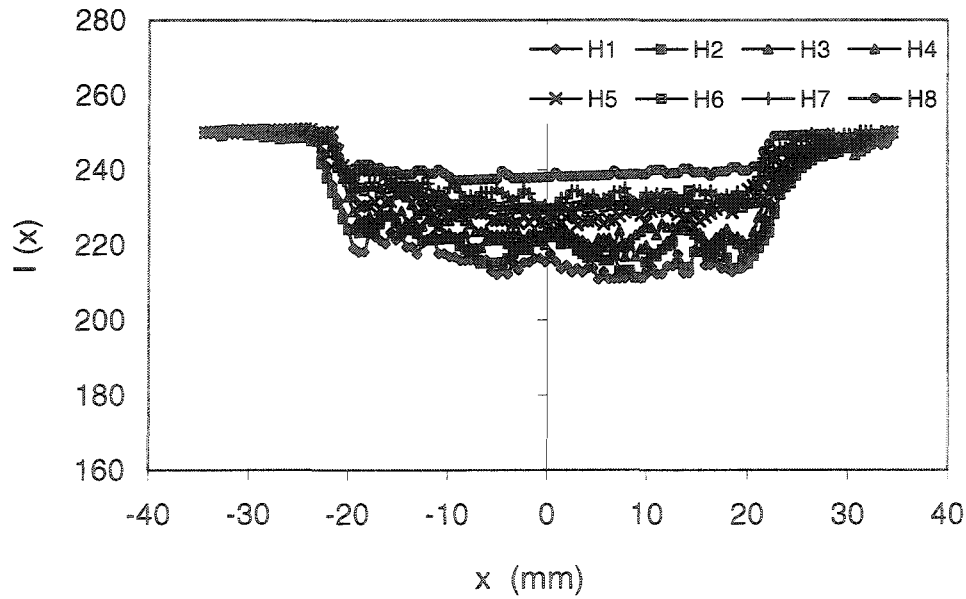


Figure 5.5(b). Profiles of the neutron intensity across the soot deposited pipe for H1 to H8 positions along the pipe. Image plane angle $\theta = 60^\circ$.

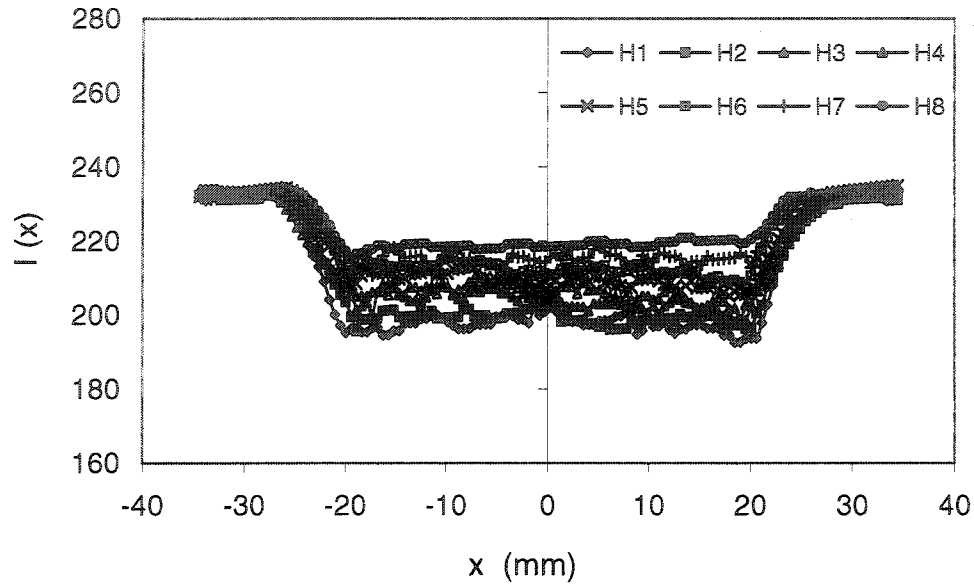


Figure 5.5(c). Profiles of the neutron intensity across the fouled pipe for H1 to H8 positions along the pipe. Image plane angle $\theta = 120^\circ$.

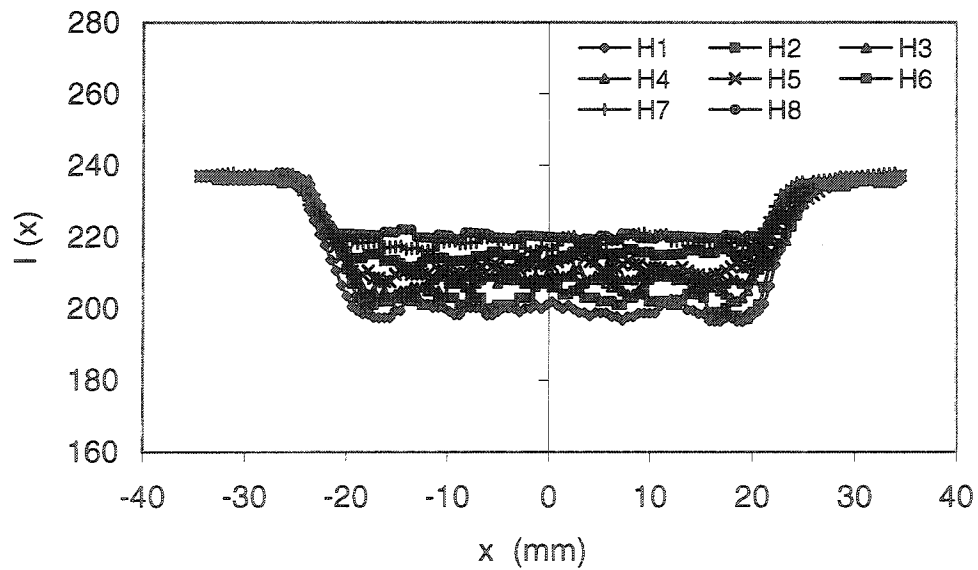


Figure 5.5(d). Profiles of the neutron intensity across the soot deposited pipe for H1 to H8 positions along the pipe. Image plane angle $\theta = 180^\circ$.

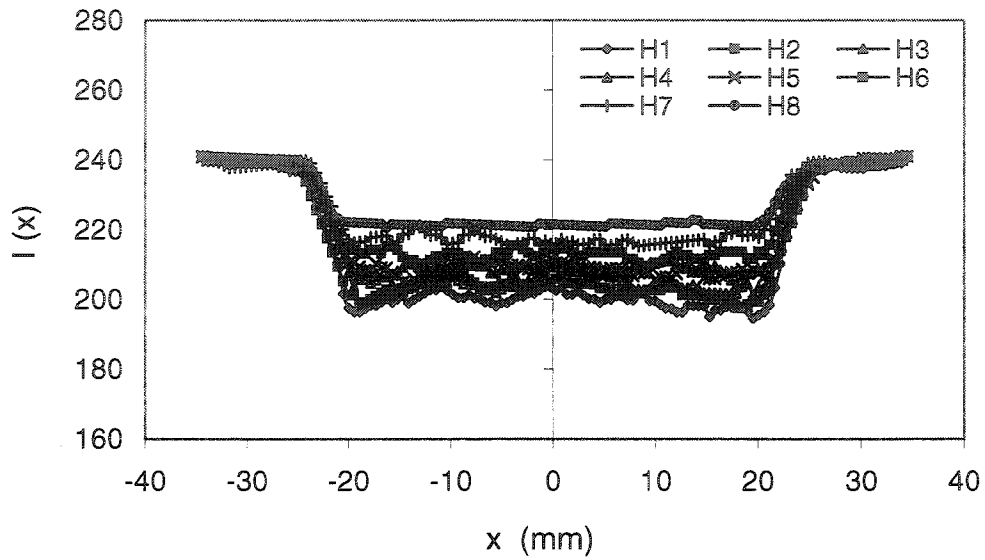


Figure 5.5(e). Profiles of the neutron intensity across the soot deposited pipe for H1 to H8 positions along the pipe. Image plane angle $\theta = 240^\circ$.

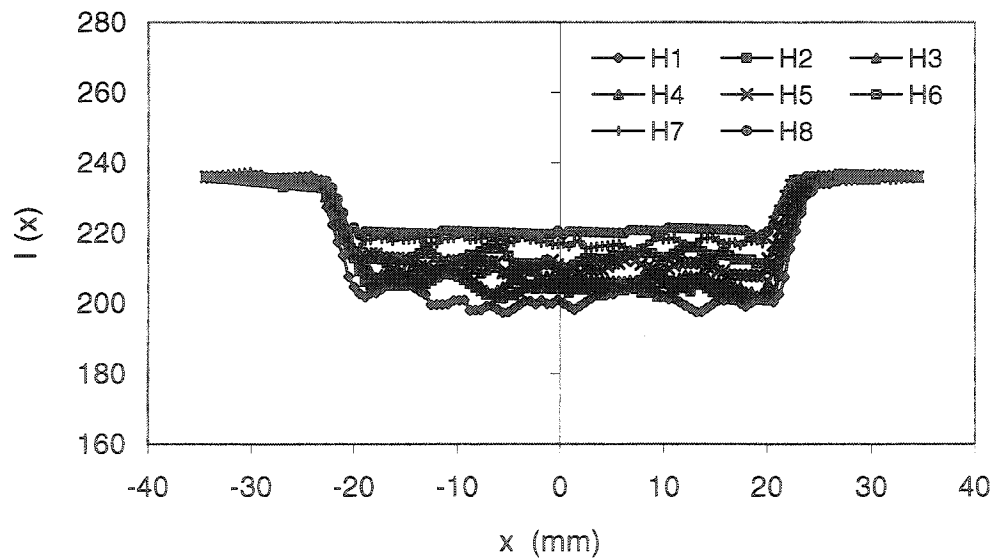


Figure 5.5(f). Profiles of the neutron intensity across the soot deposited pipe for H1 to H8 positions along the pipe. Image plane angle $\theta = 300^\circ$.

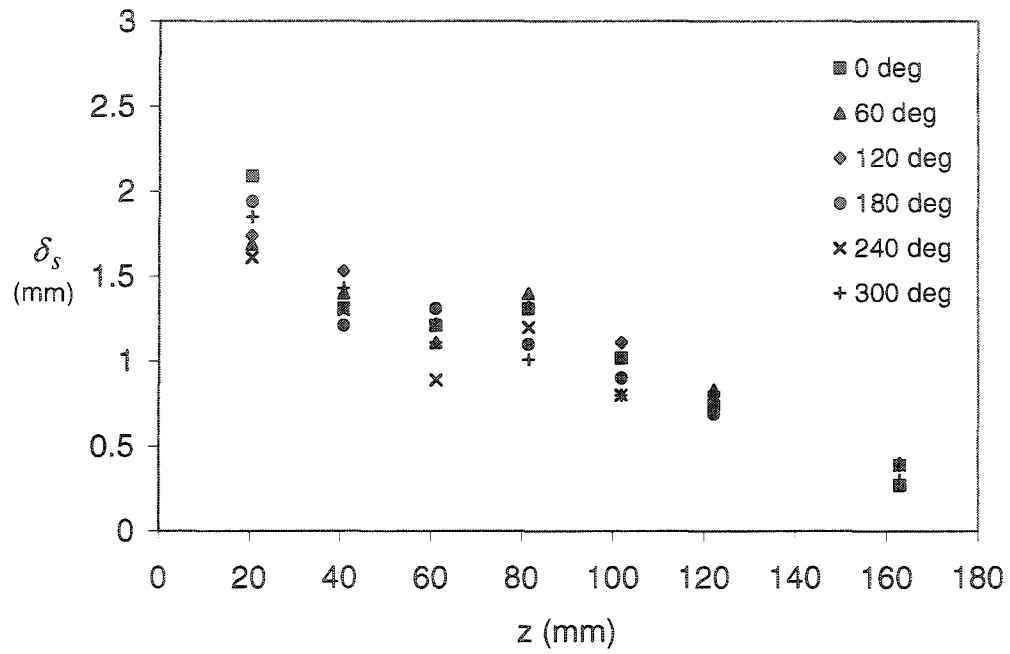


Figure 5.6. Change in the soot thickness profile along the pipe at different azimuthal positions measured using the digital neutron radiography technique.

10 to 26% of the local average thickness, with the largest variation being near the midsection of the pipe, indicating that the soot profile is three-dimensional.

The pipe was then sectioned at the different locations along its length that matched the locations examined in the neutron radiography test. The sectioning process was performed by slowly paring the tube on the lathe machine and then breaking it by hand once only a very thin wall of the tube remained, thus effectively eliminated the chance that the deposited soot layer would be affected. The thickness of the soot deposited layer at the sections was measured using the optical microscope system, as discussed in chapter 4. Photographs of the images of the soot layers are shown in Figure 5.7. The thickness of the soot layer at different azimuthal angles was then determined using these photographs. The typical uncertainty in the measurements determined from the optical microscope was less than 3% due to the optical resolution of the system. The change in the local soot thickness along the pipe at typical circumferential locations measured from the sectioned pipe is shown in Figure 5.8. It is clear that the thickness of the soot did decrease along the pipe from approximately 1.8 mm at the entrance of the pipe to approximately 0.4 mm near the pipe exit. The local soot thickness varies circumferentially around the pipe by approximately 12 to 32% of the local average value. A comparison of the soot thickness profile at the entrance and exit determined using the two measurement techniques is shown in Figure 5.9. The variation of the soot thickness around the circumference of the pipe

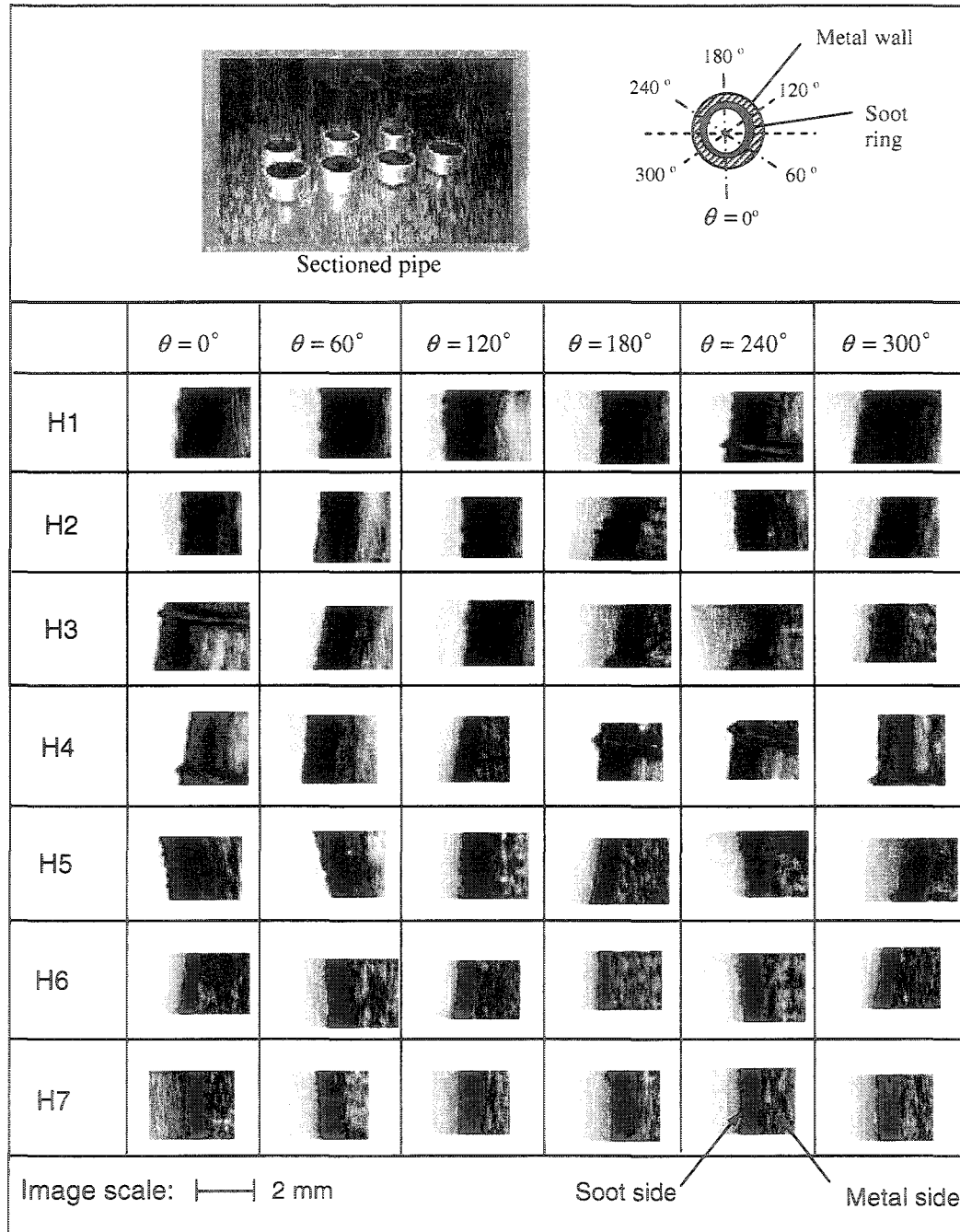


Figure 5.7. Photographs of the sectioned pieces of the soot deposited pipe from H1 to H7 at different azimuthal positions, θ , taken through an optical microscope.

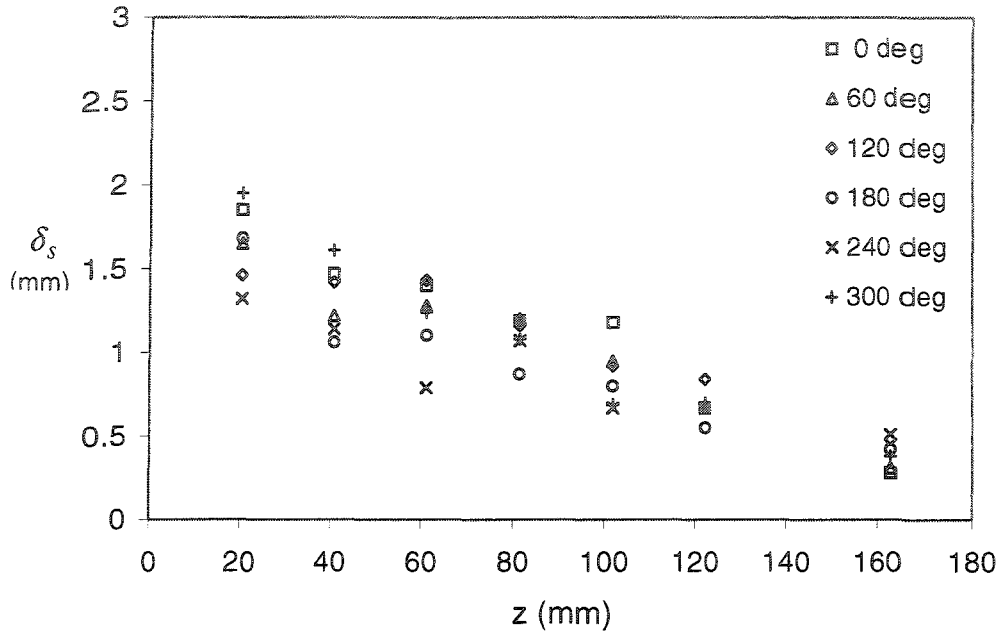


Figure 5.8. Change in the soot thickness profile along the pipe at different azimuthal positions measured from the sectioned pieces using the optical microscope.

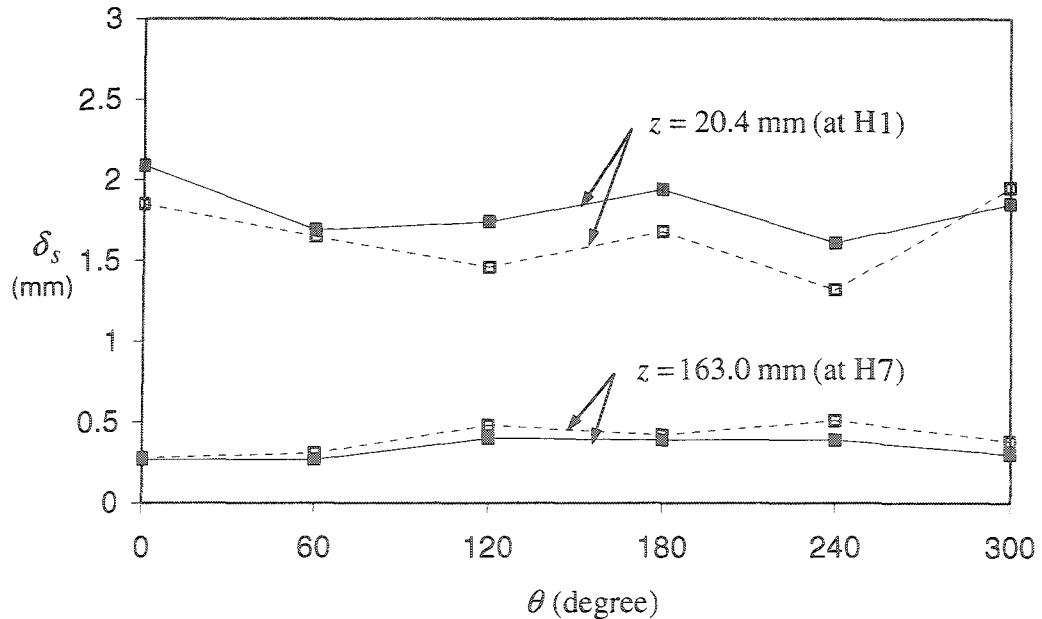


Figure 5.9. Comparison of the soot thickness profile with the azimuthal angle at two different locations along the pipe measured \square from the sectioned pieces using the optical microscope and \blacksquare using the digital neutron radiography technique.

determined using the two techniques are in reasonable agreement both in terms of the range in the thickness, and the locations of the minimum and maximum in the profiles. A comparison of the circumferentially averaged soot layer thickness profiles is also shown in Figure 5.10. The results indicate that the measurements using the digital neutron radiography technique are in good quantitative and qualitative agreement with the direct measurements, with all the results agreeing to within 16%. Thus, the neutron radiography technique is a viable method of measuring the soot profiles in EGR cooling devices.

5.2 Characterization of the Soot Thickness Profiles in the EGR Cooling Devices Using Neutron Radiography

The non-destructive neutron radiography technique was then used to characterize the three-dimensional diesel soot thickness in the generic single-tube and three-tube EGR cooling devices. The soot deposition that occurred in the tubes of the EGR cooling devices exposed to diesel exhaust was initially characterized using the 6.2 mm diameter single-tube EGR cooling devices for two different mass flow rates, 0.8 kg/hr and 2.8 kg/hr at 1, 2, and 5 hours. The secondary side average inlet water temperature was approximately 26°C and coolant flow rate was 1 l/min for all these tests. The nominal Reynolds numbers in the tube based on the clean tube diameter were 2000 and 7000, respectively, so the flow in the tube in the first case should be initially laminar while the flow in

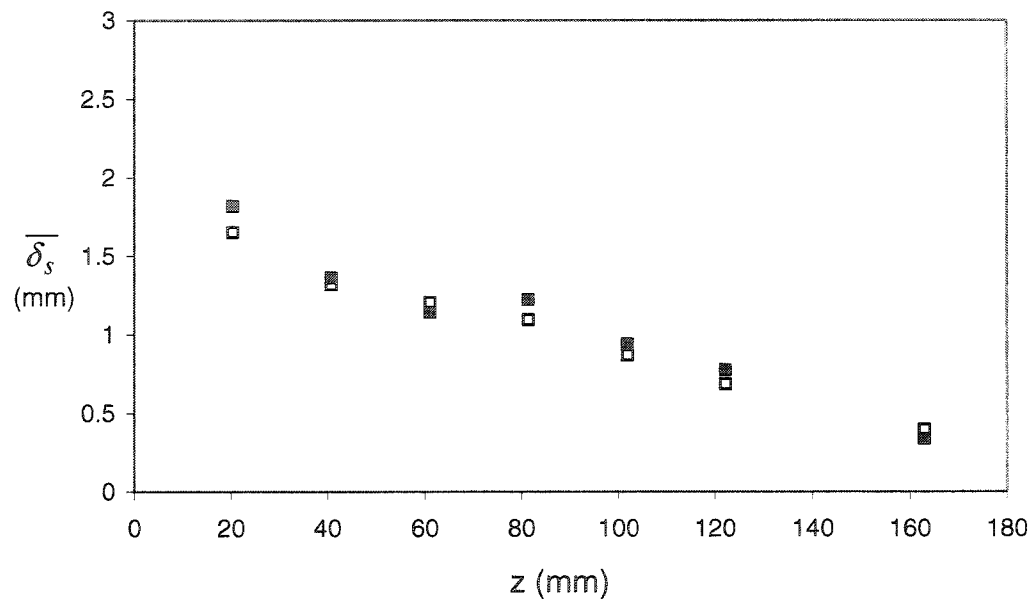


Fig. 5.10. Comparison in the circumferential average soot thickness along the pipe measured □ from the sectioned pieces using the optical microscope, and ■ using the neutron radiography technique.

the tube in the second case should be initially turbulent.

The single-tube was removed from the shell of the cooling device before the neutron radiography technique was applied to minimize the attenuation from the aluminum components. The processed images from the digital neutron radiography technique for a typical view plane angle are shown in Figures 5.11 and 5.12. The darker regions at the bottom ends of the devices were again from attenuation of the incident beam caused by scattering from the rotating table and motor components. The soot deposition measurements were performed here for the entire tube length except for 2 cm at the bottom end of the device. The inlet end of the tube was at the top in these images. The neutron attenuation through the inlet headers in the top ends of the tubes varies over time indicating that the attenuation was due to the soot deposition in the headers. The attenuation increased with time and was larger in the higher flow rate case. This was checked by visually inspecting and photographing the top surface of the device after the neutron radiography test had been completed.

The images were analyzed to determine the change in the intensity along the length of the tubes. Typical results for the single-tube devices tested for 5 hours are shown in Figure 5.13. There is a clear difference between the clean tube and the two tubes that had been soot deposited. The ratios of the intensities were then used to estimate the thickness of the soot deposited layer along the centerline of the tube. The profiles of the soot deposition thickness after 5 hours

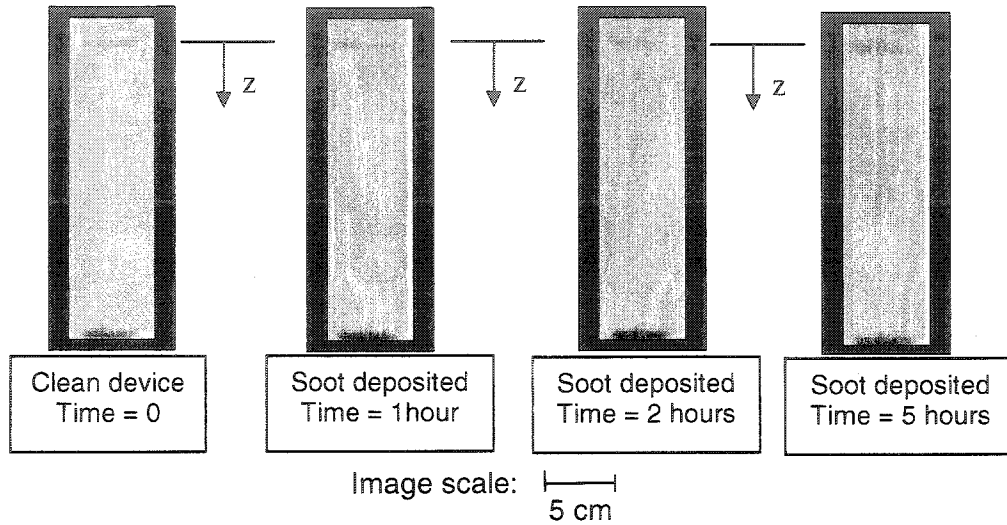


Figure 5.11. Typical neutron images for the single-tube devices tested with a mass flow rate of 0.8 kg/hr ($Re_{\text{initial}}=2000$) and average soot concentration of $C_s=45 \text{ mg/m}^3$. Images at view plane angle $\theta=300^\circ$.

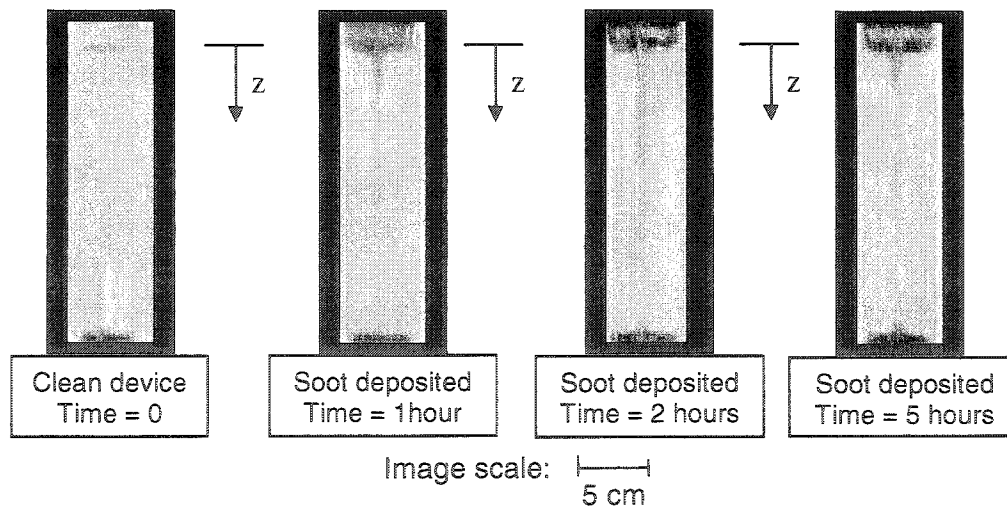


Figure 5.12. Typical neutron images for the single-tube test with a mass flow rate of 2.8 kg/hr ($Re_{\text{initial}}=7000$) and average soot concentration of $C_s=46 \text{ mg/m}^3$. Images at view angle $\theta=300^\circ$.

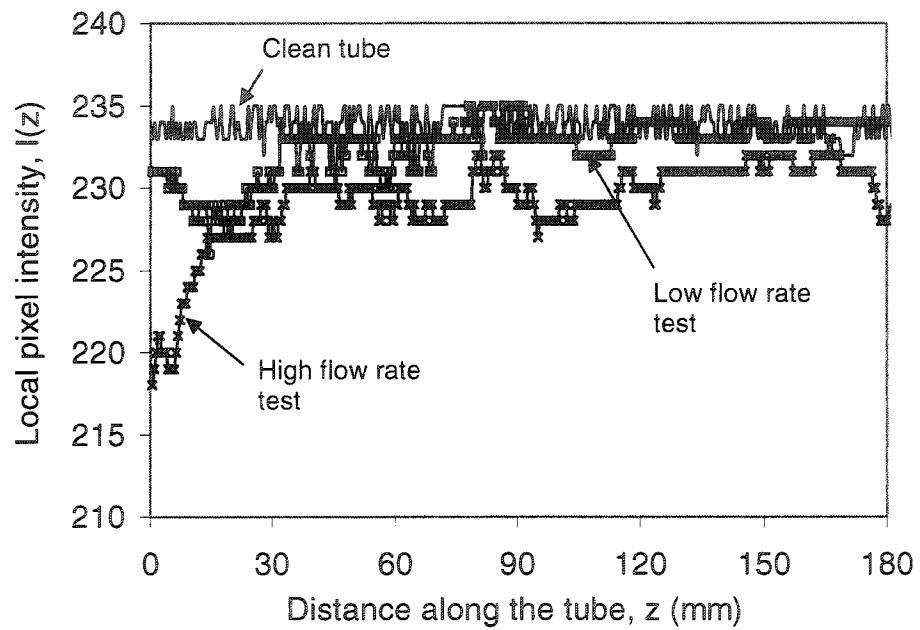


Figure 5.13. Measurement of the intensity along the centerline of the single-tube devices for 5 hour test. Image plane angle $\theta = 300^\circ$.

computed from the 6 different angles examined here, for the gas mass flow rates of 0.8 and 2.8 kg/h are shown in Figures 5.14 and 5.15, respectively. In all these cases, there was a decrease in the deposited soot layer thickness along the length of the tube. The decrease in the soot thickness is more significant in the case of the 2.8 kg/hr mass flow rate. In this case, the most significant soot deposition occurred in the first 25 mm or 4 tube diameters. This is the entrance region of the tube, so the soot deposition in this region depends on how the flow enters the tube. The variation in the soot deposition thickness throughout the rest of the tube is similar in magnitude to the layer itself indicating that the soot layer in the tube is three-dimensional. These variations could be used to estimate the three-dimensional profile of the soot deposition. Here, though, the results from the different angles were simply averaged to compute an average thickness for each longitudinal position.

The change in the circumferentially averaged soot thickness along the tubes for mass flow rates of 0.8 kg/hr and 2.8 kg/hr are shown in Figures 5.16 and 5.17, respectively. In both cases, the soot profiles in the entrance region of the tube are much thicker than in the remainder of the tube. The soot deposition in the entrance regions appears to extend further downstream after 5 hours of testing for a flow rate of 0.8 kg/hr than it does for a flow rate of 2.8 kg/hr. This is not unexpected because laminar flow typically has a longer developing region than turbulent flow. The thickness of the soot deposition layer is much larger for

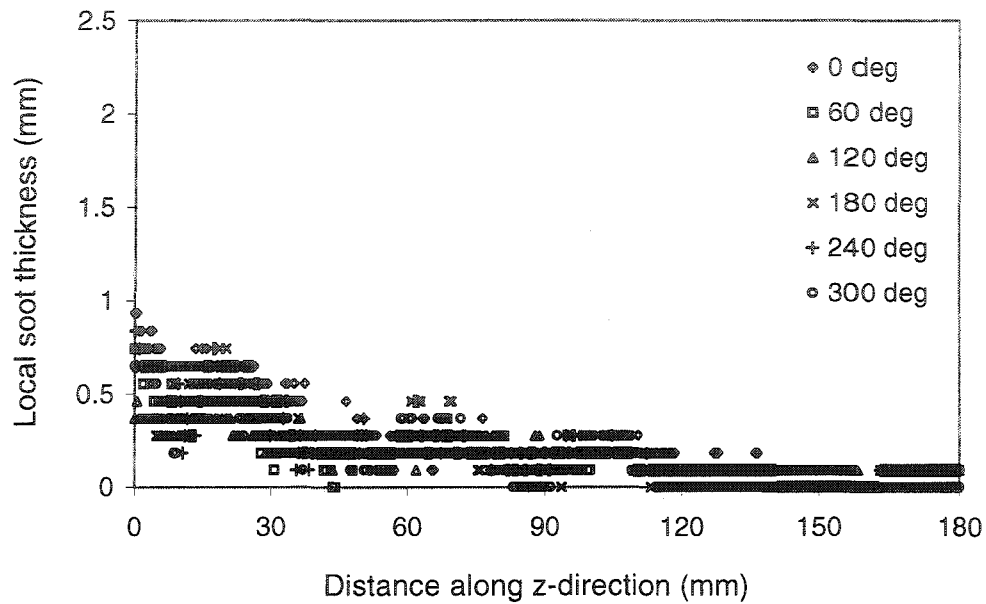


Figure 5.14. Profiles of local soot thickness along the tube at different angular position θ for the 5 hour single-tube test with a mass flow rate of 0.8 kg/hr and $C_s = 45 \text{ mg/m}^3$.

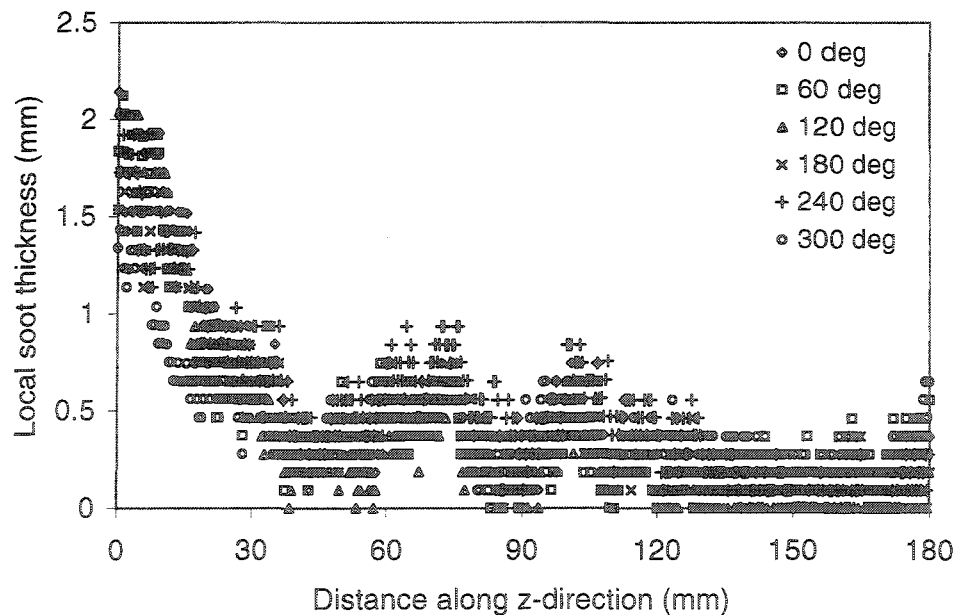


Figure 5.15. Profiles of local soot thickness along the tube at different angular position θ for the 5 hour single-tube test with a mass flow rate of 2.8 kg/hr and $C_s = 46 \text{ mg/m}^3$.

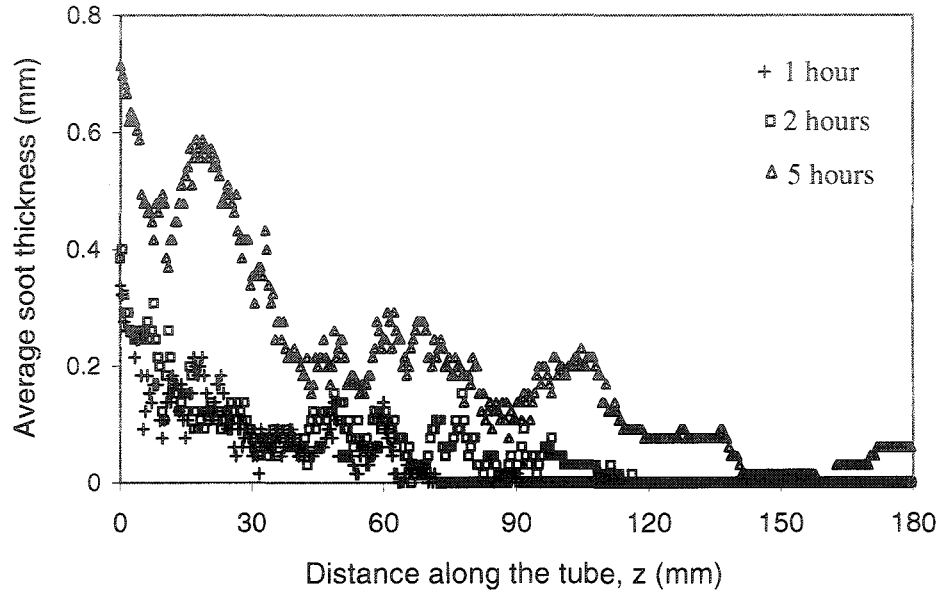


Figure 5.16: Variation in the circumferentially averaged soot thickness with time for the single-tube test with a mass flow rate of 0.8 kg/hr and $C_s = 45 \text{ mg/m}^3$.

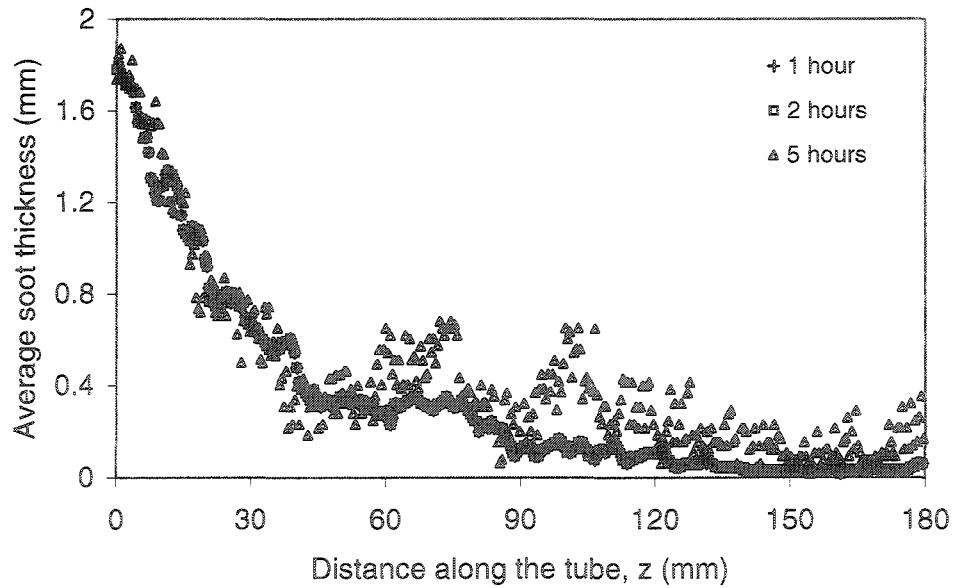


Figure 5.17: Variation in the circumferentially averaged soot thickness with time for the single-tube test with a mass flow rate of 2.8 kg/hr and $C_s = 46 \text{ mg/m}^3$.

the higher flow rate turbulent case than it is for the lower flow rate laminar case, both in the entrance region and throughout the tube. This was anticipated because the flow rate was higher and the temperature difference between the gas and tube wall was higher for the 2.8 kg/hr flow rate. This larger temperature difference could enhance the soot deposition by means of thermophoresis (Davis, 1966).

One of the most interesting features in the soot deposition profiles is the wave-like or corrugated structure exhibited in both flow regimes particularly in the midsection of the devices and more importantly for the high flow turbulent test. This pattern was likely initiated by the thermophoretic effect due to variation of the temperature gradient of the flow around the tube. This might be later caused by re-entrainment and re-deposition of the soot from the entrance region due to locally shearing effect or unsteady turbulent burst (Abu-Qudais and Kittelson, 1997). This corrugated structure was not reported in previous investigations of soot deposition layers, but this type of pattern is commonly observed in horizontal two-phase powder stratified flow, such as a moving bed pattern due to gravity (Hetsroni, 1982). This large-scale roughness would have a significant impact on the performance of the device particularly for turbulent flows. For example, after 5 hours with a mass flow rate 2.8 kg/hr, the ratio of the large-scale roughness to tube diameter on the order of 0.01 to 0.05. For a single-phase turbulent flow, this degree of roughness might be expected to increase the

pressure drop by up to 100% relative to the smooth pipe, and enhance the convective heat transfer from the gas to the soot-deposited film. For laminar flow, the pressure drop is not as significantly affected by the roughness as for turbulent flow. The total thickness of the soot deposition layer at the entrance was up to 50% of the tube diameter for the higher flow rate case that would block approximately 75% of the entrance area. The flow through this restriction would result in a significant pressure drop and would likely cause an extended flow separation in the region downstream of the tube entrance. The flow in this region will depend on the geometry of the end face of the header, where the tube is mounted, and changes as the soot deposits on the header face and tube inlet. The initial flow constriction causes the flow to accelerate and then decelerate as it passes through the entry region that would tend to cause gas-particle separation, known as venturi effect (Rudinger, 1980), that may increase the soot deposition in the entry region.

The soot deposition in the inlet header was also examined directly after the neutron radiography test was performed. Optical images of the soot deposition in the inlet header for the 5 hour test with a mass flow rate of 2.8 kg/hr are shown in Figure 5.18. It is clear there is a significant build up of soot that created an annular cone on the end face. The soot deposition would act to increase the radius of curvature at the inlet of the tube that may reduce the flow separation that occurs just inside of the tube. The soot build up on the end face

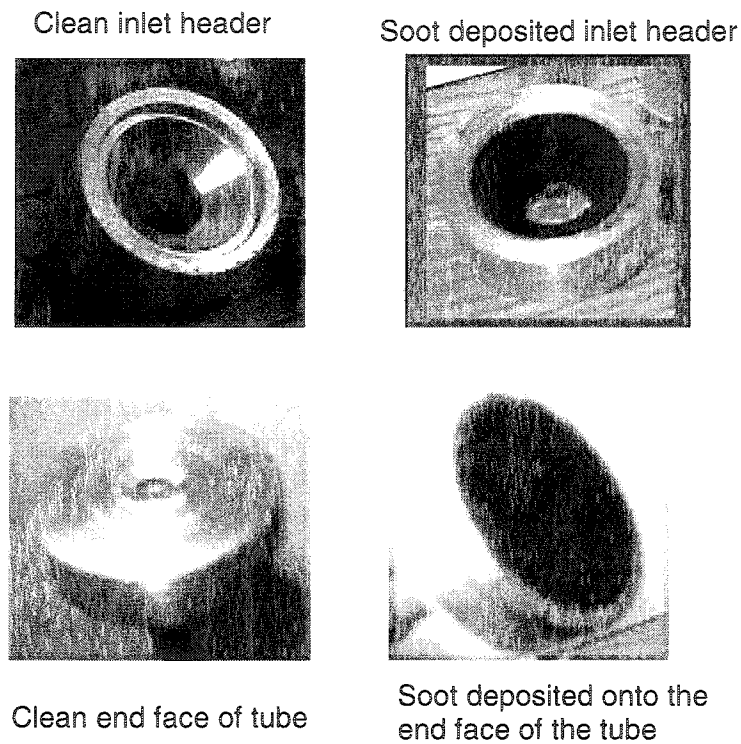


Figure 5.18. Photographs of the inlet header for the single-tube test with a mass flow rate of 2.8 kg/hr after 5 hours.

of the header can be due to deposition of the soot particles via turbulent impaction process (Soo, 1967).

Measurements were also performed for bundles of three tubes with an inner diameter of 4.1 mm, a length of 205.0 mm, and two different expansion angle inlet headers of 60° and 45°. The gas mass flow rates for these tests were all 6.0 kg/hr which corresponded to a nominal Reynolds number in the tubes of approximately 8000. The three-tube devices were exposed to diesel exhaust gas for 3 hours when the engine load was approximately 2.8 kW, and the inlet gas temperature was 210 ± 5 °C and average soot mass concentration of 46 to 47 mg/m³. The secondary side average inlet coolant temperature was approximately 25 °C and coolant flow rate was maintained at 2.5 l/min.

The typical neutron images for the bundles positioned at a view plane angle 0° are shown in Figure 5.19. The variation of the averaged soot thickness along the tube bundles with the 60° and 45° expansion angles inlet headers determined from these images are shown in Figures 5.20 and 5.21, respectively. The results show that the average soot thickness at the inlet of the tube bundles varied between 1.0 and 1.2 mm for the two devices and dropped to about one-half of this value in the first 4 to 5 diameters of the tube. The soot thickness then decreased more gradually for the remaining tube length. The entrance region for the 60° expansion inlet header was longer than the EGR cooling device with the 45° expansion inlet header. The amount of soot deposition at the tube entrance

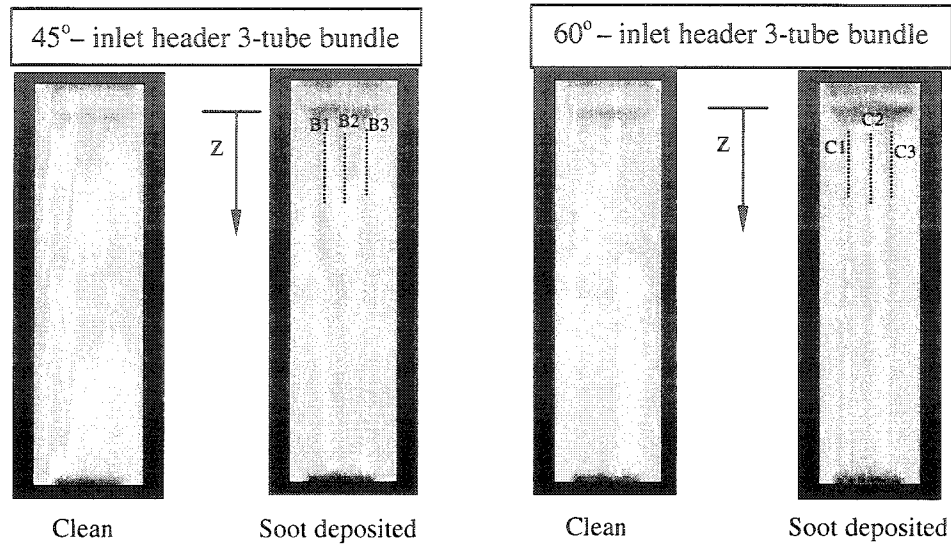


Figure 5.19. Typical neutron images for the three-tube test with a mass flow rate of 6.0 kg/hr ($Re_{initial}=8000$), and soot mass concentration of $C_s = 46-47 \text{ mg/m}^3$.

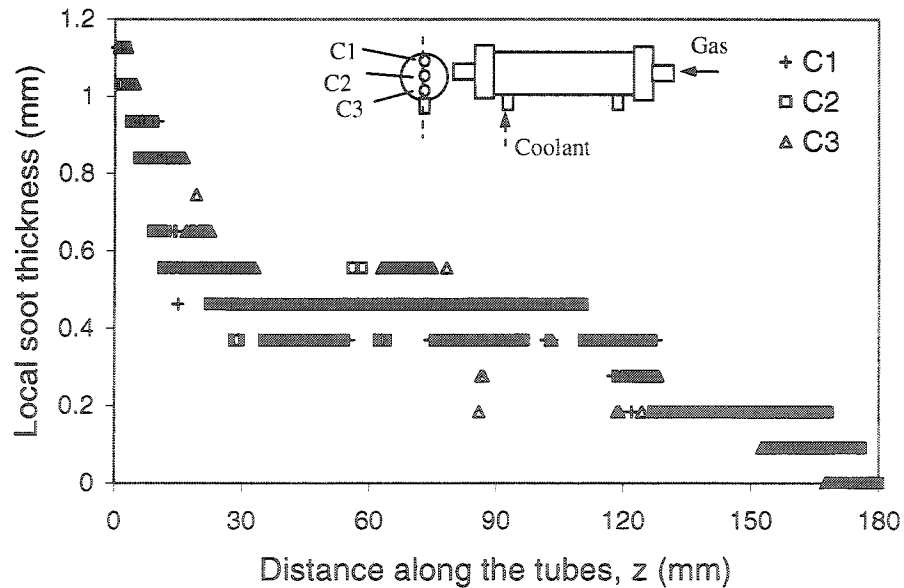


Figure 5.20. Change in the soot thickness profiles along the three-tube device with 60°-inlet header. Total gas mass flow rate = 6 kg/hr, $C_s = 46 \text{ mg/m}^3$, and 3 hours soot deposition.

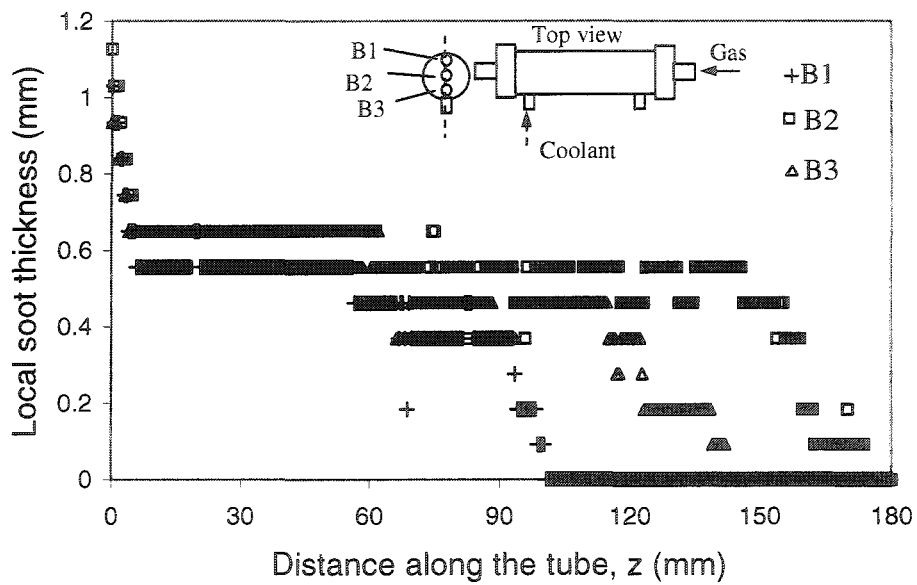


Figure 5.21. Change in the soot thickness profiles along the three-tube device with 45°-inlet header. Total gas mass flow rate = 6 kg/hr, $C_s = 47\text{mg/m}^3$, and 3 hours soot deposition.

resulted in a reduction in the cross-sectional flow area of the tube by approximately 41% causing a considerable restriction to the flow. The soot deposition was approximately evenly distributed in the tube bundle with the 60° expansion angle inlet header device as shown in Figure 5.20. This suggests that the flow may be more evenly distributed in the tube bundle. The soot deposition was unevenly distributed in the tube bundle of the EGR cooling device with the 45° expansion angle inlet header as shown in Figure 5.21. In particular, the soot seems to deposit more in the center tube, B2, than the outer ones, B1 and B3. This may be due to a maldistribution of the flow passing through the different tubes that depended on the expansion angle inlet header. Also, there was a difference in the distribution of the soot deposited profiles in the outer tubes, B1 and B3, in the region where the coolant entered the cooling device as shown in Figure 5.21. Thus, measurements were performed here to investigate the thermal characteristics of the secondary coolant flow across the three-tube EGR cooling device using the IR thermal camera system. Thermal images were acquired from top and side views of the three-tube EGR cooling devices at 0, 1, 2, and 3 hours, and then analyzed to determine the time-dependent temperature distribution for the coolant flow across the cooling device. Here, the coolant temperature was determined at cross sections spaced equally every 20 mm along the cooling device from top and side views of the cooling device shown in Figure 5.22. The results determined from the thermal images show that

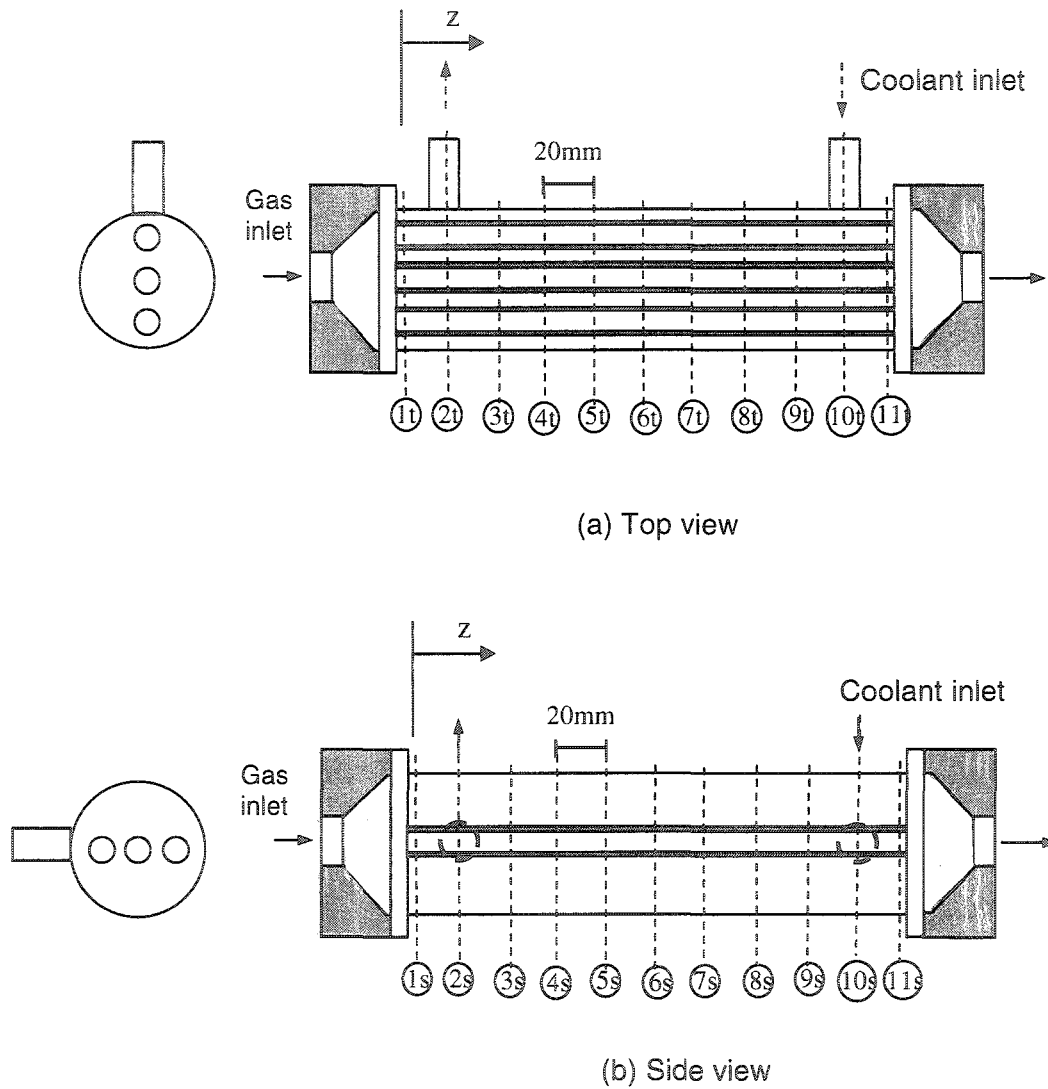


Figure 5.22. Schematic of the three-tube EGR cooling device; (a) top view and (b) side view, and the selected sections across the cooling device used to determine the temperature distribution from the thermal images.

the temperature distribution during 3 hours test decreases along the cooling device from the gas inlet region to the region near the coolant inlet as shown in Figure 5.23. Similar trends were observed for the 0, 1, and 2 hours tests as shown in Figures I.1 to I.3 of Appendix I. The results also show that the coolant flow temperature increases towards the gas inlet section. This temperature profile for the coolant flow at a particular cross section of the three-tube cooling device could cause differences observed in the soot deposition due to differences in the thermophoretic effect in the three tubes at that particular location that eventually caused the non-symmetric soot deposition profiles in the three-tube bundle shown in Figure 5.21. The significance of the soot deposition due to thermophoretic effect was assessed here using the non-dimensional thermophoresis parameter σ_p evaluated using Eq. (3.21) and the estimation of the tube wall temperature T_w at the gas inlet of the cooling device from the temperature data determined from the initial thermal images. The results indicate that $|\sigma_p|$ is on the order of 10^4 , so it is much greater than unity, thus confirming that thermophoresis was a significant effect for the soot deposition that occurred in the EGR cooling devices.

The neutron images were also analyzed to quantify the soot deposition in the inlet headers with 45° and 60° expansion angles. A schematic diagram for the sectioned slices along x-direction at different locations along the tube header in

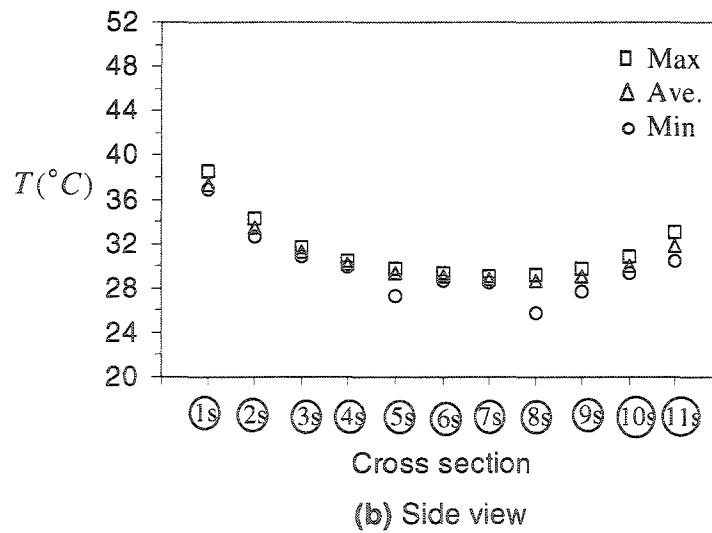
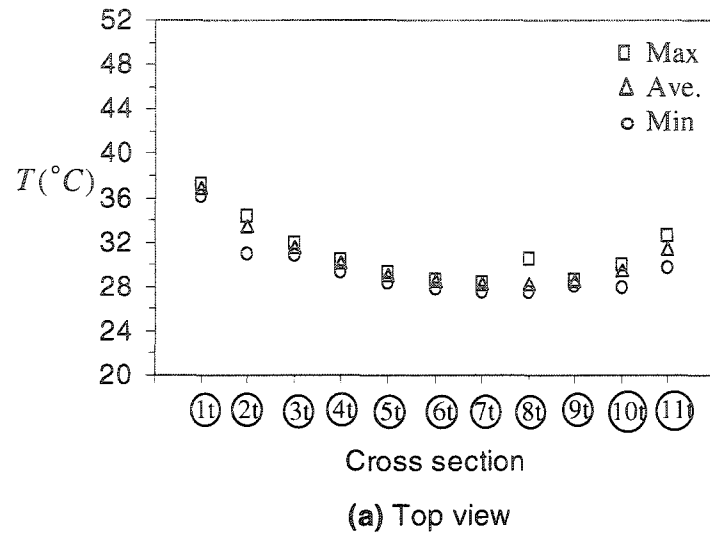


Figure 5.23. Change in the coolant shell temperature profile at different cross sections along the three-tube cooling device determined from the thermal images of the (a) top view and (b) side view during 3 hours test for the coolant flow rate of 2.5 l/min.

the y-direction is shown in Figure 5.24. The results of the two headers are shown in Figures 5.25 and 5.26. For the inlet header with the 60° expansion angle, the soot thickness increased monotonically from 0.4 to 1.2 mm suggesting the soot deposition was relatively uniform. The soot thickness in the header with the 45° expansion angle was more uniform varying from 0.5 to 0.7 mm. The circumferential variation of the soot thickness in the header was small with relatively more uniform soot deposited layers. Optical images of the soot deposition in the two different design inlet headers are shown in Figure 5.27. It can be noted that soot builds up more around the center tube in a conical form for the 45° -inlet header whereas it tends to be more uniform with the surface for the 60° -inlet header.

The fully-dispersed dilute flow model given by the one-dimensional equations in Table (3.1) and Eqs. (3.24) through (3.29) was used to predict the soot deposition profiles in the single-tube EGR cooling device. The predictions were compared with the measurement results from the neutron radiography images as shown in Figure 5.28 for the 5-hour test with gas flow rate 0.8 kg/hr and average soot mass concentration 45 mg/m^3 . The inlet gas temperature was 120°C and the inlet coolant temperature and flow rate were 25°C and 1 l/min. The predictions show that the soot deposited layer thickness decreased monotonically along the cooling device. However, the present model underpredicted the soot deposited layer thickness at the entrance of the cooling

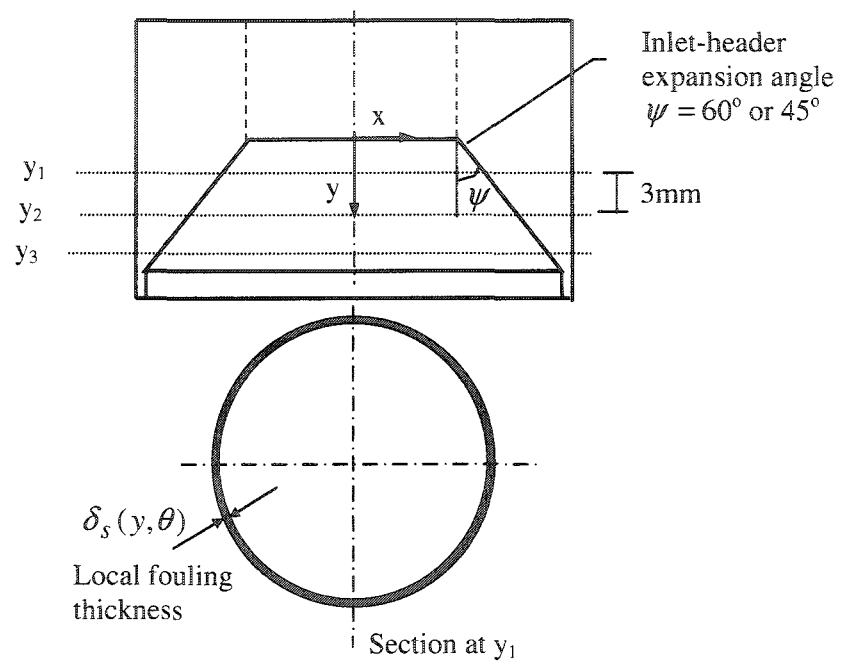


Figure 5.24. Schematic diagram showing a section of a soot-deposited layer inside a three-tube inlet header.

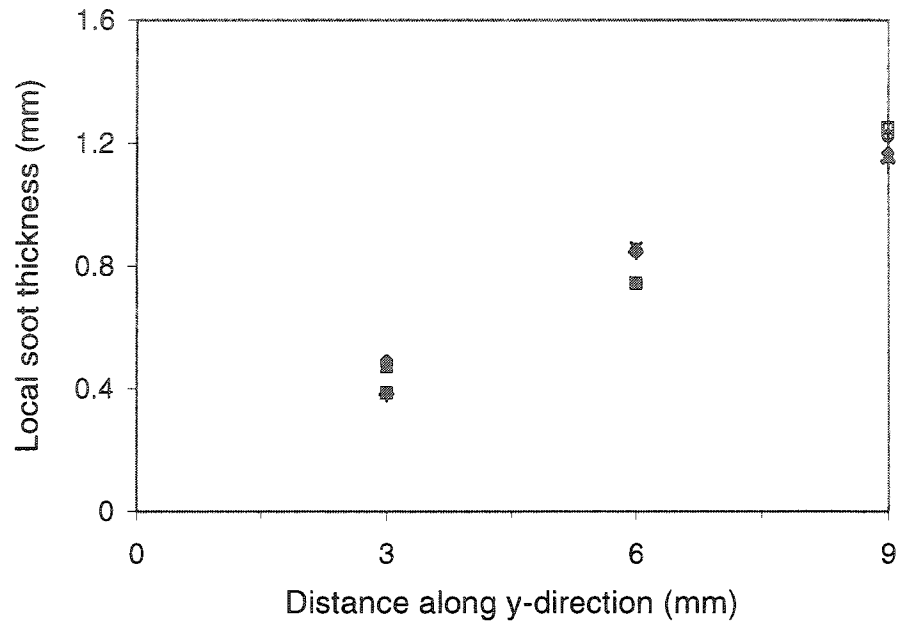


Figure 5.25. The change in the local averaged soot deposition inside the 60° expansion angle inlet header. Image view angles: ◇ 0° □ 60° △ 120° × 180° +240° ○ 300°.

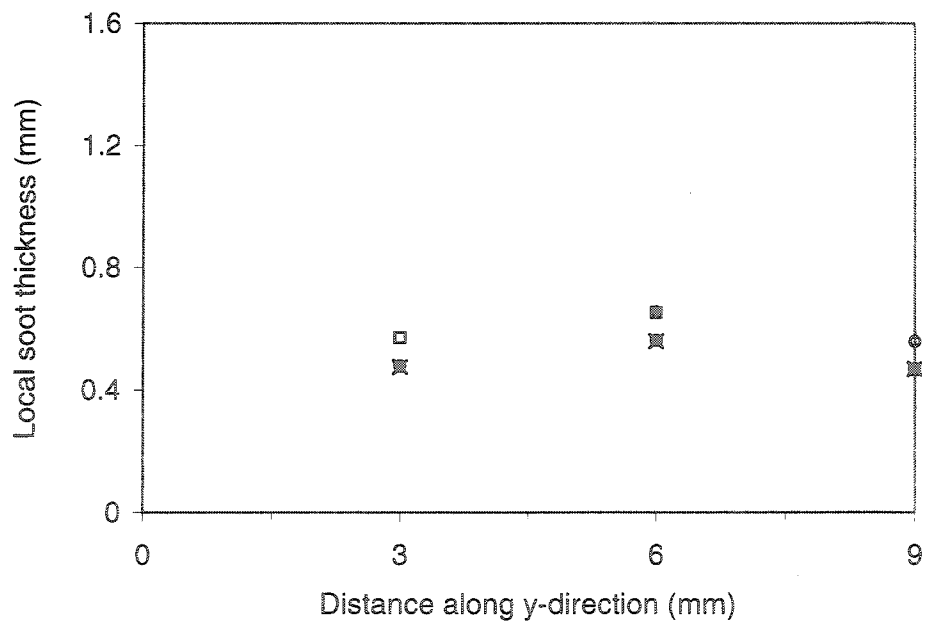


Figure 5.26. The change in the local averaged soot deposition inside the 45° expansion angle inlet header. Image view angles: ◇ 0° □ 60° △ 120° × 180° +240° ○ 300°.

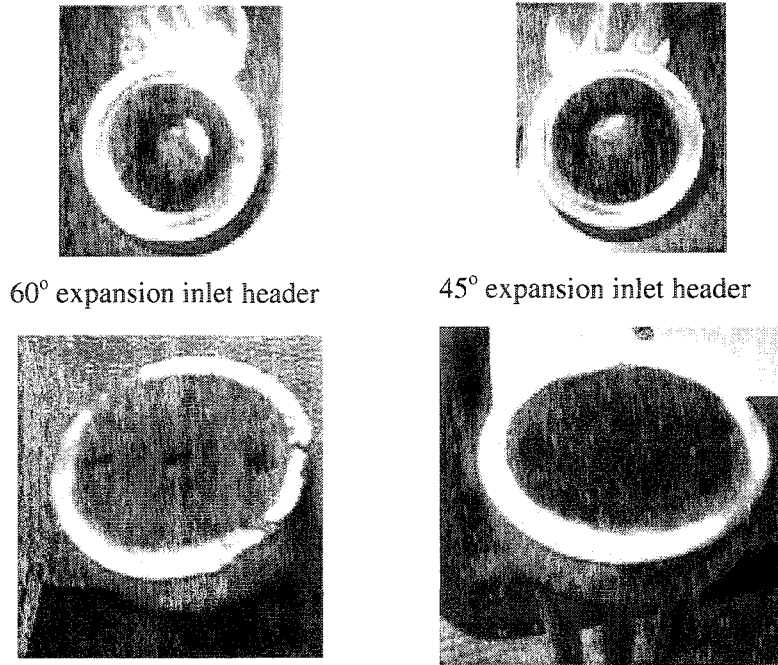


Figure 5.27. Photographs of the soot deposited three-tube cooling devices with their inlet headers.

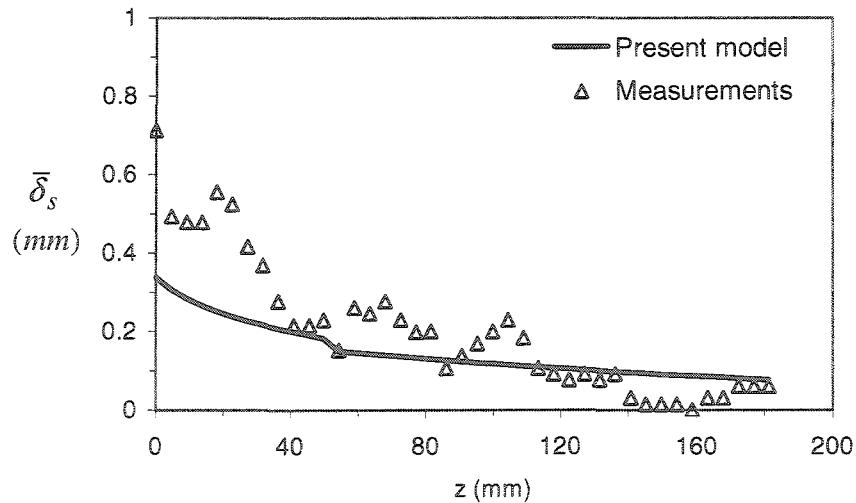


Figure 5.28. Comparison of the averaged soot deposited thickness profiles along the single-tube EGR cooling device measurement using the neutron radiography technique and predicted using the present model. (Gas flow rate= 0.8 kg/hr; 5 hours soot deposition.)

device. This indicates that the soot deposition process was influenced by the way the exhaust gas entered into the cooling device which tended to alter and seemingly enhance the deposition in the entrance region. The model was not able to predict the waviness in the soot layers observed in the experimental results, nor could it predict the three-dimensionality of the profiles. This is most likely due to the fact that the model is a 1-D model and does not incorporate the re-entrainment of particles and the adhesive interaction of the particles with the tube walls that could have an influence on the deposition process.

The assumption of dilute flow was investigated using the two-phase interactions parameters $\Sigma_{2\phi}$ and Σ_{TH} given by Eqs. (3.15) and (3.16) evaluated using the experimental measurements in the present work. The results showed that these parameters were on the order of 0.001 for soot particle size of $0.1 \mu m$ for the lower and higher flow rates regimes considered here since the particle number density was approximately 10^{10} #pt./m³ in the present case. The values of the interaction parameters, however, were found to be on the order of 0.1 for agglomerated large soot particles size of $20 \mu m$. Thus, the assumption for the dilute flow model used here would be valid only for soot particles near $0.1 \mu m$ in size. A more comprehensive and sophisticated multi-dimensional modeling (with $\Sigma_{2\phi} \geq 1$ and $\Sigma_{TH} \geq 1$) that incorporates re-entrainment process is recommended in future investigations.

CHAPTER 6: The Heat Transfer and Pressure Drop Characteristics of the EGR Cooling Devices

In this chapter, the experimental results of the heat transfer and pressure drop characteristics in the single-tube and three-tube EGR cooling devices during the soot deposition tests are presented and discussed.

6.1 The Single-Tube EGR Cooling Devices

The time-dependent heat transfer and pressure drop performance characteristics that occurred in the tubes of EGR cooling device exposed to diesel exhaust in the EGR loop of the diesel engine facility were investigated using the single-tube EGR cooling devices for exhaust flow rates of 0.8 kg/hr and 2.8 kg/hr. The change in the exhaust gas temperature, ΔT_g , across the cooling device during the 1, 2, and 5 hour tests for the flow rate 0.8 kg/hr and average soot mass concentration 45 mg/m^3 is shown in Figure 6.1. The change in the gas temperature across the cooling device was approximately 77°C at the start of the tests, and then decreased to approximately 72°C after the first hour, 69°C over the second hour, and 65°C over 5 hours. The coolant temperature rise across the single-tube EGR cooling device was approximately 0.25 and 0.3°C for these

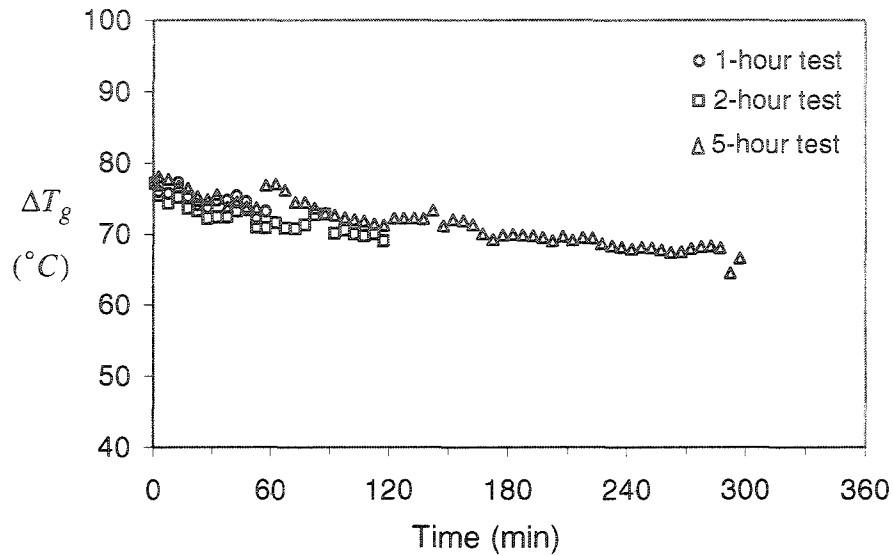


Figure 6.1. Change in the gas temperature drop with time across the single-tube EGR cooling device during 1, 2, and 5 hours tests for the gas mass flow rate of 0.8 kg/hr and soot mass concentration of 45 mg/m³.

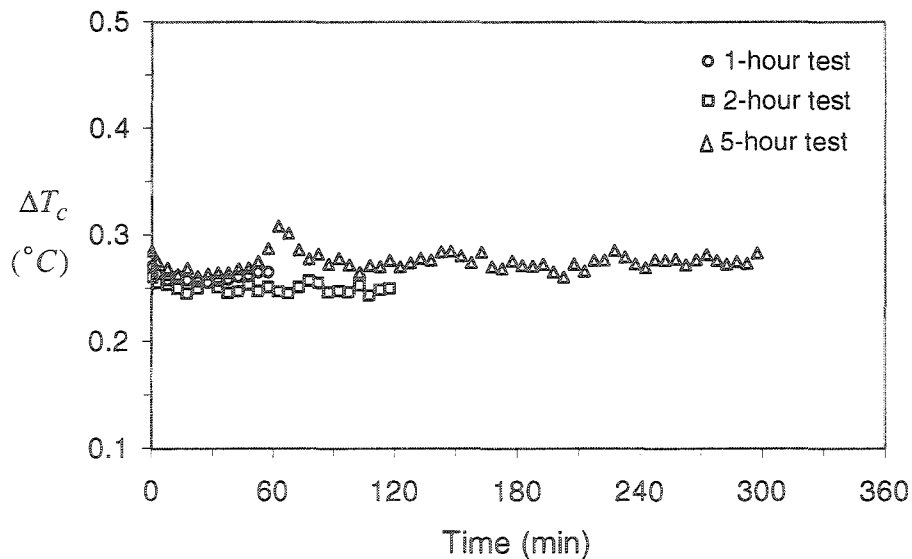


Figure 6.2. Change in the coolant temperature rise with time across the single-tube EGR cooling device during 1, 2, and 5 hours tests for the gas mass flow rate of 0.8 kg/hr and soot mass concentration of 45 mg/m³.

tests as shown in Figure 6.2. There was an increase in the temperature rise/drop across both the coolant and exhaust gas near the end of the first hour. This was caused by an increase in the inlet gas temperature at this point shown in Figure 4.14.

The change in the heat transfer rate for the gas across the single-tube EGR cooling device tested for gas flow rate 0.8 kg/hr calculated from the gas side and the water side are shown in Figures 6.3 and 6.4. The heat transfer rate from the gas side was initially 17 W, it then slowly decreased by up to 14% over the 5 hours of testing. The change in the heat transfer rate in these tests did vary slightly due to the variations in the gas mass flow rate of the tests particularly at 1 hour through the 5-hour test. The heat transfer from the water side was 10-20% larger than that from the gas side over the entire test. The temperature change in the coolant was 0.25-0.3 °C for the tests, so the uncertainty in the heat transfer rate from the water side was within $\pm 36\%$ and the agreement is surprisingly good. The uncertainty in determining the heat transfer rate from the gas was approximately $\pm 5\%$ and was taken as the more accurate measurement of the actual heat transfer rate.

The change in the thermal effectiveness of the EGR cooling device given by (Kays and London, 1984)

$$\varepsilon_{th} = \frac{\dot{Q}_g}{\dot{Q}_{max}} , \quad (6.1)$$

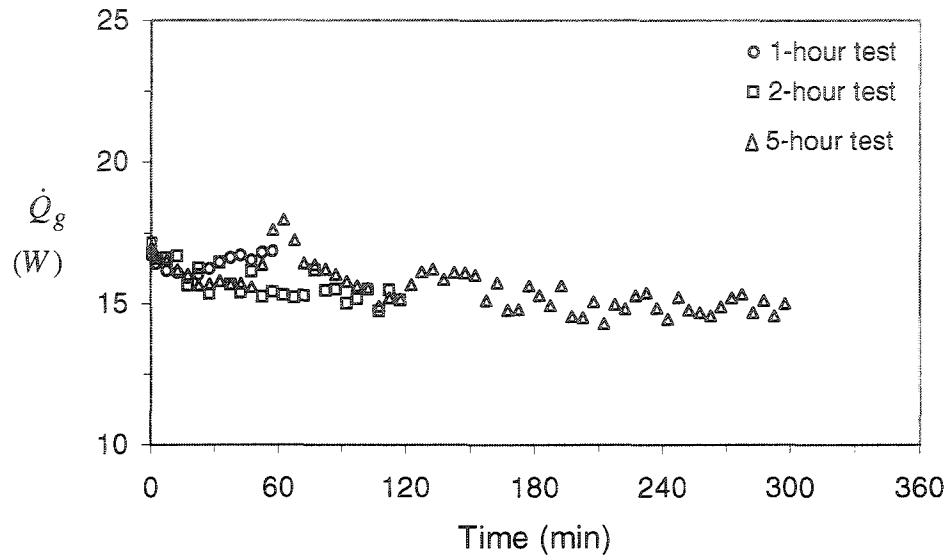


Figure 6.3. Change in the gas heat transfer rate with time for the single-tube EGR cooling device during 1, 2, and 5 hours tests for the gas flow rate of 0.8 kg/hr and soot mass concentration of 45 mg/m³.

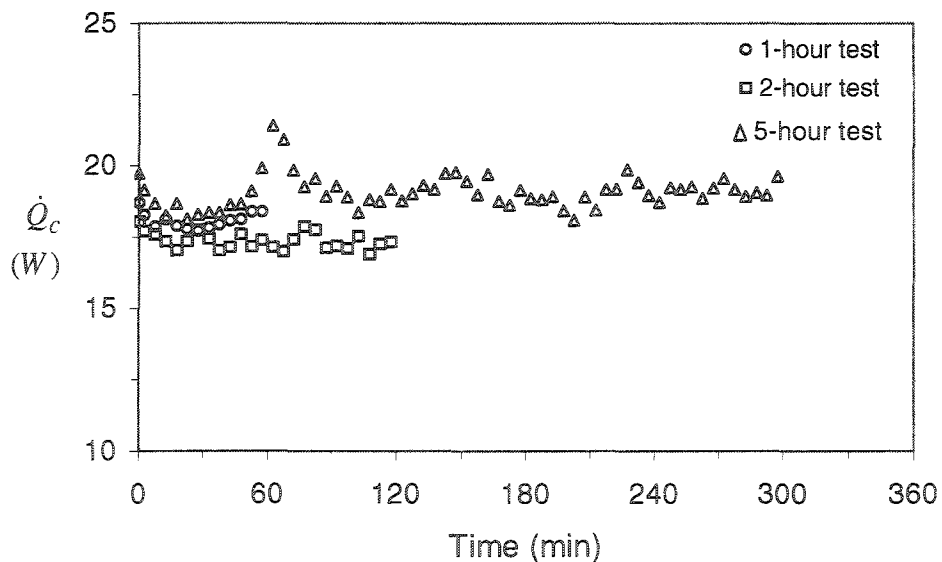


Figure 6.4. Change in the coolant heat transfer rate with time for the single-tube EGR cooling device during 1, 2, and 5 hours tests for the gas mass flow rate of 0.8 kg/hr and soot mass concentration of 45 mg/m³.

where $\dot{Q}_{\max} = (\dot{m}c_p)_g (T_{g,i} - T_{c,i})$, is shown in Figure 6.5. The effectiveness of the cooling device decreased from approximately 81% to 71% over the 5 hours of testing as the soot was deposited in the device.

The change in the average total thermal resistance R_t for the single-tube cooling device tested for 0.8 kg/hr and soot concentration 45 mg/m³ for 1, 2, and 5 hours is shown in Figure 6.6. The total thermal resistance changed from approximately 2.6 to 3.4 °C/W over approximately 2 hours before becoming nearly constant at 3.6 °C/W. This could indicate that the rate of soot deposition and removal from the tube walls became equal so that the soot thickness apparently did not vary significantly after approximately 4 hours. This result was consistent with the measurement of the soot thickness profiles along the single-tube cooling device for this test shown in Figure 5.16. The average soot thickness measured after the 2-hour test was similar to the 5-hour test, particularly beyond the first 5 diameters of the entry region. The wave-like profile of the soot thickness for the 5-hour test in Figure 5.16 could be due to the competitive mechanisms between the rate of soot layer growth to that of removal or re-entrainment in certain localized regions. The thermal resistance due to soot deposition R_s could be characterized by subtracting the initial total thermal resistance, representing the clean condition, from the total thermal resistance at the later time. The change in R_s for the single-tube EGR cooling device tested

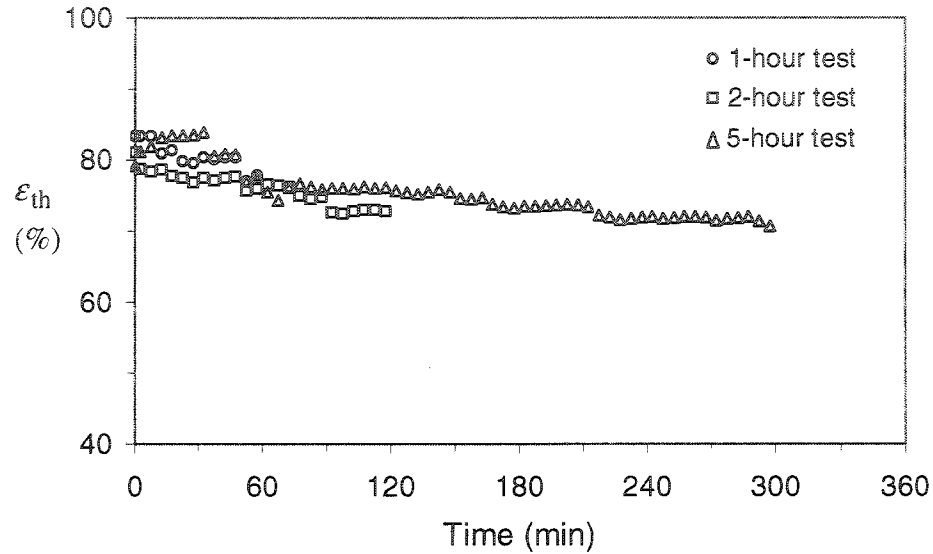


Figure 6.5. Variation in the thermal effectiveness with time for the single-tube EGR cooling device during 1, 2, and 5 hours tests for the gas flow rate of 0.8 kg/hr and soot mass concentration of 45 mg/m³.

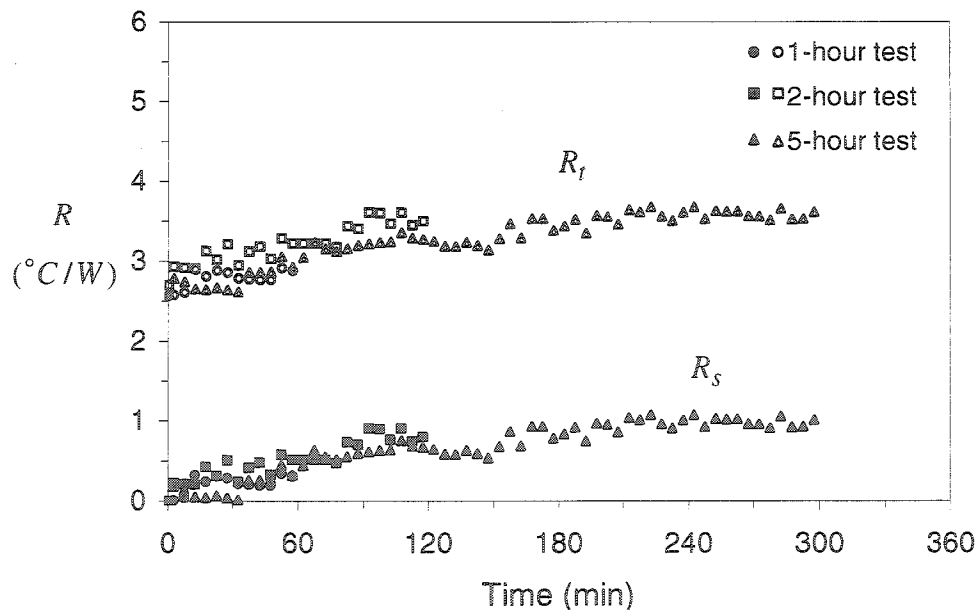


Figure 6.6. Change in the total thermal resistance (R_t), and soot deposition thermal resistance (R_s), for the single-tube EGR cooling device during 1, 2, and 5 hours tests for the gas flow rate of 0.8 kg/hr and soot mass concentration of 45 mg/m³.

for 1, 2, and 5 hours for gas flow rate 0.8 kg/hr and soot concentration 45 mg/m³ is shown in Figure 6.6. It is clear that the soot deposition resistance experienced a typical asymptotic behavior (Kern and Seaton, 1959).

The variation in the pressure drop in the exhaust gas across the single-tube EGR cooling device tested for the gas mass flow rate 0.8 kg/hr and average soot mass concentration 45 mg/m³ is shown in Figure 6.7. The initial pressure drop was between 110 and 120 Pa, but then increased over time by 15–18% over 1 hour, 36% over 2 hours, and up to 68% over 4 hours. The pressure drop was approximately constant after 4 hours of testing. This result was consistent with the experimental results using the neutron radiography technique that indicated the flow area was reduced in the entrance region of the tube due to the soot deposited layer by up to 40% and because of the roughness in the profile during 5 hours of testing.

The performance of the single-tube EGR cooling device was also characterized for the gas mass flow rate 2.8 kg/hr for 1, 2, 5 hours in order to study the effect of flow regime type on the soot deposition in the cooling device. The change in the gas temperature across the single-tube EGR cooling device during these tests is shown in Figure 6.8. The gas temperature difference across the EGR cooling device, was initially 109 °C and then decreased to approximately 84 °C after 2 hours and 58 °C after 5 hours. The change in the coolant temperature varied from approximately 1.1 - 1.5 °C in this case as shown

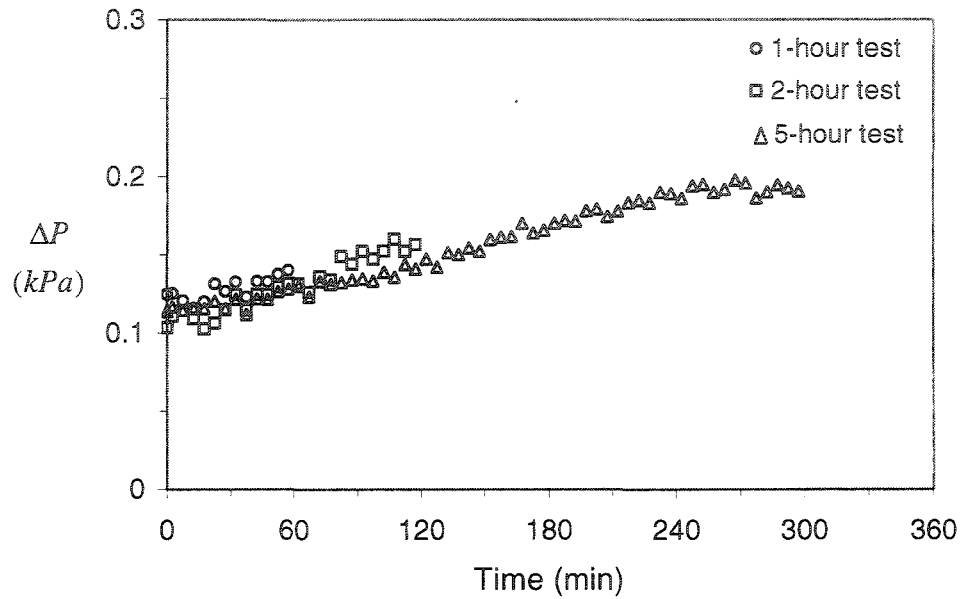


Figure 6.7. Variation in the gas pressure drop with time across the single-tube EGR cooling device during 1, 2, and 5 hours tests for the gas mass flow rate of 0.8 kg/hr and soot mass concentration of 45 mg/m³.

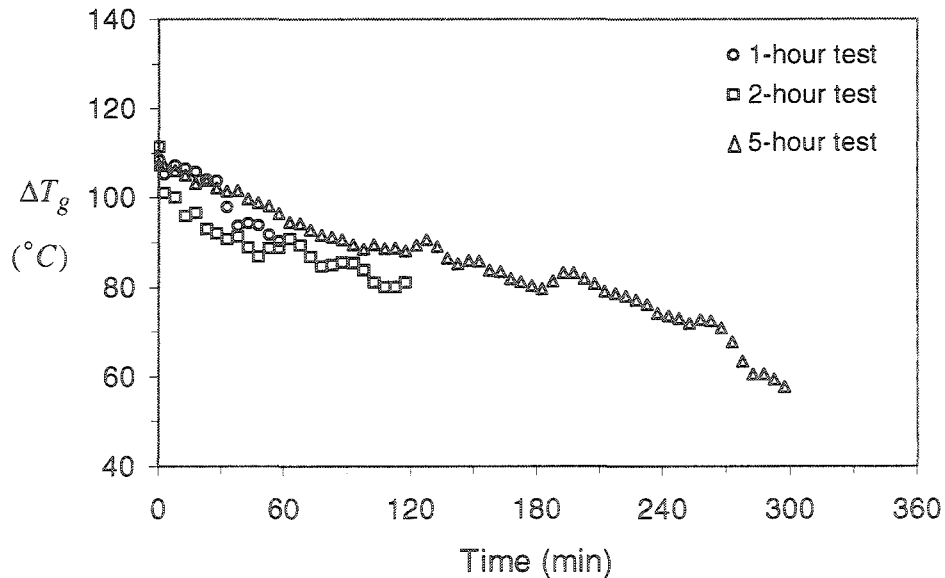


Figure 6.8. Change in the gas temperature drop across the single-tube EGR cooling device during 1, 2, and 5 hours tests for the gas flow rate of 2.8 kg/hr and soot mass concentration of 46 mg/m³.

in Figure 6.9.

The heat transfer rate computed from the exhaust gas for the test with 2.8 kg/hr and soot concentration 46 mg/m³ is shown in Figure 6.10. The gas heat transfer rate consistently decreased over the test reaching approximately 46% of the initial value over 5 hours. The heat transfer from the water side was 10-40% larger than the gas side shown in Figure 6.11. The uncertainty in computing the gas heat transfer rate for the single-tube EGR cooling device tested for 1, 2, and 5 hours for the gas flow rate 2.8 kg/hr was approximately $\pm 5.4\%$.

The change in the thermal effectiveness for the single-tube cooling device tested with 2.8 kg/hr for 1, 2, and 5 hours is shown in Fig. 6.12. The cooling device had an initial thermal effectiveness of 68% and then gradually dropped to approximately 55% in the first hour and 52% in the second hour. The thermal effectiveness then dropped more rapidly to approximately 35% over 5 hours of testing. This is a significant reduction in the thermal performance of the single-tube EGR cooling device that was not seen in the previous test for the lower gas flow rate of 0.8 kg/hr.

The change in the total thermal resistance and the resistance due to the soot deposition for the single-tube EGR cooling device tested for 1, 2, and 5 hours for the gas mass flow rate 2.8 kg/hr and soot concentration 46 mg/m³ is shown in Figure 6.13. The soot deposition thermal resistance initially increased relatively rapidly for 1 hour before slowing down between 1 and 4 hours. It then

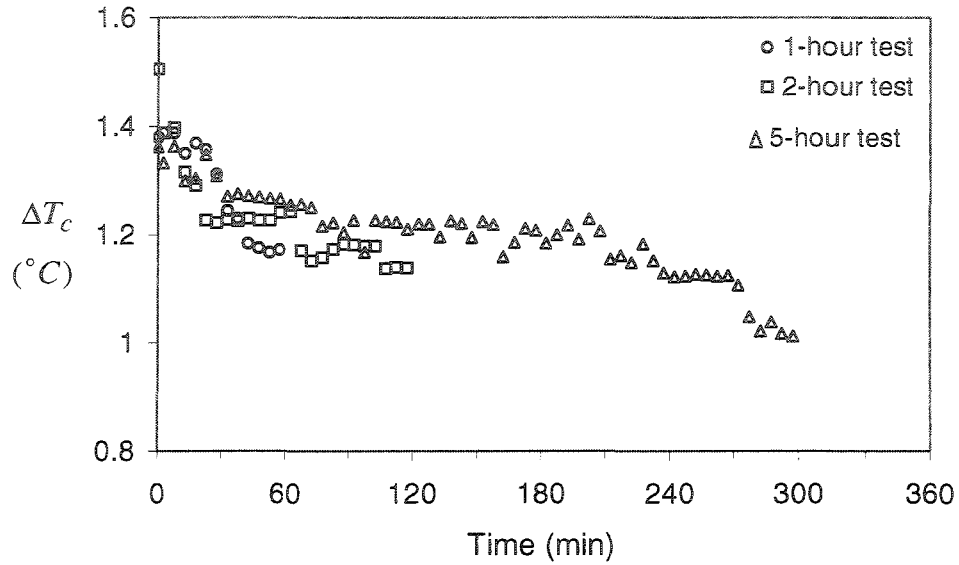


Figure 6.9. Change in the coolant temperature rise with time across the single-tube EGR cooling device during 1, 2, and 5 hours tests for the gas mass flow rate of 2.8 kg/hr and soot mass concentration of 46 mg/m³.

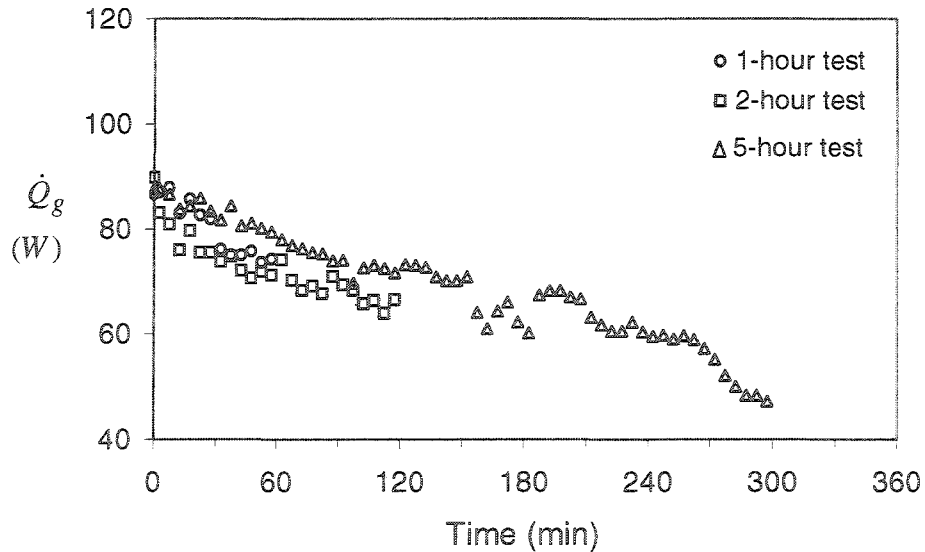


Figure 6.10. Change in the gas heat transfer rate with time for the single-tube EGR cooling device during 1, 2, and 5 hours tests for the gas flow rate of 2.8 kg/hr and soot mass concentration of 46 mg/m³.

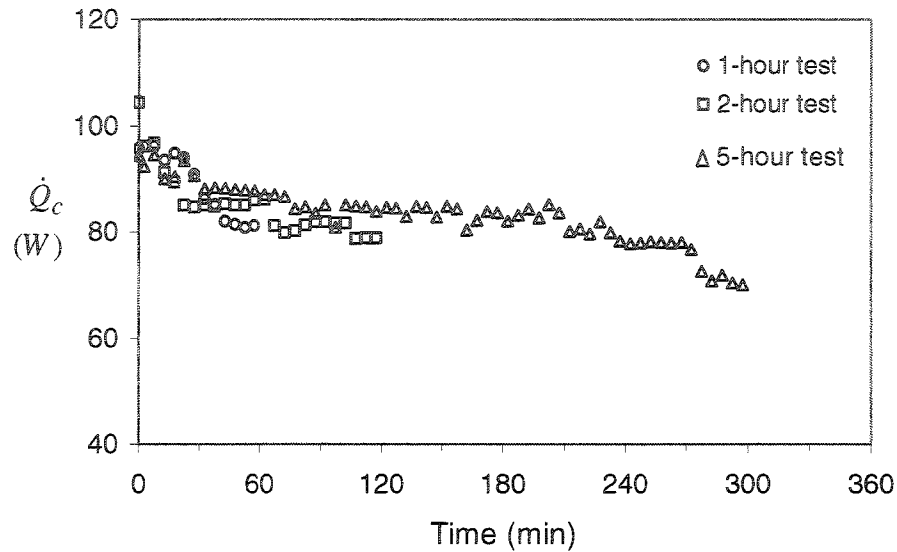


Figure 6.11. Change in the coolant heat transfer rate with time for the single-tube EGR cooling device during 1, 2, and 5 hours tests for the gas flow rate of 2.8 kg/hr and soot mass concentration of 46 mg/m³.

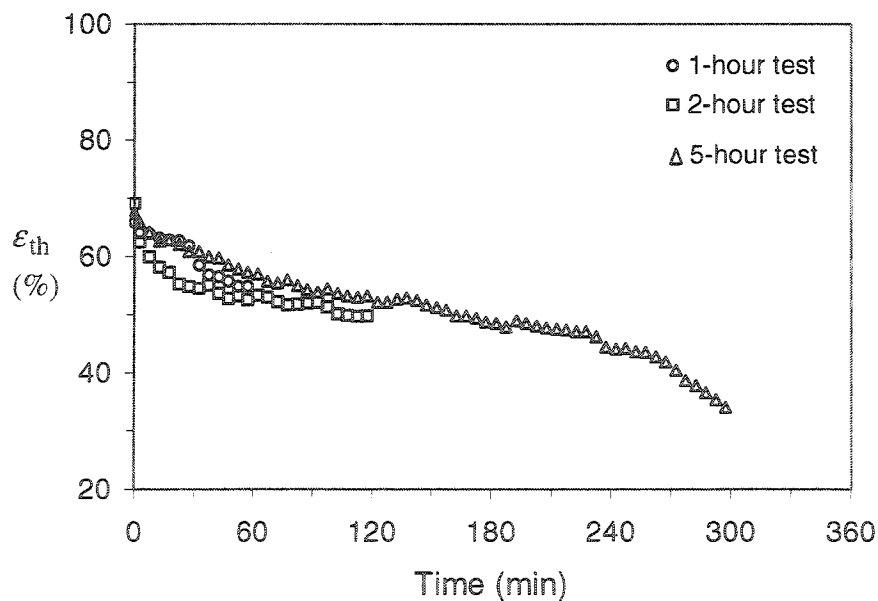


Figure 6.12. Variation in the thermal effectiveness with time for the single-tube EGR cooling device during 1, 2, and 5 hours tests for the gas flow rate of 2.8 kg/hr and soot mass concentration of 46 mg/m³.

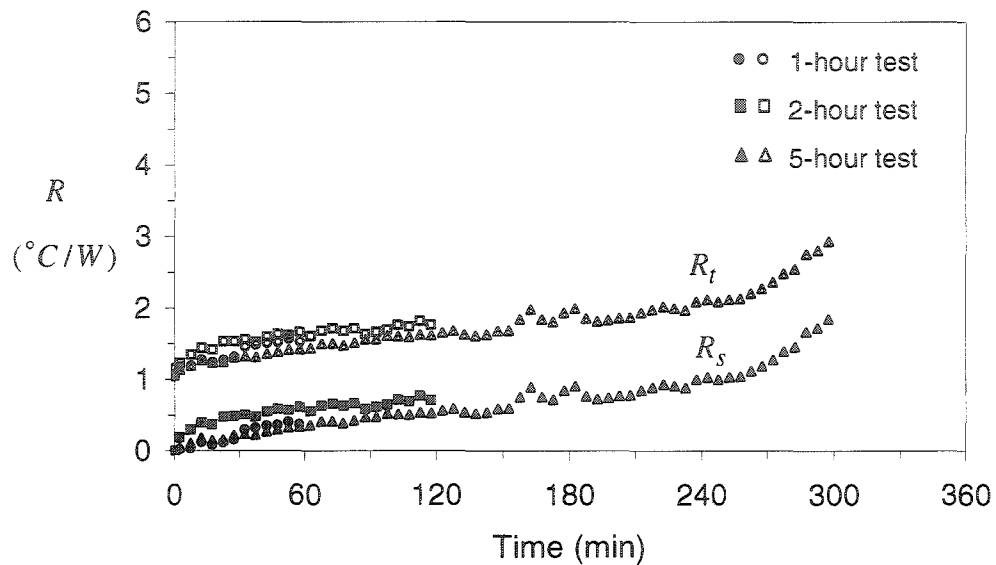


Figure 6.13. Change in the total thermal resistance (R_t), and soot deposition thermal resistance (R_s), for the single-tube EGR cooling device during 1, 2, and 5 hours tests for the gas mass flow rate of 2.8 kg/hr and soot mass concentration of 46 mg/m³.

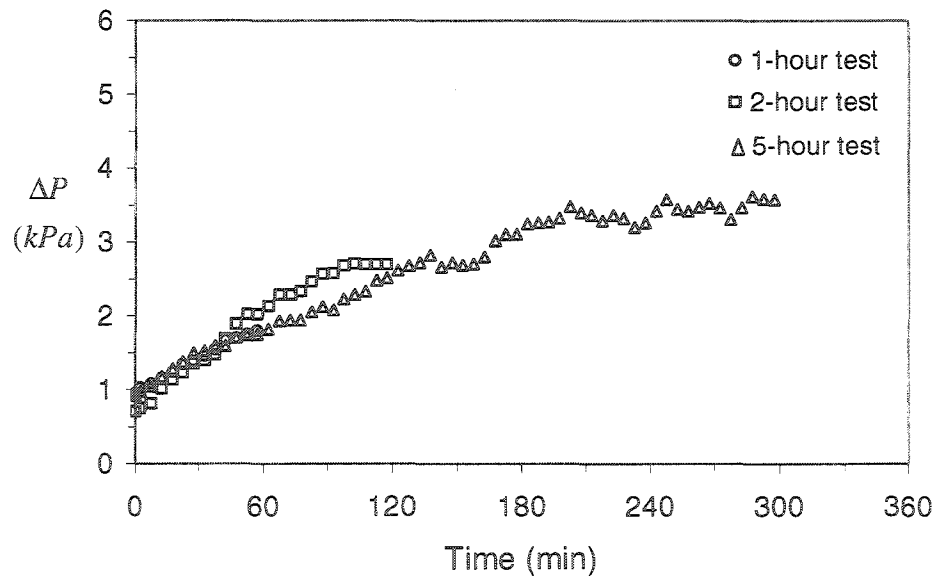


Figure 6.14. Variation in the gas pressure drop with time across the single-tube EGR cooling device during 1, 2, and 5 hours tests for the gas flow rate of 2.8 kg/hr and soot mass concentration of 46 mg/m³.

increased rapidly again after 4 hours. This result seems consistent with the experimental results from neutron radiography shown in Figure 5.17. In particular, the deposited layer thickness was relatively large in the first and second hours which explained the rapid increase in the thermal resistance caused by the deposited soot, R_s , during this period, indicating that the rate of soot deposition or growth was not likely balanced by the rate of re-entrainment of the soot deposited layer over the 5 hours of testing.

The change in the pressure drop in the exhaust gas across the single-tube EGR cooling device tested for 1, 2, and 5 hours for the gas flow rate of 2.8 kg/hr and soot concentration of 46 mg/m³ is shown in Figure 6.14. The pressure drop was initially 850 Pa, and then increased monotonically and rapidly by approximately 100% in the first hour, 150% in the second hour, and was nearly constant 3.6 kPa but with slight fluctuations after approximately 3.5 hours of testing. These fluctuations in the pressure drop may be due to the slight changes in the gas mass flow rate, shown in Figure 4.7, or the effects of re-entrainment and re-deposition of the soot. The results of pressure drop here seem consistent with the results from the neutron radiography in Figure 5.17. In particular, the neutron radiography results indicated that there was significant constriction in the gas flow area in the entry region of the cooling device by up to approximately 75% over 5 hours of testing that caused significant pressure drop in this period.

The results of the thermal effectiveness and pressure drop characteristics for the single-tube cooling device tested with gas flow rate of 0.8 kg/hr for 5 hours were compared with the predictions obtained using the 1-D model of the present study and shown in Figures 6.15 and 6.16. It is clear in this case that the model underpredicted both the change in the thermal effectiveness and pressure drop in the beginning and throughout the test period. The predictions from the model indicated that the thermal effectiveness decreased slightly and more gradually as the soot deposited in the tube, while the pressure drop across the cooling device increased steadily over the 5 hours.

6.2 The Three-Tube EGR Cooling Devices

The three-tube cooling devices with 45° and 60° expansion angles inlet headers tested for 3 hours for the average exhaust gas flow rate 6.0 kg/hr were also characterized to investigate the effect that the inlet header expansion angle had on the heat transfer and pressure drop performance characteristics of the three-tube cooling devices. The comparison in the gas temperature change across the three-tube EGR cooling devices with the 45° and 60° expansion inlet headers is shown in Figure 6.17. The change in the gas temperature drop across the three-tube cooling devices with the 45° and 60° expansion inlet headers differed slightly. In particular, the change in the gas temperature drop across the three-tube cooling device with the 45° angle expansion inlet header decreased

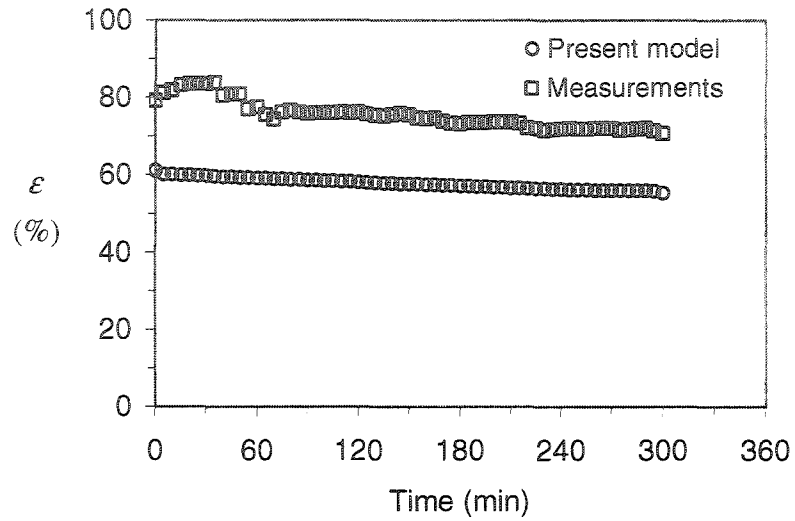


Figure 6.15. Comparison of the change in the thermal effectiveness for the single-tube cooling device tested with gas flow rate of 0.8 kg/hr for 5 hours and from predictions using the present model.

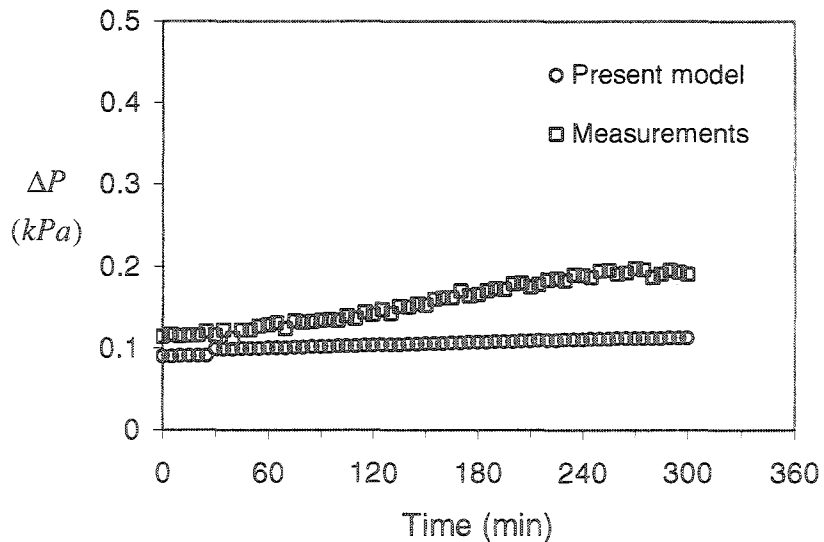


Figure 6.16. Comparison of the change in the pressure drop across the single-tube cooling device tested with gas flow rate of 0.8 kg/hr for 5 hours and from predictions using the present model.

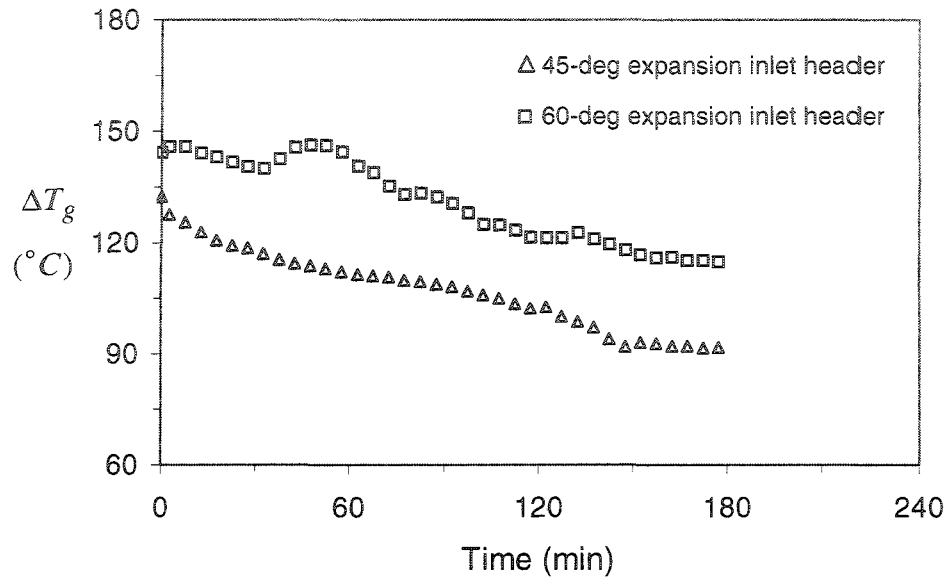


Figure 6.17. Comparison of the variation in the gas temperature drop across the three-tube EGR cooling devices with the 45° and 60° expansion inlet headers during 3 hour tests for the gas flow rate of 6.0 kg/hr and soot mass concentrations of 47 and 46 mg/m³.

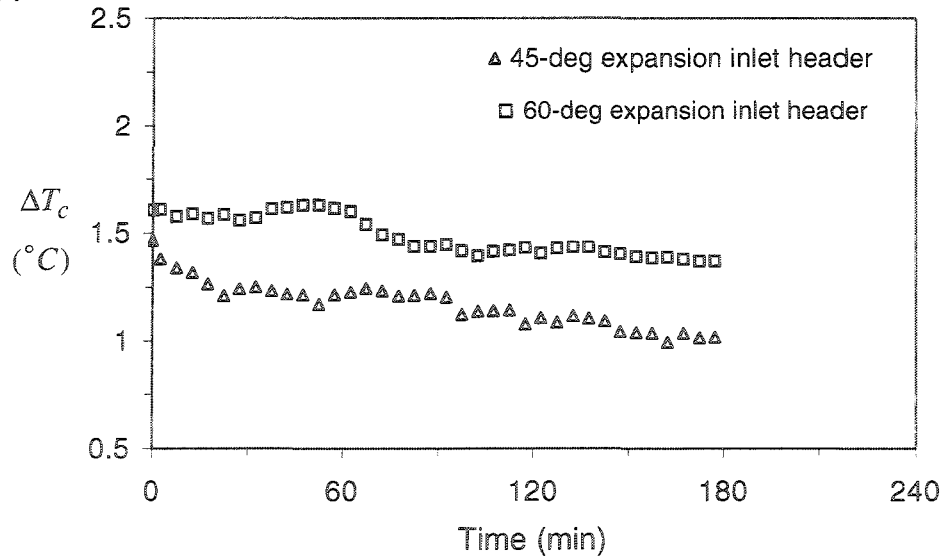


Figure 6.18. Comparison of the variation in the coolant temperature rise across the three-tube EGR cooling devices with the 45° and 60° expansion inlet headers during 3 hour tests for the gas flow rate of 6.0 kg/hr and soot mass concentrations of 47 and 46 mg/m³.

monotonically from approximately 132 °C to 92 °C during the test. The change in the gas temperature drop across the EGR three-tube cooling device with the 60° expansion inlet header decreased slightly from 144 °C to 140 °C in the first 30 minutes of testing, but then increased to approximately 146 °C during the next 20 minutes. The gas temperature change across the three-tube cooling devices continued to decrease monotonically to approximately 115 °C over the 3 hours. The coolant temperature change across the three-tube cooling devices varied between approximately 1 and 1.5 °C for the device with the 45° expansion inlet header, and 1.4 °C and 1.6 °C for the device with the 60° expansion inlet header as shown in Figure 6.18.

A comparison of the heat transfer rate calculated for the gas and coolant sides for the three-tube EGR cooling devices with the 45° and 60° expansion inlet headers tested for 3 hours for the gas flow rate 6.0 kg/hr are shown in Figures 6.19 and 6.20. The heat transfer rate determined from the gas flow rate and coolant flow rate again consistently differed by 10-20%. The results indicate that the change in the gas heat transfer rate for the cooling device with the 60° expansion inlet header was larger than the device with the 45° expansion inlet header at the flow rate of 6 kg/hr during 3 hours of testing as shown in Figure 6.19. This suggests there was more utilization of the heat transfer surface in all three tubes for the cooling device with the 60° expansion inlet header as compared to that with the 45° expansion inlet header. This is not unexpected,

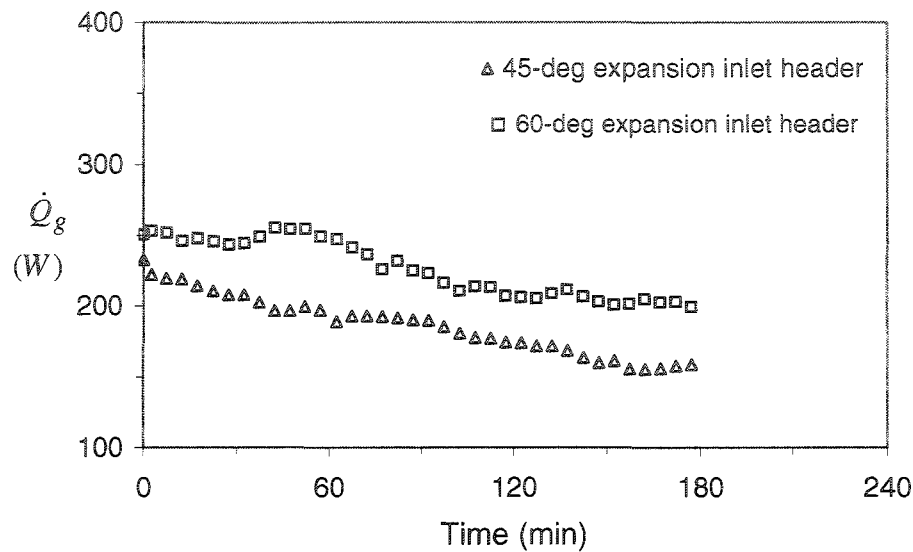


Figure 6.19. Comparison between the change in the gas heat transfer rate in the three-tube EGR cooling devices with the 45° and 60° expansion inlet headers during 3 hour tests for the gas flow rate of 6.0 kg/hr and average soot mass concentrations of 47 and 46 mg/m³.

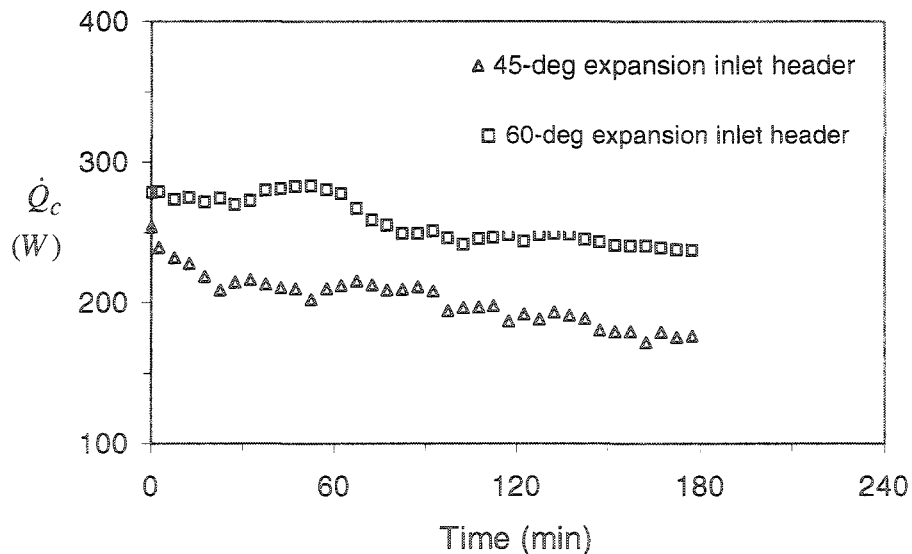


Figure 6.20. Comparison of the change in the coolant heat transfer rate in the three-tube EGR cooling devices with the 45° and 60° expansion inlet headers during 3 hour tests for the flow rate of 6.0 kg/hr and soot mass concentrations of 47 and 46 mg/m³.

since the results from the neutron radiography tests indicated that the soot deposition thickness in the device with the 60° expansion inlet header was less in 3 hours relative to that in the cooling device with the 45° expansion inlet header. The uncertainty in determining the gas heat transfer rate for the cooling devices was approximately within $\pm 5\%$, while the uncertainty in determining the coolant heat transfer rate was approximately within $\pm 8\%$.

The change in the thermal effectiveness in the three-tube EGR cooling devices with the 45° and 60° expansion inlet headers during the 3 hour tests for the gas flow rate of 6.0 kg/hr and soot mass concentrations 47 and 46 mg/m³ is shown in Figure 6.21. The thermal effectiveness of the device with the expansion angle inlet header of 60° was initially significantly larger than the device with the 45° expansion inlet header. The effectiveness also decreased more rapidly for the device with the 45° expansion inlet header during the first hour. The effectiveness of the device with the 45° expansion inlet header decreased more gradually to 58% in the second hour. The effectiveness of the device with the 60° expansion inlet header increased to approximately 82% near the end of the first hour indicating improvement on the thermal performance seen in the heat transfer measurements. The thermal effectiveness in both cooling devices then decreased, but the effectiveness for the devices with the more abrupt 60° expansion angle inlet header at the end of the 3 hours was higher at 65% than for the device with the 45° expansion angle inlet header at 52%. The thermal

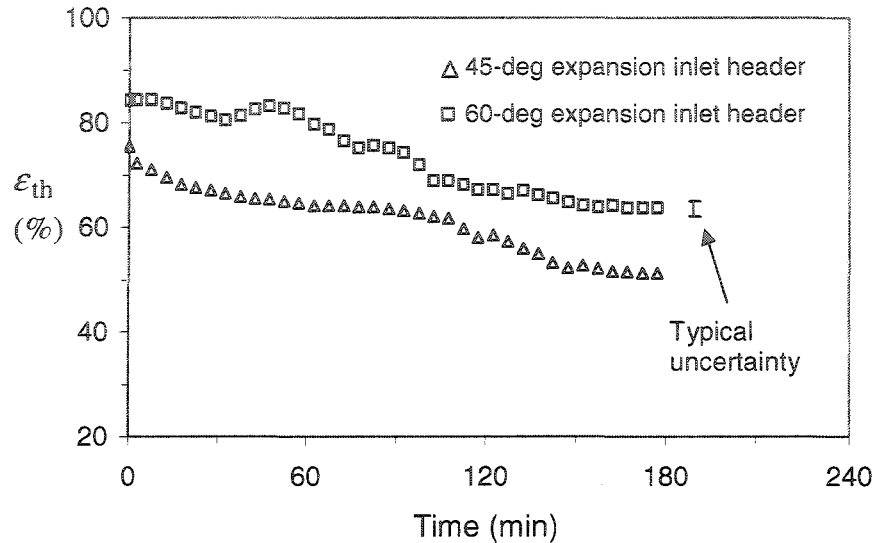


Figure 6.21. Change in the thermal effectiveness in the three-tube EGR cooling devices with the 45° and 60° expansion inlet headers during 3 hour tests for the gas flow rate of 6.0 kg/hr and average soot mass concentrations of 47 and 46 mg/m³.

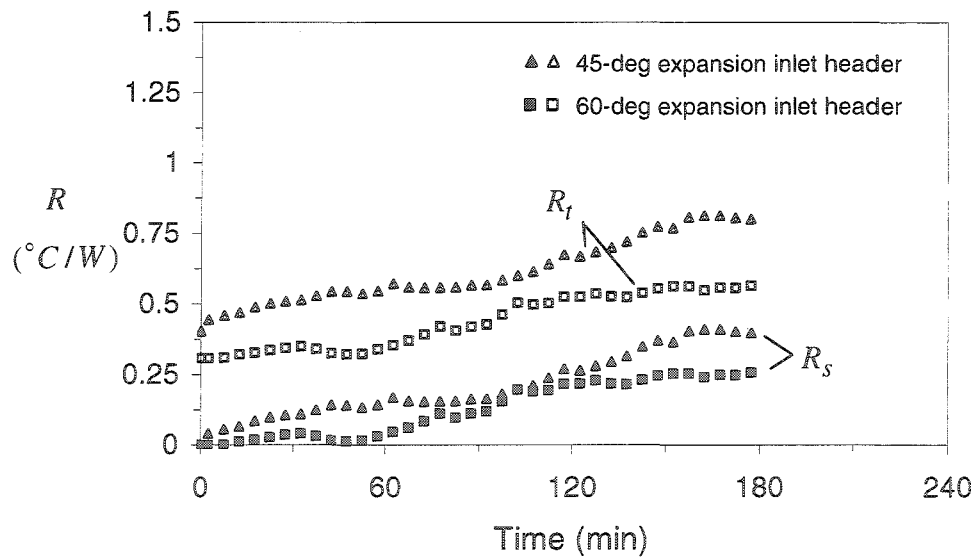


Figure 6.22. Change in the total thermal resistance (R_t), and soot deposition thermal resistance (R_s), in the three-tube EGR cooling devices with the 45° and 60° expansion inlet headers during 3 hour tests for the gas flow rate of 6.0 kg/hr and average soot mass concentrations of 47 and 46 mg/m³.

effectiveness was nearly constant for both the cooling devices for approximately the last 30 minutes of the 3 hour tests.

A comparison in the change of the total thermal resistance and the soot deposition resistance in the three-tube EGR cooling devices with the 45° and 60° expansion inlet headers tested for 3 hours for the gas flow rate 6.0 kg/hr and soot concentrations 47 and 46 mg/m³, is shown in Figure 6.22. The change in the total thermal resistance and the soot deposition resistance were larger and more rapid in the cooling device with the 45° expansion inlet header. The soot deposition thermal resistance in both devices reached an asymptotic value after approximately 2.5 hours of test. At that point, the additional thermal resistance due to the soot deposited layer was 0.4 °C/W in the device with the 45° expansion inlet header as opposed to 0.26 °C/W in the device with the 60° expansion inlet header.

The change in the pressure drop in the exhaust gas across the three-tube EGR cooling devices with the 45° and 60° expansion inlet headers is shown in Figure 6.23. The gas pressure drop was initially 1.8 kPa for the cooling device with the 45° expansion inlet header, whereas it was approximately 17% less than for the device with the 60° expansion inlet header. The pressure drop then increased more rapidly for the device with the 45° expansion inlet header as opposed to the device with the 60° expansion inlet header. The device with the 60° expansion inlet header reached an asymptotic value approximately four-fold

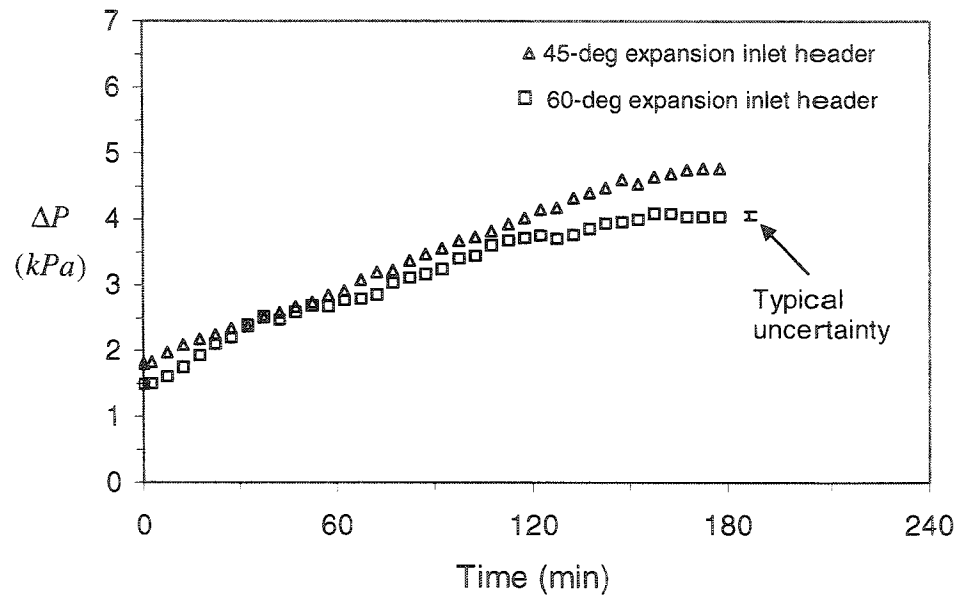


Figure 6.23. Comparison of the variation in the gas pressure drop across the three-tube EGR cooling devices with the 45° and 60° expansion inlet headers during 3 hour tests for the gas mass flow rate of 6.0 kg/hr and average soot mass concentrations of 47 and 46 mg/m³.

its initial value over 150 minutes. The device with the 45° expansion inlet header, however, reached its nearly constant value of approximately 3 times the initial value in nearly 3 hours. The pressure drop profiles here suggested that initially the gas flow rate was unequally distributed in the tube bundles of the two cooling devices since they initially exhibited two different values. This was not surprising since the two devices had two different expansion angle inlet headers, and the results indicate that the soot deposition in the device with the 45° expansion angle inlet header was more uneven, indicating there was higher flow rate passing through the central tube that caused a higher pressure drop across the device.

6.3 Thermal Characteristics of the Secondary Side Coolant Flow

Measurements were also performed to investigate the effect of the coolant flow rate on the thermal characteristics of the secondary coolant flow across the three-tube EGR cooling device using the IR thermal camera system. Tests were performed for lower coolant (water) flow rate of 2.5 l/min and higher coolant flow rate of 6 l/min. The cooling device was exposed to diesel exhaust in the diesel test facility for gas flow rate of 6 kg/hr for 3 hours. The inlet coolant temperature was maintained at approximately 25 °C for both coolant flow rates tests. Thermal images were acquired at every hour of the test duration for both coolant flow rate tests. The results determined from the thermal images show that the coolant

temperature at a particular cross section of the cooling device decreases along most of the length of the device for these tests as shown in Figures I.1 through I.7 of Appendix I. For these tests and at a particular cross section of the cooling devices, the hotter regions were furthest from the coolant inlet side of the devices. The results also show that the coolant temperature at a particular cross section of the device increased with decreasing the coolant flow rate. This was not surprising since the case with the lower coolant flow rate had larger residence times for the coolant in the shell, thus allowing more heat transfer to the coolant from the gas. The coolant flow temperature increased during the 3-hour tests for both flow rates, as shown in Figure 6.24, which may be due to increasing the thermal inertia of the device over time.

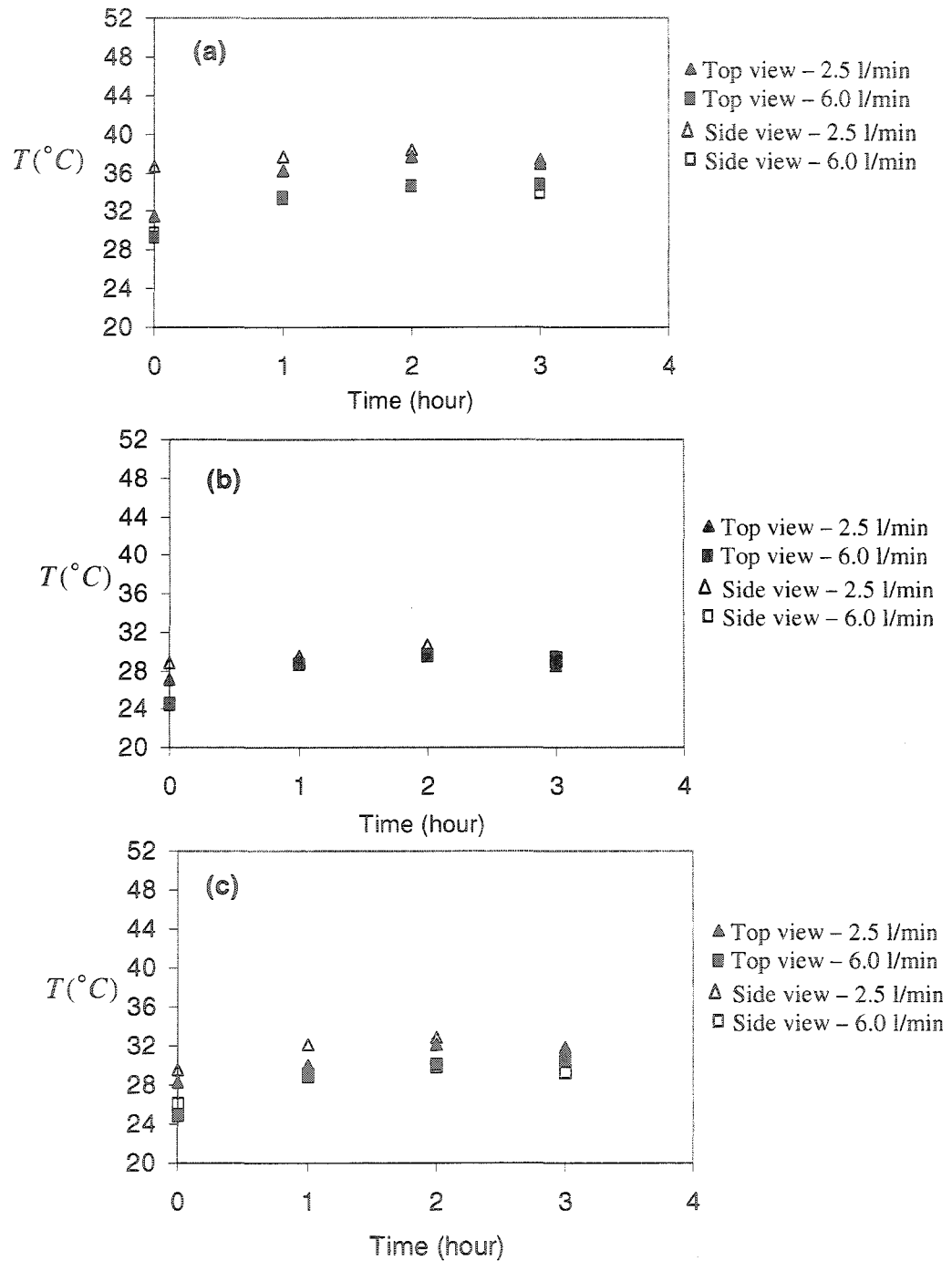


Figure 6.24. Transient average surface coolant temperature determined from top and side views at (a) gas-side entrance of cooling device ($z=0$), (b) $z=L/2$, and (c) $z=L$ for coolant flow rates tests of 2.5 and 6 l/min.

CHAPTER 7: Conclusion

NOx emissions generated from automotive engines can be significantly reduced by up to 70% by installing exhaust gas recirculation (EGR) cooling devices in EGR systems. The exhaust produced by diesel engines has high concentrations of soot so the performance of these devices tends to change over time when they are used in diesel engines due to the soot deposition in these devices. The objective of this work was to investigate in detail the time-dependent heat transfer, pressure drop, and soot deposition characteristics in EGR cooling devices exposed to diesel exhaust gases.

Controlled soot deposition tests were performed on a series of generic single-tube and three-tube EGR cooling devices that were exposed to diesel exhaust for different periods in a diesel exhaust test facility. A non-destructive technique was developed to investigate the soot deposition in the EGR cooling devices using the neutron radiography non-destructive test (NR-NDT) facility at McMaster Nuclear Reactor. The technique was initially calibrated to estimate the average neutron attenuation coefficient and build-up factor for the diesel soot. It was found that the average neutron attenuation coefficient for the soot was $0.023 \pm 0.001 \text{ mm}^{-1}$ and the build-up factor was approximately 1. The accuracy of the neutron radiography technique was then examined by comparing the

measurements of the soot thickness profiles in a soot deposited pipe using the digital neutron radiography technique to the direct measurements of the sectioned pipe with an optical microscope. The measurements of the three-dimensional soot thickness profiles using the neutron radiography technique agreed with the direct destructive measurements using the optical microscope to within 16%.

Measurements were then performed to investigate the change in the soot deposited profiles in generic single-tube and three-tube EGR cooling devices when these devices were exposed to diesel exhaust. The results showed that the soot deposited layer in the single-tube devices was much larger for the higher flow rate that corresponded to turbulent flow than the lower flow rate that corresponded to laminar flow in the entrance region and throughout the tube. The thickness of the deposited soot layer in the entrance region of the tube was much larger than the remainder of the tube. In the turbulent flow tests, approximately 75% of the entrance area was blocked. The results also showed that the soot layer profiles exhibited three-dimensional wave-like structure in all cases.

The gas temperature difference across the cooling devices was reduced by approximately 16% for the laminar flow case and by 47% for the turbulent flow case over 5 hours of testing. The thermal effectiveness decreased from approximately 81% to 71% for the low flow rate, and from 68% to 35% for the

higher flow rate during 5 hours. It was also found that the pressure drop across these devices increased by up to 320% during 5 hours of testing.

Measurements were also performed using three-tube EGR cooling devices with 45° and 60° expansion angle inlet headers when exposed to diesel exhaust for 3 hours. The results showed the soot deposition was larger in the center tube for the three-tube device with the 45° expansion inlet header indicating uneven distribution of the exhaust gas flow in the tube bundle. The soot deposited layer was more evenly distributed along the tubes for the cooling device with the 60° expansion angle inlet header. The circumferential distribution of the soot was more uniform inside the 45° expansion angle inlet header than in the 60° expansion angle inlet header.

The experimental results of the heat transfer in the three-tube tests indicated that the thermal effectiveness in both cooling devices decreased during the 3 hours of testing, but the effectiveness with the more abrupt 60° expansion angle inlet header was higher with 65% at the end of the test versus 52% for the device with the 45° expansion angle inlet header. The pressure drop across the devices increased more rapidly for the device with the 45° expansion inlet header relative to the device with the 60° expansion inlet header.

A simplified 1-D dilute flow model was developed and used to investigate the soot deposition and its effects on the thermal and hydraulic performance of the EGR cooling devices. The predictions from the model indicated that the

deposited soot layer had impact on both the heat transfer and pressure drop performance of the cooling devices, more particularly at a higher flow rate. However, it was concluded that a more comprehensive and sophisticated multi-dimensional model that includes models for re-entrainment and entrance effects is required since the 1-D model was not able to predict the wavy pattern and the three-dimensionality in the deposited soot profiles in the cooling devices that were observed from the experimental results.

CHAPTER 8: Recommendations for Future Work

As for extensions to present work, it is recommended here that further work should be conducted in a number of different areas. For the numerical prediction of the soot deposition profiles in EGR cooling devices, a more sophisticated multi-dimensional model is required that incorporates the following aspects:

1. Inclusion of the dynamic and thermal coupling effects (i.e., $\sum_{2\phi} \geq 1$ and $\sum_{TH} \geq 1$) for the interactions between the agglomerated soot particles ($d_p \geq 20\mu\text{ m}$) and the flow.
2. A model for the soot re-entrainment phenomenon and its interaction with the applicable deposition processes.

Based on the results of this investigation, it appeared that these aspects are important towards a comprehensive and more accurate modeling of the soot deposition profiles that exhibit three-dimensionality and wavy patterns in the cooling devices when exposed to diesel exhaust. The modeling should also include the entrance effects of the tube where the soot deposition was more detrimental. Obviously, this tends to add further complications in the numerical predictions of such problems, so that the benefits in carrying out this work have to be reasonably assessed.

An investigation to characterize the thermal conductivity of diesel soot as a function of its porosity should be pursued in detail leading to a correlation that could be used for more accurate modeling since the thermal conductivity was found to be an important parameter.

In the course of the experimental work, the author of the present work has made several advances in the non-destructive measurements of the three-dimensional soot deposition profiles using the digital neutron radiography imaging system. It became noticeable that some research areas related to this system need to be further upgraded. For example, the considerable amount of image processing time should be reduced and imaging quality should be further improved. The neutron images for the test objects need be directly acquired in an automated fashion using a high-speed computer processor with an advanced data translator board, and stored digitally if needed. Thus, the images can be instantaneously analyzed parallel to the time of conducting the experiment rather than at a later time by analyzing the images stored in VCR tapes. This would also benefit by enhancing imaging quality since digital image acquisition from VCR tapes normally entails loss of data causing loss of resolution of the processed image. Instantaneous image acquisition also helps decide on optimum location of the test object, in terms of its distance relative to the RTNR camera conversion screen. More particularly, placing the test object at optimum position would reduce the unwanted neutron scattering, which would result in optimum imaging

resolution and quality when images were directly processed and analyzed. This would also reduce the time by minimizing the events of repeating the experiments to obtain better results. Another area of improvement would be to incorporate a remote-controlled stage that could move the test object axially so that unnecessary events of accessing the neutron beam port could be avoided. In the present work, this was done using a manually controlled sliding table.

REFERENCES

- Abd-Alla, G. H. (2002). Using exhaust gas recirculation in internal combustion engines: a review. *Energy Conversion and Management*, vol. 43, pp. 1027-1042.
- Abu-Qudais, M. & Kittelson, D. B. (1997). Experimental and theoretical study of particulate re-entrainment from combustion chamber walls of a diesel engine. *Proc. Instn. Mech. Engrs.*, vol.211, part D, pp. 49-57.
- Agrawal, R. K., & Wood, S. C. (2001). Cost-effective NOx reduction. *Chemical Engineering*, pp. 78-82.
- Akihama, K., Takatori, Y., & Inagaki, K. (2001). Mechanism of the smokeless rich diesel combustion by reducing temperature. Society of Automotive Engineers, Inc. *SAE paper no. 2001-01-0655*.
- AQA (2000). Canada-United States Air Quality Agreement: 2000 progress report, no. EN40-388/2000E, pp.3-6&18, International Joint Commission, Washington, DC.
- Asano, H., Takenaka, N., Fujii, T., Shibata, Y., Ebisu, T., & Matsubayashi, M. (1999). Visualization and measurement of refrigerant flow in compression-type refrigerator by neutron radiography. *Nuclear Instruments and Methods in Physics research*, vol. A 424, pp. 98-103.
- Beck, M. S. & Wainwright, N. (1969). Current industrial methods of solids flow detection and measurement. *Powder Technology*, vol. 2, pp. 189-197.
- Bedford, F., Rutland, C., Dittrich, P., Raab, A., & Wirbeleit, F. (2000). Effects of direct water injection on DI diesel engine combustion. Society of Automotive Engineers, Inc. *SAE paper no. 2000-01-2938*.

- Bell, K. J. (1983). Approximate sizing of shell-and-tube heat exchangers. *Heat Exchangers Handbook*, chap.3, p.3.1.4-1, Hemisphere Publishing Corp., New York.
- Berger, C., Horvath, H., & Schindler, W. (1995). The deposition of soot particles from hot gas streams through pipes. *J. Aerosol Science*, vol. 26(2), pp. 211-217.
- Beuthe, T. G. & Chang, J.-S. (1995). Gas discharge phenomena. In *Handbook of Electrostatic Processes*. Editors: Chang, J.-S., Kelly, A. J., & Crowley, J. M. Dekker, Inc., New York.
- Bird, R., Stewart, W., and Lightfoot, E. (1960). *Transport Phenomena*. John Wiley & sons, Inc., New York.
- Bloch, R., & Muller-Steinhagen, H. (1990). Influence of particle size and particle/fluid combination on particulate fouling in heat exchangers. *The Can. J. Chem. Eng.*, vol. 68, pp. 585-591.
- Bohne, D., Fischer, S., and Obermeier, E. (1984). Thermal conductivity, density, viscosity, and Prandtl numbers of ethylene glycol-water mixtures. *Berichte Der Bunsen.*, vol. 88 (8), pp. 739-742.
- Boothroyd, M. A. (1966). Pressure drop in duct flow of gaseous suspensions of fine particles. *Trans. Instn. Chem. Engrs.*, vol. 44, pp. 306-313.
- Boothroyd, M. A. (1970). Experimental investigation of heat transfer in the entrance region of a heated duct conveying fine particles. *Trans. Instn. Chem. Engrs.*, vol. 48, pp. 109-120.
- Bott, T. R. & Bemrose, C. R. (1983). Particulate fouling on the gas-side of finned tube heat exchangers. *Transactions of the ASME, the Heat Transfer Division*, vol. 105, pp. 178-183.
- Bott, T. R., Hays, G. F., Herman, K. W., Jones, A. E., Knudsen, J. G., Miller, E. R., Muller-Steinhagen, H., Palen, J. W., Panchal, C. B., & Wilson, D. I. (1999).

- Type of heat exchanger and fouling potential. *Heat Exchangers Handbook*, vol.3, p.317.7-1, Begell House, Inc., New York.
- Brown, A. R. & Thomas, M. A. (1965). Combined free and forced convection heat transfer for laminar flow in horizontal tubes. *Journal of Mechanical Engineering Science*, vol. 7, pp. 440-448.
- Burtscher, H., Kunzel, S., & Huglin, C. (1998). Characterization of particles in combustion engine exhaust. *Journal of Aerosol Science*, 29, 389-396.
- Byers, R. L., & Calvert, S. (1969). Particle deposition from turbulent streams by means of thermal force. *I & EC Fundamentals*, vol.8(4), pp.646-655.
- Chang, J. S., & E. C. Morala (1990). Determination of two-phase interfacial areas by an ultrasonic technique. *Nuclear Engineering and Design*, vol.122, pp.143-156.
- Chang, J.-S. (1991). Theory of dust particle unipolar diffusion charging under non-thermal equilibrium conditions. *Inst. Phys. Conf. Ser.*, vol. 118 (5), pp. 305-310.
- Chang, J.-S., Kelly, A. J., & Crowley, J. M. (1995). *Handbook of Electrostatic Processes*. Marcel Dekker, Inc., New York.
- Chen, Y. K. & Yu, C. P. (1993). Particle deposition from duct flows by combined mechanisms. *Journal of Aerosol Science and Technology*, vol. 19, pp. 389-395.
- Cleaver, J. W. & Yates, B. (1973). Mechanism of detachment of colloidal particles from a flat substrate in a turbulent flow. *Journal Colloid and Interface Science*, vol.44, p.3.
- Chapman, S., & Cowling, T. G. (1960). *The mathematical theory of non-uniform gases*. Cambridge University Press, Cambridge.
- Chen, C.-S., Laframboise, J. G., & Chang, J.-S. (1983). Diffusion and sedimentation of aerosol particles from laminar flow in inclined channels. *Journal of Aerosol Science*, 14, pp. 1-6.

- Cohen A. J., & Higgins, M. W. P. (1995). Health effects of diesel exhaust: Epidemiology. In: Diesel exhaust: A critical analysis of emissions, exposure, and health effects. *A Special Report of the Institute's Diesel Working Group*. Health Effects Institutes, Cambridge, MA, USA.
- Cumberland, D. J. & Crawford, R. J. (1987). The packing of particles. *Handbook of powder technology*, vol. 6. Elsevier Publishing Co., Amsterdam.
- Davies, C. N. (1966). *Aerosol Science*. Academic Press, London.
- Davies, C. N. (1973). Diffusion and sedimentation of aerosol particles from poiseuille flow in pipes, *Journal of Aerosol Science*, vol. 4, pp. 317-328.
- Davazoglou, D. (1997). Determination of optical dispersion and film thickness of semiconducting disordered layers by transmission measurements: application for chemically vapor deposited Si and SnO₂ film. *Appl. Phys. Lett.*, vol. 70(2), pp. 246-248.
- Delhaye, J.-M., Giot, M., & Riethmuller, M. L. (1981). *Thermohydraulics of two-phase systems for industrial design and nuclear engineering*. Hemisphere, Washington, DC.
- Dickey, D. W., Ryan III, T. W., & Matheaus, A. C. (1998). NO_x control in heavy-duty diesel engines – what is the limit ?. Society of Automotive Engineers, Inc. *SAE paper no. 980174*.
- Drew, D. A. & Lahey, R. T. (1977). Application of general constitutive principles to the derivation of multidimensional two-phase flow equations. *Int. J. Multiphase Flow*, vol.5, pp.243-264.
- Duderstadt, J. J. & Hamilton, L. J. (1996). *Nuclear reactor analysis*. John Wiley & Sons, New York.
- Epstein, N. (1999). Types of fouling. *Heat Exchangers Handbook*, vol.3, p.317.2-1, Begell House, Inc., New York.
- Fan, L.-S., and Zhu, C. (1998). *Principles of gas-solid flows*. Cambridge University Press, Cambridge.

- Filippov, L. P. (1970). *Studies on the thermal conductivity of liquids*. Izd. Moskov Gos. Univ., pp. 188-209.
- Fox, R. W., McDonald, A. T. & Pritchard, P. J. (2004). *Introduction to fluid mechanics*, 6th edition, John Wiley & Sons Inc., New York.
- Fryer, P. J., & Slater, N. K. H. (1985). A direct simulation procedure for chemical reaction fouling in heat exchangers. *The Chemical Engineering Journal*, vol. 31, pp. 97-107.
- Gallant, R. W. (1970). *Physical Properties of Hydrocarbons*. Gulf Publishing, Houston.
- Gentry, C. C., Young, R. K., & Small, W. M. (1982). *Proc. 7th Int. Heat Transfer Conf.* – Munich, vol. 6, pp. 197-202. Hemisphere Publ. Corp., Washington, DC.
- Glassman, I. (1987). *Combustion*. 2nd edition, Academic Press Inc., California, USA.
- Glickstein, S. S., Vance, W. H., & Joo Hansem (1995). Void fraction measurement using neutron radiography. *Nuclear Science and Engineering*, vol. 121, pp.153-161.
- Gnielinski, V. (1999). Forced convection in ducts. *Heat Exchangers Handbook*, vol.3, p.2.5.1-1, Begell House, Inc., New York.
- Groehn, H. G. (1991). Thermal-hydraulics of helical-type helium/helium intermediate heat exchangers for nuclear process heat applications of high-temperature gas-cooled reactors- fundamental research and large scale tests. *Nuclear Engineering and Design*, vol.126, pp. 285-290.
- Hammer, T. & Boroer, S. (1999). Proceedings of non-thermal plasma for exhaust emission control: NOx, HC, and particles. *Society of Automotive Engineers, Inc. SAE paper no. 1999-01-3633*.

- Harris, S. J. & Maricq, M. M. (2001). Signature size distributions for diesel and gasoline engine exhaust particulate matter. *Journal of Aerosol Science*, vo. 32, pp. 749-764.
- Harvel, G. D. & Chang, J. S. (1995). Electrostatic multiphase flow measurement techniques. *Handbook of Electrostatic Processes*, Editors: J. S. Chang, A. J. Kelly, and J. M. Crowley, Marcel Dekker, Inc., New York.
- Harvel, G. D., Chang, J. S., & Krishnan, V. S. (1995). Determination of time-dependent void fraction distribution in bubbly two-phase flow by a real-time neutron radiography technique. *Nuclear Technology*, 109(1), pp. 132-141.
- Harvel, G. D., Chang, J. S., & Krishnan, V. S. (2000). Investigation of large amplitude stratified waves in CANDU-type 37 rod nuclear fuel channel by a real-time neutron radiography technique. *Nuclear Engineering and design*, vol. 200, pp. 221-231.
- Heat Transfer Data Book. (1974). Sections 503.2 and 503.3. General Electric Company.
- Hetsroni, G. (1982). *Handbook of multiphase systems*. Hemisphere Publishing Corporation, New York.
- Hieber, C. A. (1981). Mixed convection in an isothermal horizontal tube: somerecent theories. *Int. J. Heat & Mass Transfer*, vol. 24, pp. 315-322.
- Hieber, C. A., & Sreenivasan, S. K. (1974). Mixed convection in an isothermally heated horizontal pipe. *Int. J. Heat & Mass Transfer*, vol. 17, pp. 1337-1348.
- Hinds, W. C. (1982). *Aerosol technology: properties, behavior, and measurement of airborne particles*. John Wiley & Sons. Toronto.
- Hoard, J. & Lou Balmer, M. (1998). Analysis of Plasma-Catalysis for Diesel NOx Remediation. *Society of Automotive Engineers, Inc. SAE paper no. 982429*.
- Holman, J. P. (1989). *Experimental methods for engineers*. 5th edition. McGrawhill, Inc. New York.

- Honma, J., Murao, T., Yamashita, Y., Tsujita, M., & Sugihara, H. (2004). Development of a highly efficient and reliable multi-tube EGR cooler. *Society of Automotive Engineers, Inc. SAE paper no. 2004-01-1446*.
- Idelchick, I. E. (1986). *Handbook of hydraulic resistance*. 2nd edition, Hemisphere Pub. Corp., Washington.
- Ingham, D. B. (1975). Diffusion of aerosols from a stream flowing through a cylindrical tube. *Aerosol Science*, vol. 6, pp.125-132.
- Ingham, D. B. (1976). Diffusion and sedimentation of aerosol particles in rectangular tubes, *Journal Aerosol Science*, vol. 7, pp.373-380.
- Irons, G. A. & Chang, J. S. (1983a). Particle fraction and velocity measurement in gas-powder streams by capacitance transducers. *Int. J. Multiphase Flow*, 9(3), pp. 289-297.
- Irons, G. A. & Chang, J.-S. (1983b). Dispersed powder flow through vertical pipes. *Powder Technology*, vol. 34, pp. 233-242.
- Ishiguro, I., Takatori, Y., & Akihama, K. (1997). Microstructure of diesel soot particles probed by electron microscopy: First observation of inner core and outer shell. *Combustion & Flame*, vol. 108, pp. 231-234.
- Ishii, M. (1975). *Thermo-fluid dynamic theory of two-phase flow*. Eyrolles, Paris (also Scientific and Medical Publication of France, NY).
- Ishii, M. & Mishima, K. (1984). Two-fluid model and hydrodynamic constitutive relations. *Nucl. Eng. Des.*, vol. 82, pp.107-126.
- Ismail, B., Zhang, R., Ewing, D., Chang, J.-S., & Cotton, J. (2002). The heat transfer characteristics of exhaust gas recirculation (EGR) cooling devices. *Proceedings of the ASME International Mechanical Engineering Congress and Exposition (IMECE)*, LA, USA. ASME paper No. IMECE HT-34559.
- Kakac, S., Berggles, A. E., & Fernandes, E. O. (1987). *Two-phase flow heat exchangers: Thermal hydraulic fundamentals and design*. Kluwer Academic Publishers, London, UK.

- Kays, W. M. (1950). Loss coefficients for abrupt changes in flow cross section with low Reynolds number flow in single and multiple tube systems. *Trans. ASME*, vol.72, pp. 1067-1074.
- Kays, W. M., & Crawford, M. E. (1980). *Convective heat and mass transfer*. 2nd edition, New York: McGraw-Hill Book Company.
- Kays, W. M., & London, A. L. (1984). *Compact heat exchangers*. 3rd ed, McGraw-Hill Book, Inc., New York.
- Kern, D. & Seaton, R. (1959). A theoretical analysis of thermal surface fouling. *Brit. Chem. Eng.*, vol. 4, No. 5, pp. 258-262.
- Kern, D. Q., & Kraus, A. D. (1972). *Extended surface heat transfer*. McGraw-Hill Book Company, New York.
- Kittelson, D., Johnson, J., Watts, W., Wei, Q., Drayton, M., Paulsen, D, & Bukowiecki, N. (2000). Diesel aerosol sampling in the atmosphere. Society of Automotive Engineers, Inc. *SAE paper no.* 2000-01-2212.
- Knudsen, J. (1999). Analysis of the fouling process. *Heat Exchangers Handbook*, vol. 3, p.317.3-1, Begell House, Inc., New York.
- Knudsen, J., Hays, G., Bott, T., & Epstein, N. (1999). Fouling in heat exchangers. *Heat Exchangers Handbook*, vol. 3, pp.317.1-1 – 317.2-5, Begell House, Inc., New York.
- Ladommatos, N., Abdelhalim, S. M., & Zhao, H. (1998). Effects of EGR temperature on diesel engine combustion and emissions. *Proc. Instn. Mech. Engrs*, part D, vol. 212, pp. 479-500.
- Lapuerta, M., Hernandez, J., & Gimenez, F. (2000). Evaluation of exhaust gas recirculation as a technique for reducing diesel engine NO_x emissions, *Proc. Instn. Mech. Engrs*, part D, vol. 214, pp. 85-93.
- Lapuerta, M., Salavert, J. M., & Domenech, C. (1995). Modelling and experimental study about the effect of exhaust gas recirculation on diesel

- engine combustion and emissions. Society of Automotive Engineers, Inc. *SAE paper no.950216*.
- Lloyd, A. C., and Cackette, T. A. (2001). Diesel Engines: Environmental impact and control. *J. Air & Waste Manage*, vol. 51, pp. 809-847.
- Malet, J., Alloul, L., Michielsen, N., Boulaud, D., & Renoux, A. (2000). Deposition of nanosized particles in cylindrical tubes under laminar and turbulent flow conditions. *J. Aerosol Science*, vol. 31(3), pp.335-348.
- Maquin, B., Goyeheneche, J. M., Derre, A., Chadeyron, P., & Dehhaes, P. (1999). Thermal conductivity of submicrometer particles: carbon blacks and solid solutions containing C, B, and N. *J. Phys. D: Applied Physics*, vol. 33(1), pp. 8-17.
- Mattarelli, E., Bianchi, G., & Ivaldi, D. (2000). Experimental and numerical investigation on the EGR system performance of a new automotive diesel engine. Society of Automotive Engineers, Inc. *SAE paper no. 2000-01-0224*.
- Melgar, A., Horrillo, A., Gabaco, G., Castano, C., & Grande, J. A. (2004). Theoretical and experimental methodology for the improvement of EGR-coolers design. *Society of Automotive Engineers, Inc. SAE paper no. 2004-01-0052*.
- Messerer, A., Niessner, R., & Poschl, U. (2003). Thermophoretic deposition of soot aerosol particles under experimental conditions relevant to modern diesel engine exhaust gas systems. *J. Aerosol Science*, vol.34, pp. 1009-1021.
- MOE 2000: Air Quality in Ontario (2000). Air Quality and Metrology Section, Air Resources Branch; Environment Ontario.
- Moody, L. F. (1944). Friction factors for pipe flow. *Trans. ASME*, vol.66, p. 671.
- Muller-Steinhagen, H., Reif, F., Epstein, N., & Watkinson, A. P. (1988). Influence of operating conditions on particulate fouling. *The Canadian Journal of Chemical Engineering*, vol. 66, pp.42-50.

- Ning, Z., Cheung, C. S., & Liu, S. X. (2004). Experimental investigation of the effect of exhaust gas cooling on diesel particulate. *Journal of Aerosol Science*, vol. 35, pp. 333-345.
- Nishio, G., Kitani, S., & Takahashi, K. (1974). Thermophoretic deposition of aerosol particles in a heat-exchanger pipe. *Ind. Eng. Chem, Process Des. Develop.*, vol.13(4), pp.408-415.
- Ou, J. W. & Cheng, K. C. (1977). Natural convection effects on Graetz problem in horizontal isothermal tubes. *Int. J. Heat & Mass Transfer*, vol. 2, pp. 953-960.
- Petukhov, B. S., & Kirillov, V. V. (1958). Heat exchangers for turbulent flow of liquid in tubes. *Teploenergetika*, vol. 4, pp. 63-68.
- Pich, J. (1972). Theory of gravitational deposition of particles from laminar flows in channels. *Journal Aerosol Science*, vol. 3, pp. 351-361.
- Reynolds, W. M., Hatnett, J. P., & Ganic, E. N. (1969). *Journal of Basic Engineering*, vol. 91, pp. 87-94.
- Romay, F. J., Takagaki, S. S., Pui, D. Y. H., & Liu, B. Y. H. (1998). Thermophoretic deposition of aerosol particles in turbulent pipe flow. *J. Aerosol Science*, vol.29(8), pp.943-959.
- Root, L. F. & Kaufman, I. (1992). Noncontacting low-cost instrument for film thickness measurement. *IEEE Trans. On Instrumentation and Measurement*, vol. 41(6), pp. 1014-1019.
- Rudinger, G. (1980). *Fundamentals of gas-particle flow*. Elsevier Scientific Publishing Company, Amestterdam.
- Satoh, K., Zhang, L., Hatanaka, H., Takatsuki, T., & Yokota, K. (1997). Relationship between NOx and SM emissions from DI diesel engine with EGR. *JSAE Review*, vol. 18, pp. 369-375.
- Shah, R. K. (1981). Classification of heat exchangers. In *Heat exchangers-thermal hydraulic fundamentals and design*, edited by S. Kakac, A. E. Bergles, and F. Mayinger. McGraw-Hill Book Co., New York.

- Shah, R. K., & Bhatti, M. S. (1987). Assessment of test techniques and correlations for single phase heat exchangers. 6th NATO Advanced Study Institute, thermal/hydraulic fundamentals and design of two-phase heat exchangers, Povadevarzin, Portugal.
- Shah, R. K., & London, A. L. (1978). *Laminar flow forced convection in ducts*. Academic, New York.
- Sieder, E. N. & Tate, G. E. (1936). Heat transfer and pressure drop of liquids in tubes. *Ind. Engng. Chem*, vol. 28, pp. 1429-1436.
- Soo, S. L. (1967). *Fluid dynamics of multiphase systems*. Blaisdell Publishing Co, Toronto.
- Standards of Tubular Exchanger Manufacturers Association (TEMA). (1989). 7th edition. Tarrytown, New York.
- Stolz, A., Fleischer, K., Knecht, W., Nies, J., & Strahle, R. (2001). Development of EGR coolers for truck and passenger car application. *Society of Automotive Engineers, Inc. SAE paper no. 2001-01-1748*.
- Suzuki, H., Odaka, M., Kariya, T. (2000). Effect of start of injection on NO_x and smoke emissions in homogeneous charge diesel combustion. *JSAE Review*, vol. 21, pp. 385-416.
- Taborek, J. (1983). Shell-and-tube heat exchangers: objectives and backgrounds. *Heat Exchanger Design Handbook*, chapter 3, Hemisphere Publishing, New York.
- Taborek, J. (1995). Longitudinal flow in tube bundles with grid baffles. *Heat Exchangers Handbook*, vol.3, p.3.3.12-1, Begell House, Inc., New York.
- Takenaka, N., Asano, H., Fujii, T., & Matsubayashi, M. (1998). Three dimensional visualization of void fraction distribution in steady two-phase flow by thermal neutron radiography. *Nuclear Engineering and design*, vol. 184, pp. 203-212.

- Talbot, L., Cheng, R. K., Schaefer, R. W., & Willis, D. R. (1980). Thermophoresis of particles in a heated boundary layer. *J. Fluid Mech.*, vol. 101 (4), pp. 737-758.
- Tan, C. W., & Hsu, C.-J. (1971). Diffusion of aerosols in laminar flow in a cylindrical tube. *Journal of Aerosol Science*, vol. 2, pp. 117-124.
- Taulbee, D. B., and Yu, C. P. (1975). Simultaneous diffusion and sedimentation of aerosols in channel flows. *Journal of Aerosol Science*, vol. 6, pp. 433-441.
- Taulbee, D. B., & Yu, C. P. (1977). Simultaneous diffusion and sedimentation of aerosols in a horizontal cylinder. *J. Aerosol Science*, vol. 8, pp. 309-316.
- Taylor, R. (2003). Pollution probe conference on climate change. Railway Association of Canada (RAC), April 28-29, 2003, Toronto, Canada.
- Tennison, P., Lambert, C., & Levin, M. (2004). NOx control development with urea SCR on a diesel passenger car. *Society of Automotive Engineers, Inc. SAE paper no. 2004-01-1291*.
- Thomas, L. C. (1999). *Heat transfer –professional version. 2nd ed.*, Capstone Publishing Corporation, Oklahoma, USA.
- Thompson, D., Brown, T. D., & Beer, J. M. (1972). NOx formation in combustion. *Combustion and Flame*, vol. 19, pp. 69-79.
- Tyufyakov, N. D. (1983). Determination of hydrogen content in materials and products by neutron radiography method. *Neutron Radiography Handbook*, Editors: Barton J. P., & Hardt, V. D., pp. 303-307.
- Umekawa, H., Ozawa, M., Takenaka, T., & Matsubayashi, M. (1999). Visualization of bed material movement in a simulated fluidized bed heat exchanger by neutron radiography. *Nuclear Instruments and Methods in Physics Research*, vol. A 424, pp. 77-83.
- UNFCCC. A guide to the climate change convention and the Kyoto protocol. (2003). Issued by the climate change secretariat (UNFCCC), Courir-Druck GmbH, Bonn, Germany.

- Urashima, K., Tong, X., Chang, J. S., Miziolek, A., & Rosocha, L. A. (1999). Proc. of non-thermal plasma for exhaust emission control: NO_x, HC, and particles. *Society of Automotive Engineers, Inc. SAE paper no. 1999-01-3634*.
- U.S. EPA (1998). Inventory of US Greenhouse Gas Emissions and Sinks:1990-1996, report no. EPA 236-R-98-006.
- Usui, S., Ito, K., & Kato, K. (2004). The effect of semi-circular micro riblets on the deposition of diesel exhaust particulate. *Society of Automotive Engineers, Inc. SAE paper no. 2004-01-0969*.
- Vyskubenko, Y. A., Maslennikov, V. M., & Tsalko, E. A. (1979). Heat transfer and precipitates in the initial section of a pipe during cooling of a flow of dispersed gas. *High Temperature*, vol.17 (5), pp.854-858.
- Wahi, M. K. (1977). Heat transfer to flowing gas-solid mixtures. *J. Heat Transfer*, vo.99, pp. 145-148.
- Walsh, M. P. (2001). Global trends in diesel emissions regulation-2001 update. *Society of Automotive Engineers, Inc., SAE paper no. 2001-01-0183*.
- White, F. M. (1991). *Viscous Fluid Flow*, 2nd edition, McGraw-Hill Book Company, New York.
- Wilkinson, G. T., Norman, B. E., & Norman, J. R. (1967). Heat transfer to a suspension of solids in a gas. *Trans. Instn. Chem. Engrs.*, vol.45, pp. 314-318.
- Yan, Y., & Byrne, B. (1997). Measurement of solids deposition in pneumatic conveying. *Powder Technology*, vol. 91, pp. 131-139.
- Zehenka, A., & Reczek, C. (1998). Cooled EGR- A key technology for future efficient HD diesels. *Society of Automotive Engineers, Inc. SAE paper no. 980190*.
- Zeldovich, J. (1946). The oxidation of nitrogen in combustion and explosion, *Acta Physiochem USSR*, vol. 21 (4), pp. 577-628.

- Zhang, R. (2003). Characterization of the EGR cooling devices used in diesel exhaust gas recirculation systems. *Masters of Science Thesis*, Department of Mechanical Engineering, McMaster University, Hamilton, Canada.
- Zhang, R., Charles, F., Ewing, D., Chang, J.-S., & Cotton, J. S. (2004). Effect of diesel soot deposition on the performance of exhaust gas recirculation cooling devices. Society of Automotive Engineers, Inc. *SAE paper no.2004-01-0122*.
- Zukauskas, A. (1987). Convective heat transfer in crossflow. *Handbook of Single-Phase Convection Heat Transfer*, edited by S. Kakac, R. K. Shah, and W. Aung. John Wiley & sons, Inc., New York.

Appendix A: Predictions Results

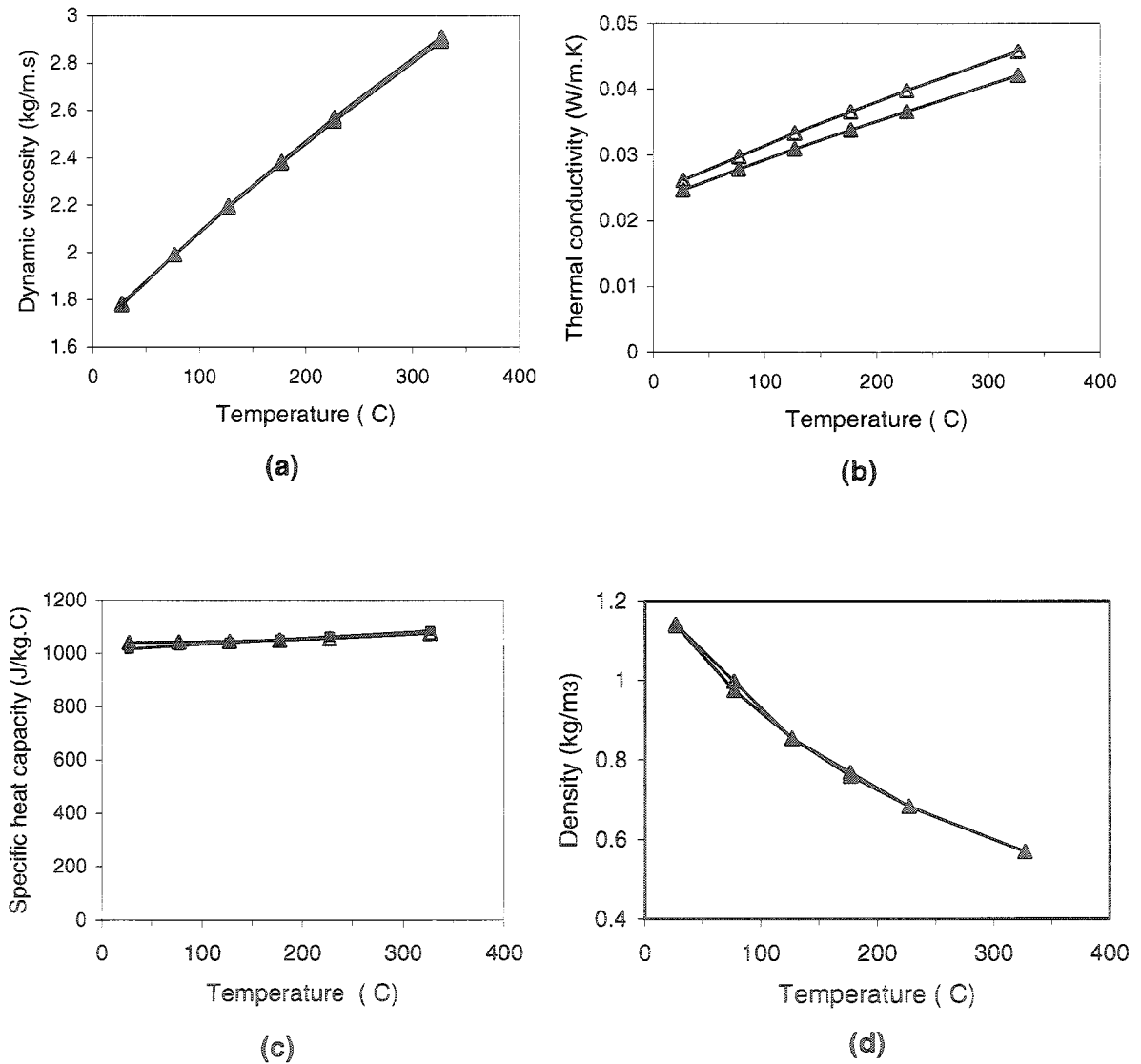


Figure A.1. Comparison of the change in the thermo-physical properties: (a) dynamic viscosity; (b) thermal conductivity; (c) specific heat capacity; and (d) density of air mixture determined using \blacktriangle the present model, and \triangle from look-up tables.

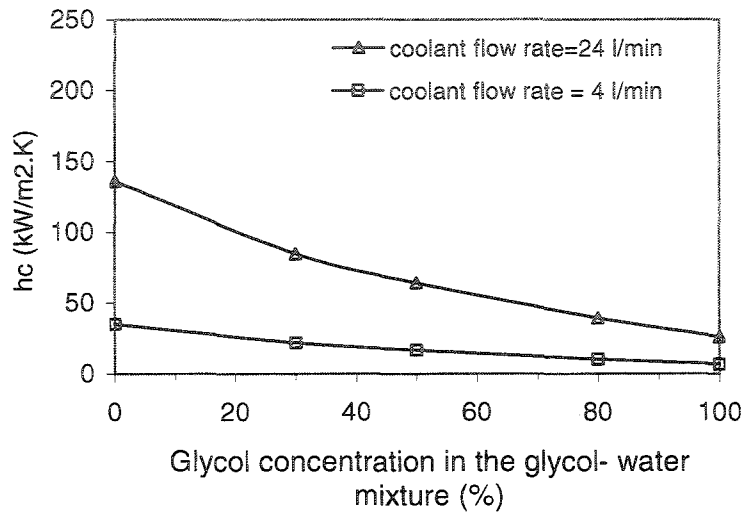


Figure A.2. Simulations of the effect of the ethylene-glycol concentration in the glycol-water mixture on the convective heat transfer coefficient of the coolant mixture in the six-tube EGR cooling device, using the present model. ($\dot{m}_g = 3$ kg/hr, $T_{g,i} = 450$ °C, $T_{c,i} = 60$ °C.)

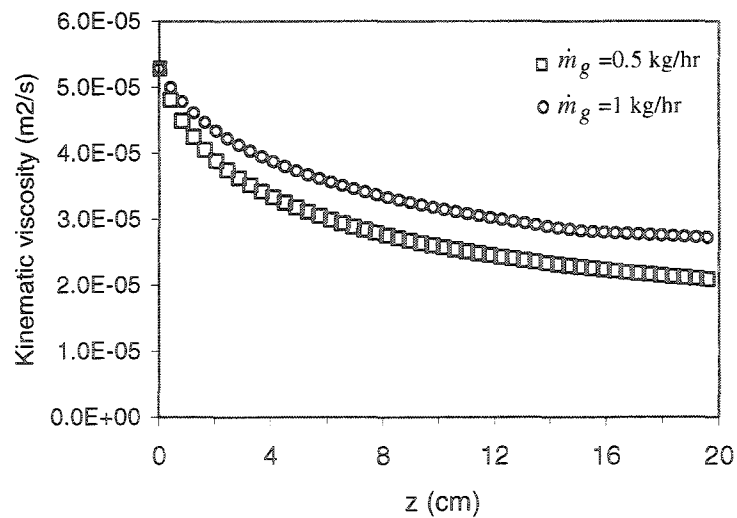


Figure A.3. The change in the kinematic viscosity of the exhaust gas along the EGR cooling device predicted using the present model, for two different gas flow rates, and $T_{g,i} = 450$ °C and $T_{c,i} = 60$ °C.

Appendix B: Additional Experimental Work

This appendix provides additional experimental results of a “concept” non-conventional single-tube EGR cooling device with short twisted tape inserted in the gas inlet side of the cooling device to investigate the heat transfer and the soot deposition characteristics in the non-conventional device.

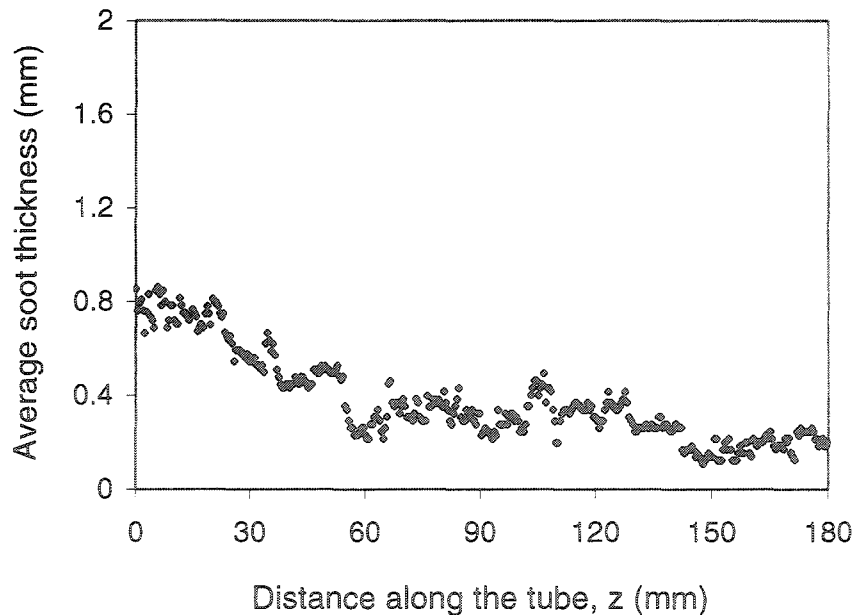


Figure B.1. Variation in the circumferentially averaged soot deposited thickness measured using the neutron radiography technique, for the single-tube EGR cooling device with twisted tape insert for 5-hour test with a mass flow rate of 2.8 kg/hr and $C_{PM}=45 \text{ mg/m}^3$.

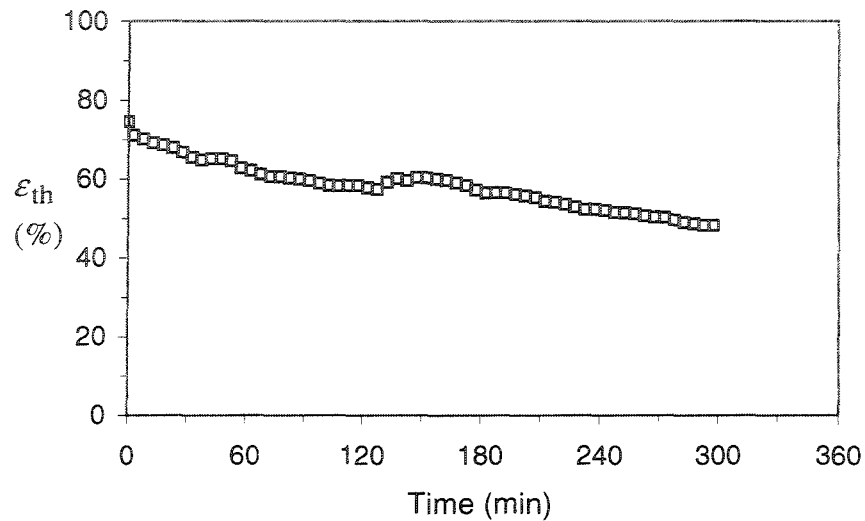


Figure B.2. The change in the thermal effectiveness of the non-conventional single-tube EGR cooling device with the twisted tape insert during 5 hours of testing for gas flow rate 2.8 kg/hr and soot concentration 45 mg/m³.

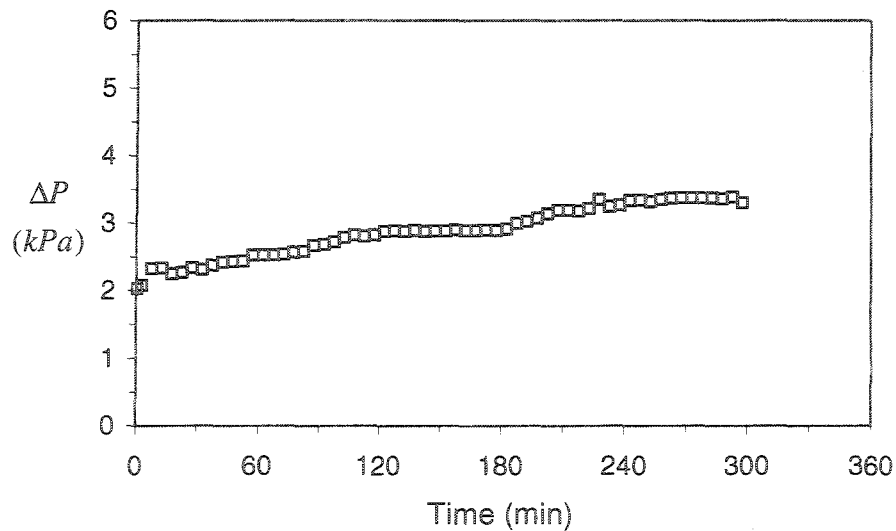


Figure B.3. The change in the pressure drop in the exhaust gas across the non-conventional single-tube EGR cooling device with the twisted tape insert during 5 hours of testing for gas flow rate 2.8 kg/hr and soot concentration 45 mg/m³.

Appendix C: Calibration of the IR Thermal Camera System

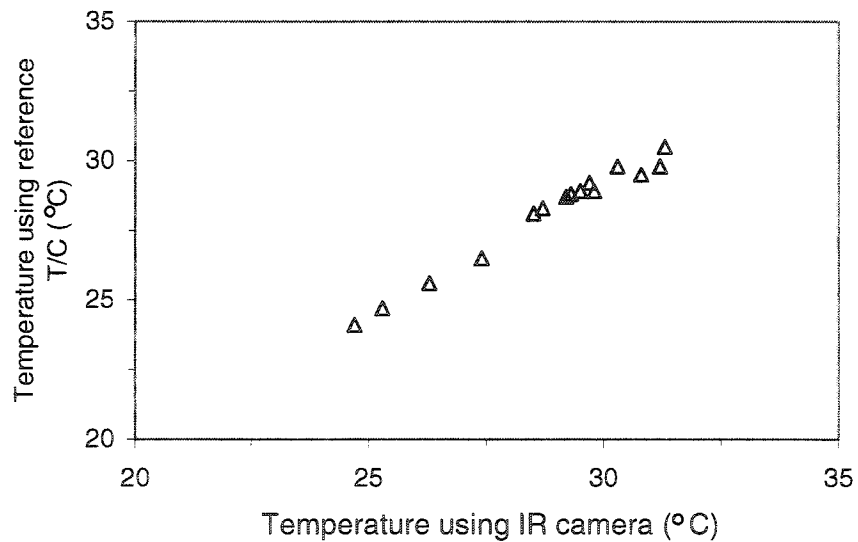


Figure C.1. Comparison of the temperature measurements for the secondary side coolant flow across the three-tube EGR cooling device, using the infrared (IR) thermo-imaging camera and the reference T-type thermocouple.

Appendix D: The Two-Phase Flow Conservation Equations and Constitutive Relations

For the Eulerian or two-fluid model, the transient three-dimensional conservation equations for each phase can be written as (Ishii, 1975)

$$\frac{\partial(\alpha_k \rho_k)}{\partial t} + \nabla \cdot (\alpha_k \rho_k \bar{u}_k) = \Gamma_k \quad (\text{D.1})$$

$$\frac{\partial(\alpha_k \rho_k \bar{u}_k)}{\partial t} + \nabla \cdot (\alpha_k \rho_k \bar{u}_k \bar{u}_k) = -\nabla \alpha_k p_k + \nabla \cdot [\alpha_k (\bar{\bar{v}}_k + \bar{\bar{v}}_k^T)] + \alpha_k \rho_k \bar{g}_k + \bar{M}_{ik} \quad (\text{D.2})$$

and

$$\frac{\partial(\alpha_k \rho_k e_k)}{\partial t} + \nabla \cdot (\alpha_k \rho_k e_k \bar{u}_k) = -\nabla \cdot [\alpha_k (\bar{q}_k + \bar{q}_k^T)] + \nabla \cdot (\alpha_k \bar{\bar{v}}_k \cdot \bar{u}_k) + \alpha_k \rho_k \bar{g}_k \cdot \bar{u}_k + E_{ik}, \quad (\text{D.3})$$

where, $k = p$ for the particle phase and $k = g$ for gas phase. The other variables are described in Table D.1. The approach results in interfacial terms that must be related to the mean variables of the two phases using constitutive models often written as empirical correlations. The correlating turbulent stresses, $\bar{\bar{v}}_k^T$ appearing in Eq. (D.2), are the Reynolds stresses that can be modeled using the standard turbulence, models such as $k - \varepsilon$ model (Fan and Zhu, 1998). For the two-phase flow, the transport equations for $k - \varepsilon$ included source terms induced by the influence of the particles on the flow (Drew and Lahey, 1977).

Table D.1: Description of notations used in Eqs. (D.1) through (D.10).

Variable notation	Description
∇	“Nabla” operator (3-D spacial differential operator)
t	Temporal variable
α_k	Phasic volume fraction ($k = p$, particle volume fraction $\alpha_p = 1 - \alpha_g$, $k = g$ gas volume fraction)
\bar{u}_k	Absolute phasic velocity
ρ_k	Material phasic density
\bar{g}_k	Acceleration due to gravity
p_k	Average pressure of phase k
$\bar{\tau}_k$	Shear or viscous stress tensor
$\bar{\tau}_k^T$	Turbulent viscous stress tensor
\bar{q}_k	Conductive or diffusive heat flux
\bar{q}_k^T	Turbulent heat flux
e_k	Specific total energy=sum of specific internal energy and of the kinetic energy due to mean and fluctuating motions
Γ_k	Interfacial mass transfer or the rate of mass generation of phase k at the interface
\bar{M}_{ik}	Interfacial momentum transfer or the rate of momentum generation of phase k at the interface
E_{ik}	Interfacial energy transfer or the rate of generation of energy to phase k across the interface
Superscript T	Turbulent correlation terms between fluctuating variables
L_i	$1/L_i = a_i$ is the interfacial area per unit mixture volume
F_{ik}^D	Interfacial drag force
h_{ik}	Interfacial heat transfer coefficient

The interfacial terms on the right hand side of the equations also obey the conservation laws at the interface given by (Ishii, 1975)

$$\sum_k \Gamma_k = 0 \quad (D.4)$$

$$\sum_k M_{ik} = \sum_k (p_{ik} \nabla \alpha_k + F_{ik}^D) = 0 \quad (D.5)$$

and

$$\sum_k E_{ik} = \sum_k (\Gamma_k e_{ik} + q_{ik} / L_i) = 0, \quad (D.6)$$

where the variables appearing in Eqs. (D.4) through (D.5) are given in Table D.1.

The interfacial heat flux and drag force are normally modeled using constitutive relations depending on flow regimes. For example, Soo (1967), and Ishii and Mishima (1984) modeled the heat flux at the interface for gas-particle flow using the driving force, temperature difference, for a heat transfer using

$$q_{g-p} = N_p h_{g-p} A_p (T_g - T_p), \quad (D.7)$$

where $A_p = \pi d_p^2$, $(T_g - T_p)$ is the mean temperature difference between the two phases, and h_{g-p} is the interfacial heat transfer coefficient that can be estimated using a correlation for Nusselt number, such as the correlation for the spherically shaped particle (Rudinger, 1980)

$$Nu_{g-p} = 2.0 + 0.6 Re_p^{0.5} Pr_g^{0.33} \quad (Re_p < 700) \quad (D.8)$$

where

$$\text{Re}_p = \frac{d_p |(\bar{u}_p - \bar{u}_g)|}{\nu_g} \quad (\text{D.9})$$

The interfacial gas-particle drag force can be modeled using (Soo, 1967)

$$\bar{F}_{g-p} = N_p K_p (\bar{u}_g - \bar{u}_p), \quad (\text{D.10})$$

where N_p and K_p are the number particle density and the coefficient of interfacial drag resistance, respectively. The simplest model for K_p is given by (Soo, 1967)

$$K_p = 3\pi\mu_g d_p \quad (\text{D.11})$$

Appendix E: The Equations and Correlations Used for the 1-D Heat Transfer Model

The thermal performance of the counter-current flow heat exchanger could be predicted using the incremental heat transfer rate, $d\dot{Q}$, that can be written using the Newton's law of cooling in analogy to a steady-state flow of electrical current as (Kays and London, 1984)

$$d\dot{Q} = U_z dA_{s,i} (T_g - T_c), \quad (\text{E.1})$$

where $dA_{s,i}$ is the incremental heat transfer tube surface area based on the inner tube diameter, T_g and T_c are the local bulk-stream gas and coolant temperatures, and U_z is the local overall heat transfer coefficient that can be determined using the thermal resistances in series as (Kays and London, 1984)

$$U_z dA_{s,i} = \frac{1}{R_{tot}}, \quad (\text{E.2})$$

where R_{tot} represents the total thermal resistance across the tube wall that could be written in terms of the sum of individual thermal resistances as

$$R_{tot} = R_{conv,g} + R_f + R_w + R_{conv,c}, \quad (\text{E.3})$$

where $R_{conv,g}$ and $R_{conv,c}$ are the thermal resistances due to the forced convective heat transfer for the gas and coolant. R_f and R_w are the thermal resistances due to deposited layers and tube wall. These resistances can be determined using a thermal circuit analogy shown in Figure E.1, where the overall heat transfer coefficient based on clean conditions was given as (Kays and London, 1984)

$$\frac{1}{U_{clean,z}} = \frac{1}{h_g} + R_w dA_{s,i} + \frac{dA_{s,i} / dA_{s,o}}{h_c}, \quad (E.4)$$

where h_g and h_c are the gas and coolant local forced convective heat transfer coefficients for tube flow that could be estimated using existing heat transfer correlations. The heat transfer coefficient for gas, h_g , can be estimated using Nusselt number defined (Kays and Crawford, 1980) as

$$Nu_g = \frac{h_g d_i}{k_g}, \quad (E.5)$$

where k_g is the thermal conductivity of the gas, and d_i is the tube inside diameter. Nusselt number is a function of the tube entrance and geometry, thermal boundary conditions, the local Prandtl number for the gas, Pr_g , and flow regime that depends on the Reynolds number for the gas, Re_g . Re_g is given by

$$Re_g = \frac{\rho_g u_g d_i}{\mu_g}, \quad (E.6)$$

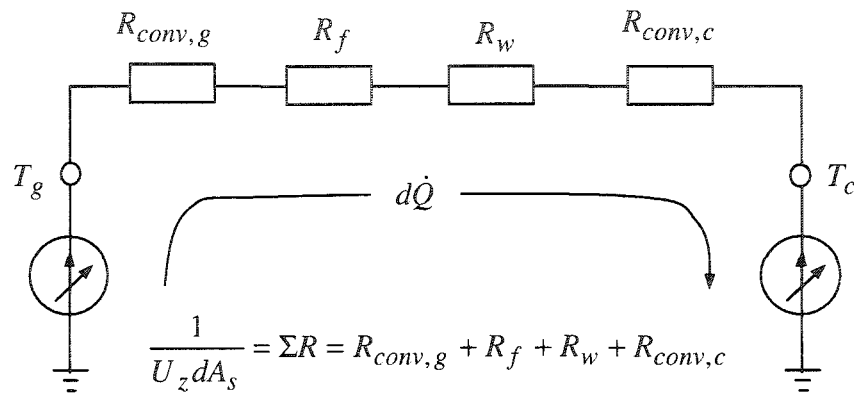


Figure E.1. A thermal circuit representation for the heat transfer rate equation, Eq. (E.1), (Kays and London, 1984). $R_{conv,g}$: thermal resistance due to convective gas; R_f : thermal resistance due to fouling layer; R_w : thermal resistance due to tube wall; $R_{conv,c}$: thermal resistance due to convective coolant; T_g : gas bulk temperature; T_c : coolant bulk temperature; U_z : local overall heat transfer coefficient; dA_s : incremental surface area.

$$\text{Re}_g = \frac{u_g d_i}{\nu_g}, \quad (\text{E.7})$$

and Pr_g is defined as

$$\text{Pr}_g = \frac{\mu_g c_{p,g}}{k_g}. \quad (\text{E.8})$$

where u_g is the bulk stream local gas velocity, and ρ_g, μ_g, ν_g are the local bulk stream thermo-physical properties of density, dynamic viscosity and kinematic viscosity for the gas evaluated at T_g . The correlations used in this work are summarized in Table E.1.

The heat transfer coefficient for the fluid or coolant in the shell side, h_c , was determined using Nusselt number from commonly used correlations. Here, the Nusselt number and Reynolds number for the coolant is given by (Kays and Crawford, 1980)

$$\text{Nu}_c = \frac{h_c D_h}{k_c}, \quad (\text{E.9})$$

$$\text{Re}_c = \frac{\dot{m}_c D_h}{A_f \nu_c}, \quad (\text{E.10})$$

where k_c is the thermal conductivity of the coolant or liquid, and D_h is the hydrodynamic diameter defined by

$$D_h = \frac{4 \times \text{flow area}}{\text{wetted parameter}} = \frac{4 A_f}{P_w}, \quad (\text{E.11})$$

Table E.1: Correlations for convective heat transfer coefficient used in this work.

Flow regime	Nusselt number
(I) Laminar flow $Re \leq 2300$	
Fully developed flow (Shah and London, 1978)	$Nu_{Lam} = 3.66$ (constant wall temperature)
Developing flow ($x/d_i \leq 0.05 Re$) (Kays and Crawford, 1980)	$Nu_{Lam} = 3.66 + \frac{0.104 \frac{Re Pr}{x/d_i}}{1 + 0.016 \left(\frac{Re Pr}{x/d_i} \right)^{0.8}}$
(II) Transitional to turbulent $2300 < Re < 8000$	
Fully developed flow (Gnielinski, 1999)	$Nu_{Trans} = (1 - \gamma)Nu_{Lam,2300} + \gamma Nu_{T,8000}$ $\gamma = \frac{Re - 2300}{8000 - 2300} \quad 0 \leq \gamma \leq 1$
Developing flow (Gnielinski, 1999)	$Nu_{Trans,dev} = (1 - \gamma)Nu_{Lam,dev,2300} + \gamma Nu_{T,dev,8000}$
(III) Turbulent flow $Re \geq 8000$	
Fully developed flow (Petukhov and Kirilov, 1958; White, 1991)	$Nu_T = \frac{(f/2) Re Pr}{1.07 + 12.7 \sqrt{f/2} (Pr^{2/3} - 1)}$
Developing flow ($x/d_i \leq 1.36 Re^{0.25}$) (Shah and Bhatti, 1987; Reynolds et al., 1969)	$Nu_{T,dev} = Nu_T * [1 + 0.8 * (1 + 70000 * Re^{-3/2}) * (x/d_i)^{-1}]$

The equations used to determine D_h and A_f for a given tube bundle layout in the shell-and-tube heat exchanger are summarized in Table E.2. The flow regime in the shell could be cross-flow type, longitudinal type, or both types. The correlations used in this work to estimate the Nusselt number are shown in Tables E.3 and E.4.

For cases where there are large temperature differences in the heat exchanger, such as those applications involving EGR cooling devices, buoyancy effects can become important. The combined convection heat transfer could be considered when the Gr/Re^2 falls toward a value that is typically greater than 10% of this ratio (Thomas, 1999). Gr is Grashof number given by

$$Gr = \frac{g \beta |T_w - T_g| (d_i / 2)^3}{\nu_g^2}, \quad (\text{E.12})$$

where $\beta = 1/T_g$ is the thermal expansion coefficient for the gas, T_w is the tube wall temperature, and g is the gravity acceleration constant. A compiled correlation equation, based on extensive data from existing correlations, recommended by General Electric Company (Heat Transfer Data Book, 1974) seems to reasonably predict natural convection effects within approximately 20% accuracy of compiled data. In this correlation, the heat transfer Nusselt number for combined natural and forced convection in a horizontal tube is given by

$$Nu_{combined} = C_{Natural} Nu_{Forced}, \quad (\text{E.13})$$

Table E.2: The definition of the hydraulic diameter D_h , and flow area A_f , used in Eq. (E.11). (Taborek, 1995.)

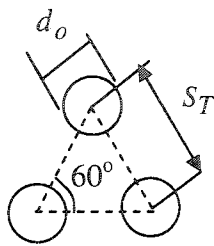
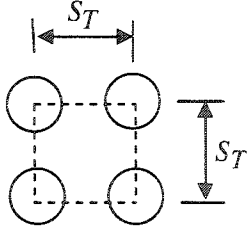
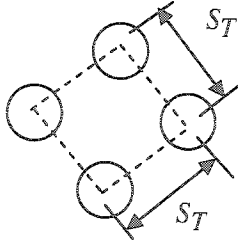
Layout of tube bundle	D_h & A_f
	$A_f = \frac{0.866 S_T^2}{2} - \frac{\pi d_o^2}{8}$ $D_h = \frac{3.464 S_T^2}{\pi d_o} - d_o$
	$A_f = S_T^2 - \frac{\pi d_o^2}{4}$ $D_h = \frac{4 S_T^2}{\pi d_o} - d_o$
	$A_f = S_T^2 - \frac{3\pi d_o^2}{16}$ $D_h = \frac{5.332 S_T^2}{\pi d_o} - d_o$

Table E.3: The correlations used to estimate the Nusselt number for a longitudinal flow regime in the shell.

Flow regime	Nusselt number
Laminar flow $400 < Re \leq 2000$ (Gentry et al., 1982)	$Nu = 0.128 Re^{0.6} Pr^{0.4}$
Transitional and Turbulent flow $Re > 2000$ (Taborek, 1995)	Dittus-Boelter type equation $Nu = C_t (0.023 Re^{0.8} Pr^{0.4})$ $C_t = -0.1315 + 1.5658 PR - 0.415 PR^2$ $PR = \frac{S_T}{d_o}, 1.15 < PR < 2$

Table E.4: Selected correlations used to estimate the Nusselt number for a cross-flow regime in the shell. (Zukauskas, 1987.)

$Nu = C Re^m Pr^n$				
Configuration	Range of Re	C	m	n
In-line	1-100	0.9	0.4	0.36
	100-1000	0.52	0.5	0.36
	1000-2x10 ⁵	0.27	0.63	0.36
	>10 ⁵	0.033	0.8	0.4
Staggered	1-500	1.04	0.4	0.36
	500-1000	0.71	0.5	0.36
	1000-2x10 ⁵	$0.35(S_T/S_L)^{0.2}$	0.6	0.36
	>10 ⁵	$0.031(S_T/S_L)^{0.2}$	0.8	0.36

where Nu_{Forced} is the Nusselt number for forced convection as given in Table E.1, and $C_{Natural}$ is the correction factor to include the effects of natural convection given by

$$C_{Natural} = \left\{ 1 + \left(\frac{0.0083}{\pi} \right) \left[8 \left(\frac{2 - \gamma}{2} \right) Gr Pr \right]^{0.75} \left(\frac{x/d_i}{Re Pr} \right) \right\}^{1/3}, \quad (E.14)$$

where the parameter γ is given by

$$\gamma = \frac{T_g - T_{g,i}}{T_w - T_{g,i}}. \quad (E.15)$$

The thermal performance of the heat exchanger is often characterized using the overall heat transfer coefficient, U , given by (Kays and London, 1984)

$$\dot{Q} = (UA_s) \Delta T_{lm}, \quad (E.16)$$

where \dot{Q} is the overall heat transfer rate across the exchanger, A_s is surface area of the tube bundle, based on inner or outer tube diameters, and ΔT_{lm} is the log-mean temperature difference, for the counter-current exchanger given by

$$\Delta T_{lm} = \frac{(T_{g,i} - T_{c,o}) - (T_{g,o} - T_{c,i})}{\ln \frac{(T_{g,i} - T_{c,o})}{(T_{g,o} - T_{c,i})}}, \quad (E.17)$$

where $T_{g,i}$ and $T_{g,o}$ are inlet and outlet temperatures for the gas, $T_{c,i}$ and $T_{c,o}$ are the inlet and outlet temperatures for the coolant. The thermal performance of

the heat exchanger is also characterized using the heat exchanger thermal effectiveness, ε_{th} , given by (Kays and London, 1984)

$$\varepsilon_{th} = \frac{\dot{Q}}{\dot{Q}_{max}}, \quad (E.18)$$

where \dot{Q}_{max} is the maximum possible heat transfer rate. This is given by

$$\dot{Q}_{max} = (\dot{m}c_p)_{min} \Delta T_{max}, \quad (E.19)$$

where $\Delta T_{max} = (T_{g,i} - T_{c,i})$, and $(\dot{m}c_p)_g$ is the heat capacity rate for the gas.

The pressure drop across a tubular passage consists of a variety of components, shown in Figure E.2, given by (Shah, 1981)

$$\Delta p_{1-2} = \Delta p_{1-i} + \Delta p_{i-o} + \Delta p_{o-2}, \quad (E.20)$$

where Δp_{i-o} is the core pressure loss caused by conventional frictional losses. It is given by (Kays and London, 1984)

$$\Delta p_{i-o} = \frac{\rho_b u_b^2}{2} \left(f \frac{L}{D_h} \right), \quad (E.21)$$

where, ρ_b, u_b , and f are the fluid bulk-stream density and velocity in the tube (or tubes) inside the heat exchanger core, and Moody (or Darcy) friction factor for a fully developed flow, respectively. The pressure drop due to entrance, Δp_{1-i} , is given by (Kays and London, 1984)

$$\Delta p_{1-i} = \frac{\rho_b u_b^2}{2} \left[(1 - \sigma^2) + K_c \right], \quad (E.22)$$

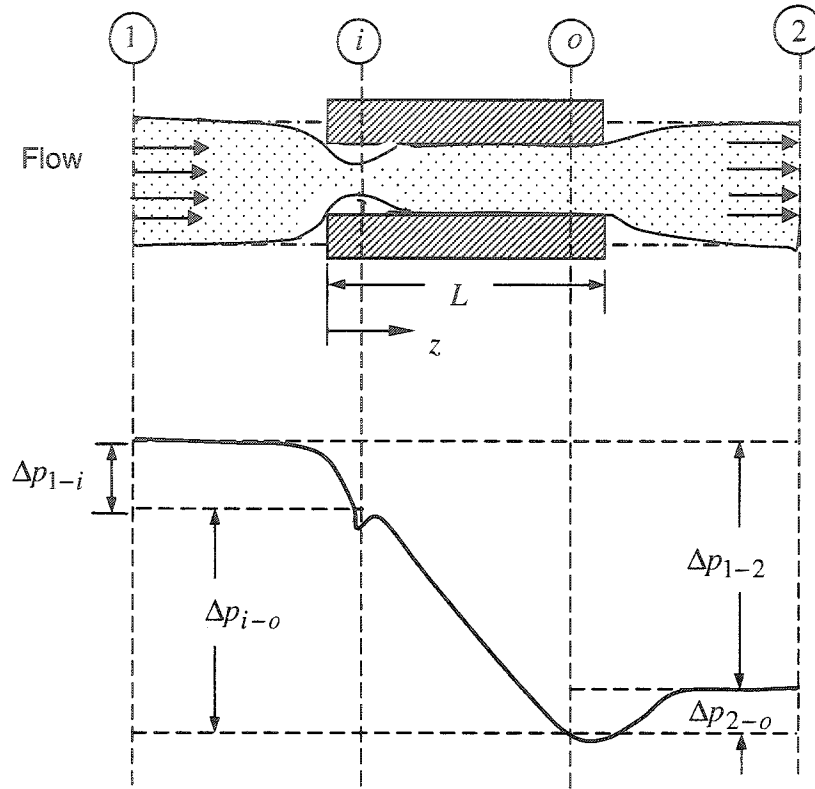


Figure E.2. Components of total pressure change for a flow through a tubular passage. (Shah, 1981.)

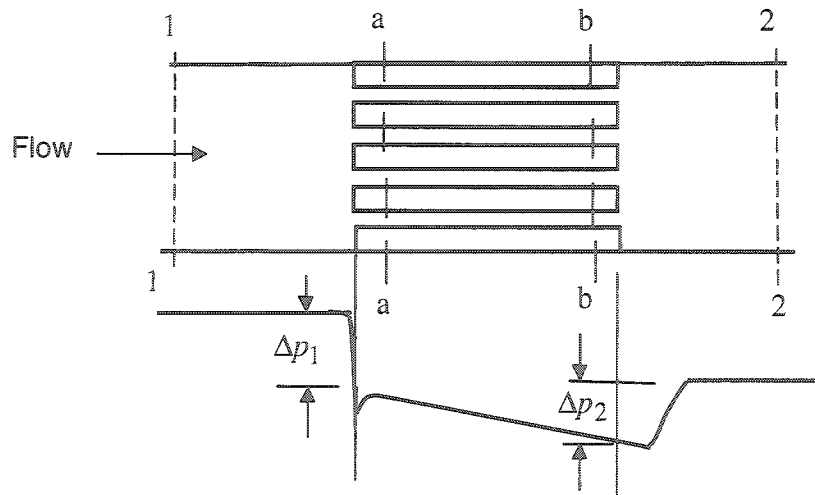


Figure E.3. Heat exchanger core model for pressure drop analysis. (Kays and London, 1984.)

where K_c is the entrance-loss coefficient, and σ is the flow area contraction ratio. Δp_{1-i} is made up of the pressure drop which would occur due to flow-area change alone (without friction), and the pressure loss due to the irreversible free-expansion that always follows the abrupt contraction caused by boundary-layer separation, and the consequent pressure change due to change of momentum rate associated with changes in downstream velocity profile. The exit pressure change, Δp_{o-2} is given by (Kays and London, 1984)

$$\Delta p_{o-2} = \frac{\rho_b u_b^2}{2} [(\sigma^2 - 1) + K_e], \quad (\text{E.23})$$

where K_e is the abrupt expansion or exit coefficient. The exit pressure change consists of the pressure rise which would occur due to area change (without friction) which is identical to the corresponding term in the entrance pressure drop, and the pressure loss caused by the irreversible free expansion and momentum changes downstream of an abrupt expansion. The total pressure change for a gas flow inside a core of multi-channel heat exchanger, shown in Figure E.3, can be modeled with a large temperature difference, as

$$\Delta p_{1-2} \approx \frac{G^2}{2} v_1 \left[(K_c + 1 - \sigma^2) + 2 \left(\frac{v_2}{v_1} - 1 \right) + f \frac{L}{D_h} \frac{v_{avg}}{v_1} - (1 - \sigma^2 - K_e) \frac{v_2}{v_1} \right], \quad (\text{E.24})$$

where G , v_1 , and v_2 are the gas mass flux ($G = \rho u$), and the gas specific volume at inlet and exit ($v = 1/\rho$). The entrance- and expansion-loss coefficients,

K_c and K_e , are functions of the contraction and expansion geometry and, in some cases, of the Reynolds number in the channels. These coefficients were determined analytically by Kays (1950) and reported graphically by Kays and London (1984) as shown in Figure E.4. The flow at the tube entrance separates from the inner surface, including a local flow separation, if the inlet to the tube edge is not sufficiently rounded, that is a major source of the entrance pressure losses.

The friction factor can be determined from the Moody diagram (Moody, 1944). Selected correlations that reasonably approximate the friction factor are summarized in Table E.5. The friction factor is independent of surface roughness for laminar flow unless the roughness is sufficient to cause significant changes in the flow pattern. The friction factor increases with surface roughness, e , for turbulent flow regime. At large Reynolds number the friction factor becomes approximately independent of Reynolds number in the rough region. For laminar flow regime, typical of low flow velocity, the thickness of the viscous layer near the tube wall is typically larger than the roughness protuberances, shown in Figure E.5a, so that the latter are entirely covered with this layer. In this case, the fluid moves smoothly past surface irregularities so that they have no effect on the flow character. Therefore, the roughness of the tube wall, unless it is very significant, does not affect the flow resistance. With an increase in the Reynolds number, the inertia forces begin to dominate, and the viscous sublayer becomes

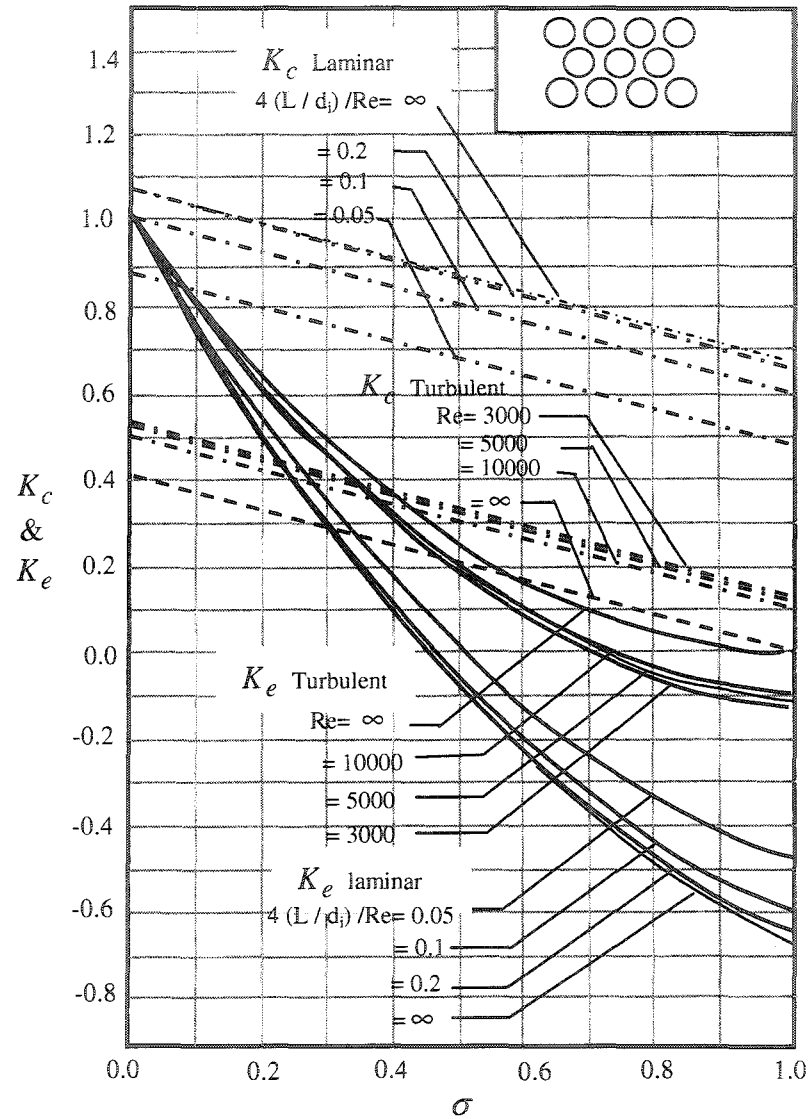


Figure E.4. Entrance and exit pressure-loss coefficients for a multiple-circular-tube heat exchanger core with abrupt-contraction entrance and abrupt-expansion exit (Kays and London, 1984). σ : tube contraction ratio = tube cross-sectional area divided by tube frontal area; K_c : entrance-loss coefficient; K_e : exit-loss coefficient; Re: Reynolds number; L: tube; d_i : tube diameter.

Table E.5: Selected correlations for friction factor for fully developed tube flow used in the present model (Thomas, 1999; Fox et al., 2004).

Flow regime	Friction factor
Laminar flow $Re \leq 2300$	$f = \frac{64}{Re}$ $f_{corr} = f \left(\frac{T_w}{T_b} \right) : \text{correction for the variation of the flow properties over tube cross section.}$
Transitional to turbulent flow $2300 < Re < 4000$	$f_{Trans} = (1 - \gamma) f_{Lam,2300} + \gamma f_{T,4000}$ $\gamma = \frac{Re - 2300}{4000 - 2300} \quad 0 \leq \gamma \leq 1$
Turbulent flow	$f = 0.316 Re^{-0.25} \quad Re \leq 2 \times 10^4, \text{ smooth tube}$ $f = 0.184 Re^{-0.2} \quad Re > 2 \times 10^4, \text{ smooth tube}$ $f = (0.790 \ln Re - 1.64)^{-2} \quad 3000 \leq Re \leq 5 \times 10^6, \text{ smooth tube}$ $\frac{1}{f^{0.5}} = -2.0 \log \left(\frac{e/d_t}{3.7} + \frac{2.51}{Re f^{0.5}} \right) \quad Re > 1 \times 10^4, \text{ rough tube}$ $f_{corr} = f \left(\frac{T_w}{T_b} \right)^{-0.1} : \text{correction for the variation of the flow properties over tube cross section.}$

thinner, and at a high Reynolds number, it becomes smaller than the height of the roughness asperities as shown in Figure E.5b (Idelchick, 1986). The asperities cause the sublayer to separate, thus enhance the formation of vortices or eddies, which promote more turbulence, and hence increase the flow resistance to turbulent flow that tends to increase the pressure losses.

The thermal and hydraulic characteristics in single-phase shell-and-tube heat exchangers could be related. The pressure drop, Δp , is approximately directly proportional to the flow velocity, u , for the laminar flow, and proportional to $u^{1.6-1.8}$ for the turbulent flow. The convective heat transfer coefficient is related to the flow velocity by $h \propto u^{0.3}$ for the laminar flow, and $h \propto u^{0.6-0.8}$ for the turbulent flow, thus the heat transfer coefficient could be related to the pressure drop by $h \propto \Delta p^{0.3}$ for the laminar flow, and $h \propto \Delta p^{0.4}$ for the turbulent flow (Bell, 1983).

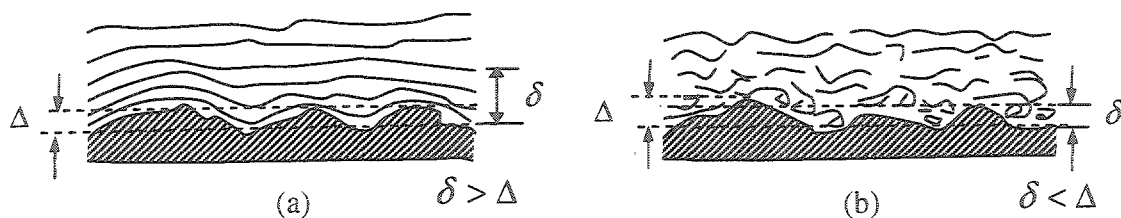


Figure E.5. Schematic of flow passing roughness asperities for laminar and turbulent flow regimes: (a) $\delta > \Delta$; (b) $\delta < \Delta$. (Idelchick, 1986.)

Appendix F: The Numerical Scheme Used in this Investigation

A schematic showing the numerical scheme used in the present model is shown in Figure F.1. The heat transfer and pressure drop computational equations used in the present model are given in Table F.1, and a simplified flow chart showing the computation procedure is shown in Figures F.2(a) through (c).

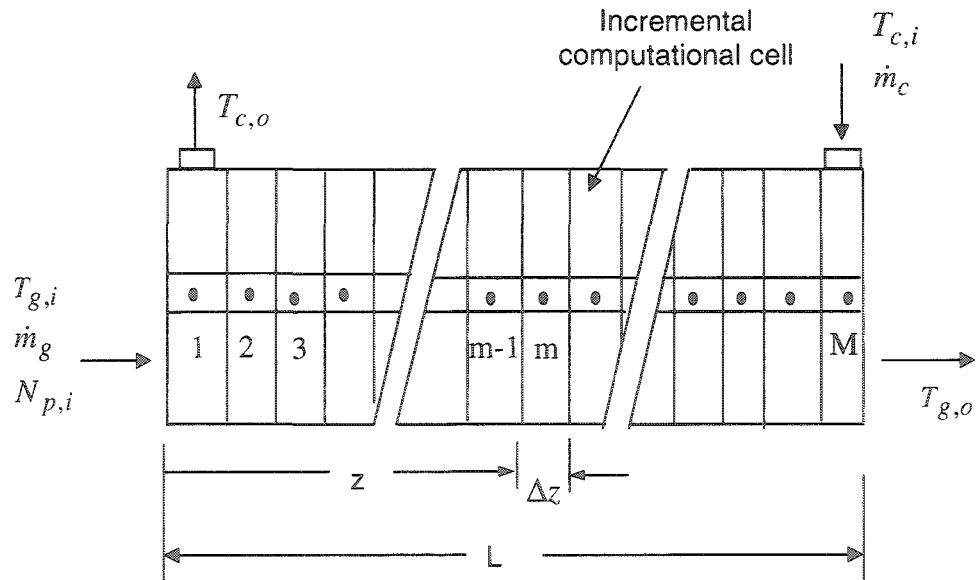
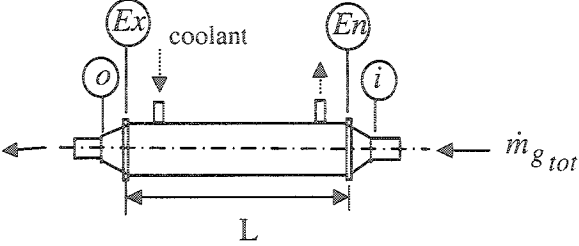


Figure F.1. The numerical scheme used in the present model.

Table F.1: The heat transfer and pressure 1-D computational equations used in the present model.

Heat transfer	$\Delta q_m = U_m \Delta A_s (T_g - T_c)_m$ $\Delta q_m = C_g (T_{g,m} - T_{g,m+1}), \Delta q_m = C_c (T_{c,m+1} - T_{c,m})$ $C_c = (\dot{m}c_p)_c, C_g = (\dot{m}c_p)_g$ $U_m = \frac{1}{\Delta A_{s_m} R_{tot_m}}, \frac{1}{U_m} = \frac{1}{U_{clean_m}} + r_{s_m}$ $R_{tot_m} = R_{c,g_m} + R_{s_m} + R_w + R_{c,c_m}$ $\frac{1}{U_{clean_m}} = \frac{1}{h_{g_m}} + R_w \Delta A_{s_m} + \frac{\Delta A_{s_m} / \Delta A_{s,o}}{h_{c_m}}$ $r_{s_m} = R_{s_m} \Delta A_{s_m} = \Delta A_{s_m} \frac{\ln(d_i / d_{s_m})}{2\pi k_s \Delta z} = \frac{d_o}{2k_s} \ln \frac{d_i}{d_{s_m}} \quad (d_i = \text{inner diameter, } d_o = \text{outer diameter, } d_s = \text{inner diameter based on soot thickness})$ $d_s = d_i - 2\delta_s, \Delta A_{s_m} = \pi d_o \Delta z, \Delta z = \frac{1}{M-1}, M = \text{total number of cells.}$
Gas Pressure drop	$(\Delta P)_{m+1-m} = \frac{G^2}{2} \left(\frac{K_m}{\rho_{g_m}} + \frac{K_{m+1}}{\rho_{g_{m+1}}} \right) + 2f_m \frac{\Delta z}{d_t \bar{\rho}_b} G^2 + G^2 \left(\frac{1}{\rho_{g_{m+1}}} - \frac{1}{\rho_{g_m}} \right)$ $G = \frac{\dot{m}_g}{A_t}, \Delta P_{i-ent} = \frac{G^2}{2\rho_{b_i}} \left[1 - \left(\frac{A_{ent}}{A_i} \right)^2 \right], \Delta P_{ex-o} = \frac{G^2}{2\rho_{b_{ex}}} \left[\left(\frac{A_{ex}}{A_o} \right)^2 - 1 \right]$ $\Delta P_{total} = \Delta P_{En-Ex} + \Delta P_{i-En} + \Delta P_{Ex-o}$
 <p style="text-align: center;">EGR cooling device</p>	

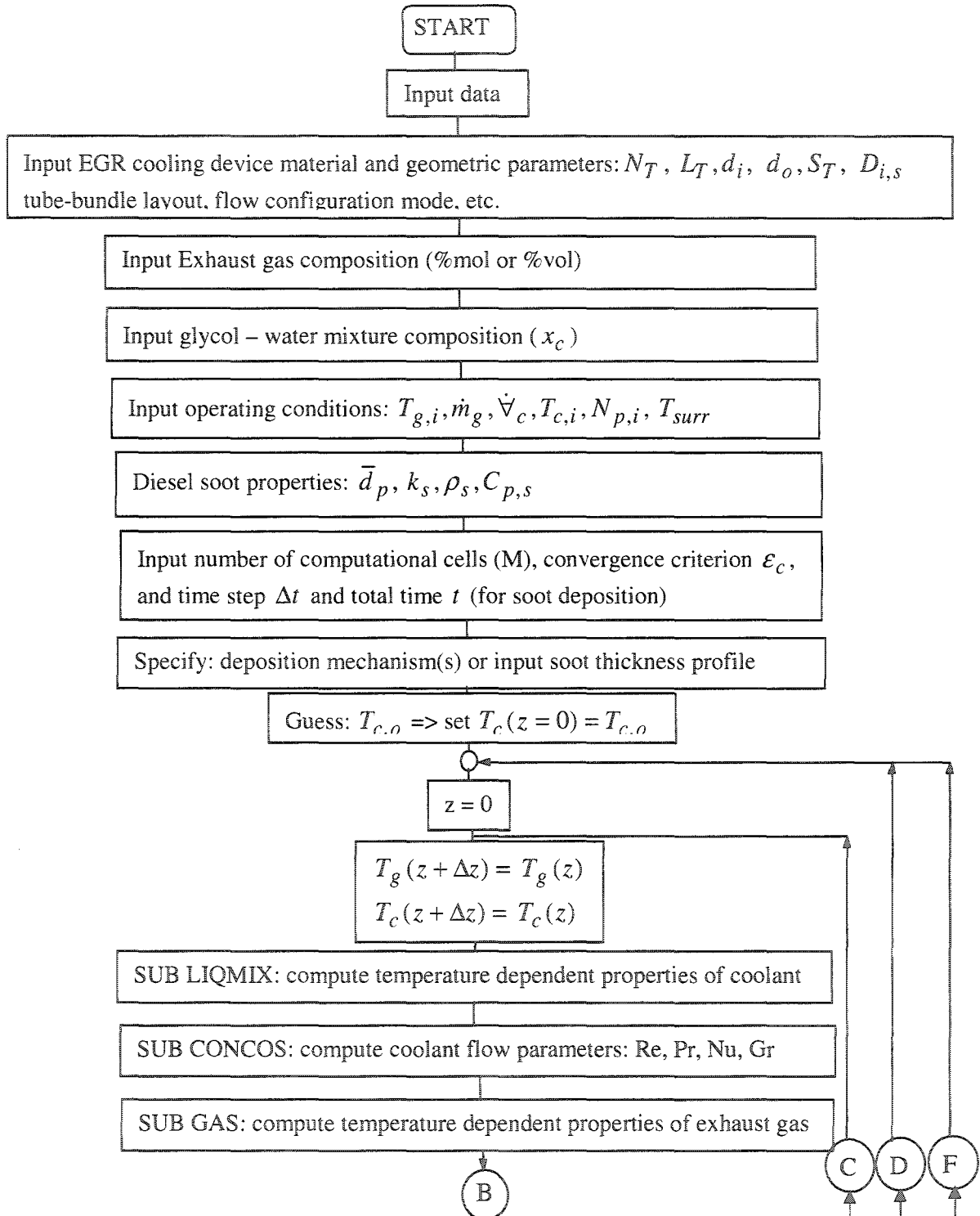


Figure F.2(a). Flow chart for computation of heat transfer and soot deposition characteristics in EGR cooling device.

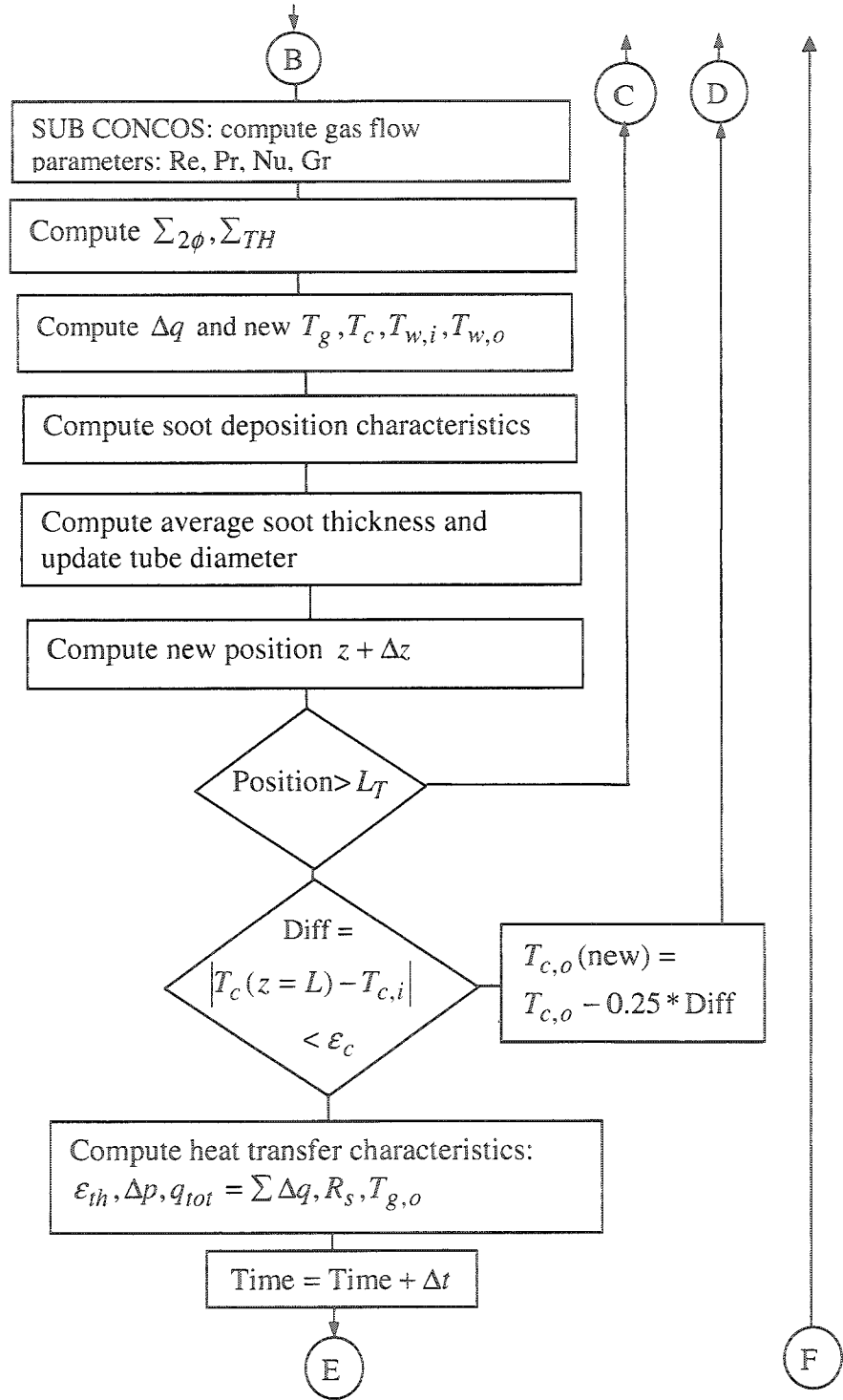


Figure F.2(b). Continued: Flow chart for computation of heat transfer and soot deposition characteristics in EGR cooling device.

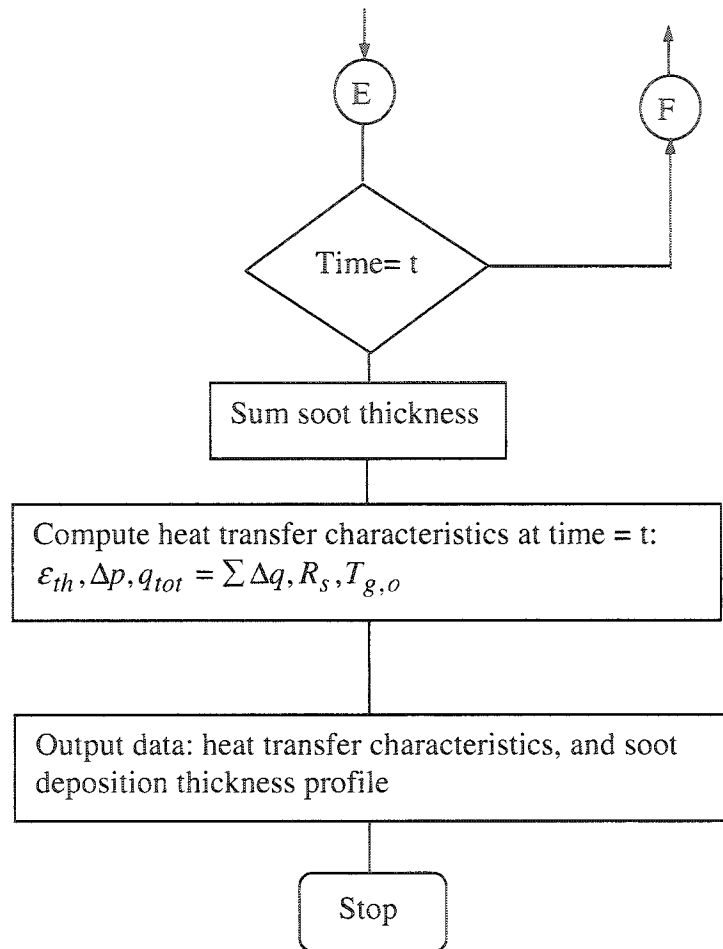


Figure F.2(c). Continued: Flow chart for computation of heat transfer and soot deposition characteristics in EGR cooling device.

Appendix G: Uncertainty Analysis

The total uncertainty in a performance parameter of interest P is commonly represented to first order accuracy by a root-sum-square equation of the form (Holman, 1989)

$$U_P = \pm \sqrt{\sum_{j=1}^n (\Phi_j U_{x_j})^2} , \quad (\text{G.1})$$

where Φ_j is the sensitivity increment of each experimental input parameter, x_j , and U_{x_j} is the uncertainty in x_j . The sensitivity increment is defined by

$$\Phi_j = \frac{\partial P}{\partial x_j} . \quad (\text{G.2})$$

For example, the total uncertainty in the gas side heat transfer rate, $U_{\dot{Q}_g}$, is determined using

$$U_{\dot{Q}_g} = \left[(\rho_g c_{p_g} \Delta T_g U_{\dot{V}_g})^2 + (\rho_g c_{p_g} \dot{V}_g U_{\Delta T_g})^2 \right]^{1/2} , \quad (\text{G.3})$$

and the total uncertainty for the coolant heat transfer rate is given by

$$U_{\dot{Q}_c} = \left[(\rho_c c_{p_c} \Delta T_c U_{\dot{V}_c})^2 + (\rho_c c_{p_c} \dot{V}_c U_{\Delta T_c})^2 \right]^{1/2} \quad (\text{G.4})$$

The relative uncertainty of the coolant temperature difference, $U_{\Delta T_c}$, was determined by calibrating the coolant T-type thermocouple measurements that were recorded for the isothermal coolant flow and then subtracting this offset from the actual temperature difference. It was determined that $U_{\Delta T_c} \approx \pm 0.25^\circ C$.

Appendix H: Image Processing Procedure

A simplified flow chart of the image processing procedure for the digital neutron radiography used in this investigation is shown in Figure H.1.

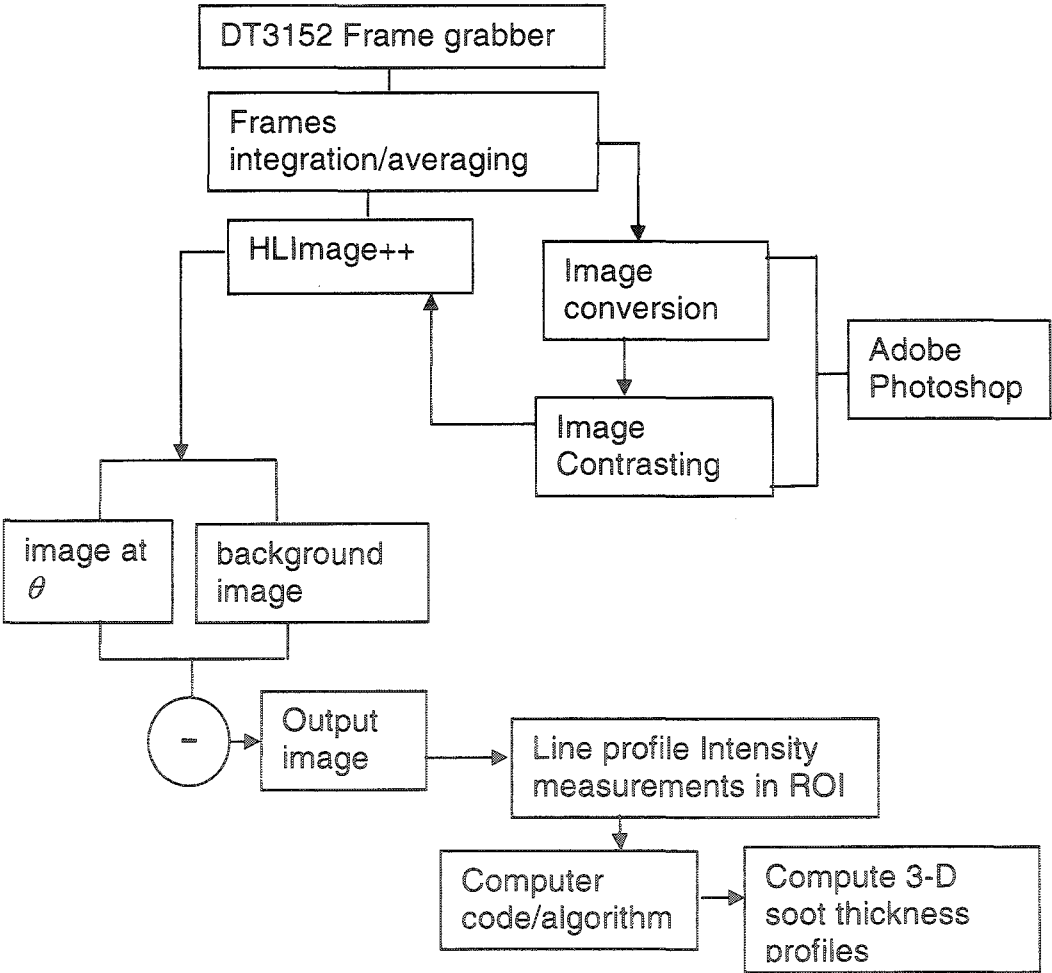
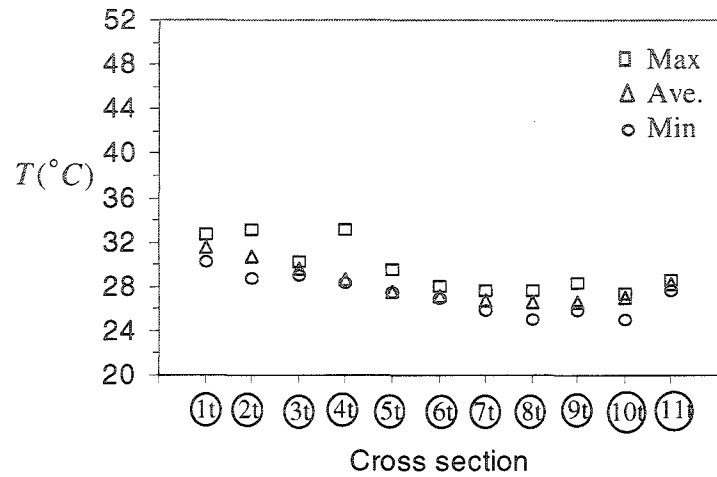


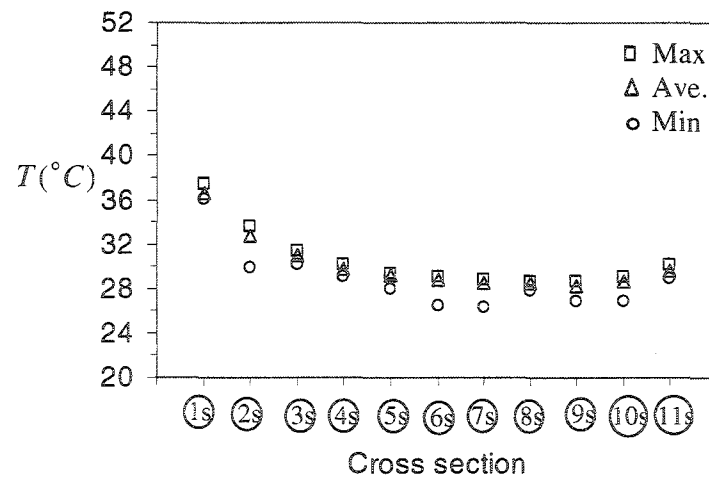
Figure H.1. A simplified flow chart of the image processing procedure used in the present work.

Appendix I: Additional Results of the Thermal Characteristics of the Secondary Coolant Flow across the Three-Tube EGR Cooling Device

Following are the experimental results of the time-dependent thermal characteristics of the secondary coolant flow across the three-tube EGR cooling device flow coolant rate of 2.5 l/min and higher coolant flow rate of 6 l/min determined using the IR thermal camera system. For all these tests, the cooling device was exposed to diesel exhaust in the EGR section in the diesel test facility at gas flow rate of 6 kg/hr, while the inlet coolant temperature was maintained at approximately 25 °C. Thermal images were acquired from top and side views of the three-tube EGR cooling device at every one hour of the test duration for both coolant flow rates tests. The images were then analyzed to determine the time-dependent temperature distribution for the coolant flow across the cooling device for both coolant flow rates. The minimum, average, and maximum coolant temperatures were determined at cross sections spaced equally with distance 20 mm along the cooling device for top and side views of the cooling device as shown in Figure 5.22.

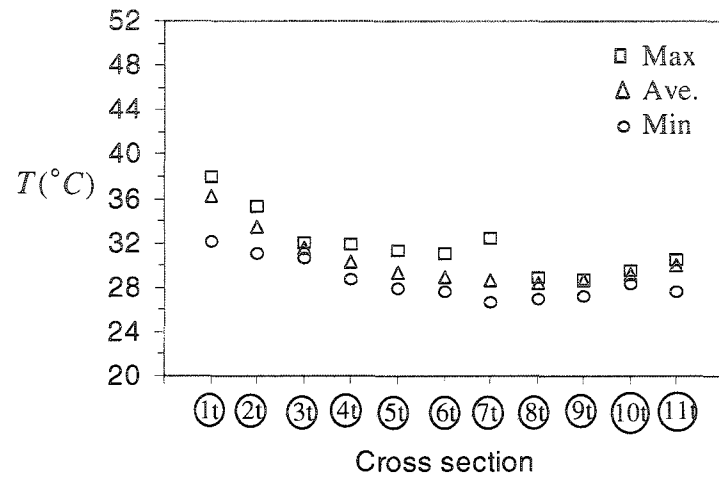


(a) Top view

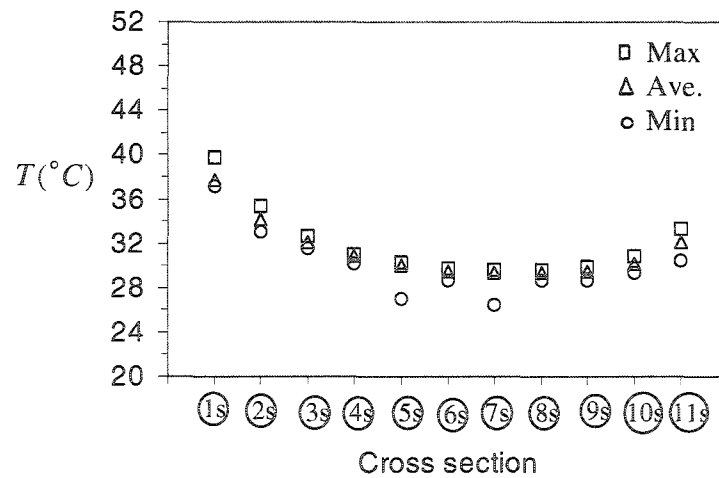


(b) Side view

Figure I.1. Change in the coolant temperature at different cross sections along the three-tube cooling device determined from the initial thermal images of the (a) top view, and (b) side view for the coolant flow rate test of 2.5 l/min.

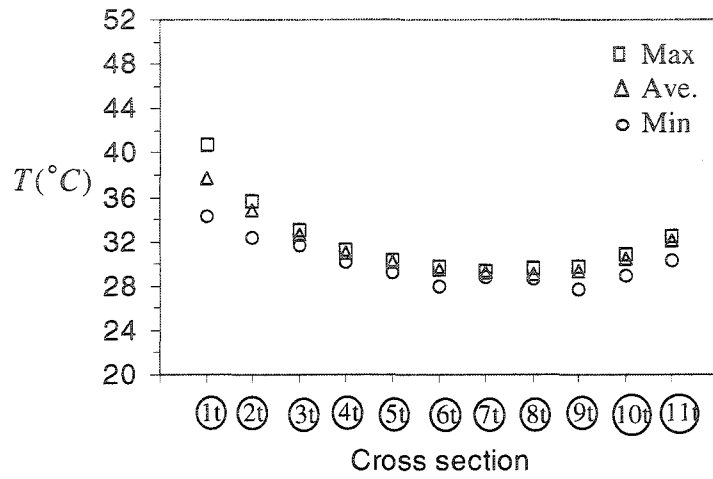


(a) Top view

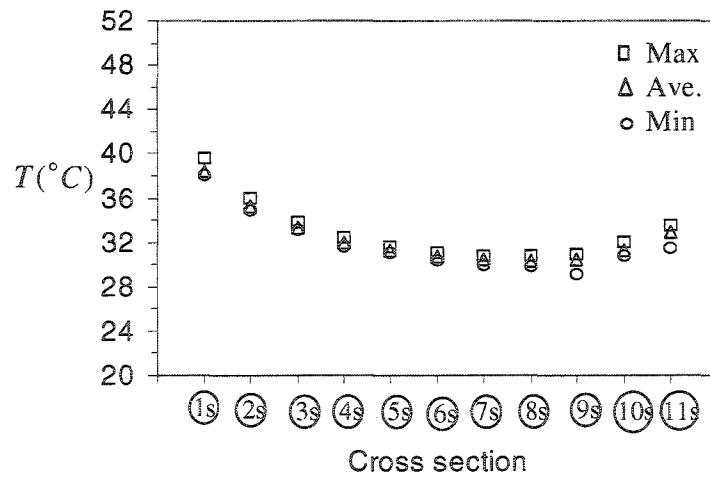


(b) Side view

Figure 1.2. Change in the coolant temperature at different cross sections along the three-tube cooling device determined from the thermal images of the (a) top view, and (b) side view for 1 hour test with coolant flow rate of 2.5 l/min.

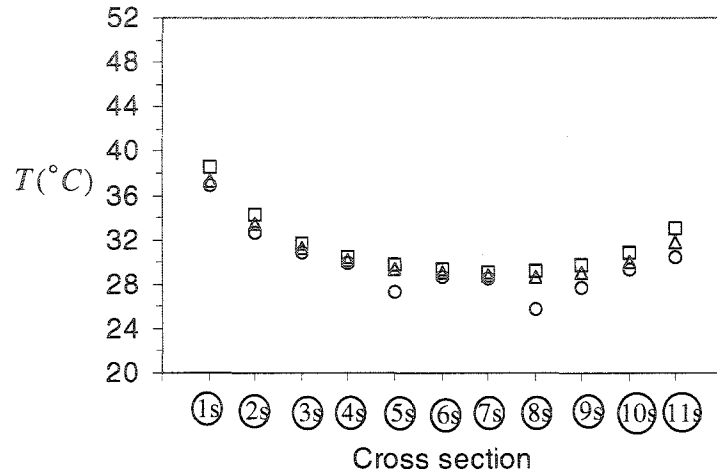


(a) Top view

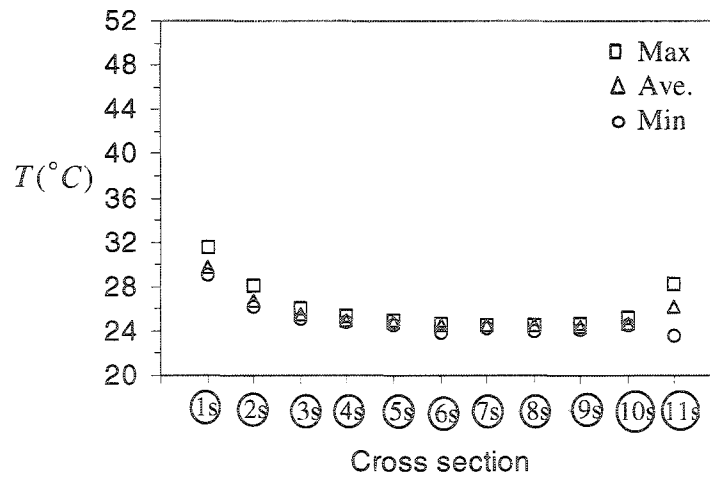


(b) Side view

Figure I.3. Change in the coolant temperature at different cross sections along the three-tube cooling device determined from the thermal images of the (a) top view, and (b) side view for 2 hour test with coolant flow rate of 2.5 l/min.

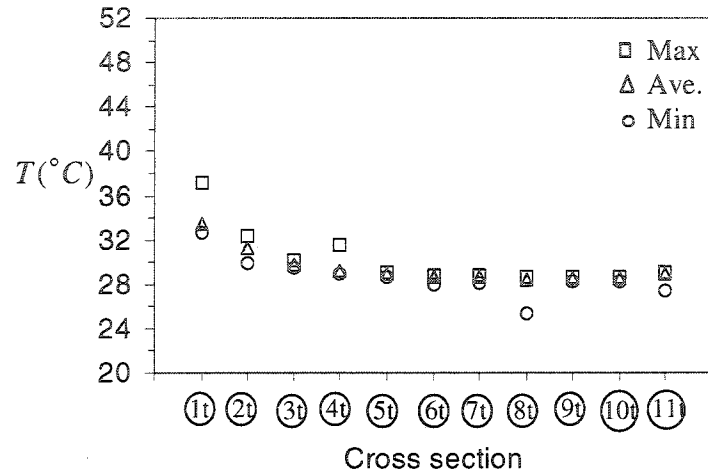


(a) Top view

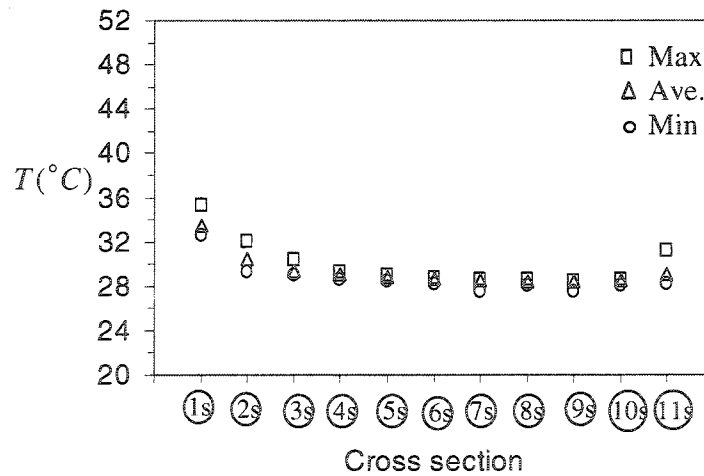


(b) Side view

Figure I.4. Change in the coolant temperature at different cross sections along the three-tube cooling device determined from the initial thermal images of the (a) top view, and (b) side view for the coolant flow rate test of 6 l/min.

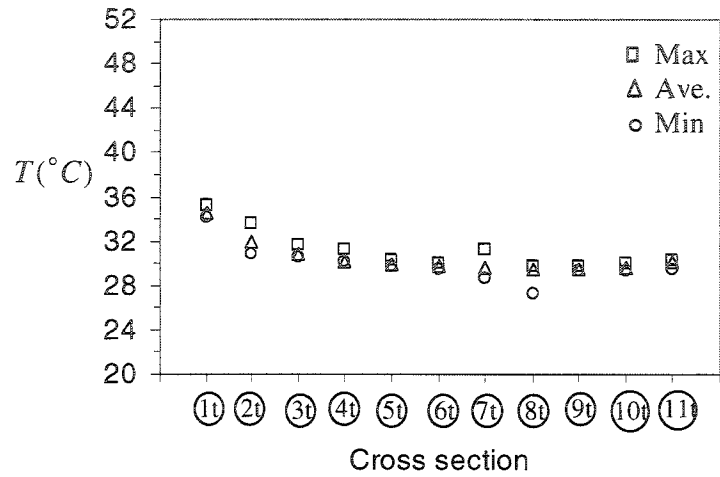


(a) Top view

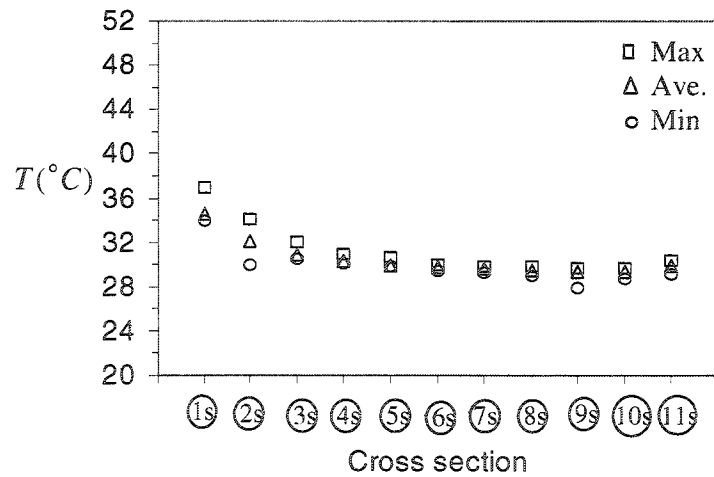


(b) Side view

Figure I.5. Change in the coolant temperature at different cross sections along the three-tube cooling device determined from the thermal images of the (a) top view, and (b) side view for 1 hour test with coolant flow rate of 6 l/min.

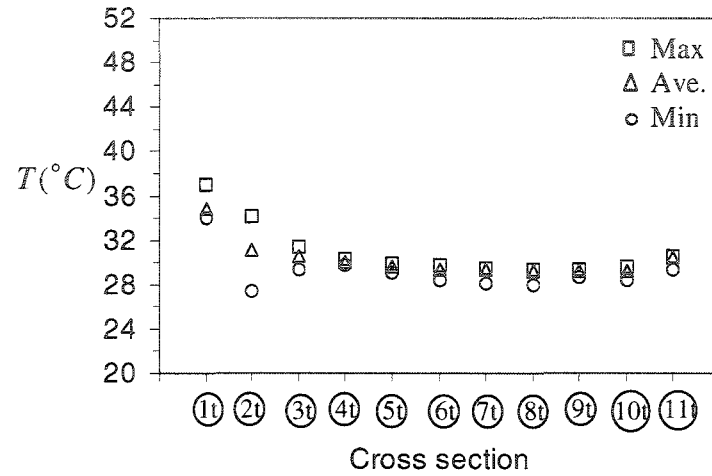


(a) Top view

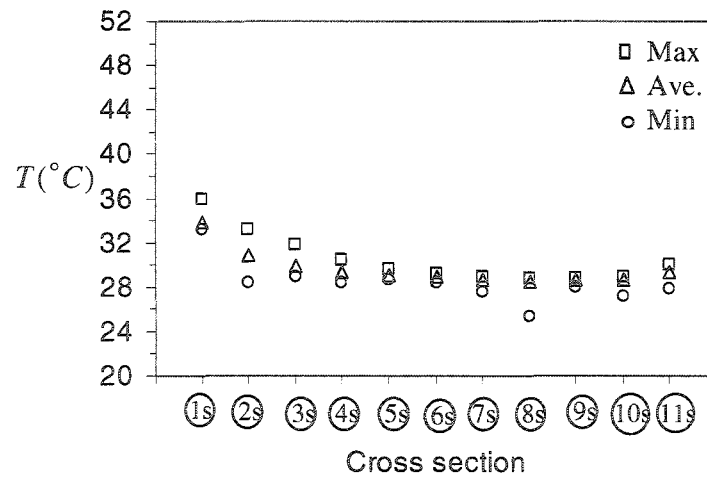


(b) Side view

Figure I.6. Change in the coolant temperature at different cross sections along the three-tube cooling device determined from the thermal images of the (a) top view, and (b) side view for 2 hours test with coolant flow rate of 6 l/min.



(a) Top view



(b) Side view

Figure I.7. Change in the coolant temperature at different cross sections along the three-tube cooling device determined from the thermal images of the (a) top view, and (b) side view during 3 hours test with coolant flow rate of 6 l/min.

Appendix J: Author's Publications

J.1 Publications Based on the Results of this Dissertation

Ismail, B., Ewing, D., Chang, J.-S., & Cotton, J. S. (2004). Development of a non-destructive neutron radiography technique to measure the three-dimensional soot deposition profiles in diesel engine exhaust systems. *Journal of Aerosol Science*. In press.

Ismail, B., Ewing, D., Cotton, J. S. & Chang, J.-S. (2004). Characterization of the soot deposition profiles in diesel engine exhaust gas recirculation (EGR) cooling devices using a digital neutron radiography imaging technique. *Society of Automotive Engineers, Inc. Transactions of SAE*. In press.

Ismail, B., Ewing, D., Cotton, J. S. & Chang, J.-S. (2004). Characterization of the soot deposition profiles in diesel engine exhaust gas recirculation (EGR) cooling devices using a digital neutron radiography imaging technique. *Society of Automotive Engineers, Inc. SAE paper no. 2004-01-1433*.

Ismail, B., Ewing, D., & Chang, J.-S. (2003). Modeling the deposition of the soot from diesel exhaust gases in tubes of heat exchangers. *The 53rd Canadian Chemical Engineering Conference (CSCChE)*, Hamilton, Canada, p. 232.

Ismail, B., Ewing, D., Chang, J.-S., & Cotton, J. S. (2003). Measurement of diesel soot deposition profiles in exhaust gas tubes by a digital neutron radiography imaging system. *European Aerosol Conference (EAC) Madrid. Journal of Aerosol Science*, special edition, pp.S1205-S1206.

Ismail, B., Chang, J.-S., Ewing, D., & Cotton, J. S. (2002). Carbon soot deposition profile measurement for diesel engine exhaust gas recirculation system cooler by a digital neutron radiography system. *Journal of Aerosol Science*, special edition. pp.S1057-S1058.

Ismail, B., Zhang, R., Ewing, D., Chang, J.-S., & Cotton, J. (2002). The heat transfer characteristics of exhaust gas recirculation (EGR) cooling devices. *Proceedings of the ASME International Mechanical Engineering Congress and Exposition (IMECE)*, ASME paper No. IMECE HT-34559, LA, USA.

Other Contributions on the Results of this Dissertation

Ismail, B., Ewing, D., Chang, J.-S., & Cotton, J. (2003). Characterizing the heat transfer performance of EGR cooling devices for diesel engines emissions control. *CRESTech Innovation network conference*, Toronto.

Ismail, B., Ewing, D., Chang, J.-S., & Cotton, J. (2002). Characterizing the heat transfer performance of EGR cooling devices for diesel engines emissions control. *CRESTech Innovation network conference*, Toronto.

Ismail, B., Ewing, D., Chang, J.-S., & Cotton, J. (2001). Characterizing the heat transfer performance of EGR cooling devices for diesel engines emissions control. *CRESTech Innovation network conference*, Toronto.

Ismail, B. & Ewing, D. (2001). Modeling the heat transfer performance of EGR cooling devices. *5th 1000 Island Fluid dynamics meeting*, 1000 Islands, Canada.

J.2 Publications Unrelated to this Dissertation

- Al-Sulaiman, F. A., & Ismail, B. (1997). Estimation of monthly average daily and hourly solar radiation impinging on a sloped surface using the isotropic sky model for Dhahran, Saudi Arabia. *Renewable Energy*, vol. 11, No. 2, pp. 257-262.
- Said, S.A.M., Kadry, H., & Ismail, B. (1996). Climatic Conditions for Saudi Arabia. *ASHRAE Transactions*, vol. 102, Pt.1, P. 3935.
- Al-Sulaiman, F. A., & Ismail, B. (1995). Exergy analysis of major recirculating multi-stage flash desalting plants in Saudi Arabia. *Desalination*, vol. 103, Iss. 3, pp. 265-270.
- Said, S.A.M., Suleiman, Y. M., & Ismail, B. (1995). Theoretical performance of HCFC123 as an alternative to CFC11. *Energy*, vol.20, Iss. 3, pp.205-208.
- Said, S.A.M., & Ismail, B. (1994). Exergetic Assessment of the Coolants HCFC123, HFC134a, CFC11, and CFC12. *Energy*, vol.19, Iss. 11, pp. 1181-1186.
- Sulieiman, Y. M., Said, S.A.M., & Ismail, B. (1994). HCFC22 as a replacement for CFC12. *Applied Energy*, vol.49, Iss 1, pp.1-8.

Appendix K: Copyright Exceptions

It is understood that the copyrights for the material in this dissertation is shared between the author and supervisors, D. Ewing, and J.-S. Chang.